DISSERTATION

THE DYNAMIC EVOLUTION OF ACTIVE-REGION-SCALE MAGNETIC FLUX TUBES IN THE TURBULENT SOLAR CONVECTIVE ENVELOPE

Submitted by

Maria Ann Weber

Department of Physics

In partial fulfillment of the requirements

For the Degree of Doctor of Philosophy

Colorado State University

Fort Collins, Colorado

Summer 2014

Doctoral Committee:

Advisor: David Krueger
Co-Advisor: Yuhong Fan

Roger Culver
Wayne Schubert

ABSTRACT

THE DYNAMIC EVOLUTION OF ACTIVE-REGION-SCALE MAGNETIC FLUX TUBES IN THE TURBULENT SOLAR CONVECTIVE ENVELOPE

The Sun exhibits cyclic properties of its large-scale magnetic field on the order of $\sim$22 years, with a $\sim$11 year frequency of sunspot occurrence. These sunspots, or active regions, are the centers of magnetically driven phenomena such as flares and coronal mass ejections. Volatile solar magnetic events directed toward the Earth pose a threat to human activities and our increasingly technological society. As such, the origin and nature of solar magnetic flux emergence is a topic of global concern.

Sunspots are observable manifestations of solar magnetic fields, thus providing a photospheric link to the deep-seated dynamo mechanism. However, the manner by which bundles of magnetic field, or flux tubes, traverse the convection zone to eventual emergence at the solar surface is not well understood. To provide a connection between dynamo-generated magnetic fields and sunspots, I have performed simulations of magnetic flux emergence through the bulk of a turbulent, solar convective envelope by employing a thin flux tube model subject to interaction with flows taken from a hydrodynamic convection simulation computed through the Anelastic Spherical Harmonic (ASH) code. The convective velocity field interacts with the flux tube through the drag force it experiences as it traverses through the convecting medium.

Through performing these simulations, much insight has been gained about the influence of turbulent solar-like convection on the flux emergence process and resulting active region

properties. I find that the dynamic evolution of flux tubes change from convection dominated to magnetic buoyancy dominated as the initial field strength of the flux tubes increases from 15 kG to 100 kG. Additionally, active-region-scale flux tubes ($10^{21} - 10^{22}$ Mx) of 40 kG and greater exhibit properties similar to those of active regions on the Sun, such as: tilt angles, rotation rates, and morphological asymmetries. The joint effect of the Coriolis force and helical motions present in convective upflows help tilt the apex of rising flux tubes toward the equator in accordance with Joys Law.

Utilizing these simulations, I find that rotationally aligned, columnar convective structures called *giant cells* present near the equatorial regions of the ASH simulation organizes flux emergence into a large-scale longitudinal pattern similar to the active longitude trend on the Sun and other solar-like stars. The effect of radiative diffusion across the radiation zone-convection zone interface on the buoyant rise of magnetic flux tubes is also studied. Incorporating this effect into the flux tube model, flux tubes with magnetic field strengths of 60 kG or less no longer anchor in the stably stratified overshoot region. These flux tubes still have average emergence properties that agree with observations of solar active regions, although tilt angles have a larger scatter about the mean value. Finally, I will discuss possible future research problems that can be investigated through the thin flux tube approach, such as convection-induced twisting of the flux tube magnetic field lines and flux emergence properties on a young Sun rotating at 5 times the current solar rate.

ACKNOWLEDGEMENTS

My acknowledgements section is probably larger than what is found in most PhD dissertations. However, it is the people and places I have encountered in my life that have made this document a reality. This section is only a small token of my many thanks.

My most heartfelt gratitude goes to my advisor at High Altitude Observatory (HAO), Dr. Yuhong Fan. She has been the most wonderful, attentive, and patient advisor I could ask for. I have learned so much, and have grown leaps and bounds as a scientist under her care. I am so grateful that she decided to take me on as a PhD student in 2010, and I am privileged to have been her first PhD student thus far. Her work ethic and dedication to science are traits I hope to carry with me throughout my career. Thanks Yuhong! (P.S. I occasionally describe her to my friends as my own personal Yoda.)

Dr. David Krueger was my professor for two semesters of quantum mechanics and two semesters of electricity and magnetism at Colorado State University (CSU). Despite this, he still agreed to be my CSU faculty advisor! I appreciate his willingness to take me on as his final graduate student. We have learned many things from each other. Particularly, I have taught him a little bit about solar physics, and he has reminded me to never forget about first principles. I have thoroughly enjoyed our monthly on-campus meetings. While I have been immersed in the solar physics community at HAO for the past four years, my meetings with David always bring me back to my physics roots.

Until I arrived at HAO, I knew next to nothing about stellar convection. Admittedly, I still have much to learn, but I owe many thanks to Dr. Mark Miesch for guiding me through the convection and stellar dynamo zoo. His insight and suggestions regarding my research

and papers have been most helpful, always leading to a deeper understanding on my part. Additionally, Mark performed the ASH simulations I have used throughout much of the research in this dissertation.

Of course I could not have passed my masters exam, prelim, or oral dissertation defense without my committee members: David Krueger, Yuhong Fan, Roger Culver, and Wayne Schubert. Whether through classes, mentoring, or overseeing me as a graduate student TA, all members of my committee have contributed to my growth as a scientist and teacher, for which I am truly thankful.

I would like to express my gratitude to the ASH *mob* for welcoming me with open arms. Particularly, Mark Miesch, Benjamin Brown, Nicholas Featherstone, Juri Toomre, and Kyle Augustson. To parallel the ASH simulations performed by Mark, Benjamin Brown performed for me ASH simulations of the Sun rotating at 5 times the current solar rate. Ben was kind enough to spend a week with me at the University of Wisconsin-Madison, discussing ASH, rotationally constrained convection, and teaching me a bit about VAPOR. As a postdoc at HAO, Nicholas Featherstone also helped me understand a bit more about convection, and taught me how to run a few of my own ASH simulations on NASA supercomputers, providing me with a library of IDL codes to interpret and visualize my results. Juri Toomre graciously agreed to host me at CU/JILA if I received the NSF AAPF postdoc. Despite my unsuccessful attempt at receiving this postdoc, I deeply appreciate his time and effort reading my proposal and offering comments. Ben Brown was also a wonderful mentor to me while writing this postdoc proposal, engaging in lengthy and productive conversations with me on multiple occasions. Both Juri and Ben's mentoring efforts during my proposal writing process carried over a few months later as I prepared many other postdoc applications and

proposals. Finally, I am grateful to Kyle Augustson for responding to some of my silly email questions in length and great detail regarding convection and differential rotation as a function of rotation rate and spectral type in solar-like stars.

My scientific relationship with the Sun began during the summer of 2007 in Sunspot, New Mexico. My advisors that summer, and the following, were Dr. Alexandra Tritschler and Dr. Friedrich Wöger through the National Solar Observatory's REU program. I have fond memories of my summers in Sunspot, and the many wonderful people I met during my time there. Without this seminal research experience, my trajectory through the world of physics would probably be remarkably different, as I turned down another REU where I would have experimented with capacitor materials for this one in solar physics. I am forever grateful to Ali and Fred, and for my REU experience, which undoubtedly started me on my path toward the Sun.

During the summer of 2009, I was fortunate enough to have a part-time research position in Dr. Krueger's LIDAR group at CSU. While there, I worked closely with Dr. Jia Yue, who was then a graduate student working toward his PhD. Jia had a post-doc at HAO, and was kind enough to introduce me to Yuhong. Without Jia introducing me to some scientists at HAO, I fear that I never would have returned solar physics. I am so very thankful for him reaching out to Yuhong on my behalf.

Having a graduate research fellowship at HAO has afforded me with so many opportunities I otherwise would not have experienced. At HAO, I am surrounded by leading scientists in the field who are always available and willing to help me in any way possible. My funding has also allowed me to travel to many conferences, and I have been fortunate enough to publish three first author papers in leading peer-reviewed journals. HAO has truly been a

home for me the past four years, and I will sadly miss the many colleagues and friends I have made. I will even miss my little cubical. During many of these years, my cube neighbor DJ Schmit was a great friend and was always ready for a visit to Boulder Beer.

Colorado State University's physics department has been like a second family to me. Particularly, some of my fellow graduate students: Raj Das, Jackie Schwehr, Jason Liu, Tim Walton, Matthew Bass, Michael Gussert, Eric Conrad, Ben Gookin, Big T, Sam Ronald, William Johnston, Megan Longo, and Kathrine Zaunbrecher. They have provided me with endless hours of entertainment, and were always available for a beer, whether to celebrate times of happiness and triumph, or times of sadness and failure. I must also recognize our fabulous secretary Wendy Johnson, who is the goddess of all things admin related.

Many people comment that my undergraduate degree in both Physics and Philosophy is an *unusual* combination for a double major. However, for me it makes perfect sense, as I feel that physics and philosophy go hand-in-hand. My philosophy professors at the University of Evansville, Anthony Beavers and Richard Connolly, were truly two of the most influential professors in my educational career. In fact, if I didn't get accepted to graduate school for physics, I was going to apply to philosophy of science graduate programs. I attribute my scientific writing skills specifically to these two professors. Through their classes, I learned how to construct a convincing dialog and logically support my findings and inferences. My undergraduate physics professors, specifically John Stamm and Lowell Boone, were paramount in instilling my love of physics. Lowell's computational physics class got me super excited about the possibility of pursing programming and numerical methods in my future career. While I was a bit annoyed to discover the book *Numerical Recipes* only

after I finished his course, I am nevertheless grateful that he taught me how to build my numerical methods toolbox from scratch.

While performing my research at HAO, I found it necessary to supplement my income. I decided to pursue private tutoring in mathematics and physics as a second job. For four years, I have tutored students in the area where I live and work. I have found it to be much more fulfilling and fun that I ever thought possible. From every student, and every session, I learned a bit more about teaching and myself. In addition, tutoring a wide range of subjects forced me to always remember physics and mathematics principles, which I find I often lose track of when deep in a research project. For these, and many other reasons, I am deeply indebted to all of my previous students.

My parents Fred and Diane Weber, my sister Christine, and my aunt Nora Weber, have always been my best of cheerleaders. I appreciate everything they have done for me, and the support they have given me during my 10 years of higher education. I know my parents have made sacrifices on my behalf to help fulfill my educational goals, and for that I am forever thankful. They believed that this small town girl from Southern Indiana could some day become a physicist, and that support has made all the difference in the world.

I would also like to thank my beloved Patrick for his unwavering support and encouragement during these past four years. When I am nervous or frustrated, he is always the first person to hear about it, and is always the one who calms me down (although he would probably beg to differ!). I am so grateful to have him in my life, and am humbled by the faith he has always had in me, which at times was more than the faith I had in myself.

The typesetting of this manuscript was made possible by Dr. Leif Anderson. As the CSU graduate school does not provide a LaTeX file for use of the graduate students (ridiculous!),

Leif took it upon himself to make this LaTeX template available online. His template has saved me numerous, numerous hours of formatting woes.

Finally, this dissertation would not have been possible without the support of NASA SHP grant NNX10AB81G to the National Center for Atmospheric Research (NCAR).

PREFACE

I believe that the following quote is a very poetic way to describe our unique relationship with the Sun:

> "... be not afraid of greatness: some are born great, some achieve greatness,
>
> and some have greatness thrust upon them."
>
> William Shakespeare, *Twelfth Night*

The Sun is just one of ∼300 billion stars in the Milky Way galaxy alone, which is only one of the ∼170 billion galaxies in the entire universe. It is true that the Sun is a rather unremarkable species compared to the exotic celestial bodies that make up the universal zoo. So why do we care to study such an ordinary subject? Because it is ours! With a little bit of chance, and a little bit of physics, our solar system formed, resulting in eight diverse planets (plus Pluto). One of these was situated at a distance from its star that was *just right* to sustain complex life. This *Goldilocks planet*, known as Earth, has nurtured a plethora of diverse lifeforms, of which we are one. Our understanding of stellar physics is driven by what we have learned about the Sun, our own astrophysical laboratory in our celestial backyard. It is important for us to better understand the volatile nature of our magnetic star, in particular how it sustains its magnetic field, and how this magnetic field manifests itself, learning about other stars in the process.

My first formal introduction to the Sun occurred during the summer of 2007 while I was a REU (Research Experience for Undergraduates) student at the National Solar Observatory on Sacramento Peak, in quaint Sunspot, NM. Although remote, I found it to be an extraordinary setting for learning about solar physics. Working and living in an entire

community devoted to the sole purpose of pursuing the mysteries of our beloved star etched a lasting impression on me. The Sun and I parted ways for $\sim$1.5 years while I pursued teaching and other avenues of physics during graduate school at Colorado State University. But alas, the universe was determined to make a solar physicist out of me. I found myself once again studying the Sun at another renowned institution, High Altitude Observatory (HAO) in Boulder, CO. I am fortunate to have had such wonderful research opportunities so early in my career, all of which have contributed to this dissertation. The next chapter of my career will take place at the University of Exeter in Exeter, UK, where I have accepted a postdoctoral research position. My research will involve investigating flux emergence and the near surface shear layers of low-mass stars, particularly fully convective M-type stars. I'm excited to apply what I have learned during the course of my PhD studies to other solar-like, main sequence stars.

TABLE OF CONTENTS

LIST OF TABLES

LIST OF FIGURES

CHAPTER 1

Motivation and Background

Although the Sun is our closest star and serves as a nearby astrophysical laboratory, there are still many mysteries regarding its behavior that we have yet to untangle. Foremost among these is the nature of the solar dynamo mechanism. Rotation, global-scale plasma motions, and shearing at the convection zone-radiative zone interface all contribute to the generation of solar magnetic fields. However, the manner by which the dynamo-generated magnetic field, the progenitors of sunspots, traverse the convection zone to eventual emergence at the solar surface remains unclear. We provide a connection between the solar dynamo and sunspots by performing simulations of magnetic flux emergence through the bulk of turbulent stellar convection zones. This chapter introduces the relevant background and motivation pertaining to this research.

Section 1.1 discusses the nature of the solar cycle and active region observations, while Section 1.2 introduces theoretical and phenomenological models of the solar dynamo. Stellar convection and differential rotation is discussed in Section 1.3, with observations shown to support the existence of such phenomena on the Sun. Modeling efforts used to address magnetic flux emergence through the solar interior and above are reviewed in Section 1.4, and the solar/stellar connection is addressed in Section 1.5. A brief outline of this thesis, including the methods used and research objectives, can be found in Section 1.6.

1.1. Active Region Observations and the Solar Cycle

Sunspots serve as a photospheric touchstone of solar magnetic activity, and are the oldest solar observable. As early as the 4th century B.C., sunspots were observed by one of Aristotle's students, Theophrastus of Athens, with his naked eye. By ∼23 B.C., systematic observations of sunspots began to be recorded by Chinese scholars. It was generally believed that these sunspots as we know them today were transiting planets, satellites of the Sun, or even smoky clouds. With the invention of the telescope in the early 1600's, it became clear to Galileo that sunspots were indeed affixed to the solar disk, and changed in shape, position, and number over time. This caused a tremendous uproar, as it contradicted Aristotle's beliefs, adopted by the Catholic Church, that heavenly bodies were perfect and unchanging spheres (e.g. Drake 1957). Eventually the existence of spots on the Sun became a widely accepted and studied phenomenon. The connection between sunspots and magnetism was made in 1908 by George Ellery Hale through the use of a device called the spectroheliograph, and the knowledge that certain spectral lines split into multiple components in the presence of a static magnetic field, known as the Zeeman Effect (Hale 1908).

The large scale magnetic activity pattern on the solar photosphere is in the form of bipolar magnetic regions, with the leading magnetic polarity area (leading in the direction of solar rotation) of opposite polarity sign of the following region (see Figure 1.1, left). A line drawn between these two polarity areas is often East – West oriented. The strongest of these regions appear as sunspots when observed in white light (Figure 1.1, right). More is revealed when the Sun is observed in extreme ultraviolet wavelengths (Figure 1.2). The bipolar magnetic regions, or active regions, are the source regions of strong solar activity, such as solar flares, and serve as footprints for coronal loops. Active regions exhibit many

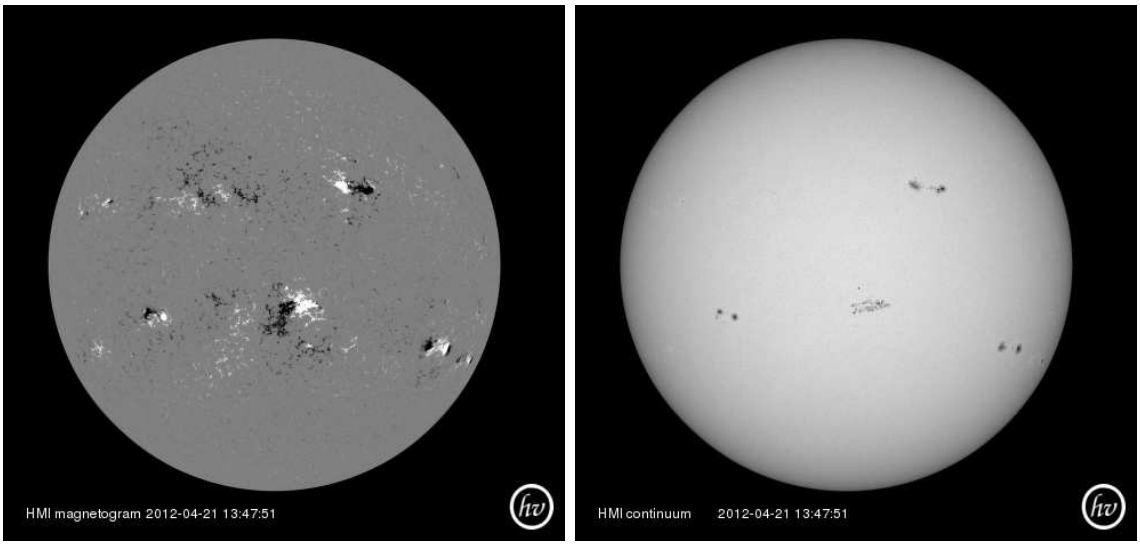

FIGURE 1.1. SDO HMI Magnetogram (left), and SDO HMI continuum intensity image (right) of the solar disk on April 21, 2012. For the magnetogram, white (black) regions indicate the magnetic field direction is out of (into) the plane. These images show that active regions tend to emerge in latitudinal belts, illustrating the toroidal nature of the solar dynamo mechanism. The strongest of these active regions appear as dark spots on the solar photosphere, which are referred to as sunspots. Images generated using Helioviewer.org.

properties, some of which systematically vary on a timescale of ∼11 years, or ∼22 years, and some of which tend to remain constant.

In 1843, Schwabe proposed that the frequency of sunspot occurrence varies on a timescale of ∼11 years (Priest 1982). This pattern is shown in the bottom of Figure 1.3 for longer than 120 years, covering 11 such sunspot frequency cycles. Indeed, the ∼11 year magnetic activity cycle of the Sun has been shown to exist for millions of years by using the amount of radionuclides such as ^{10}Be and ^{14}C present in sedimentary rock layers (Mann *et al.* 2012), ice cores (Beer *et al.* 1990), and tree rings (Steinhilber *et al.* 2012) as proxies for direct solar observations. It is known that cosmic ray particles interact with atmospheric nitrogen and hydrogen to produce so-called *cosmogenic radionuclides* ^{10}Be and ^{14}C (Steinhilber *et al.* 2012). The production rates of these nuclides are directly related to the cosmic ray flux,

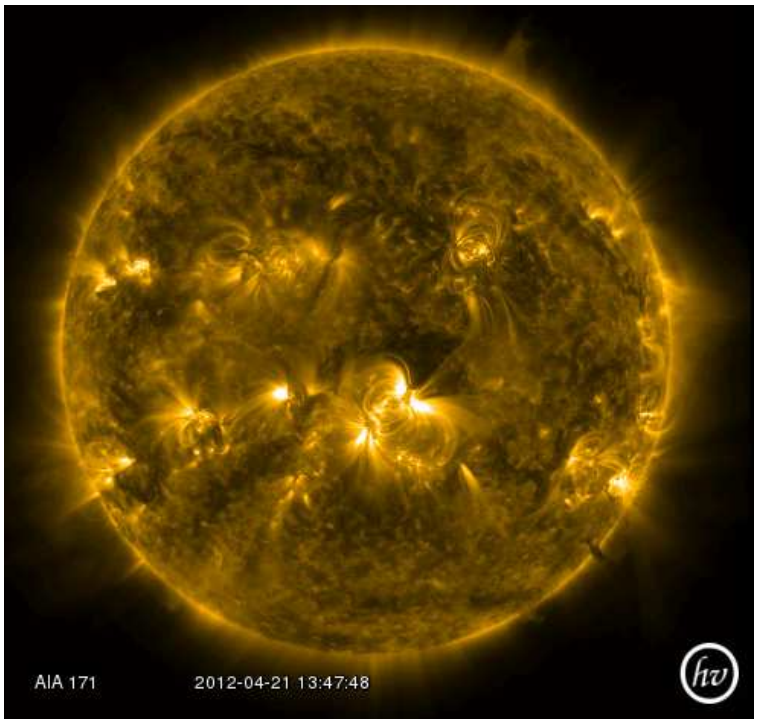

FIGURE 1.2. SDO AIA 171 Angstrom wavelength channel image on April 21, 2012. This wavelength band images the quiet corona and transition region, illustrating that coronal loop footprints are associated with active regions. Image generated using Helioviewer.org.

which is inversely proportional to the solar cycle, as stronger heliospheric magnetic fields associated with solar maximum prevent cosmic rays from reaching the Earth (see review by Usoskin 2013). Therefore, the population of radionuclides is largest during solar minimum.

The question as to why the Sun is obliged to have an ∼11 year sunspot cycle is still a mystery. Regardless of the reason for the Sun's activity timescale, it exhibits a number of cyclic traits that never fail to manifest themselves. Firstly, active regions on the Sun are loosely confined to two toroidal (parallel to lines of latitude) bands, each of which are roughly equidistant from the solar equator in both hemispheres (see Figure 1.1). Following Spörer's Law, these bands migrate steadily from mid-latitudes of ∼40° toward the equator during the course of a sunspot cycle (Spörer 1890). This progression is represented well in so-called butterfly diagrams (Figure 1.3, top). The maximum of solar magnetic activity

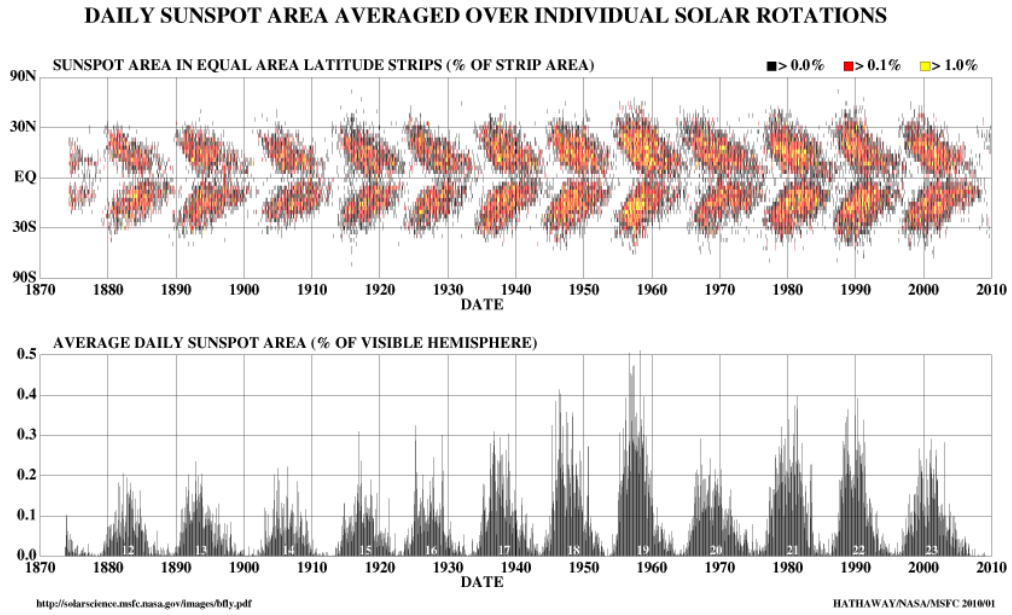

FIGURE 1.3. The butterfly diagram (top) and corresponding sunspot number (bottom) from Hathaway (2010). Butterfly diagrams depict the equatorward progression of active regions during a solar cycle, with the maximum sunspot number varying from cycle to cycle.

occurs when the active region bands reach a latitude of $\sim 15^\circ - 20^\circ$. Known as Hale's Law, the magnetic polarity sense (direction of the magnetic field in to or out of the solar surface) of active regions are of opposite sign in each hemisphere (Hale *et al.* 1919). With the start of a new sunspot cycle, the leading polarities of active regions in both hemispheres switch sign. Therefore, it takes $\sim$22 years for each hemisphere to complete a full magnetic cycle, although the progression of the toroidal, active region belts from mid-latitudes to the equator takes $\sim$11 years. This $\sim$11 year cycle is typically referred to as the *solar cycle*.

The magnetic flux of active regions spans a few orders of magnitude, from 10^{18} Mx for small, ephemeral regions up to 10^{22} Mx or even 10^{23} Mx for the strongest sunspots (Hagenaar, Schrijver, and Title 2003). Typical values of sunspot magnetic field strengths range from $\sim 1 - 4$ kG. With variable lifetimes, active regions can live for a few hours or many months, long enough to complete more than one rotation on the Sun (see review by Solanki 2003).

Active regions exhibit some asymmetries between their leading (in the direction of solar rotation) and following polarities, which have been attributed to the effect of the Coriolis force on the legs of rising magnetic flux loops. One such property is the systematic tilt of the active region, with the leading polarity in the direction of solar rotation usually appearing closer to the equator than the following polarity (D'Silva and Choudhuri 1993; Caligari, Moreno-Insertis, and Schüssler 1995). Known as Joy's Law, this tilt is largest at higher emergence latitudes, and decreases toward being strictly parallel to the East – West axis as the latitude of active region emergence approaches the equator (Hale *et al.* 1919). Additionally, the Coriolis force is thought to be responsible for the apparent faster motion of the leading polarity of an active region as compared to the following (Caligari, Moreno-Insertis, and Schüssler 1995; van Driel-Gesztelyi and Petrovay 1990), as well as the observed more coherent morphology of the leading polarity of an active region as compared to the following (Fan, Fisher, and Deluca 1993; Caligari, Moreno-Insertis, and Schüssler 1995; Caligari, Schüssler, and Moreno-Insertis 1998).

More sophisticated instrumentation has resulted in the ability to decipher the magnetic field orientation of photospheric active regions. Vector magnetograms of sunspots indicate that active regions have a small, but significant twist of their associated magnetic field (Pevtsov, Canfield, and Metcalf 1995; Pevtsov, Canfield, and Latushko 2001). The sign of this twist is dependent on the hemisphere of sunspot origin, but independent of the solar cycle, and is usually of a left-handed sense (negative) in the Northern hemisphere, and right-handed (positive) in the Southern hemisphere. The twisted nature of the emerging flux tube may be required to maintain the cohesiveness of the flux tube as it rises through the convection zone (Fan, Abbett, and Fisher 2003; Fan 2008). In addition, the twist and

associated magnetic helicity of active regions are important for the buildup of free magnetic energy in the solar corona for driving flares and coronal mass ejection.

It is also noted that individual sunspots rotate faster than the surrounding surface plasma (Howard and Harvey 1970; Golub and Vaiana 1978). According to inversions of helioseismic observations, there is an increase in the differential rotation of the Sun from the surface to ∼40 Mm below the photosphere, called the near-surface shear layer (see reviews by Thompson *et al.* 2003; Howe 2009). As such, the solar surface plasma has an angular velocity ($\Omega/2\pi$) of ∼10 nHz less than the plasma at $\sim 0.95 R_\odot$. Furthermore, it appears that sunspots tend to rotate prograde at approximately the same angular velocity as the plasma at a depth of $0.95 R_\odot$ as shown in Figure 1.4, suggesting that perhaps the progenitor magnetic flux tubes responsible for sunspots may be anchored at a depth of $0.95 R_\odot$, near the surface shear layer interface (e.g. Zhao, Kosovichev, and Duvall 2004; Hiremath and Lovely 2007).

One more peculiar property of solar active regions is their tendency to emerge near the location of previous or currently existent magnetic flux (e.g. Bumba and Howard 1965; Gaizauskas *et al.* 1983; Harvey and Zwaan 1993). Solar observations show that the emergence of active features is distributed inhomogeneously in longitude according to sunspot activity (de Toma, White, and Harvey 2000; Berdyugina and Usoskin 2003), solar flares (Zhang *et al.* 2011), and coronal streamers (Li 2011). These preferential longitudes of solar activity are commonly referred to as active longitudes. The physical mechanism responsible for the active longitude phenomenon are not well understood, although it may be related to the dynamo mechanism and/or large-scale convective structures known as giant cells.

The solar cycle also manifests itself in coronagraph images of the Sun. A coronagraph instrument occults the disk of the Sun, allowing a detailed view of the tenuous corona. Until

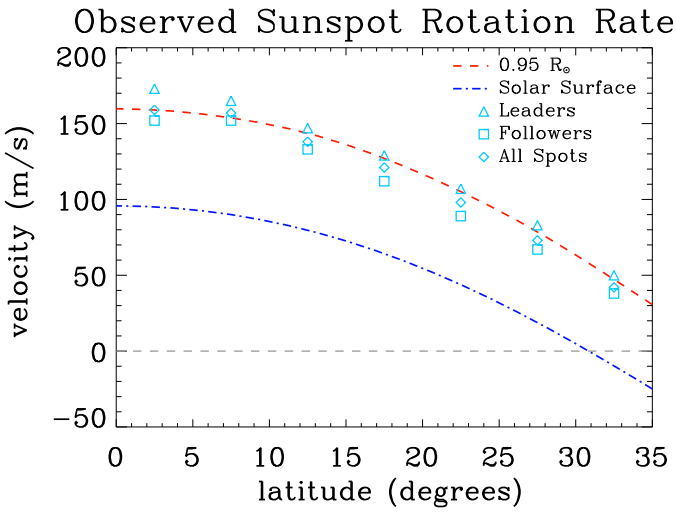

FIGURE 1.4. Rotation rate of leader, follower, and all sunspots derived from Gilman and Howard (1985), plotted with the observed azimuthal rotation rate of the solar plasma at the surface (blue dash-dotted line) as determined from surface spectroscopic Doppler-velocity measurements (Thompson *et al.* 2003) and the rotation rate at $r = 0.95\mathrm{R}_\odot$ (red dashed line) as found via inversions of helioseismic observations (Howe *et al.* 2000). All values are plotted with reference to the solid body rotation rate (i.e. rotation rate of solidly rotating interior) of $\Omega_0 = 2.7{\times}10^{-6}$ rad s^{-1} ($\sim$430 nHz), so that the zero line is the solid body rotation of the Sun. This image suggests that sunspots rotate at nearly the same rate as the solar plasma at $0.95\mathrm{R}_\odot$.

the coronagraph was invented in 1930 by Lyot (e.g. Priest 1982), the corona could only be viewed during a total solar eclipse. The shape of the corona changes throughout the solar cycle, from a dipolar-like configuration during solar minimum (Figure 1.5, left) to a more spherically symmetric shape during solar maximum (Figure 1.5, right). At solar minimum, polar plumes are faintly visible, showing poloidal (parallel to lines of longitude) magnetic field lines that extend outward, similar to a bar magnet. During this phase, the *streamer belt* at mid-latitudes is the prominent feature. Coronal streamers are the result of hot coronal plasma being held down by a series of closed magnetic field lines over a polarity inversion line (PIL) on the photosphere (e.g. Low 1996). Pointed peaks at the end of these streamers are caused by the interaction of the solar wind and magnetic reconnection between the closed

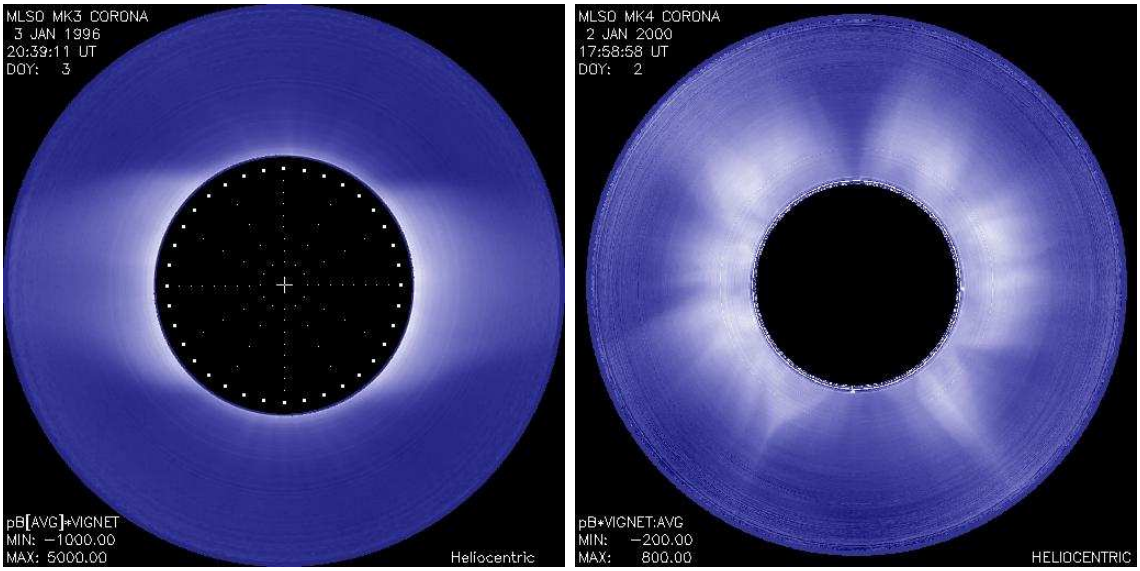

FIGURE 1.5. Coronagraphs during solar cycle 23 taken near solar minimum on January 3, 1996 (left), and near solar maximum on January 2, 2000 (right). The structure of the corona changes shape drastically between solar maximum and solar minimum. These images were captured using the Mark-III and Mark-IV coronameter instruments at High Altitude Observatory's Mauna Loa Solar Observatory. Images courtesy of High Altitude Observatory, National Center for Atmospheric Research, sponsored by the National Science Foundation.

field lines of the streamer and neighboring open field lines (e.g. Koutchmy and Livshits 1992; Wang, Sheeley, and Rich 2007).

Since the large-scale structure of the magnetic field is dipolar at solar minimum, usually one continuous, although meandering, PIL may be drawn around the equatorial region of the Sun. Subsequently, the closely packed magnetic fields lines above the PIL result in the appearance of an equatorial streamer belt in coronagraphs. As magnetic activity increases, the emergence of many bipolar active regions creates a more complicated series of polarity inversion lines, resulting in a more complex coronal structure. Typically the classification of solar maxima and minima are determined based on sunspot count, but it can also be determined through the morphology of the corona.

The observational properties of solar active regions and their relation to the solar cycle have been well categorized and studied. While it is still not yet possible to predict the exact nature of active region emergence on the Sun, we do have general expectations of the flux emergence trend based on observations. Through some means, the Sun exhibits an unerring magnetic cycle of distinct order and organization. In a remarkable way, nature allows a dynamo mechanism and turbulent convective motions to work together in the Sun, producing active regions with a distinctive pattern of large scale properties. The question as to *how* these active regions emerge, and *why* they behave as they do is a problem best addressed through theory and computational/numerical modeling, motivated and supported by observational means.

1.2. The Solar Dynamo

Our Sun is a magnetically active star, exhibiting cyclic properties of its large-scale magnetic field and flux emergence behavior. It is perhaps conceivable that the Sun's magnetic field is primordial in nature, originating in an earlier epoch of the universe, preserved by the high electrical conductivity of the solar plasma. In fact, the time it would take for the decay of the global magnetic field is $\tau = L^2/\eta$, where L in this case is the solar radius and η is the magnetic diffusivity dependent on the electrical conductivity of the solar plasma, with $\tau = 10^9$ years (Priest 1982). This value is comparable to the $\sim$10 billion years the Sun will live as a main sequence star. However, $\tau \sim 10^9$ years is most likely a severe overestimate.

Given the fact that the solar convection zone is turbulent in nature, a turbulent eddy magnetic diffusivity ($\eta_t = vl$) operating in the bulk of the convection zone would significantly drop the magnetic diffusion time scale to $\sim$10 years (Priest 1982). Additionally, it is also the case that magnetic fields can *escape* from the Sun by means other than diffusion, depleting

the primordial solar magnetic field much earlier in its lifetime (Parker 1979). For instance, strong magnetic fields are susceptible to the magnetic buoyancy instability (see latter part of this Section), a form of the hydromagnetic Rayleigh-Taylor instability, which can expel the field from the convection zone on time scales of a few months to a few years depending on the initial strength of the magnetic field.

The cyclic nature of solar magnetic activity and the ordered appearance of active regions as discussed in Section 1.1 points to the existence of a large-scale, subsurface toroidal magnetic field maintained by a dynamo mechanism, rather than sustained by a primordial magnetic field. However, the global solar field is actually weakly poloidal in nature during solar minimum; roughly dipolar (see Figure 1.5, left). The poloidal field is thought to be stretched and amplified in a thin shearing region called the tachocline, that exists between the solidly rotating radiative interior and differentially rotating convective envelope (e.g. Gilman 2000; Charbonneau 2010). At this shearing interface, kinetic energy is effectively converted in to magnetic energy. Through this mechanism, the toroidal magnetic field suggested by the latitudinal bands of active regions is born. It may also be the case that magnetic flux can be pumped downward by turbulent convective downflows and accumulate in the tachocline or stably stratified overshoot region below the convection zone, where the magnetic field can then be amplified through the same shearing process (Browning *et al.* 2006).

In this context, a dynamo loop is referred to as the process by which the global poloidal magnetic filed is converted to a toroidal magnetic field and back again. The poloidal-to-toroidal portion of the dynamo is fairly well understood. However, the toroidal-to-poloidal component of the solar dynamo is more complicated. After the toroidal field amplification process shown in panels *a*-*b* in Figure 1.6, the phenomenological Babcock-Leighton model

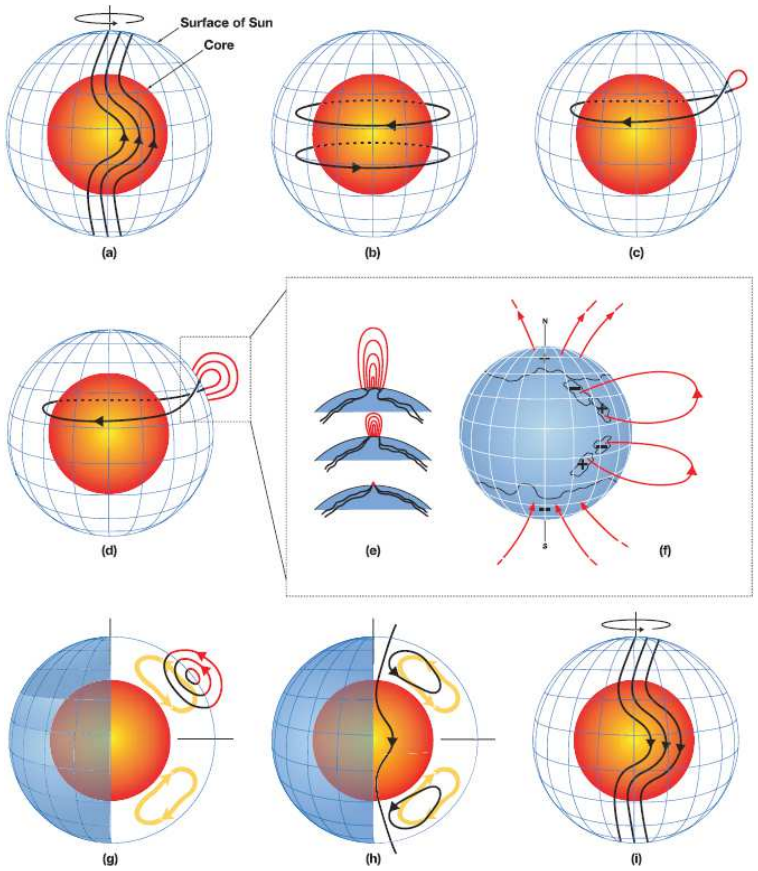

FIGURE 1.6. Schematic of a solar Babcock-Leighton/Flux-Transport dynamo process. The red inner sphere represents the Sun's radiative interior and core, while the blue mesh indicates the solar surface. (*a*) The Sun's differential rotation, which is prograde fastest at the equator, shears the poloidal field near the base of the convection zone. (*b*) A toroidal field is produced due to shearing by differential rotation, referred to as the Ω-effect in mean-field dynamo theory. (*c*) When the toroidal magnetic field is amplified to a threshold field strength, buoyant magnetic flux loops rise toward the surface, eventually emerging through the photosphere to form active regions, twisting and tilting toward the equator due to rotational influences. A poloidal component of the magnetic field is thus achieved from helical action in the convection zone, akin to the α-effect from mean-field theory interface dynamos. (*d-f*) Additional flux emerges (*d-e*), then spreads (*f*) in latitude and longitude from decaying active regions. (*g*) Meridional flows in the (r, θ) plane (yellow circulation with arrows) carry surface magnetic flux poleward, eventually inducing a polar field reversal. (*h*) Some of the flux is transported downward to the bottom of the convection zone and toward the equator by meridional circulation. These poloidal fields have sign opposite to those at the beginning of the sequence in (*a*). This action can also account for the equatorial migration of active region bands during the course of the solar cycle. (*i*) The reversed poloidal field is then again sheared near the bottom of the convection zone by differential rotation, producing a toroidal field opposite of that shown in (*b*), and the solar cycle marches on. Figure from Dikpati and Gilman (2007).

(Babcock 1961; Leighton 1964, 1969) suggests that the observed Joy's and Hale's laws, active region decay, and transport of magnetic flux by meridional circulation and turbulent diffusion results in a net global polar field of opposite polarity from the previous cycle, depicted in panels *c*-*g* of Figure 1.6. Buoyant toroidal loops of magnetic flux rise to the surface and subsequently form active regions, tilting toward the equator due to rotational influence provided by the Coriolis force. These tilted bipolar regions possess a poloidal magnetic component of opposite sign to the existing polar field in each hemisphere. They are then transported poleward by large-scale circulating cells in the (r,θ) plane known as meridional circulation, where they then interact with the polar field of opposite polarity. Thereby, the following polarity portion of active regions in each hemisphere then become the progenitors for the poloidal field of the next sunspot cycle.

A rigorous study of the solar dynamo process involves solving the full set of three-dimensional (3D) magnetohydrodynamic (MHD) equations simultaneously for both the magnetic field and the form of the turbulent flow field in the convection zone. These numerical simulations of convective dynamos are both complicated and computationally expensive, although it has been attempted to some degree of success in rotating, fully convective shells exhibiting self-organized cyclic dynamos (Brown *et al.* 2011; Nelson *et al.* 2013). Another approach is provided by kinematic dynamo models, which specify a priori the convective velocity field, specifically the mean flows that capture differential rotation and meridional circulation (see Section 1.3). In this case, the magnetic field evolves solely according to the magnetic induction equation (as derived in Appendix A):

$$\frac{\partial \mathbf{B}}{\partial t} = \nabla \times (\mathbf{v} \times \mathbf{B}) + \eta \nabla^2 \mathbf{B}, \tag{1.1}$$

where $\mathbf{v}$ is the fluid velocity, $\mathbf{B}$ is the magnetic field, and η is the magnetic diffusivity of the plasma. The first term on the right-hand side of the equation describes how the magnetic field is advected by the fluid, with the second term representing diffusion of the magnetic field.

Early investigations into solar kinematic dynamo theory were performed by the prolific solar physicist Eugene Parker (1955), and elaborated upon by Krause and Raedler (1980). Parker proposed that due to the turbulent nature of the solar convection zone, large-scale magnetic fields can be produced by averaging over fluctuations around the mean magnetic field:

$$\frac{\partial \langle \mathbf{B} \rangle}{\partial t} = \nabla \times (\langle \mathbf{v} \rangle \times \langle \mathbf{B} \rangle) + \nabla \times \varepsilon + \eta \nabla^2 \langle \mathbf{B} \rangle, \tag{1.2}$$

where angular brackets $\langle\ \rangle$ denote averages over small scales, $\varepsilon = \langle \mathbf{v}' \times \mathbf{B}' \rangle$ is the fluctuating electromotive force (emf), and primes indicate fluctuations about the mean such that, e.g. $\mathbf{v}' = \mathbf{v} - \langle \mathbf{v} \rangle$. Applying the case of axisymmetric spherical geometry to Equation 1.2 gives a more instructive look at the various processes involved in the generation of the mean magnetic field (see e.g. Miesch 2012):

$$\frac{\partial \langle \mathbf{B} \rangle}{\partial t} = (r \sin\theta \langle \mathbf{B_p} \rangle \cdot \nabla \Omega) \hat{\phi} + \nabla \times (\langle \mathbf{v_p} \rangle \times \langle \mathbf{B} \rangle) + \nabla \times \varepsilon + \eta \nabla^2 \langle \mathbf{B} \rangle, \tag{1.3}$$

where $r \sin\theta$ is the cylindrical radius, Ω is the rotation rate of the plasma, and the vector fields are broken up in to their toroidal and poloidal components represented by the subscripts t and p respectively such that, e.g. $\mathbf{B} = \mathbf{B_t} + \mathbf{B_p}$ and $\mathbf{B_t} = B_\phi \hat{\phi}$ and $\mathbf{B_p} = B_r \hat{r} + B_\theta \hat{\theta}$.

Each of the four terms in Equation 1.3 describe a portion of the dynamo process in the kinematic mean field regime. The first term, which follows from MHD without any additional

approximations, is known as the Ω-effect. This term indicates that the mean toroidal field $\langle B_\phi \rangle$ is generated from the mean poloidal field $\langle \mathbf{B_p} \rangle$ and rotational shearing provided by differential rotation. Advection of the magnetic field by meridional circulation is captured in the second term, and the fourth term of magnetic diffusion remains intact as in Equation 1.2.

Embedded within the fluctuating emf ε in the third term of Equation 1.3 is the so called α-effect, which is often approximated as $\varepsilon \sim \alpha \langle \mathbf{B} \rangle$, where α is a pseudo-tensor that is a statistical property of the velocity field independent of the magnetic field (e.g. Stix 2002; Priest 1982). The α-effect is less robust in nature than the Ω-effect, and generally refers to any process that can close the dynamo loop, transforming the toroidal field to a poloidal field. However, it is also the case that the α-effect can contribute to both the poloidal-to-toroidal and toroidal-to-poloidal stages of the dynamo (Miesch 2005). In which case, the process is referred to as an α^2 dynamo.

The α-effect is proportional to the kinetic helicity and kinetic energy of fluctuating fluid motions, contributing to the transfer of magnetic helicity from fluctuating to mean magnetic fields. Helical motions, most likely a result of the combination of helical convective upflows and the tilting action of buoyantly rising magnetic loops toward the equator, act to lift and twist the mean magnetic field, thereby providing a significant poloidal field component (e.g. Miesch 2012). In strictly kinematic dynamo models, the α-effect is implicit, as fluctuating fields do not explicitly appear in Equation 1.3. Through this treatment, the magnetic field is advected passively by the fluid flows according to Eq. 1.3 such that the Lorentz force $\mathbf{J} \times \mathbf{B}$ has no feedback on the system. Many mean field dynamo models now include a Lorentz force feedback loop to modify the α-effect (see review by Miesch 2012), as the Lorentz force (which

appears in the plasma momentum equation) is capable of suppressing turbulent motions for a large enough magnetic field.

Often the solar dynamo is referred to as an α-Ω dynamo since both effects act to complete the dynamo loop as observed on the Sun. The location of the α-effect and Ω-effect can coincide in the same region near the base of the convection zone, but these models suffer from a phenomenon called α-quenching. The term α-quenching refers to the suppression of the α-effect from Lorentz force feedbacks that occur when the magnetic field reaches a threshold strength (see reviews by Charbonneau 2010; Miesch 2012). Interface dynamo models solve this problem by spatially separating the Ω-effect in the tachocline or stably stratified region below the convection zone base from the α-effect somewhere within the convection zone proper (see Parker 1993; MacGregor and Charbonneau 1997; Zhang, Liao, and Schubert 2004).

Propagation of the toroidal bands of magnetic field from high latitudes toward the equator during the course of a solar cycle is also a concern of solar dynamo models. Such cyclic behavior can arise from a *dynamo wave*, which is the result of a phase shift between the α-effect and Ω-effect, allowing for traveling wave solutions to the linear, mean-field induction equation (Eq. 1.3) (see review by Charbonneau 2010; Miesch 2012). Another set of dynamo models known as flux transport models advocate the notion that the migration of active region bands toward the equator is a result of mean field advection by meridional circulation (see reviews by Dikpati and Gilman 2009; Miesch 2012), illustrated in panel h of Figure 1.6. Here, large circulating cells set up in the (r, θ) plane in each hemisphere advect magnetic flux slowly equatorward at the base of the convection zone on the order of a few m s^{-1}.

Throughout this thesis, it is assumed that the dynamo generated magnetic field is concentrated into flux tubes that rise coherently from the base of the convection zone to the solar surface. Due to the large electrical conductivity of the solar plasma, the magnetic field is essentially *frozen in* to the surrounding fluid (e.g. Stix 2002; Priest 1982, and see Appendix B for a proof of the flux frozen-in condition). Observations indicate that this fibril form of the magnetic field is ubiquitous on the photosphere (e.g. Spruit and Roberts 1983; Zwaan 1987; Stenflo 1989), and so presumably traverses the convection zone in the same form. Illustrated especially well by sunspots, magnetic flux manifests itself as intense, isolated magnetic elements surrounded by plasma with much weaker magnetic fields. The magnetic energy density of the sunspot's associated flux tube $B^2/8\pi$ is much greater than the kinetic energy density $\rho_e v_c^2/2$ of the plasma, where ρ_e is the density of the plasma environment external to the flux tube and v_c is a representative velocity of the plasma. When $B^2/8\pi = \rho_e v_c^2/2$, we say that the magnetic field is in *equipartition* with the convective flows. If the magnetic field of the flux tube is sufficiently large (i.e. super-equipartition), the flux tube will be less susceptible to distortion and fragmentation by convection.

Once formed in the deep interior, magnetic flux tubes rise to the solar surface due in part to magnetic buoyancy. If a flux tube is in thermal equilibrium with its environment, it feels a resulting radially upward directed buoyancy force per unit volume of $(\rho_e - \rho_i)g = B^2/(8\pi H_p)$, where ρ_e is the density of the external plasma environment, ρ_i is the density of the flux tube plasma, g is the acceleration due to gravity, B is the magnetic field of the flux tube, and H_p is the pressure scale height, the distance over which the pressure changes by a factor of e. In thermal equilibrium, the internal density of the flux tube must necessarily be less than the density of the external plasma due to the condition of total lateral pressure balance on

the flux tube $P_e = P_i + B^2/8\pi$, where P_e and P_i are respectively the pressure of the external and internal plasma of the flux tube. A flux tube of larger magnetic field will therefore have a larger buoyancy force. (Note: The buoyancy force per unit volume above is derived from the equation for lateral pressure balance under thermal equilibrium.) The term $B^2/8\pi$ is the magnetic energy density, but can also be interpreted as a magnetic pressure. The external plasma acts to confine the flux tube with a pressure equal to $P_i + B^2/8\pi$.

Another scenario exists where a magnetic flux tube initially in neutral buoyancy ($\rho_e = \rho_i$) may become unstable to perturbations. The criterion required for a magnetic buoyancy instability to ensue is dependent on a number of factors such as initial magnetic field strength of the flux tube, the temperature gradient of the plasma environment, and the rotation rate of the star (e.g. Gilman 1970; Ferriz-Mas and Schüssler 1993, 1995; Fan 2009a). Unstable perturbations cause the flux tube to bend, allowing plasma to drain from the flux tube apex (higher up in the stratified convection zone) to the flux tube footpoints (lower in the convection zone), enhancing the buoyancy of the flux tube apex. Magnetic buoyancy instabilities, in conjunction with convective flows in which the magnetic field is embedded, are thought to be the means by which the dynamo generated magnetic field makes its journey from the interior to the solar surface.

On the Sun, there is a hierarchy of magnetic structures in the photosphere ranging from magnetic flux values of $10^{18} - 10^{23}$ Mx with field strengths of $\sim 1 - 4$ kG, and radii of $\sim$100 km to $\sim$10 Mm. Once intersecting with the photosphere, these flux tubes extend up into the solar atmosphere forming structures such as filaments and coronal loops, and can extend even further out into the solar wind. Many other stars exhibit starspots, therefore the flux tube phenomenon is not unique to the Sun. Aside from the Sun and solar-like stars, flux

tubes are observed in the Earth's magnetosphere (e.g. Pontius and Wolf 1990), between Jupiter and its moon Io (e.g. Connerney *et al.* 1998; Bhardwaj and Michael 2002), closely interacting binary stars (e.g. Lamb *et al.* 1983), and the interstellar medium of the Milky Way and other galaxies (e.g. Florinski *et al.* 2004).

The question as to whether the dynamo process operates entirely as flux tubes in a fibril form, or a large-scale mean field that subsequently concentrates itself into discrete flux tubes before rising to the surface is still an unresolved topic (see Charbonneau 2010). In reality, there is no such thing as an isolated flux tube. The large-scale, dynamo generated toroidal magnetic field may actually be concentrated into something more like a sheet or wreath that might develop buoyant portions similar to flux tubes. In fact, recent 3D MHD simulations of solar-like stars show that concentrated wreaths of magnetic fields can be built from a seed field within a rotating, turbulently convecting envelope (Brown *et al.* 2010, 2011). When portions of these wreaths reach a threshold magnetic field strength, buoyant magnetic loops develop, which then rise toward the surface (Nelson *et al.* 2011, 2013). These simulations also show that the origin of the strong toroidal magnetic field does not need to be in the tachocline. Rather, the magnetic field could be distributed throughout the bulk convection zone.

There are a variety of ways to theoretically model solar and stellar cycles. Often, hybrid models that borrow portions from other dynamo models are used to create more desirable results, as in the Babcock-Leighton/Flux-Transport model depicted in Figure 1.6. Nevertheless, it is generally agreed upon that the toroidal field is generated by differential rotation which acts to shear and stretch the magnetic field in the deep convection zone. The formation of the poloidal field from the toroidal field is less well understood, although there are

a variety of contributing factors. A solar dynamo model must be able to self-consistently produce all of the properties of the solar cycle. The construction of a realistic 3D MHD solar/stellar dynamo is likely years in the future. However, a convergence of the solar dynamo problem is slowly taking shape as a variety of methods are sought after, tested, and compared to observations.

1.3. Convection and Differential Rotation

There are three methods of energy transport in stars: conduction, radiation, and convection (e.g. Hansen and Kawaler 1994). Energy transport by heat conduction occurs in the presence of degenerate electrons, which is generally only a concern in the deep interior of white dwarfs, neutron stars, and red supergiants. For low mass main sequence stars such as the Sun, the most effective means of energy transport is by radiation in the interior of the Sun, and convection in the outer envelope of the star. Energy generated within the star must flow from the center to the surface, therefore a temperature gradient exists. The local *steepness* or *flatness* of this temperature gradient dictates the method of energy transport for various regions within a star (e.g. Stix 2002).

The double-logarithmic gradient, represented by ∇ (unitless), is often used instead of dT/dr when discussing temperature gradients:

$$\nabla = \frac{d \ln T}{d \ln P}. \tag{1.4}$$

Here ∇_e denotes the actual local temperature gradient of the plasma environment, and ∇_{ad} is the temperature gradient required for a parcel of gas to evolve adiabatically (i.e. no heat exchange). There exists a limit to the temperature gradient ∇_e inside a star if stability of

the plasma environment is to be maintained. In a star such as the Sun, when the plasma is stable to adiabatic perturbations, convection does not occur and radiation is the means of energy transport within this region. When the local temperature gradient ∇_e is steeper than the adiabatic temperature gradient, the plasma environment becomes unstable, promoting convection. Therefore, this condition occurs when $\nabla_e > \nabla_{ad}$. In the outer $\sim$1/3 of the Sun in radius, convection is the most efficient means of energy transport. See Appendix D for the derivation of the Schwarzschild criterion for convective instablility/stability.

Convection in the Sun is driven by the temperature gradient set up between the base of the convection zone and the solar surface (see review by Nordlund, Stein, and Asplund 2009). Large entropy fluctuations caused by cooling of the plasma at the solar surface provides most of the buoyancy work to sustain convection. Plasma reaching the surface subsequently cools as thermal energy is carried away by photons, and the now more dense fluid is pulled downward by gravity. Heating at the lower boundary of the convection zone supplied by the radiative interior contributes a smaller amount of entropy fluctuations, and is primarily the supplier of heat to large-scale global convective motions. The warmer, less dense plasma then rises buoyantly against gravity toward the surface.

Evidence of the convective nature of the Sun appears as a granular pattern observed on the solar surface as in Figure 1.7. Each granule, or convective cell, is $\sim$1,000 km in diameter. In the center of each granule is a warmer region of upflowing plasma, surrounded by cooler, dark intergranular lanes. A typical granule has a lifetime of $\sim 5 - 20$ mins (e.g. Alissandrakis, Dialetis, and Tsiropoula 1987; Title *et al.* 1989; Hirzberger *et al.* 1999), therefore the granulation pattern on the Sun is constantly changing. Superimposed on the small scale granulation is the supergranular pattern. Each supergranule is $\sim 10 - 30$ Mm in diameter,

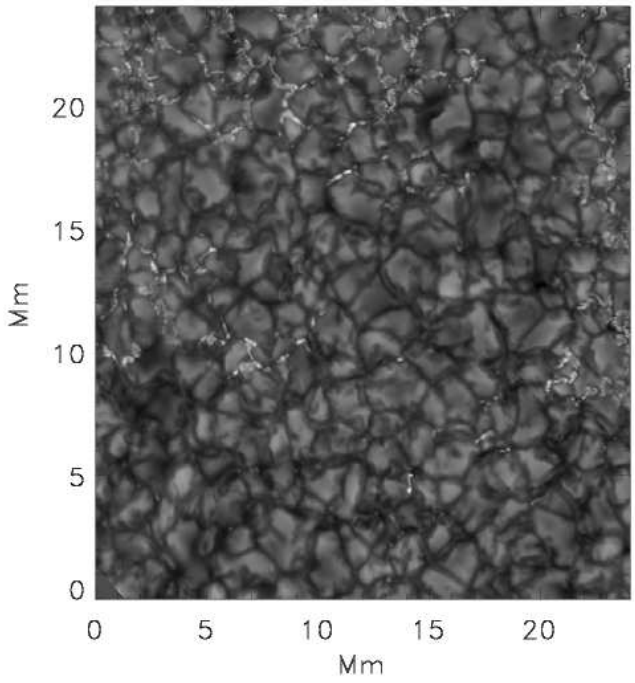

FIGURE 1.7. Image depicting convective granulation. Taken in the G-band continuum around 430 nm, this spectral region images the photosphere showing hot, lighter colored rising fluid surrounded by a network of cooler, dark intergranular lanes. The very bright regions along the intergranular network are concentrations of small-scale magnetic field. Image taken with the Swedish 1m Solar Telescope (Nordlund, Stein, and Asplund 2009).

an order of magnitude larger than granulation, and can live for $\sim 0.5 - 2$ days (Wang and Zirin 1989; Hirzberger *et al.* 2008). An even larger scale of convection known as *giant cells*, which are on the order of $\sim$100 Mm and have lifetimes of about a month, have been observed by some groups (Hathaway *et al.* 1996; Beck, Duvall, and Scherrer 1998; Hathaway, Upton, and Colegrove 2013). It is believed that these large scale convective structures must exist to efficiently transport the required heat flux across stellar convection zones (e.g. Simon and Weiss 1968).

The convection zone is also strongly stratified such that the density contrast across this region is $\sim 10^6$ (e.g. Stix 2002). Upper layers of the convection zone are more highly stratified

than lower layers such that there is a rapid decrease in density approaching the surface. The size of convective cells is highly dependent on the density scale height (e.g. Nordlund, Stein, and Asplund 2009), the distance over which the density of a fluid parcel changes by a factor of e. As a result, a hierarchy of convective scales exist on the Sun, from granules with shorter density scale heights to giant cells with much larger density scale heights. Smaller cells are thought to be advected laterally by larger scales of convection (De Rosa, Gilman, and Toomre 2002). Presumably this occurs due to the fact that downflows from small-scale cells (i.e. granules) entrain into larger scale downflow structures (i.e. supergranules, giant cells) deeper in the stratified environment.

To probe the nature of the solar interior, a method known as helioseismology is used. Helioseismology is the study of propagating acoustic waves in the solar interior, and the inversion of the obtained data to gather information about the interior structure and dynamics of the Sun (see for an overview Howe 2009). The direct observable of global helioseismology are provided by photospheric Doppler velocities taken at a cadence of $\sim$1 min continuously for timespans of months to years. These observations are decomposed into their spherical harmonic components to reveal information about acoustic modes traveling within the convection zone and below. Waves observed through helioseismology are acoustic in nature, meaning that they are dependent on the speed of sound in the solar interior. For the purposes of measuring the internal solar rotation profile, these waves have frequencies of $\sim$1.5 to 5 mHz. Thus far, the only acoustic waves observed on the Sun are p-waves, so called because pressure is their restoring force (Howe 2009). Gravity, or g-waves where gravity is the restoring force, have been posited to exist in the radiative interior of the Sun, but have not been observed.

The solar interior acts like a wave-guide, or cavity, with the solar surface as the upper boundary and the lower boundary as the wavelength dependent depth at which certain acoustic waves are refracted back toward the surface. Wave modes with longer horizontal wavelengths (low spherical harmonic degree ℓ) penetrate deeper in the Sun and are fairly long-lived (Howe 2009). For measurements of the interior rotation profile, modes of $\ell \leq 200$ are used. Conversely, modes with much shorter horizontal wavelengths, high ℓ where $\ell \geq 200$, penetrate to shallower depths and are short-lived, so they are used for local helioseismology rather than global. Local helioseismology is useful for learning about flows in the upper convection zone related to meridional circulation, active regions, and super-granulation (see Gizon and Birch 2005). Through this method, it is possible to gain information about active regions during a small window of time before they are visible on the solar surface (Ilonidis, Zhao, and Kosovichev 2011; Birch *et al.* 2013), or about active regions on the far side of the Sun which we may not be able to observe (Lindsey and Braun 2000; Braun and Lindsey 2001).

The major triumph of global helioseismology is the determination of the solar differential rotation and the rotation rate of the radiative interior. Figure 1.8 shows the major features of solar interior rotation as inferred from an average of ∼12 years of MDI (Michelson Doppler Imager) data, an instrument aboard SOHO (Solar and Heliospheric Observatory). Results tend to indicate that the radiative interior rotates uniformly, although it is unclear as to whether the core rotates at a different rate than the upper radiative zone (see Thompson *et al.* 2003; Howe 2009). The transition between the solidly rotating radiative interior and the differentially rotating convection zone is a thin layer of ∼0.05 $R_\odot$ called the tachocline.

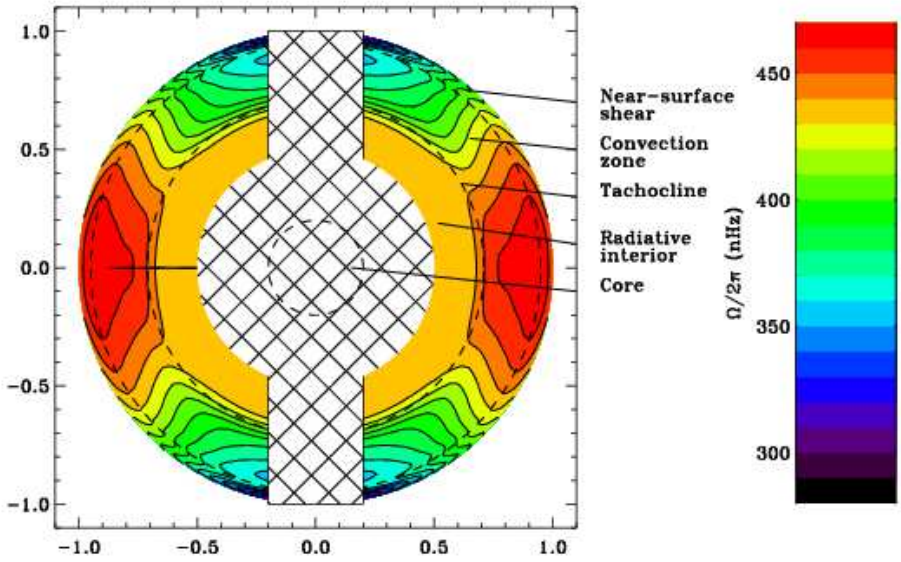

FIGURE 1.8. Cross-section of the solar interior. Contours of constant rotation show that the plasma in the convection zone rotates faster at the equator than at the poles, and highlights features such as the near-surface shear layer, tachocline, and uniformly rotating radiative interior. Cross-hatches indicate regions where helioseimsology is not yet capable of reliably capturing the interior structure. Figure from Howe (2009).

The discovery of this shearing layer prompted the idea that the tachocline is the seat of the dynamo's toroidal magnetic field generation and amplification.

Differential rotation on the solar surface has been known to exist for many years as a result of sunspot tracking, as sunspots tend to rotate faster in the prograde direction closer to the equator (e.g. Gilman and Howard 1985). Helioseismic results show that this differential rotation does indeed extend throughout the entirety of the convection zone. Maintenance of the solar differential rotation is a result of angular momentum redistribution of non-axisymmetric motions, particularly convection, through Reynolds stresses (see e.g. Miesch 2005). It may also be the case that the presence of a large-scale magnetic field in the convention zone could alter the Reynolds stress or redistribute angular momentum through the Lorentz force.

As shown in Figure 1.8, contours of constant rotation in the solar convection zone are conical in shape. In the absence of latitudinal (θ) entropy (S) gradients such that $\partial S/\partial\theta = 0$, the rotation profile will be cylindrical following the Taylor-Proudman theorem (e.g. Miesch 2005), as is the case in a large number of early convection zone simulations (e.g. Gilman 1977; Gilman and Miller 1986; Miesch *et al.* 2000). However, if the system is in thermal wind balance and there is a latitudinal entropy variation that increases from low to high latitudes, a solar-like conical rotation profile can be created. Such conditions would require the solar poles to be $\sim$5 K warmer than equatorial regions (e.g. Miesch 2005). Unfortunately, detecting such small variations of the solar thermal profile is beyond the current capabilities of helioseismology.

Whether the magnetic field in question resides on the solar surface, the bulk of the convection zone, or the tachocline, it will interact with surrounding convective motions. The magnetic field can be advected by convective flows, or stretched and amplified by shearing motions. Therefore, in the context of this thesis, it is important to understand the nature of convection and differential rotation in order to study how these fluid motions influence the dynamic evolution of active-region-scale magnetic flux tubes.

1.4. Simulations of Solar Magnetic Flux Emergence and Convection

Numerical simulations have shed light on the solar flux emergence process and the nature of fluid motions in the bulk of the solar convection zone. Advances in numerical methods and high-performance supercomputing have allowed for sophisticated models that make contact with solar observations. Here some selected models that pertain to solar flux emergence and convection are reviewed.

Valuable insights into the nature and evolution of rising magnetic flux loops through a stably stratified, quiescent solar convective envelope have been gained through the use of the thin flux tube (TFT) approximation by a plethora of authors (e.g. Spruit 1981a,b; Moreno-Insertis 1986; Ferriz-Mas and Schüssler 1993; Longcope and Klapper 1997). Such studies indicate that the Coriolis force is responsible for a variety of active region behavior such as: tilt angles in accordance with Joy's Law (D'Silva and Choudhuri 1993; Caligari, Moreno-Insertis, and Schüssler 1995), the apparent faster proper motion of the leading polarity of an emerging active region on the solar surface (van Driel-Gesztelyi and Petrovay 1990; Moreno-Insertis, Caligari, and Schüssler 1994; Caligari, Moreno-Insertis, and Schüssler 1995), and an asymmetry where the leading polarity shows a more coherent morphology (Fan, Fisher, and Deluca 1993; Caligari, Moreno-Insertis, and Schüssler 1995; Caligari, Schüssler, and Moreno-Insertis 1998).

These simulations also help to shed some light on the dynamo generated magnetic field strength, suggesting that the toroidal magnetic field strength at the base of the convection zone needs to be between $30 - 100$ kG for active-region-scale magnetic flux tubes to exhibit properties similar to those of active regions on the Sun (Choudhuri and Gilman 1987; D'Silva and Choudhuri 1993; Schüssler *et al.* 1994; Caligari, Moreno-Insertis, and Schüssler 1995). The TFT model has also been used to explore the possibility of polar flux emergence on rapidly rotating Suns (e.g. Schüssler and Solanki 1992), the twist of magnetic field lines resulting from helical turbulence in the weakly twisted TFT regime (e.g. Longcope and Klapper 1997; Longcope, Fisher, and Pevtsov 1998), and flux emergence in early-type stars with convective cores and radiative exteriors (MacGregor and Cassinelli 2003).

Equations describing the evolution of the TFT model are derived from ideal MHD by performing a first order expansion of the governing equation with respect to a/L, where a is the cross-sectional radius of the flux tube and L is the length scale variation (for a first formulation see Spruit 1981a,b). All physical quantities of the flux tubes are taken as averages over the cross-section, and only vary along the flux tube axis, therefore it is considered to be a one-dimensional (1D) model. As such, TFT models are computationally inexpensive to perform, providing a useful platform for a parameter space study. Although useful, the 1D nature of the TFT approximation does not capture the possible fragmentation of the flux tube and its internal structure, nor does it resolve the interaction of the flux tube cross-section with its environment. Additionally, the TFT approximation is not satisfied in the upper $\sim 0.05 R_\odot$ portion of the convection zone where the radius of the flux tubes is on the order of the local pressure scale height (e.g. Moreno-Insertis 1992).

An approach to resolving the interaction of the flux tube cross-section with a quiescent model solar convection zone environment is provided by two-dimensional (2D) MHD studies (e.g. Fan, Zweibel, and Lantz 1998; Emonet and Moreno-Insertis 1998), followed by 3D MHD models in Cartesian boxes both with and without rotational effects (e.g. Abbett, Fisher, and Fan 2000, 2001; Fan 2001), and rotating spherical shells or shell sectors (e.g. Jouve and Brun 2007; Fan 2008). These studies show that the flux tube cross-section does not remain coherent, but rather fragments as it rises, and develops trailing magnetic wakes. It is also found that the fragmentation of the tube can be suppressed by a sufficient twist of the magnetic field lines comprising the flux tube.

The next step for flux emergence models was then to include the effects of turbulent solar-like convection on 3D models of buoyantly rising magnetic flux tubes. Using a flux

tube model in a horizontal convecting box, Fan, Abbett, and Fisher (2003) find that weakly equipartition and weakly super-equipartition magnetic field strength flux tubes are susceptible to deformations by convective flows. Strong downdrafts pin portions of the flux tube to the bottom of the domain, while parts of the flux tube within upflows are boosted toward the surface. Considering that the solar convection zone is highly turbulent, it is likely that similar processes influence the evolution of flux tubes as they traverse the convection zone.

Early models of rotating, 3D stellar convection were relatively laminar with limited spatial resolution (e.g. Gilman 1978, 1979; Gilman and Miller 1981; Glatzmaier 1984). However, they do produce traveling, rotationally aligned convection cells of low order periodic longitudinal structure (m$\sim$10), as predicted by linear theory (e.g. Busse 1970). Taking advantage of more recent scalable, massively parallel supercomputers, a numerical model knows as the Anelastic Spherical Harmonic (ASH) code was developed (e.g. Miesch *et al.* 2000; Brun, Miesch, and Toomre 2004). The ASH code solves the 3D anelastic fluid equations, wherein fluid motions are considered to be subsonic, using a pseudo spectral method with both spherical harmonic and Chebyshev basis functions.

The ASH code is highly versatile, having been used to great success in the solar regime (e.g. Brun and Toomre 2002; Miesch *et al.* 2008), including rapidly rotating young Suns (Brown *et al.* 2008, 2010; Nelson *et al.* 2013), and for other main sequence stars with convective cores (Brun, Browning, and Toomre 2005), convective outer shells (Matt *et al.* 2011; Augustson *et al.* 2012), or M-type stars that are fully convective (Browning 2008). Such simulations intrinsically capture large scale flows such as differential rotation and meridional circulation in stars with convective envelopes. Solar convection simulations computed with

ASH match closely the solar differential rotation profile as found via helioseismology (e.g. Miesch, Brun, and Toomre 2006; Miesch *et al.* 2008).

The first 3D MHD simulation of an isolated magnetic flux tube evolving in a spherical, rotating convective velocity field were performed with the ASH code by Jouve and Brun (2009), followed by Jouve, Brun, and Aulanier (2013), and then Pinto and Brun (2013) where the flux tube is embedded in a background dynamo field. Another model investigates the same phenomenon using a finite-difference spherical anelastic MHD (FSAM) approach (Fan, Featherstone, and Fang 2013). The objective of these models is to gain a better understanding of the global interaction between convection and buoyantly rising magnetic flux tubes.

While these simulations are highly attractive due to their complex 3D nature, they suffer undesirable consequences because of the same reason. Direct MHD simulations must discretize the three-dimensional domain, and thus are subject to numerical diffusion. To adequately resolve the flux tube such that numerical diffusion is negligible, the spatial extent of the domain is severely limited. Alternately, the problem can be resolved by increasing the magnetic flux of the isolated tube such that it does not suffer a significant erosion of its magnetic buoyancy and magnetic tension due to numerical diffusion (i.e. the flux tube does not preserve the flux frozen-in condition). Unfortunately this results in unreasonably large magnetic flux values of $\sim 10^{23}$ Mx, an order of magnitude larger than most sunspot magnetic flux. In addition, to favor the creation of a buoyantly rising loop in a realistic time frame, tubes with such large flux are given an ad hoc entropy perturbation to promote a magnetic buoyancy instability.

The aforementioned models in this section must introduce an isolated magnetic flux tube to the computational domain. Recent ASH simulations in solar-like convective domains rotating at three times the current solar rate are able to self-consistently create wreaths of magnetism from seed fields (Brown *et al.* 2010, 2011; Nelson *et al.* 2013). Such wreaths exhibit cyclic behavior, and are capable of developing buoyant loops in certain circumstances. These simulations demonstrate that persistent toroidal fields of moderate strength can be generated by and coexist with turbulent convection.

Of course the journey of a magnetic flux tube does not stop where the TFT approximation or anelastic approximation no longer hold. Fully compressible MHD simulations are required in the upper levels of the convection zone near the solar surface where velocities are no longer subsonic and active-region-scale flux tubes are no longer thin. Due to the sharp density stratification in the upper $\sim$20 Mm of the convection zone, it is not yet computationally possible to perform 3D MHD simulations that span from the base of the convection zone to the photosphere and above. Also, ionization and radiative processes that occur at the photosphere are complicated effects not included in global convective models. As a result, simulations modeling flux emergence through the upper few Mm of the convection zone and up into the lower solar atmosphere are decoupled from flux emergence simulations in the convection zone proper (for a few example simulations, see Martínez-Sykora, Hansteen, and Carlsson 2008; Fan 2009b; Fang *et al.* 2012). However, the time is ripe to work toward creative solutions which allow for coupling of these dynamic regimes, covering multiple pressure scale heights and therefore various scales of required spatial resolution.

None of the methods to numerically model flux emergence presented in this section are ultimately *better* than another. They are all complementary, and together paint a more

coherent picture of the flux emergence process in the Sun. Within the context of this thesis, the global flux emergence process in the bulk of the convection zone is addressed through a hybrid approach, employing a thin flux tube model embedded in a rotating spherical shell of turbulent, solar-like convection computed via the ASH code as described in Chapter 2.

1.5. The Solar/Stellar Connection

In order of decreasing mass, radius, and surface temperature, stars along the main sequence are given spectral class designations of: O, B, A, F, G, K, and M, as shown in the Hertzsprung-Russell diagram of Figure 1.9. Many cool dwarf (main sequence F, G, K, and M-type) stars exhibit magnetic activity. The Sun, a G2 dwarf, is only one of ∼300 billion stars in the Milky Way, thus reminding us that the in-depth observations of our magnetic star represent a negligible portion of the varieties of stellar behavior. Exoplanet hunting telescopes such as ESA's CoRoT and NASA's Kepler satellite missions have identified numerous Earth-like planets orbiting solar-like stars. As such, comparative studies of solar and stellar magnetism will help to decipher the dynamo mechanism in magnetic stars, and may shed light on the possible space weather conditions in the vicinity of exoplanets in the habitable zone.

Modulation in magnetic activity can be detected on cool stars by observing their chromospheres. The chromosphere is the region of a stellar atmosphere directly above the photosphere, but below the corona. Throughout most of this region, the temperature actually increases outward from the photosphere, rather than falling off with increasing distance. Mechanical energy is input into the chromosphere from the underlying photosphere, heating the decreasingly dense plasma to values above what is expected from radiative equilibrium

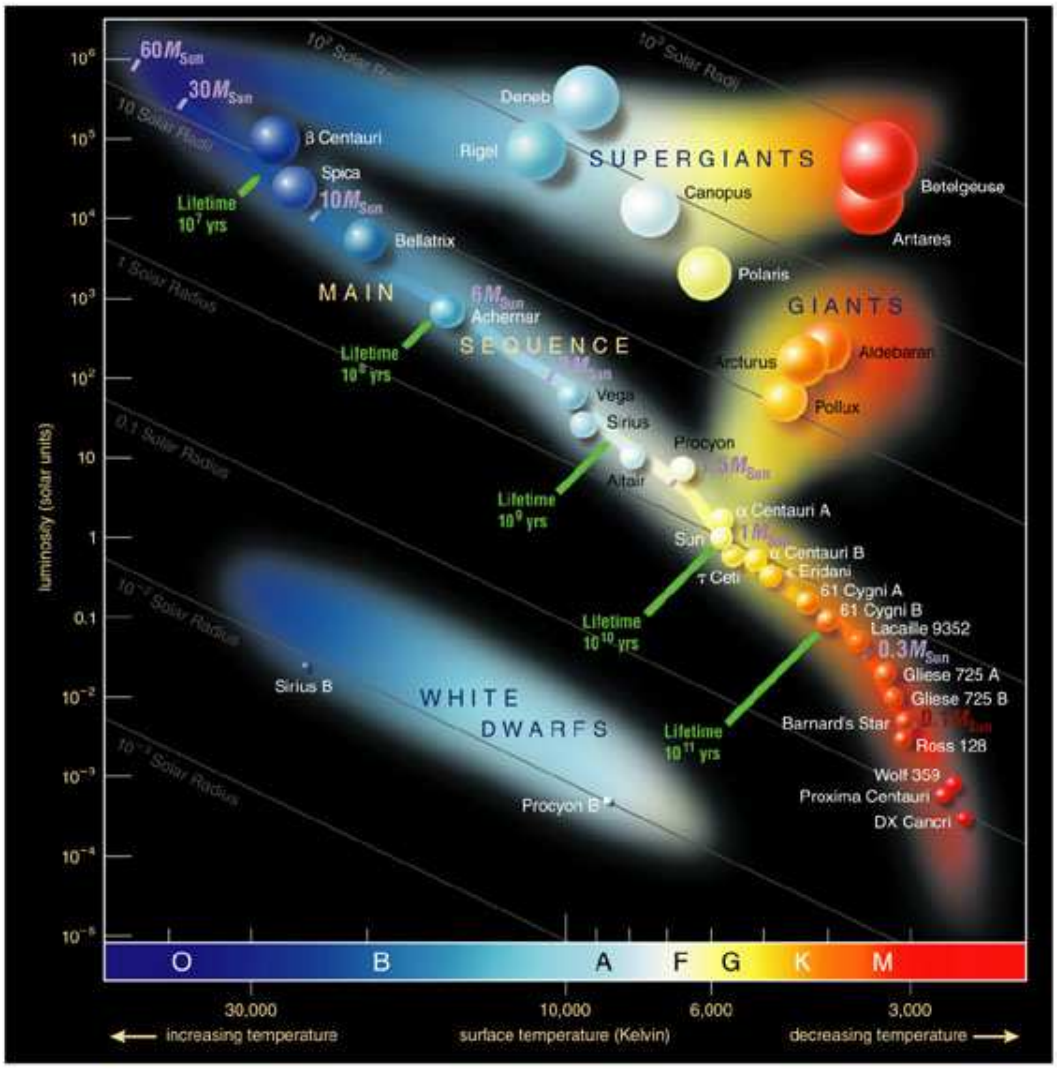

FIGURE 1.9. Hertzsprung-Russell diagram depicting the relationship between stellar spectral types, temperature, luminosity, and size.

(e.g. Hall 2008). Stellar chromospheres are best observed in the Ca II H and K emission lines, which arise from singly ionized calcium.

Böhm-Vitense (2007) compares the activity cycle period (P_{cyc}) obtained from Ca II emission fluxes as a function of rotation period (p_{rot}) for 25 solar-like (F7V-K7V) stars, and finds interestingly that the Sun's position on the graph is between the so-called active sequence (indicated by A) and the inactive sequence (indicated by I), as shown in the left panel of

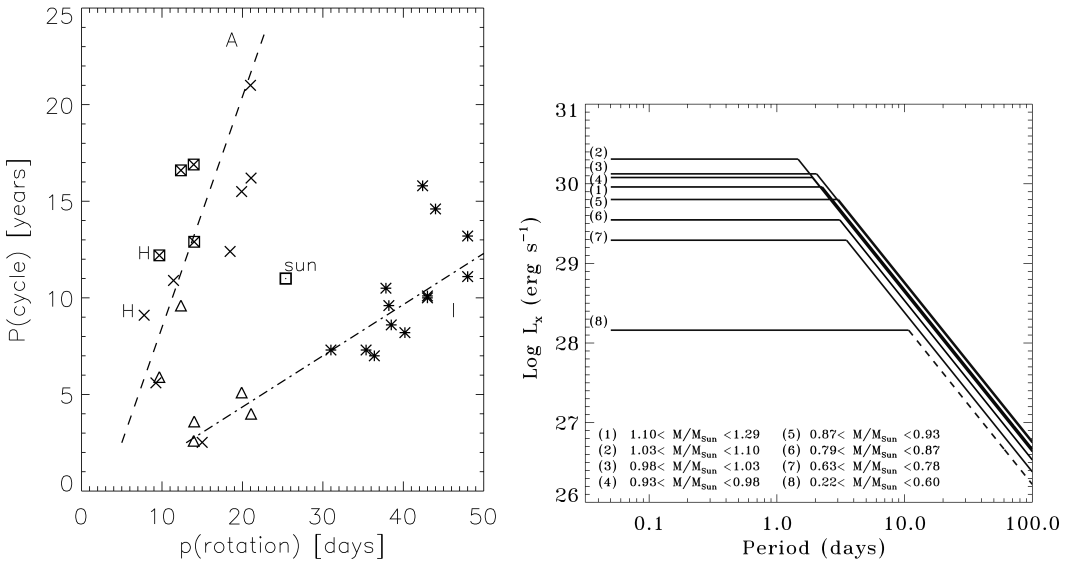

FIGURE 1.10. (Left) Activity cycle period as a function of rotation period for 26 F7V-K7V stars. The Sun's position on this plot is unusual compared to the other stars. Figure from Böhm-Vitense (2007). (Right) X-ray activity as a function of rotation period for 259 low mass dwarfs. Activity increases with increasing rotation rate until reaching a saturation level. Figure from Pizzolato *et al.* (2003).

Figure 1.10. As a result, the author states: *Clearly the Sun is not a good standard star for the discussion of stellar activity*, thus prompting further studies of the link between stellar magnetism and rotation, and how the Sun fits into this puzzle. Baliunas *et al.* (1995) perform a similar investigation of 111 F-M spectral type stars over a period of 25 years, and find that 46% exhibit activity cycles from 2.5 years to at least 25 years. Another 26% show variability with no periodicity, and the remaining 28% show little to no variability. Most of the stars with irregular cycle variability tend to be young and rapidly rotating.

Older cool dwarfs rotate much slower than their younger counterparts, as their associated stellar winds remove angular momentum in a process known as magnetic breaking (e.g. Wood 2004). It is likely that the rapidly rotating young Sun had a much higher level of magnetic activity and less cyclic, more irregular periods of variability (e.g. Güdel 2007). This trend of

increasing activity levels with more rapid rotation is seen in other low mass (F through M-type) dwarfs, as activity levels increase with rotation rate until reaching a saturation point, as shown in the right panel of Figure 1.10 where X-ray activity is taken as an indicator of magnetic activity (e.g. Pizzolato *et al.* 2003; Reiners 2012).

It is difficult to assess the average magnetic field strength of most F through K-type dwarfs because they have such rapid rotation rates. However, observations of active M-type dwarfs reveal an average magnetic field strength of around a few kG (e.g. Reiners 2012). Compared to the Sun's $\sim 10 - 10^2$ G magnetic field strength (which varies based on determination methods), this is remarkably large, although it is the case that average magnetic fields of a few kG have been observed on cool stars of all spectral types (e.g. Reiners 2012). A good estimate for the upper limit of a star's magnetic field can be obtained by calculating the expected equipartition (i.e. pressure-balancing) magnetic field as $B_{eq} \propto P_{gas}^{1/2}$, where P_{gas} is the photospheric gas pressure (Saar 1990). The magnetic field may saturate when the rotation reaches a critical rate, associated with the rotation rate when the Rossby number $R_o = P_{rot}/\tau_{conv} \sim 0.1$, where P_{rot} is the rotational period of the star and τ_{conv} is the convective turnover time scale (e.g. Reiners 2012).

Solar-like main sequence stars of F, G, and K-type possess outer convection zones, and radiative cores where the most efficient means of energy transport is by radiation. As a result, such stars are all assumed to have tachoclines, shearing interfaces between the radiative zone and convection zone, where magnetic fields are generated, similar to the solar dynamo paradigm. Stellar luminosity increases with increasing mass, while the radial fraction of the outer convective envelope of these stars decreases such that $0.5\mathrm{M}_\odot - 1.3\mathrm{M}_\odot$ stars have convection zone depths of $\sim 44\% - 14\%$, respectively, of their total radius. Therefore, convection

becomes more vigorous with increasing stellar mass, as the amount of required energy flux transport increases and the convection zone becomes shallower in radius. Indeed, convective radial velocities increase for simulations of global-scale convection in more massive F-type stars as compared to solar-like G-type stars (for a comparison, see e.g. Brown *et al.* 2010; Augustson *et al.* 2012). These same simulations indicate that that rapidly rotating stars with outer convection zones have a stronger differential rotation, weaker meridional circulation, and more modulated convection in the equatorial regions (e.g. Brown *et al.* 2008; Matt *et al.* 2011; Augustson *et al.* 2012). At very large rotation rates, localized patterns of convection emerge creating *nests of convection* (see Brown *et al.* 2008; Augustson *et al.* 2012).

The most massive main sequence stars of O, B, and A-types are thought to have convective interiors and radiative outer shells. These stars tend to be less magnetically active, although $\sim$10% of A-type stars have observable magnetic fields (see Moss 2001). The question as to whether or not their magnetism is the result of a fossil field of primordial origin, dynamo action in the convective core, or the interaction of the core dynamo with a fossil field is still not resolved (see Featherstone *et al.* 2009). These stars also have a shorter lifetime on the main sequence branch, as the mass loss by stellar winds for massive stars is much greater than in low mass stars (e.g. Prialnik 2000).

The lowest mass main sequence stars of M-type are fully convective. Although lacking a tachocline, these stars are magnetically active, and often exhibit strong flaring events, suggesting that fully convective stars can generate volatile magnetic fields. In fact, it is found from simulations of rotating, spherical convecting shells in stellar regimes that dynamo action can be sustained without a tachocline (e.g. Browning 2008; Brown *et al.* 2010; Augustson *et al.* 2012). What is clear is that shearing motions in the stellar interior contributed by

a tachocline region and/or differential rotation is needed to sustain a dynamo (e.g. Reiners 2012).

Similar to the Sun, most stars with convective outer layers exhibit starspots. There are a variety of observational tools and techniques that can be used to create maps of stellar surfaces (for a description of methods, see reviews by Berdyugina 2005; Strassmeier 2009). One method of starspot detection utilizes high-precision photometry proved by the CoRoT and Kepler missions. Deviation in stellar light curves during planetary transits can be identified as signatures of starspots through light curve modeling efforts (e.g. Silva-Valio and Lanza 2011). Such observations are crucial as they provide constraints on the operation of the underlying dynamo and subsequent flux emergence process.

Recovered starspot latitudes suggest that some stars may actually have concentrations of magnetic flux emergence at or near the poles, unlike the current Sun (e.g. Berdyugina 2005; Strassmeier 2009). This behavior could be accounted for by the Coriolis force acting on rising magnetic flux tubes in rapidly rotating stars (e.g. Schüssler and Solanki 1992; Schüssler *et al.* 1996), or by the presence of a deeper convection zone. Some active stars exhibit spots in multiple latitude ranges simultaneously (e.g. Barnes *et al.* 1998; Frasca *et al.* 2011), suggesting perhaps more than two toroidal bands of dynamo activity, deviating from the generally accepted solar paradigm. Additionally, some stars exhibiting both polar spots and low latitude spots still show cycles of variation similar to stars without polar spots (see Strassmeier 2009). This suggests that the low latitude spots follow a cyclic variation on a separate timescale from the evolution of polar spots. It may also be the case that starspots can propagate from low latitudes to high latitudes during the course of a stellar

cycle, opposite of the latitudinal migration pattern for spots on the Sun (Vogt *et al.* 1999; Strassmeier and Bartus 2000).

Active longitudes, longitudinal regions of preferred starspot emergence, have been observed on the Sun (e.g. de Toma, White, and Harvey 2000; Berdyugina and Usoskin 2003) and young solar analogs such as AB Doradus (K0V) (Järvinen *et al.* 2005), LQ Hydrae (K2V) (Berdyugina, Pelt, and Tuominen 2002), and Kepler-17 (G2V) (Bonomo and Lanza 2012). Often, stars exhibiting active longitudes, the Sun included, have two preferred regionss of longitudinal flux emergence that tend to be separated by 180°, and *flip-flop* such that one active longitude may be more pronounced than another. The physical mechanisms responsible for the active longitude phenomenon are not well understood for single, solar-like stars. Although some theories have been put forward suggesting that active longitudes result from non-axisymmetries in the dynamo generated magnetic field (Ruzmaikin 1998; Nelson *et al.* 2013), simultaneous instabilities in both the tachocline and toroidal magnetic field band (Dikpati and Gilman 2005), or from large-scale organization of flux emergence by giant cell convective structures present in the convection zone proper as discussed in this thesis in Chapter 5.

Stellar flaring events are an explosive result of the release of stored magnetic energy. Flares, typically associated with the location of active regions, are observed as sudden brightenings in stellar atmospheres, and are capable of emitting radiation across the entire electromagnetic spectrum. Solar flares were first observed in the white light continuum in 1859 (e.g. Benz 2008). Detection of flaring events on other stars is done through the identification of intense, short-lived peaks in the stellar light curve, or enhancements in certain emission lines (e.g. Pettersen 1989; Maehara *et al.* 2012). The quintessential flaring stars are

main-sequence M-type stars, although flaring occurs on a significant portion of stars with outer convection zones, and has occasionally been observed on A-type stars (e.g. Pettersen 1989).

Finally, starspots are useful in identifying the rotation rate of stars and the differential rotation of their convective zones (e.g. Berdyugina 2005; Strassmeier 2009). Assuming that starspots live for several rotations, periodic modulations in the stellar light curve provide a measurement of the star's rotation rate (for a large collection of Kepler target stars, see e.g. Basri *et al.* 2011; Nielsen *et al.* 2013). If the approximate latitude of starspots are known via starspot modeling, tracking their relative rotation rates give an indication of the star's differential rotation (e.g. Collier Cameron, Donati, and Semel 2002; Oláh, Jurcsik, and Strassmeier 2003; Barnes *et al.* 2005). Astroseismology is also another promising way to detect differential rotation on solar-like stars, as discussed in Gizon and Solanki (2004). The difficulty with using astroseismology or starspot tracking to obtain information about stellar rotation rates and differential rotation is the need for long-term observations of about a month or longer. As such, available literature on these topics are extremely biased toward rapidly rotating stars, however Lund, Miesch, and Christensen-Dalsgaard (2014) have made some progress in using astroseismology to investigate differential rotation in stars with moderate rotation rates closer to that of the Sun.

Our Sun represents one example of the varieties of stellar behavior. In order to understand the intricacies of the Sun's dynamo, we must perform comparative studies of a multitude of main-sequence stars. Such studies will help to sort out the complicated processes involved in the generation and sustainment of stellar dynamos across the Hertzsprung-Russell diagram.

1.6. Objectives and Proposed Methods

A large statistical study of the global interaction of convection with rising active-region-scale magnetic flux tubes in the bulk of the solar convection zone for a variety of initial parameters has never before been accomplished. Attempting such a study in the fully 3D MHD regime is not currently computationally viable. We present an alternative by employing a *hybrid* flux emergence simulation. We model isolated magnetic flux tubes using the 1D thin flux tube (TFT) approximation, coupling them to a 3D time-dependent simulation of solar-like convection in a rotating spherical shell computed separately from the TFT model via the ASH code, as described in Chapter 2. For each grid point along the flux tube at every timestep of the flux tube evolution, we retrieve the corresponding velocity field components from the ASH simulation through an interpolation method. The ASH velocity field then interacts with the flux tube through the drag force it experiences as it traverses through the turbulent, convective medium. This scheme eliminates the need to solve for the interaction of the flux tube cross-section with the surrounding environment, and does not require the velocity field and evolution of the flux tube to be solved simultaneously. As such, a simulation run solving for the evolution of an individual flux tube can be performed on a standard desktop computer with adequate memory and disk space in less than an hour in most cases.

This method captures the dynamical effects of convection on rising magnetic flux tubes while circumventing the problem of artificial diffusion. These simulations also develop flux tube buoyancy instabilities self-consistently, as convective upflows and downflows perturb rising magnetic loops. As the thin flux tube approximation itself is computationally inexpensive, many flux tube simulations can be conducted in a reasonable timeframe, allowing for

a large statistical study of solar active-region-scale magnetic flux tubes subject to interaction with flows taken from a hydrodynamic ASH simulation.

Summarized below are the main topics this thesis proposes to address through the use of our simulation scheme:

- Identify the magnetic-buoyancy-dominated and convection-dominated regimes for active-region-scale flux tubes of equipartition to super-equipartition magnetic field strengths (Chapter 3)
- Characterize the influence of large-scale, global convection on flux tube properties at the simulation upper boundary - a proxy for active regions observed on the solar surface (Chapter 4 and Chapter 5)
- Better constrain the dynamo generated magnetic field strength by comparing simulation results to those of active region observations (Chapter 4)
- Address the influence of radiative diffusion through the base of the convection zone on the dynamic evolution of magnetic flux tubes (Chapter 6)
- A discussion on possible future research using our simulation scheme (Chapter 7) to (1) determine whether convective motions are capable of inducing a twist of flux tube magnetic field lines, as seen in observations of sunspots, and (2) investigate flux emergence properties on the young, rapidly rotating Sun, (3) paving the way for future simulations of flux emergence across the Hertzsprung-Russell diagram

Through our novel hybrid TFT+ASH approach to address the above topics, we have shed some light on current solar and stellar physics issues, enriching our understanding of stellar magnetism and its relation to processes in the convection zone of cool stars.

CHAPTER 2

Model Description: Flux Emergence Simulations

Starspots are observable manifestations of magnetism on stellar surfaces, thus providing a photospheric link to the deep-seated dynamo mechanism. The work in this thesis provides a connection between the solar dynamo and active regions by performing simulations of magnetic flux emergence through the bulk of the turbulent solar convection zone. This chapter describes the methods employed to investigate flux emergence in a solar-like star, which involves taking a hybrid approach by combining a thin flux tube model with a three-dimensional, rotating spherical shell of turbulent solar-like convection.

2.1. The Thin Flux Tube Model

In the case of ideal MHD where the plasma is treated as a perfectly conducting fluid, which is a good assumption for the solar interior, magnetic field lines and plasma elements behave as if they are tied together (see Appendix B). Bundles of magnetic field are confined by plasma into tubular structures called magnetic flux tubes. The observational existence of such flux tubes is illustrated especially well by sunspots/starspots, appearing when rising magnetic flux tubes intersect with the stellar surface.

Valuable insights into the nature and evolution of dynamo-generated, isolated, rising magnetic flux loops through a quiescent solar convection zone have been gained through the use of the thin flux tube (TFT) approximation by a plethora of authors (e.g. Spruit 1981a,b; Moreno-Insertis 1986; Ferriz-Mas and Schüssler 1993; Longcope and Klapper 1997). Spruit (1981a) develops the basic equations for the motion of a thin flux tube from ideal MHD by

assuming that the cross-sectional radius of the flux tube a is small compared to both its total length L and the local pressure scale height, corresponding to an expansion in lowest order of the MHD equations in powers of a/L. Choudhuri and Gilman (1987) extends the thin flux tube equations to include the effect of solar rotation and the drag force that the flux tube experiences as it traverses through the solar plasma. All physical quantities of the flux tubes are taken as averages over the cross-section, only varying spatially along the flux tube axis, therefore the TFT approximation is a one-dimensional model.

Using the idealized construction of an isolated thin flux tube, we study the dynamic evolution of concentrated flux tubes influenced by the integrated forces acting on each segment of the tube. A derivation of the thin flux tube equations from ideal MHD, and the subsequent equations derived for use in the computational model, can be found in Appendix C. For this thesis, the equations that describe the evolution of each segment of the thin flux tube are:

$$\begin{aligned} \rho\frac{d\mathbf{v}}{dt} &= -2\rho(\mathbf{\Omega_0}\times\mathbf{v}) - (\rho_e-\rho)[\mathbf{g}-\mathbf{\Omega_0}\times(\mathbf{\Omega_0}\times\mathbf{r})] + \frac{\partial}{\partial s}\left(\frac{B^2}{8\pi}\right)\mathbf{l} + \frac{B^2}{4\pi}\mathbf{k} \\ &\quad -C_d\frac{\rho_e|(\mathbf{v}-\mathbf{v}_e)_\perp|(\mathbf{v}-\mathbf{v}_e)_\perp}{(\pi\Phi/B)^{1/2}}, \end{aligned} \tag{2.1}$$

$$\frac{d}{dt}\left(\frac{B}{\rho}\right) = \frac{B}{\rho}\left[\frac{\partial(\mathbf{v}\cdot\mathbf{l})}{\partial s} - \mathbf{v}\cdot\mathbf{k}\right], \tag{2.2}$$

$$\frac{1}{\rho}\frac{d\rho}{dt} = \frac{1}{\gamma P}\frac{dP}{dt} - \nabla_{ad}\frac{\rho}{P}T\frac{dS}{dt}, \tag{2.3}$$

$$P = \frac{\rho RT}{\mu}, \tag{2.4}$$

$$P + \frac{B^2}{8\pi} = P_e, \tag{2.5}$$

where, $\mathbf{r}$, $\mathbf{v}$, B, ρ, P, T, which are functions of the time t and arc length s measured along the tube, denote respectively the position, velocity, magnetic field strength, gas density, pressure, and temperature of a Lagrangian tube segment, $\mathbf{l} \equiv \partial\mathbf{r}/\partial s$ is the unit vector tangential to the flux tube, $\mathbf{k} \equiv \partial^2\mathbf{r}/\partial s^2$ is the tube's curvature vector, subscript '$\perp$' denotes the component perpendicular to the flux tube, Φ is the constant total flux of the tube, ρ_e, P_e, and μ, which are functions of depth only, are respectively the pressure, density, and mean molecular weight of the surrounding external plasma, $\mathbf{g}$ is the gravitational acceleration that is a function of depth only, $\mathbf{\Omega_0}$ is the angular velocity of the reference frame co-rotating with the sun, with $\Omega_0 = 2.7 \times 10^{-6}$ rad/s in all Chapters, $C_d = 1$ is the drag coefficient, γ is the ratio of specific heats, S is the entropy per unit mass, ∇_{ad} is the adiabatic temperature gradient, and $\mathbf{v}_e(\mathbf{r}, t)$ (discussed in Chapter 2.2) is a time dependent velocity field (relative to the rotating frame of reference) that impacts the dynamics of the thin flux tube through the drag force term (last term in Eq. 2.1). The term $\mathbf{v}_e$ accounts for both the local convective flows and mean flows such as differential rotation. In the above equations, we do not introduce an explicit magnetic diffusion or kinematic viscosity term. The thin flux tube is untwisted (i.e. magnetic field lines do not twist about the flux tube axis), and is discretized with 800 uniformly spaced grid points along its arc length s. The numerical methods used to solve for the flux tube evolution as determined by the above set of equations has been described in detail in Fan, Fisher, and Deluca (1993) and in Appendix E.

For the stratification of the external field free plasma, namely ρ_e, P_e, T_e, μ, g, γ, and the super-adiabaticity, we use the reference solar model by Christensen-Dalsgaard *et al.* (1996)

for the solar convection zone with an extension of a simple polytropic, sub-adiabatically stratified thin overshoot layer, as described in Fan and Gong (2000). Profiles of T_e, ρ_e, P_e, and the super-adiabaticity $\delta = \nabla - \nabla_{ad}$, where $\nabla = d\ln T_e / d\ln P_e$ and ∇_{ad} is the value of ∇ one obtains by considering local adiabatic perturbations, are shown in Figure 2.1. We define the base of the convection zone as 5.026×10^{10} cm, which is the radius of the reference solar model where the plasma changes from sub-adiabatic (stably stratified) to super-adiabatic (unstably stratified). The bottom left panel of Figure 2.1 shows the sub-adiabaticity of the thin overshoot layer, which extends from 4.8×10^{10} cm to 5.026×10^{10} cm. The bottom right panel shows the logarithm of the super-adiabaticity in the convection zone, which extends from 5.026×10^{10} cm to 6.75×10^{10} cm.

The equation of motion of the flux tube is given by Eq. 2.1. More specifically, the right-hand side (RHS) of this equation gives the various forces per unit volume experienced by each mass element along the flux tube length. The first term on the RHS of the equation represents the Coriolis force. The second term corresponds to the buoyancy force, where $\mathbf{g} - \mathbf{\Omega_0} \times (\mathbf{\Omega_0} \times \mathbf{r})$ is the apparent gravitational acceleration in the rotating reference frame, taking into account the centrifugal acceleration. The next two terms are related to a pressure gradient along the flux tube and the magnetic tension, respectively. Finally, the last term in this equation is the drag force per unit volume that the flux tube experiences as it traverses through the turbulent convection zone. This describes the interaction of the external fluid with the flux tube in a high Reynolds number regime (e.g. Batchelor 1967), with the drag coefficient C_d believed to be $\sim$1. The drag force is non-zero only when fluid flows relative to the flux tube are perpendicular to the flux tube, and the relative velocity of the flux tube element with respect to the surrounding fluid flows ($\mathbf{v}_e$) is given by $\mathbf{v} - \mathbf{v}_e$.

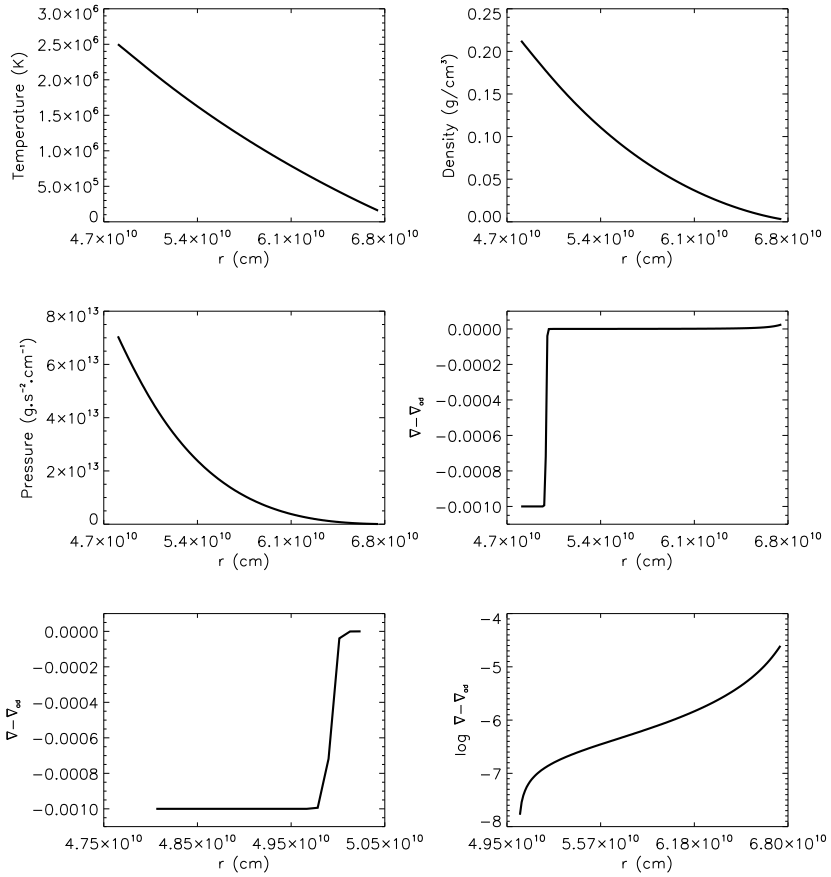

FIGURE 2.1. Profiles of T_e, ρ_e, P_e, and adiabaticity factor δ for the entire simulation domain as a function of solar radius r for the reference solar model. The bottom left panel shows the sub-adiabaticity in the overshoot region, whereas the bottom right panel shows the logarithm of the super-adiabaticity in the convection zone.

Derived from the Walén Equation, which is a combination of the MHD continuity and Induction Equations, Eq. 2.2 describes the evolution of the magnetic field of the flux tube with respect to its density for a thin magnetic flux tube where $\mathbf{B} = B\mathbf{l}$ (see Appendix C for a full derivation). More specifically, this equation describes the change in length of a flux tube segment, as $B/\rho = (\phi\ \delta s)/(\pi\ \delta m)$, where δm is the mass of the flux tube element and δs is the length of the flux tube element. Stretching (first term on RHS of Eq. 2.2) and bending (second tern on RHS) both contribute to the change in length, and therefore change in B/ρ, of the flux tube.

It is also assumed that the plasma gas pressure is determined by an equation of state, which is taken to be the ideal gas law (Eq. 2.4). Due to the thin flux tube limit, the sound speed crossing time of the flux tube diameter is small compared to other relevant timescales of the system. As a result, there is an instantaneous lateral pressure balance assumed between the tube and the external unmagnetized plasma, given by Eq. 2.5.

The energy equation for the flux tube is given by Eq. 2.3. With the exception of Fan and Fisher (1996), other thin flux tube models assume that the flux tube evolves adiabatically, such that the entropy per unit mass is $dS/dt = 0$. However, near the base of the convection zone, and in the convective overshoot region, there is a non-zero divergence of radiative heat flux from the solar interior. In the lower $\sim$1/3 of the convection zone, the contribution from radiative heating to the buoyancy evolution of the flux tube plays an important role in the flux emergence process. In this thesis, flux tubes evolving adiabatically with $dS/dt = 0$ are assumed, with the exception of Chapter 6 where the effect of radiative heating on the evolution of the flux tube is examined.

2.2. The Convection Simulation

To capture solar-like convection on a global scale, the Anelastic Spherical Harmonic (ASH) code is used to create a time-varying convective velocity field, performed separately from the thin flux tube simulations. In the anelastic regime, fluid motions are considered to be subsonic, which is the case throughout most of the convection zone. Additionally, thermodynamic perturbations are considered to be small variations about their mean values. The ASH code solves the 3D anelastic Navier-Stokes fluid equations using a pseudo-spectral method with both spherical harmonic and Chebyshev basis functions, explicitly resolving

the largest scales of motion, while treating small turbulent eddies with sub-grid techniques. Sub-grid techniques refer to the inclusion of an eddy viscosity ν and eddy diffusivity κ.

The ASH hydrodynamic equations are fully nonlinear in velocity variables, linearized in thermodynamic variables with respect to a spherically symmetric background state taken from a 1D solar structure model. While this structure model is different from the external environment the flux tube experiences as discussed in Section 2.1 and shown in Fig. 2.1, the two deviate little ($\sim$10%). The mean thermodynamic variables are density $\bar{\rho}$, pressure $\bar{P}$, temperature $\bar{T}$, and specific entropy $\bar{S}$, with perturbations about the mean state of ρ, P, T, and S. The equations describing conservation of mass, momentum, and energy in a rotating reference frame for the ASH model are given as:

$$\nabla \cdot (\bar{\rho}\mathbf{v}) = \mathbf{0}, \tag{2.6}$$

$$\bar{\rho}\left[\frac{\partial \mathbf{v}}{\partial t} + (\mathbf{v}\cdot\nabla)\mathbf{v} + \mathbf{2\Omega_0}\times\mathbf{v}\right] = -\nabla\mathbf{P} + \rho\mathbf{g} - \nabla\cdot\mathbf{D} - \left[\nabla\bar{\mathbf{P}} - \bar{\rho}\mathbf{g}\right], \tag{2.7}$$

$$\bar{\rho}\bar{T}\frac{\partial S}{\partial t} = \nabla\cdot\left[\kappa_r\bar{\rho}c_p\nabla(\bar{T}+T) + \kappa\bar{\rho}\bar{T}\nabla(\bar{S}+S)\right]$$
$$-\bar{\rho}\bar{T}\mathbf{v}\cdot\nabla(\bar{\mathbf{S}}+\mathbf{S}) + \mathbf{2}\bar{\rho}\nu\left[\mathbf{e_{ij}e_{ij}} - \frac{\mathbf{1}}{\mathbf{3}}(\nabla\cdot\mathbf{v})^{\mathbf{2}}\right], \tag{2.8}$$

where $\mathbf{v} = (\mathbf{v_r}, \mathbf{v}_\theta, \mathbf{v}_\phi)$ is the local velocity in spherical coordinates in the rotating frame of constant angular velocity $\mathbf{\Omega_0}$, c_p is the specific heat at constant pressure, $\mathbf{g}$ is the gravitational acceleration, κ_r is the radiative diffusivity, and $\mathbf{D}$ is the viscous stress tensor, with components:

$$D_{ij} = -2\bar{\rho}\nu\left[e_{ij} - \frac{1}{3}(\nabla\cdot\mathbf{v})\delta_{\mathbf{ij}}\right], \tag{2.9}$$

where e_{ij} is the strain rate tensor. In these equations, ν and κ are the effective turbulent viscosity (eddy viscosity) and thermal diffusivity (eddy diffusivity), respectively, that represent unresolved subgrid-scale processes. In the simulations conducted for Chapters 3 - 6, $\nu = 2{\times}10^{13}$ cm^2 s^{-1} and $\kappa = 4{\times}10^{13}$ cm^2 s^{-1} at the simulation outer boundary, and each decreases with depth in proportion to the inverse square root of the background density $\bar{\rho}^{-1/2}$. Finally, to close the set of equations, the linearized relations for the thermodynamic fluctuations are:

$$\frac{\rho}{\bar{\rho}} = \frac{P}{\bar{P}} - \frac{T}{\bar{T}} = \frac{P}{\gamma \bar{P}} - \frac{S}{c_p}, \tag{2.10}$$

assuming the ideal gas law:

$$\bar{P} = R\bar{\rho}\bar{T}, \tag{2.11}$$

where R is the ideal gas constant.

The computational domain for the ASH simulations in all Chapters except Chapter 7.2 extends from $r = 0.69R_\odot$ to $r = 0.97R_\odot$ ($4.8{\times}10^{10}$ cm to $6.75{\times}10^{10}$ cm), and the density contrast across the domain is $\sim$69, which corresponds to 4.2 density scale heights. This yield a mid-convection zone Rayleigh number R_a of $5{\times}10^6$ and Reynolds number R_e of order 50. The Rayleigh number is defined here as $R_a = gr^2 d\Delta S/(\nu\kappa C_P)$ where g is the gravitational acceleration and $d = r_2 - r_1$ is the depth of the layer. The Reynolds number is given by $v_{rms}d/\nu$ where v_{rms} is the root mean square velocity relative to the rotating reference frame.

The ASH simulation in all but Chapter 7.2 is resolved by a grid of 129 points in r, 256 points in θ, and 512 points in ϕ. Horizontal and vertical basis functions are given by spherical harmonics and Chebyshev polynomials, eached de-aliased by keeping only the

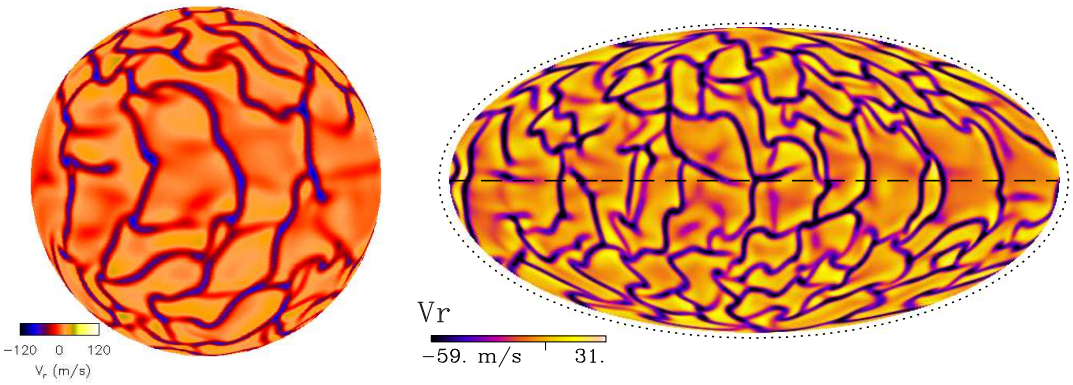

FIGURE 2.2. Snapshots of ASH convective radial velocities (left) at a depth of 25 Mm below the solar surface in an orthographic projection, and (right) at a depth of 23 Mm in a Mollweide projection with the dotted line representing the solar radius $r = R_\odot$. Strong downflow lanes (blue/purple) at the boundary of giant convective cells surround upflow regions (yellow). Also known as banana cells, the structures at low latitudes are rotationally aligned and propagate prograde.

lowest 2/3 of modes (maximum spherical harmonic degree $\ell_{max} = 170$ and Chebyshev degree $n_{max} = 86$). Similar to Case AB3 in Miesch, Brun, and Toomre (2006), a latitudinal entropy gradient is imposed on the lower boundary in order to implicitly capture thermal coupling to the tachocline: $S(\theta, r_1) = c_p\,(a_2 Y_{20} + a_4 Y_{40})$, where S is the specific entropy per unit mass, r_1 is the inner boundary, c_p is the specific heat at constant pressure, $Y_{\ell m}(\theta, \phi)$ is the spherical harmonic of degree ℓ and order m, $a_2 = 1.7 \times 10^{-6}$, and $a_4 = -0.43 \times 10^{-6}$. This helps promote a conical rotation profile. The radial entropy gradient imposed at the outer boundary is steeper, more in line with solar structure models (e.g. Christensen-Dalsgaard *et al.* 1996); $\partial S/\partial r = -10^{-5}$ erg g^{-1} K^{-1} cm^{-1} in this case compared to -10^{-7} erg g^{-1} K^{-1} cm^{-1} in Case AB3.

Figure 2.2 shows snapshots of the radial velocity of the giant-cell convection at depths of 25 and 23 Mm below the solar surface, respectively. The convective flow pattern shows broad upflow cells surrounded by narrow and intense downflow lanes, with a convective

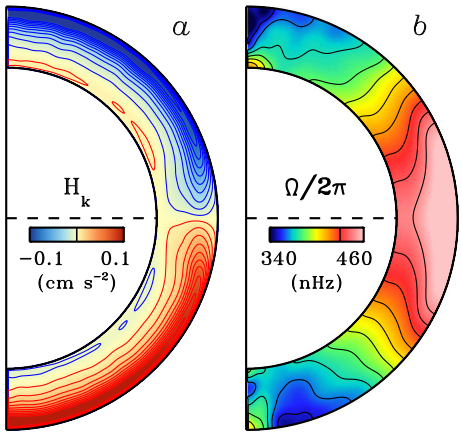

FIGURE 2.3. (a) Mean kinetic helicity and (b) angular velocity (with respect to the inertial frame) of the convection simulation, averaged over longitude and time (1366 days). Color tables saturate at the values indicated, with extrema ranging from (a) -.122 to 0.133 cm s^{-2} and (b) $326 - 468$ nHz. This ASH simulation produces a solar-like, conical differential rotation profile.

turnover timescale of $\tau \sim 2{\times}10^6$ s, or about 23 days. The maximum downflow speed in the convective envelope reaches nearly 600 m s^{-1} at a depth of about 86 Mm below the surface. Throughout most of the convection zone, the combined influence of the Coriolis force and the density stratification induces anti-cyclonic vorticity in expanding upflows and cyclonic vorticity in contracting downflows. This yields a mean kinetic helicity density $H_k = \langle \omega \cdot \mathbf{v} \rangle$ which is negative in the northern hemisphere and postive in the southern hemisphere (Fig. 2.3*a*), where $\omega = \nabla \times \mathbf{v}$ is the vorticity of the convective flow with velocity $\mathbf{v}$. Vorticity can be described as the local *spinning* motion of the fluid, whereas helicity is related to a corkscrew-like motion. There is a weak sign reversal of H_k in the lower convection zone where downflows expand and recirculate, inducing anti-cyclonic vorticity. Such a helicity pattern is typical for rotating, compressible convection (e.g. Miesch and Toomre 2009).

At low latitudes there is a preferential alignment of elongated downflow lanes with the rotation axis, reflecting the presence of so-called "banana cells" (Fig. 2.2). These features

propagate in a prograde sense relative to polar regions, due in part to the differential rotation and in part to an intrinsic phase drift akin to traveling Rossby waves (e.g. Miesch and Toomre 2009). Such structures dominate the convective Reynolds stress, maintaining a strong differential rotation comparable to that inferred from helioseismic inversions. In particular, the total angular velocity $\Omega/2\pi$ (with respect to the inertia frame) decreases monotonically from about 470 nHz at the equator to about 330 nHz at the poles and exhibits nearly conical contours at mid latitudes (see Fig. 2.3*b*), as in the solar convection zone (Thompson *et al.* 2003).

2.3. Combining TFT and ASH

The ASH convective velocity field interacts with the thin flux tube through the drag force it experiences as it traverses through the turbulent convecting plasma, the last term in Eq. C.35, where $\mathbf{v}_e(\mathbf{r}, t)$ is the temporal and spatially dependent velocity field relative to the rotating frame of reference. In this way, an isolated flux tube experiences both the local and mean flows associated with the ASH simulation, however the flux tube has no back reaction on the external velocity field. For each timestep of the TFT simulation, a four-dimensional interpolation (three spatial dimensions, and one temporal dimension) is performed to extract the plasma velocity components from the ASH simulation for each mass element along the flux tube.

Our simulations start with toroidal magnetic flux rings in mechanical equilibrium (neutral buoyancy), located at a radial distance to the center of the Sun $r = r_0 = 5.05 \times 10^{10}$ cm, slightly above the base of the solar convection zone at $r = r_{\rm czb} = 5.026 \times 10^{10}$ cm. Figure 2.4 shows a snapshot of the radial velocity at an arbitrary azimuthal angle ϕ, with the green dot representing the radius (to scale) of the largest flux tube, which occurs for magnetic field

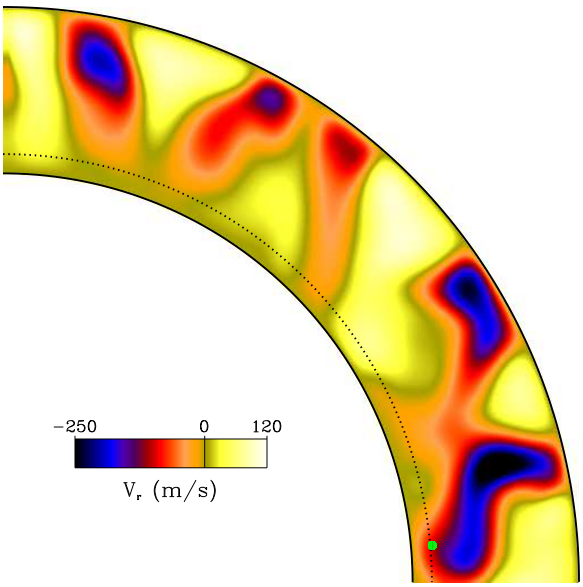

FIGURE 2.4. Snapshot of a slice of the radial velocity field ($r = 0.69\mathrm{R}_\odot - 0.97\mathrm{R}_\odot$, θ from north pole to equator) at an arbitrary azimuthal angle ϕ, with a cross section of a 15 kG flux tube (green, shown to scale), at its initial starting radius 6° above the equator. The dotted line represents the base of the convection zone at 5.026×10^{10} cm.

strengths of 15 kG. This figure shows the flux tube at its initial starting position compared to the base of the convection zone. Note that the convective velocity field is allowed to penetrate into the overshoot region. To ensure initial neutral buoyancy, the internal temperature of the flux tube is reduced compared to the external temperature.

We consider a range of initial magnetic field strengths from 15 kG to 100 kG, at initial latitudes θ_0 ranging from 1° to 40° for the toroidal flux ring. Considering the root mean square (rms) of the convective downflows from the ASH simulation at the base of the convection zone, which are on the order of 35 m/s, the equipartition magnetic field is on the order of $B_{eq} \sim 5$ kG. In this case, we are investigating flux tubes on the order of $3 - 20\ B_{eq}$. The flux of the tube is constant, where we use values of 10^{20}, 10^{21}, and 10^{22} Mx. This range of magnetic flux is typical of ephemeral regions and pores to large active regions with the strongest sunspots (Zwaan 1987).

We perform at least 7 groups of simulations sampling different time ranges of the ASH convective flow at each magnetic field strength, initial latitude, and magnetic flux in both the northern and southern hemispheres, considering both adiabatic evolution of the flux tube, and heating due to radiative diffusion. The flux tubes comprising one group are released at the base of the convection zone at the same starting time, although they do not interact with each other (i.e. are isolated) and are allowed to evolve until some portion of the flux tube reaches the top of the simulation domain. The flux tube release times for the groups are arbitrarily chosen, but are at least separated by the convective turnover timescale of the ASH convection simulation, which is $\sim$30 days. In this way, the flux tubes are able to sample significantly different portions of the convective velocity field. A snapshot of one of the simulated flux tubes subject to the ASH convective flow is shown in Figure 2.5. From this figure, it is clear that convective flows are impacting flux tube evolution. Strong downflows pin portions of the flux tube down to the base of the convection zone, while convective upflows aid in pushing the flux tube toward the surface.

The toroidal ring in neutral buoyancy is perturbed with small undular motions which consist of a superposition of Fourier modes with azimuthal order ranging from $m = 0$ through $m = 8$ with random phase relations. These perturbations are required to promote magnetic buoyancy instabilities in thin flux tubes not subjected to convective flows, which are often used as *control* cases for comparison to the flux tubes that evolve with the influence of convective flows. Such perturbations are not needed for flux tubes subjected to convection because those provided by the convective velocity field are much stronger in amplitude, but they have been included in the initiation of all flux tube simulations in order to facilitate

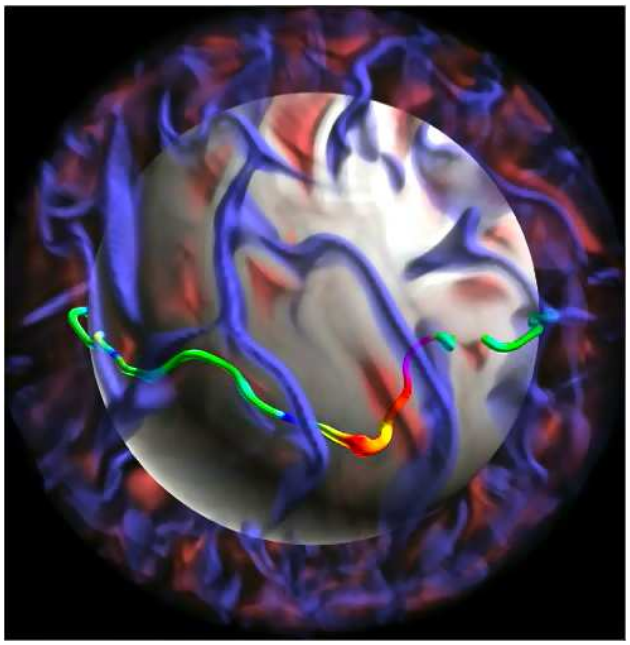

FIGURE 2.5. Snapshot of a magnetic flux tube evolving in solar-like turbulent convection. Strong downflows (blue) pin portions of the flux tube to the base of the convection zone (gray sphere), while strong upflows (red) aid in boosting the flux tube toward the surface. The flux tubes is color-coded according to its density deficit $\Delta\rho = \rho_e - \rho$ (teal: 0, yellow: maximum density deficit for snapshot). Image generated by Tim Sandstrom and Chris Henze of NASA Advanced Supercomputing (NAS).

comparison between flux tubes properties with and without convection. Removing the random phase relations from the thin flux tube model embedded in convection has a negligible effect on the dynamics and properties of the flux tube at all magnetic field strengths and magnetic flux.

2.4. Model Advantages and Limitations

The model we have designed to study the interaction of active-region-scale magnetic flux tubes with a turbulent, solar-like convection zone is advantageous in many regards. However, we recognize that like all computational models, these simulations have limitations, and are

unable to capture some aspects of solar flux emergence best addressed by other methods. In this section, we identify the advantages and limitations of the hybrid TFT+ASH approach.

A triumph of ASH simulations is the attainment of magnetic self-organization in rapidly rotating stars by solving the 3D MHD equations. Shearing flows provided by differential rotation generate wreaths of magnetism (e.g. Brown *et al.* 2010, 2011), with some developing buoyant loops (Nelson *et al.* 2011, 2013), thus demonstrating that persistent toroidal fields of moderate strength can be generated by and coexist with turbulent convection. Due to the impenetrable upper boundary of these simulations, buoyant portions of the magnetic wreaths decelerate and disperse as they near the top of the domain. In addition, buoyant loops in these simulations, as well as 3D MHD simulations of isolated magnetic flux tubes, suffer from numerical magnetic diffusion, for which the *effective* diffusion greatly exceeds solar plasma values. This has undesirable consequences, as the flux tubes therefore suffer erosion of their magnetic buoyancy and tension forces, and therefore they do not preserve Alfven's flux frozen-in condition. This problem is resolved in 3D MHD flux tube simulations by increasing the the magnetic flux to $\sim 10^{23}$ Mx, an order of magnitude larger than most sunspots. The problem of numerical diffusion is circumvented through the TFT+ASH formulation, as the TFT Lagrangian formulation of the motions of individual flux tube segments preserves ideal flux frozen-in conditions. As such, these simulations can be performed with realistic magnetic flux values of $10^{20} - 10^{22}$ Mx, on the same order of magnitude of solar active regions, without suffering erosion of the magnetic field.

In 3D MHD simulations, to favor the creation of buoyantly rising flux loops in a realistic timescale, tubes with such large magnetic flux values ($\sim 10^{23}$ Mx) are given an ad hoc entropy perturbation, even when in the presence of turbulent convective flows (e.g. Abbett, Fisher,

and Fan 2000; Fan, Abbett, and Fisher 2003; Jouve, Brun, and Aulanier 2013). Using the hybrid flux emergence situations as discussed in this Chapter ($10^{20} - 10^{22}$ Mx), magnetic buoyancy instabilities develop self-consistently as convective upflows and downflows perturb the flux tubes, instead of imposing an initial ad hoc buoyancy.

Global 3D MHD simulations prove to be both computationally expensive and time consuming. However, 1D TFT simulations can be performed on standard desktop computers with ample memory. Each individual flux tube simulation, as the formulation currently stands, requires only $\sim$10 mins to 1 hr to complete depending on the initial conditions of the flux tube. The ASH hydrodynamic simulation, which does require supercomputing resources, only needs to be performed once to obtain the 3D convective flows, and is stored in an easily accessible location for use by the TFT code. As such, using this hybrid TFT+ASH approach, many realizations of flux emergence using a variety of realistic solar parameters can be computed and used for statistical studies. These statistical studies are useful for comparison with observations of solar active regions.

While the TFT model is useful in some regards, we acknowledge that it also has fundamental limitations. The TFT formulation treats physical quantities as averages over the flux tube cross section and implicitly assumes that the flux tube does not break up. Simulations 2D and 3D in nature are able to resolve the interaction of the flux tube with its environment, and can explicitly track the configuration of the magnetic field inside the flux tube. It may also be the case, especially in upper regions of the convection zone, that flux tubes could become shredded due to convective flows and weakening of the magnetic field as the flux tube expands. Additionally, our TFT+ASH model does not allow for the flux tube to react back on the plasma in which it is effectively embedded. A strong enough magnetic field is

capable of suppressing convective motions in its vicinity via the Lorentz force. The presence of a large number of magnetic flux tubes (e.g. a magnetic wreath) of sufficient strength may alter the differential rotation of the star.

The particular ASH simulation used here is more laminar than some others done with the ASH code (e.g. Miesch *et al.* 2008; Jouve and Brun 2009). However, the convection simulation possesses all the relevant features necessary to investigate global scale interaction with magnetic flux tubes, including columnar, asymmetric, rotationally-aligned cells at low latitudes (density-stratified banana cells), a rapidly-evolving downflow network at higher latitudes in the upper convection zone, dominated by helical plumes, and a strong, solar-like differential rotation. Since even the highest-resolution simulations exhibit similar basic features, we do not expect the essential results to change significantly with a more turbulent flow field. The principle effect we expect at higher Rayleigh and Reynolds numbers is an increase in the random scatter due to stochastic turbulent fluctuations, and perhaps a stronger anchoring effect of the flux tube due to stronger convective downflows. Decoherence of large-scale motions and turbulent drag from small-scale motions could also slightly reduce flux tube rise times, but we expect this effect to be minor since we believe that large-scale, columnar banana-like cells must persist even in highly turbulent parameter regimes in order to provide the requisite Reynolds stresses to account for the solar differential rotation.

Finally, these simulations do not extend to the photosphere, but most stop at $\sim 0.97 R_\odot$, or $\sim$21 Mm below the solar surface. The ASH simulation is incapable of resolving granule and supergranule motions due to the sharp density stratification in the upper-most portion of the convection zone. The ASH model also does not capture ionization and radiative effects at the simulation upper boundary, which is also important for granulation and super-granulation.

Additionally, fluid flows are no longer subsonic near the photosphere, therefore the anelastic approximation breaks down and fully compressible MHD simulations are required. The TFT approximation is also no longer satisfied when the radius of the flux tube is on the order of the local pressure scale height, which too occurs in the upper layers of the convection zone.

CHAPTER 3

Dynamic Properties of Rising Magnetic Flux Tubes in Turbulent Solar-like Convection

We use a thin flux tube model in a rotating spherical shell of turbulent convective flows as described in Chapter 2 to study the global and local dynamic evolution of active-region-scale flux tubes as they traverse the solar-like convective envelope. We investigate toroidal flux tubes originating at the base of the convection zone with initial magnetic field strengths ranging from 15 kG (equipartition) to 100 kG (super-equipartition), and initial latitudes ranging from 1° to 40° in both hemispheres, assuming in this Chapter that the flux tubes evolve adiabatically such that $dS/dt = 0$. These simulations are performed for an ensemble of flux tubes with a constant magnetic flux of 10^{20}, 10^{21}, and 10^{22} Mx, on the order of solar active regions. In this Chapter, we begin with a qualitative discussion of the effects convection has on the global evolution of magnetic flux tubes (see Section 3.2). The dynamic evolution of the flux tube changes from being convection dominated to magnetic buoyancy dominated as the initial field strength and flux of the tube increases (see Section 3.3). The average time it takes for the flux tube to traverse the convection zone in the presence of a solar-like convective velocity field is investigated, and it is found that convective flows can reduce the rise time of a majority of flux tubes from years to months (Section 3.4). The radial components of the acceleration of a representative flux tube apex are also studied in order to better understand the contribution of various forces acting on the flux tube during the emergence process (see Section 3.5).

3.1. Introduction

Previous thin flux tube studies (e.g. Spruit 1981a,b; Moreno-Insertis 1986; Ferriz-Mas and Schüssler 1993; Longcope and Klapper 1997; Caligari, Moreno-Insertis, and Schüssler 1995; Caligari, Schüssler, and Moreno-Insertis 1998; Fan, Fisher, and Deluca 1993) neglect the effects of turbulent, solar-like convection on buoyantly rising magnetic flux loops. Following Fan, Abbett, and Fisher (2003), the initial magnetic field strength B_0 of a flux tube needs to be $B_0 > (H_p/a)^{1/2} B_{eq}$ for magnetic buoyancy to dominate the hydrodynamic effects on the flux tube from convective flows, where the pressure scale height is $H_p = P_e/\rho_e g$, a is the flux tube cross-sectional radius, and B_{eq} is the equipartition magnetic field strength. Therefore, the magnetic field B_0 of a flux tube needs to be greater than $(H_p/a)^{1/2} B_{eq}$ for the neglect of convection on rising magnetic flux tubes to be a valid assumption.

The magnetic field strength of a flux tube is said to be in equipartition when its magnetic energy density (magnetic pressure) is equal to the kinetic energy density of convection such that:

$$\frac{B^2}{8\pi} = \frac{1}{2}\rho_e v_c^2 \rightarrow B_{eq} = 2v_c\sqrt{\pi\rho_e}, \tag{3.1}$$

where v_c is a representative velocity for convective flows and ρ_e is the density of the external plasma environment. At the base of the convection zone, taking $\rho_e \sim 0.17$ g cm^{-3} from the 1D solar structure model by Christensen-Dalsgaard *et al.* (1996), and $v_c \sim 3.5\times10^3$ cm s^{-1} for the root-mean-squared (rms) downflow speed of the ASH simulation, $B_{eq} \sim 5$ kG for our simulation setup. This is slightly smaller than the ∼10 kG equipartition field strength derived based on the local mixing length description of solar convection (e.g. Fan 2009a), which may not properly capture the intensity of strong convective downflows compared to

weaker convective upflows. Also calculated from the 1D solar structure model, $H_p \sim 5.6\times10^9$ cm at the base of the convection zone, and the cross-sectional radius of the flux tube ranges from 1.8×10^7 cm ($\Phi = 10^{22}$ Mx, $B_0 = 100$ kG) to 4.6×10^8 cm ($\Phi = 10^{20}$ Mx, $B_0 = 15$ kG). With this in mind, for magnetic buoyancy to dominate convective effects following Fan, Abbett, and Fisher (2003), B_0 must be greater than $55 - 90$ kG for 10^{20} Mx flux tubes, $30 - 50$ kG for 10^{21} Mx flux tubes, and $15 - 30$ kG for 10^{22} Mx flux tubes.

Results from thin flux tube models without the influence of convective flows suggest that the field strength of the toroidal magnetic field at the base of the solar convection zone needs to be in the range of about 30 kG to about 100 kG in order for the latitude of emergence and the tilt angles of the emerging loops to be consistent with the observed properties of solar active regions. If the field strength is $\leq$20 kG, the poleward deflections of the trajectories of the rising flux tubes by the Coriolis force are too large such that the emerging latitudes are inconsistent with the observed sunspot latitudes (e.g. Caligari, Moreno-Insertis, and Schüssler 1995). However, solar cycle dynamo models which take into account the dynamic effects of the Lorentz force from the large-scale mean fields suggest that the toroidal magnetic field generated at the base of the convection zone is $\sim$15 kG, and most likely cannot exceed 30 kG (e.g. Rempel 2006b,a).

It is clear that there still is a debate as to the magnetic field strength at which the solar dynamo may be operating. Within the range of $15 - 100$ kG for the possible values of B_0, there are different convection-dominated and magnetic-buoyancy-dominated regimes for the dynamic evolution of active-region-scale flux tubes depending on their magnetic flux values. In this Chapter, we investigate how solar-like convective flows can affect flux tube evolution

in relation to other forces (i.e. magnetic buoyancy, magnetic tension, Coriolis force) acting on the rising flux tubes.

3.2. Flux Tube Morphology

In the absence of convection, rising buoyant loops develop solely as a results of the non-linear growth of the magnetic buoyancy instability of the initial toroidal flux tube. While a magnetic flux tube may be in equilibrium in a stratified environment, it may become unstable to wavelike perturbations if the magnetic field strength decreases sufficiently with height. Unstable perturbations cause the flux tube to bend, allowing plasma to drain from the flux tube apex (higher in the stratified convection zone) to the flux tube footpoints (lower in the convection zone), enhancing the buoyancy of the flux tube apex. This scenario is really a form of a hydrodynamic Rayleigh-Taylor instability. The stability analysis of toroidal flux tubes in the solar convection zone have been performed by a number of authors (e.g. Roberts and Webb 1978; Acheson 1979; Spruit and Zweibel 1979; Spruit and van Ballegooijen 1982b,a; Ferriz-Mas and Schüssler 1993; Schüssler *et al.* 1994).

Snapshots of three flux tubes allowed to evolve without the influence of convection are shown in Figure 3.1. In the bottom panel of Fig. 3.1, which shows an equatorial view of the flux tubes, it is apparent that the rise of the buoyant loop becomes more radial with increasing magnetic field strength. As the magnetic field strength of the flux tube decreases, the Coriolis force acting on the flux tube apex is larger in comparison to the magnetic buoyancy force, causing the flux tube apex to deflect poleward. In fact, for the flux tubes in Fig. 3.1, the 15, 40, and 100 kG flux tubes are each deflected 17.3°, 12.8°, and 1.8° respectively from their initial latitude θ_0 of 6°. When looking upon the flux tube from the pole, we also note the appearance of predominately $m = 2$ undular modes for magnetic field

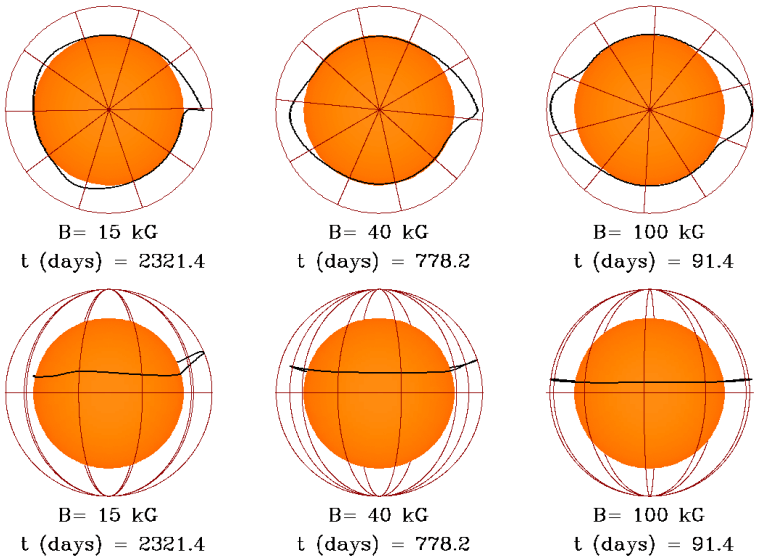

FIGURE 3.1. Snapshots of rising flux tubes in the absence of convection, each with $\Phi = 10^{22}$ Mx and $\theta_0 = 6°$, at a time when its apex has reached the simulation upper boundary. Initial magnetic field strengths B_0 of the flux tubes are 15, 40, and 100 kG respectively from left to right. The top images show a polar view, whereas the bottom images show an equatorial view. In all cases, the image has been rotated such that the flux tube apex is on the right, and at the 3 o'clock position if looking down from the north solar pole. The orange sphere has a radius of 4.9×10^{10} cm.

strengths of 40 kG and 100 kG. The 15 kG flux tube shows a predominately $m = 1$ mode, superposed with a very small amplitude $m = 3$ mode. The results are similar to those in Fan and Gong (2000), where the toroidal flux ring develops a buoyancy instability (e.g. Caligari, Moreno-Insertis, and Schüssler 1995), with $m = 1$ and $m = 2$ being the dominant unstable modes, and Ω-shaped rising loops subsequently form.

Snapshots of rising flux tubes with the same initial condition as Fig. 3.1, except subject to the convective velocity field, are shown in Fig. 3.2. For flux tubes of 10^{22} Mx with low initial field strengths of 15 kG, the development of the rising loops are highly susceptible to convection, and the flux tube no longer resembles its counterpart (see Fig. 3.1) in the absence of convection. However, at a large magnetic field strength of 100 kG, the development of the

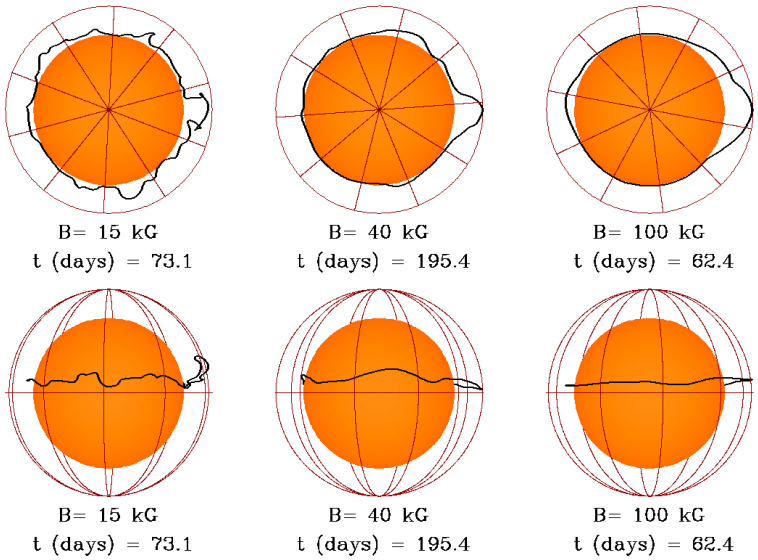

FIGURE 3.2. Same as Figure 3.1, except the flux tube is subjected to the external convective flow. Convection significantly deforms weak magnetic field strength flux tubes, while only the strongest downflows impact the evolution of 100 kG flux tubes.

rising loops are still mainly dominated by magnetic buoyancy, with the strongest downdrafts producing some moderate perturbations to the final emerging loop, and the dominate $m = 2$ mode is still discernible. The evolution of the 40 kG flux tube shown in Fig. 3.2 falls on a continuum somewhere between convection-dominated and magnetic-buoyancy dominated evolution. As we shall see in later sections of this Chapter, magnetic buoyancy effects and convective effects are of the same magnitude for ∼40 kG field strength flux tubes with $\Phi = 10^{22}$ Mx.

3.3. Convection vs. Magnetic Buoyancy

To understand the importance of convection on flux tube evolution, we compare the magnitude of the magnetic buoyancy force with that of the drag force from the external convective flows, following Fan, Abbett, and Fisher (2003). For the drag force to dominate

the buoyancy force (which acts in the radial direction):

$$\frac{C_D \rho_e v_{cr}^2}{(\pi\Phi/B)^{1/2}} > (\rho_e - \rho)g \tag{3.2}$$

$$\frac{C_D \rho_e v_{cr}^2}{\pi a} > \frac{B^2}{8\pi H_p}, \tag{3.3}$$

where H_p is the local pressure scale height, a is the flux tube radius $(\Phi/\pi B)^{1/2}$, v_{cr} is the component of convective velocity in the radial direction. In addition, the ideal gas law Eq. 2.4 and the condition for pressure balance Eq. 2.5 have been used to arrive at the right-hand side (RHS) of Eq. 3.3. Here we will refer to the magnetic buoyancy force as $(\rho_e - \rho)g \sim B^2/8\pi H_p$, assuming thermal equilibrium, where the buoyancy force on a flux tube unit segment is written in terms of the magnetic field inside the flux tube and the local pressure scale height of the external plasma. For an order of magnitude estimate of the magnetic buoyancy, we have assumed thermal equilibrium between the flux tube and the external fluid. Assuming $2C_D/\pi$ is of order 1, then equation 3.3 simplifies to

$$v_{cr} > v_a \left(\frac{a}{H_p}\right)^{1/2}. \tag{3.4}$$

i.e. in order for convection to dominate, the convective flow speed v_{cr} needs to be greater than the Alfvén speed $v_a = B/(4\pi\rho_e)^{1/2}$ multiplied by $(a/H_p)^{1/2}$.

In Figure 3.3, we have plotted as a function of depth the peak downflows and upflows, and the root mean square (rms) of the downflows and upflows of the convection velocity field at each constant r surface. In comparison, we have also plotted the right hand side of Eq. 3.4 evaluated at the apex (portion of flux tube with largest r value) for a selection of flux tubes with various initial magnetic field strengths and flux. These flux tubes all start with

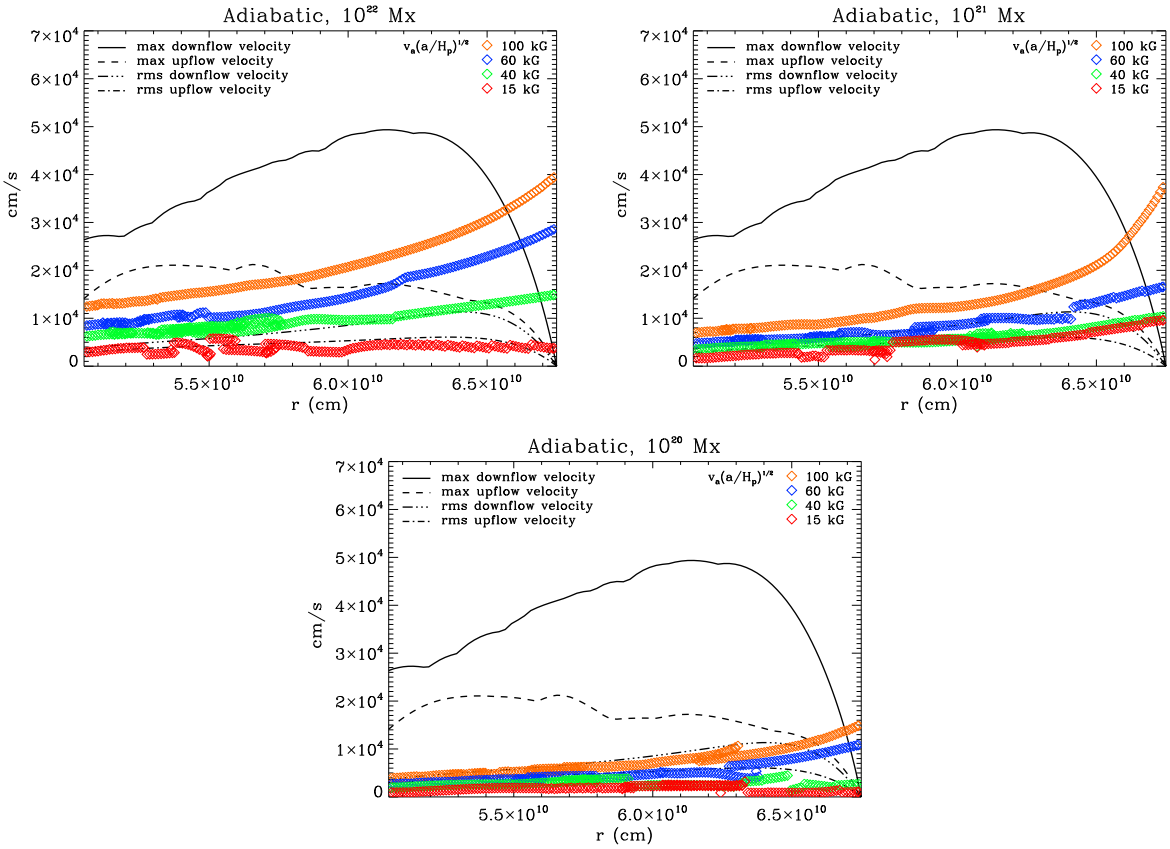

FIGURE 3.3. Peak downflows and upflows, and the root mean square (rms) of the downflows and upflows of the convective velocity field at each constant r surface as a function of r. Also plotted is the right-hand side of Eq. 3.4 at the apex of each flux tube with initial various initial field strengths and magnetic flux. The dynamic evolution of the flux tube becomes increasingly convection dominated as the field strength and flux are decreased.

$\theta_0 = 15°$ in the Northern hemisphere, and are subject to the same convective flows. Looking at all three panels of Fig. 3.3, it is clear that tubes of weaker magnetic field and weaker flux are more susceptible to convective effects.

For 10^{22} Mx flux tubes, on the order of magnetic flux associated with the largest sunspots, tubes of $60 - 100$ kG are only affected by the strongest upflows and downflows during their rise toward the surface. Flux tubes of 10^{22} Mx and near-equipartition field strength of 15 kG are continually buffeted by all convective flows, as the magnetic buoyancy force for these weak field strength flux tubes is not large enough to overcome convective effects,

explaining the general morphology of the left-most flux tube in Fig. 3.2. In the case of 40 kG flux tubes of 10^{22} Mx, all of the convective velocity field (in the radial direction) contributes to the development of rising loops, except for the rms upflows. Interestingly, as we will point out in Section 3.4, 40 kG, 10^{22} Mx flux tubes take the longest time, on average, to rise toward the surface. This is due to the fact that the RHS of Eq. 3.4 is nearly equal to the rms downflow velocity of the convection simulation. When the apex of a loop develops a large enough buoyancy force to rise toward the surface, it is quickly pushed down again by convective downflows that are nearly the same magnitude as $v_a(a/H_p)^{1/2}$. Therefore, there is a continuous *tug-of-war* between the magnetic buoyancy of rising loops and convective downflows in this regime, until one loop eventually overcomes effects from convective downflows. Often, these loops become caught in broad convective upflows and are boosted toward the surface.

Flux tubes of 10^{20} and 10^{21} Mx and below are severely affected by convection, with the exception of 100 kG, 10^{21} Mx flux tubes. Due to the reduced cross-sectional radius $a = (\Phi/\pi B)^{1/2}$ of these tubes compared to those of 10^{22} Mx, the RHS of Eq. 3.4 is reduced such that flux tube evolution is dominated by convection rather than magnetic buoyancy. The evolution of the 10^{21} Mx, 60 kG flux tube plotted in the right upper panel of Fig. 3.3 takes longer to rise than the 15, 40, and 100 kG flux tubes shown on the same graph. Similar to the 10^{22} Mx, 40 kG flux tube in the left upper panel, this is a result of the rms downflow speeds having nearly the same value as the RHS of Eq. 3.4. From the bottom center panel of Fig. 3.3, it is evident that the evolution of all 10^{20} Mx flux tubes in the range of 15-100 kG are dominated by convection.

Note that in Figure 3.3, there are occasionally a concentration of points, especially in the middle to lower convection zone, for the plot of the RHS of Eq. 3.4 at the apex of the flux tube. There are also often *jumps* or discontinuities in the plotted curve. This is due to the fact that the flux tube is continually buffeted by convection, with strong downflows pushing downing a flux tube apex such that a new rising loop will then have the greatest distance r for Sun center, which is the portion of the flux tube we track in Fig. 3.3.

Downflows in the convective velocity field dominate in amplitude, however their spatial extent is small compared to the upflows as indicated by the narrow downflow lanes shown in Figure 2.2. Strong downflows can pin the flux tubes to the base of the convection zone at the beginning of the simulation faster than the Fourier mode perturbations can in the case without convection (see Chapter 2.3). Especially at low magnetic field strengths where the tube is highly susceptible to convection deformation, many portions of the tube will become anchored as compared to the case without convection. Also, rising loops can be significantly boosted by broad upflows such that they emerge at the top of the simulation domain much faster than in the case without convection, where only buoyancy aids in driving the tube to the surface. Convection can also enhance buoyancy instabilities by introducing finite-amplitude perturbations and subsequent gravity induced draining of fluid from the flux tube apex.

Figure 3.4 shows snapshots (one individual time instance) of the radial distance r from Sun center of $\Phi = 10^{22}$ Mx, $\theta_0 = 15^\circ$ flux tubes as a function of the azimuthal angle ϕ (black lines), as well as the external radial velocity experienced by the tube at the height r of each tube segment (red lines). Snapshots are shown at times when the apex of the flux tube first reaches $r = 0.80R_\odot, 0.88R_\odot$, and $0.97R_\odot$, thereby showing the evolution of these

flux tubes in time. From this figure, it is evident that at large magnetic field strengths, only the strongest downflows can perturb the tube. However, at small magnetic field strengths, all flows are capable of deforming the flux tube, further supporting the findings shown in Fig. 3.3. As noted in Section 3.2, the dominant $m = 2$ unstable modes brought on by the magnetic buoyancy instability are still discernible in the 60 and 100 kG flux tubes. However, at weaker field strengths, these modes are wiped out as convective flows pummel and deform the flux tubes due to their weaker magnetic tension and magnetic buoyancy.

The time it takes for the apex of the flux tube to reach $0.80R_\odot, 0.88R_\odot$, and $0.97R_\odot$ are also indicated in the heading of each plot in Fig. 3.4. For all cases in this figure, the flux tube spends the majority of its rise time near the base of the convection zone. Due to the decreasing density in height of the external plasma environment, the flux tube accelerates quickly upward (nearly exponentially) due to the buoyancy of the flux tube apex in the upper level of the convection zone (see Section 3.4). Especially in the 40 kG case, the flux tube spends a substantial time in the lower $\sim 1/3$ of the convection zone, as buoyantly rising loops are continually pushed back down by convective downflows. Generally, once the flux tube apex reaches $\sim 0.88R_\odot$, the magnetic buoyancy of the flux tube is strong enough to overcome the rms velocity of convective downflows, and so will continue to rise buoyantly toward the surface. At the end of its rise, the apex of the 40 kG flux tube shown in Fig. 3.4 is deformed substantially by a strong downflow lane.

3.4. Flux Tube Rise Times

The drag force term (the last term in Equation 2.1) depends upon the magnetic field B and the flux Φ through the ratio of $(\Phi/B)^{1/2}$, which is proportional to the cross-sectional radius of the thin flux tube. As this ratio appears in the denominator of the drag force term,

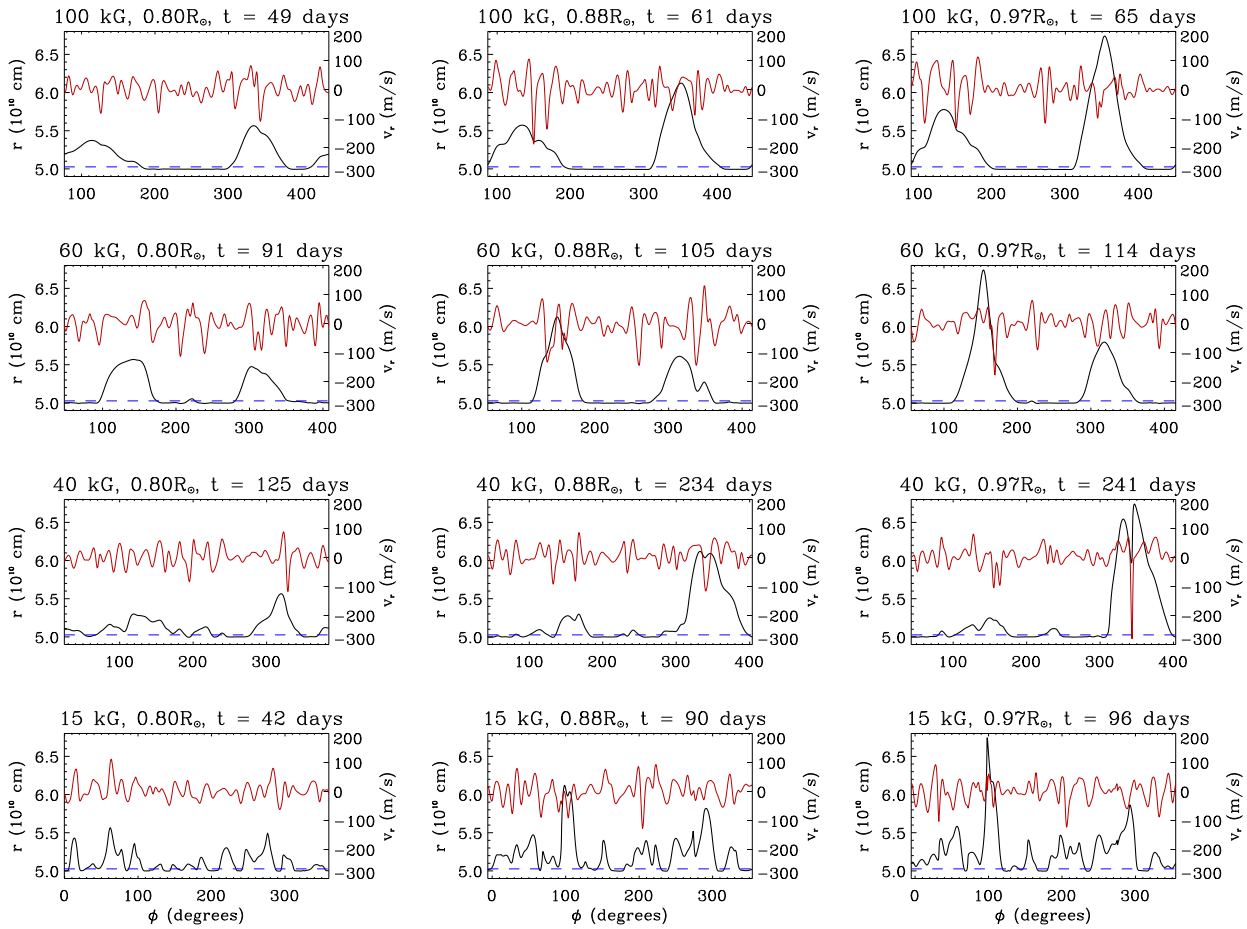

FIGURE 3.4. Flux tube radial distance from Sun center r (black line), plotted with the external radial velocity experienced by the flux tube at the height r of the flux tube segment (red line), both as functions of the azimuthal angle ϕ. These snapshots are for flux tubes with $\Phi = 10^{22}$ Mx, $\theta_0 = 15°$, and the dashed line represents the base of the convection zone, below which is the stably stratified overshoot region. These plots show the evolution of the flux tubes in time for various initial magnetic field strengths, and also illustrate how the evolution of flux tubes can be affected by convection, especially strong downflows.

thinner tubes will experience more drag. For any given magnetic field, the diameter of the flux tube can be reduced by decreasing the magnetic flux. In the absence of convection, the drag force acting on the rising tube reduces the velocity of the flux tube in all directions, increasing its rise time and reducing its latitude of emergence. The left side of Figure 3.5 shows a trend of increasing rise time of the flux tube simulations for both a decreasing magnetic field strength and a decreasing magnetic flux in the absence of convection, which has been found in previous thin flux tube simulations without the influence of convection (e.g. Moreno-Insertis 1983; Choudhuri and Gilman 1987; D'Silva and Choudhuri 1993; Fan, Fisher, and Deluca 1993). Taking these effects into consideration, a tube with a reduced flux and a reduced magnetic field should take the longest to rise, as is shown in the left hand side of Figure 3.5, with 15 kG, 10^{20} Mx tubes taking the longest time to rise.

However, with the addition of convection, flux tubes with smaller magnetic flux exhibit a shorter rise time, except for those with an initial magnetic field strength of 80 and 100 kG, as shown in the right side of Figure 3.5. In this case, the drag force term affects how strongly the flux tube is coupled with the convective velocity field. Rising flux tubes with lower magnetic flux are advected strongly by convection. This aids the flux tube in emerging at the surface faster than it could at a larger magnetic flux, provided the drag force due to convection is significant compared to the buoyancy force. On the other hand, the magnetic buoyancy and magnetic tension of flux tubes with an initial magnetic field strength of 100 kG dominate the drag force due to convection. As a result, flux tubes of 10^{20} Mx still take a longer time to emerge than those with a flux of 10^{22} Mx, as is the trend without convection. Flux tubes with mid-field strengths of $40-60$ kG take the longest time to emerge. For these flux tubes, the average convective downflows and magnetic buoyancy of the flux tube are of

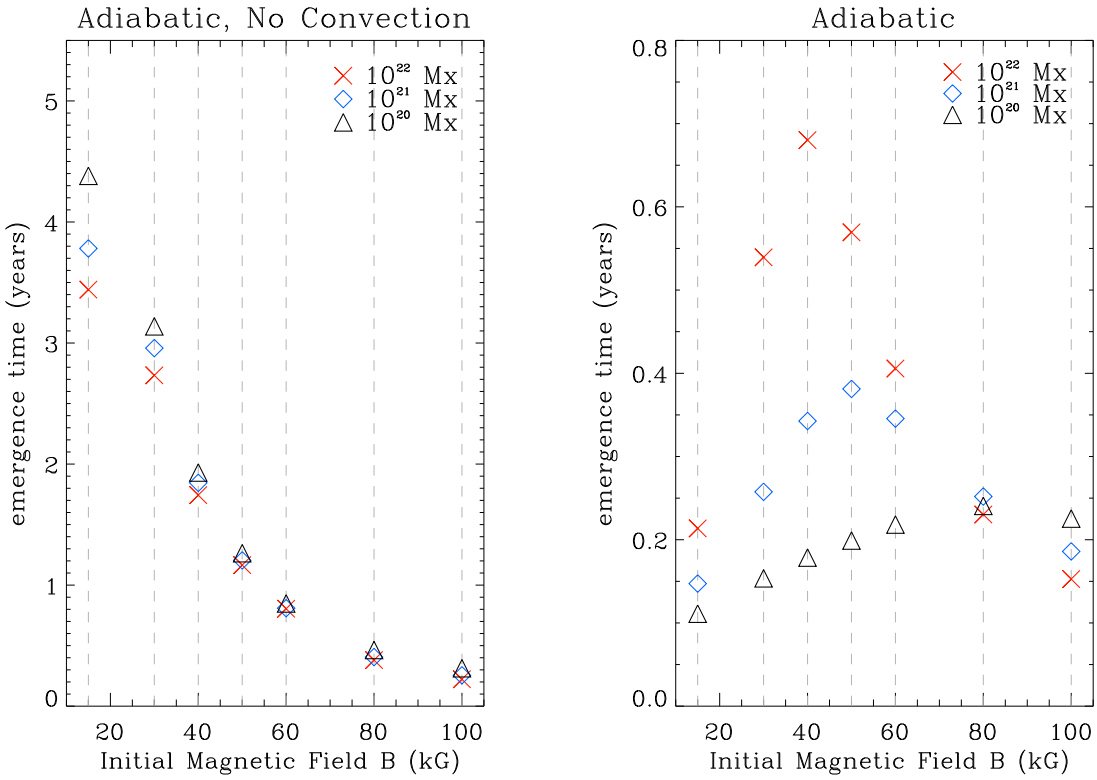

FIGURE 3.5. (Left) Avarage rise times for flux tube simulations without the influence of convection. This figure shows a decrease in emergence time with an increase in magnetic field strength and flux. (Right) Average rise times for the flux tube simulations with the influence of convection. With the addition of convection, rise times of the flux tubes are shorter for tubes with smaller magnetic flux, except at 100 kG where the trend is reversed, and at 80 kG where the average rise times are nearly the same. Flux tubes of mid-field strength now take the longest time to emerge.

similar magnitudes (see Fig. 3.3). A $tug - of - war$ exists between these two effects until one eventually dominates. At 80 kG, the average rise times for all three of the flux values converge, between 60 kG and less where 10^{22} Mx take the longest time to rise, and 100 kG where 10^{20} Mx flux tubes take the longest time to rise. Considering the ∼11-year duration of the solar cycle, for flux tubes originating near the convection zone base, a maximum rise time of about eight months for flux tubes subject to convective effects is much more realistic than a maximum rise time of about five years without convection.

3.5. Flux Tube Radial Acceleration

To gain a better understanding of the flux tube's rise through the convection zone, it is instructive to break down the acceleration of the flux tube apex according to the various forces acting on the flux tube. From Eq. 2.1, the acceleration of a flux tube element can be written as:

$$\begin{aligned} \mathbf{a} &= -2(\mathbf{\Omega_0} \times \mathbf{v}) - \frac{(\rho_e - \rho)\mathbf{g}}{\rho} + \frac{(\rho_e - \rho)}{\rho}[\mathbf{\Omega_0} \times (\mathbf{\Omega_0} \times \mathbf{r})] + \frac{1}{\rho}\frac{\partial}{\partial s}\left(\frac{B^2}{8\pi}\right)\mathbf{l} \\ &+ \frac{B^2}{4\pi\rho}\mathbf{k} - C_d\frac{\rho_e|(\mathbf{v}-\mathbf{v}_e)_\perp|(\mathbf{v}-\mathbf{v}_e)_\perp}{\rho(\pi\Phi/B)^{1/2}}. \end{aligned} \tag{3.5}$$

In Figure 3.6, the radial components of the acceleration vector $\mathbf{a} \cdot \hat{r}$ are plotted as a function of distance from Sun center r for a $\Phi = 10^{22}$ Mx, $B_0 = 60$ kG, $\theta_0 = 15^\circ$ flux tube, both without (left) and with (right) convective effects. For the flux tube evolving through a stratified convective envelope without the influence of turbulent convective flows (left-hand side of Fig. 3.6), the radial acceleration is dominated by positive contributions from the buoyancy force once the tube apex reaches $\sim$1/3 of the way through the convection zone. This contribution from the buoyancy force increases nearly exponentially as the apex rises into increasingly less dense layers of the convection zone. The drag force acts to reduce the acceleration of the flux tube in the upper $\sim$1/3 of the convection zone. As the flux tube rises, the tube develops legs that have a velocity component perpendicular to the flux tube rather than parallel to the flux tube. This perpendicular motion of the tube segments slows down the flux tube rise in all directions as it moves through the external plasma. As the apex of the tube rises and moves away from the rotation axis, conservation of angular momentum drives a retrograde flow of fluid inside the tube near the apex, which continues to increase in

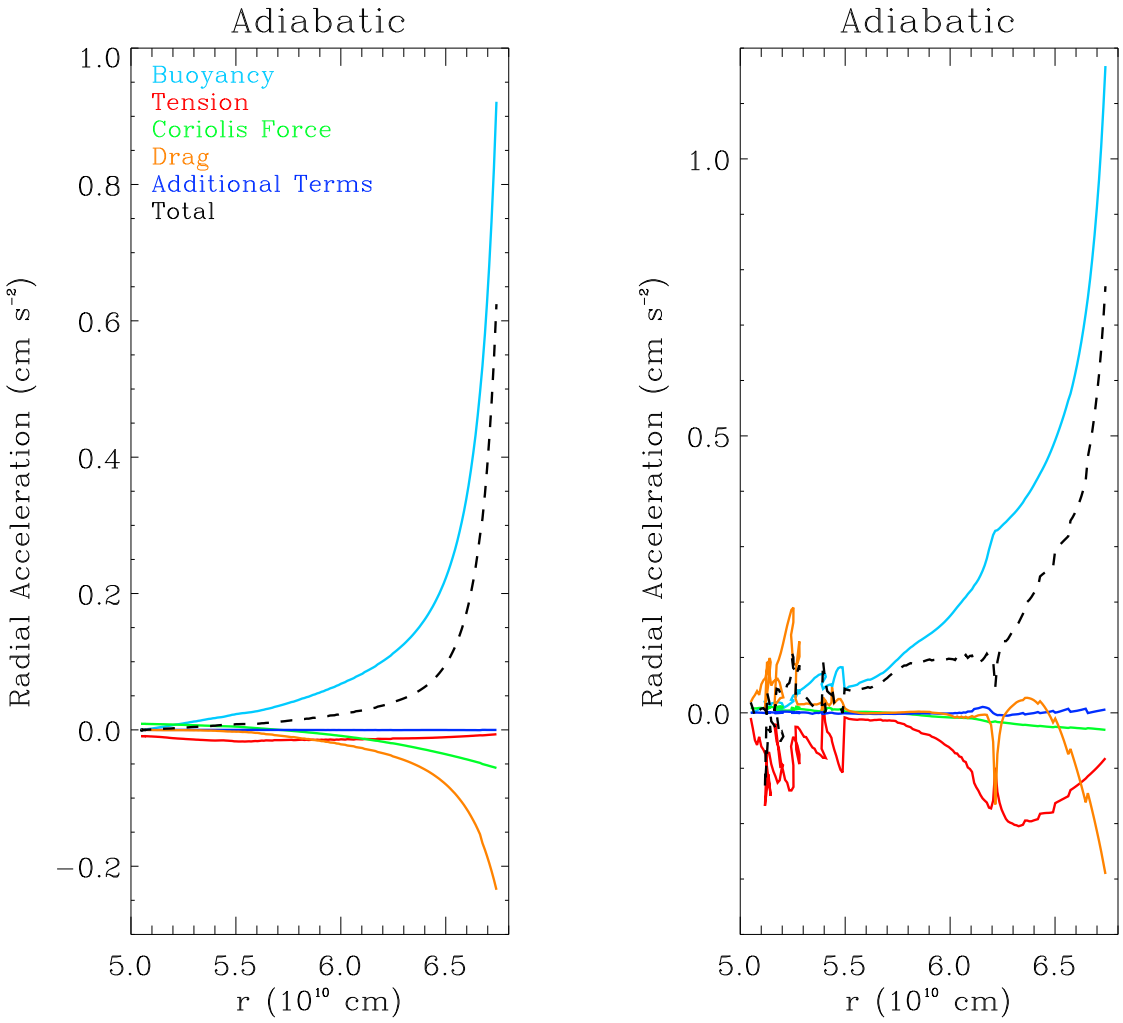

FIGURE 3.6. Radial acceleration of the flux tube apex for a flux tube of $\Phi = 10^{22}$ Mx, $B_0 = 60$ kG, $\theta_0 = 15°$, without (left) and with (right) convective effects. Components contributing to the radial acceleration following Eq. 3.5 are plotted as a function of r. Especially in the upper convection zone, buoyancy is the primary contributing factor to the acceleration of the flux tube apex.

magnitude as the tube rises toward the surface. The Coriolis force acting on this retrograde flow also acts to reduce the acceleration of the flux tube in the upper parts of the convection zone.

In the absence of convection, the magnetic tension force has a minimal negative contribution to the acceleration of the flux tube apex in the radial direction, which is proportional

to the magnetic field strength and curvature of the flux tube. The contribution from tension is largest at the bottom of the convection zone where B is greatest. As the tube rises, its magnetic field at the apex decreases as does the tension force if the flux tube is not sharply bent. Finally, the third and fourth terms in Eq. 3.5, labeled as *additional forces* in Fig. 3.6, contribute almost nothing to the radial component of the flux tube acceleration.

With the addition of convection (see RHS of Fig. 3.6), the buoyancy force is still the dominate contributor to the radial acceleration of the flux tube. However, now the drag force and magnetic tension play a larger role in the radial acceleration component. The radial acceleration curve is not as smooth as it is in the case without convection, a result of strong convective upflows and downflows impacting the apex's motion. The most striking feature of the RHS of Fig. 3.6 is the fact that the drag and tension force components tend to mirror each other. Strong upflows acting on the flux tube apex result in a positive acceleration contribution from the drag force. This stretches the rising flux loop, resulting in a larger tension, which acts to reduce the radial acceleration. This is shown well in the RHS of Fig. 3.6 in the bottom $\sim$1/3 of the convection zone. Conversely, a strong downflow encountered at the apex will create a large negative radial acceleration component, while this downflow flattens out the top of the loop, reducing the magnetic tension component. This is also depicted well in the RHS of Fig. 3.6 in the upper convection zone.

3.6. Discussion

Convection plays a significant role in the evolution of most active-region-scale flux tubes. Previous thin flux tube models have neglected the influence of turbulent, solar-like convection on active-region-scale flux tubes. As we have shown in this Chapter, convective flows have a non-negligible effect on most of the flux tubes considered in our study, especially for tubes

of $\sim$50 kG and less in the range of $10^{20} - 10^{22}$ Mx. Unlike 3D MHD flux tube studies, we are also able to investigate the global effects convection has on rising magnetic flux tubes using realistic solar active region flux values, which cannot be done in 3D simulations due to numerical diffusion.

Taking the results of Sections 3.2-3.4, flux tubes with weak magnetic flux of 10^{20} Mx require a large magnetic field strength significantly greater than 100 kG in order for neglecting the effects of convection to be a valid assumption. However, for flux tubes of 10^{22} Mx, it is valid to assume that tubes of field strength $\geq$80 kG will suffer minimal consequences due to the presence of convective flows. Convection also decreases the time it takes for flux tubes to travel the depth of the convection zone, reducing the time from at most $\sim$4.5 years in the case without convection to $\sim$8 months with convection. While the buoyancy force is the largest contributing factor to the radial acceleration of the flux tube apex, in the presence of convection, contributions to the flux tube evolution from convective upflows can act to boost the flux tube apex toward the surface faster than it could in the absence of convection. Furthermore, convective downflows, especially in the early portion of the flux emergence process, pin portions of the flux tube to the base of the convection zone and in the overshoot region, promoting a magnetic buoyancy instability as material drains out of the rising loop into the loop footprints. As such, flux tubes in our simulations are also capable of self-consistently developing their own magnetic buoyancy instabilities with the help of convection, not requiring an ad hoc initiation of the magnetic buoyancy instability.

CHAPTER 4

Constraining the Solar Dynamo Magnetic Field Strength: Comparing Simulations to Observations

The magnetic field strength regime at which the solar dynamo mechanism operates is not well known. However, studying how convection interacts with flux tubes of a wide range of initial magnetic field strengths ($15 - 100$ kG) for values of magnetic flux representative of active regions on the Sun ($10^{20} - 10^{22}$ Mx) may aid in constraining the dynamo generated magnetic field strength. In this Chapter, we compare properties of solar active regions such as emergence latitudes, tilt angle statistics, average rotation rates, and the nature of the magnetic field at the photosphere to those of an ensemble of flux tube simulations (as described in Chapter 2) once the flux tube apex has reached the simulation upper boundary. We discuss how these diagnostic properties (i.e. comparisons between our simulations and observations) constrain the initial field strength B_0 of the active-region-flux tubes at the bottom of the solar convection zone, and suggest that flux tubes of moderate to strong initial field strengths of $\geq 30 - 100$ kG are good candidates for the progenitors of large ($10^{21} - 10^{22}$ Mx) solar active regions. Through this process, we also gain a better understanding of the role convection plays in the manifestation of active region property observables.

4.1. Introduction

As of yet, the magnetic field strength at which the solar dynamo operates is not well known, nor is it directly accessible via observations. Previous thin flux tube simulations have found that the toroidal magnetic field at the base of the convection zone needs to

be in the range of ∼30 kG to ∼100 kG such that the simulated flux tubes exhibit tilt angles and latitudes of emergence that agrees well with solar active regions (Choudhuri and Gilman 1987; Schüssler *et al.* 1994; D'Silva and Choudhuri 1993; Caligari, Moreno-Insertis, and Schüssler 1995). However, solar cycle dynamo models that incorporate the Lorentz force from large scale mean fields indicate that the magnetic field strength generated and amplified at the base of the convection zone is ∼15 kG, and most likely cannot exceed 30 kG (Rempel 2006b,a).

Recent simulations of solar-like stars that rotate three times the current solar rate have shown that a rotating convective envelope can generate a dynamo that consists of opposite polarity magnetic wreaths in two hemispheres, which span the depth of the convection zone (Brown *et al.* 2010). When portions of these wreaths become strong enough, ∼35 kG or greater, a buoyant magnetic loop develops which then rises through the convecting fluid in which it is embedded (Nelson *et al.* 2011). While these dynamo-producing convection simulations are not meant to reproduce the solar dynamo directly, they do demonstrate that persistent toroidal magnetic fields of moderate strength can coexist with convection. In light of these studies, it is important to understand how toroidal flux tubes of weak to moderate field strengths, $\sim 15 - 50$ kG, behave as they rise through a turbulent solar convective envelope. Some studies have been performed that investigate the buoyant rise of fully three-dimensional isolated flux tubes in a turbulent convective velocity field (e.g. Fan, Abbett, and Fisher 2003; Jouve and Brun 2009). However, due in part to the limited numerical resolution of these simulations, large values of magnetic flux must be used, which are greater than typical active region flux, in order to keep the tube from dissipating as it rises.

We use a thin flux tube model as described in Chapter 2 in an effort to constrain the magnetic field strength at which the solar dynamo may be operating. This thin flux tube model is useful because it circumvents the problem of artificial diffusion, includes the effects of solar-like turbulent flows in a 3D convection zone, and is computationally inexpensive such that a large ensemble of simulations with various initial parameters can be amassed. In the process of constraining the dynamo magnetic field strength, we also learn more about the effect convection plays has on local flux emergence properties, such as: latitude of emergence (Section 4.2), tilt angle statistics (Section 4.3), and active region rotation rates (Section 4.4). We also discuss the magnetic field asymmetry of the leading and following portions of the bipolar emerging region (Section 4.5.1), and the magnetic field strength of the flux tube apex at the simulation upper boundary (Section 4.5.2).

In this Chapter, we investigate adiabatically evolving ($dS/dt = 0$) flux tubes specifically with $B_0 = 15$, 30, 40, 50, 60, 80, and 100 kG; $\Phi = 10^{20}, 10^{21}$, and 10^{22} Mx; and $\theta_0 = 1^\circ - 40^\circ$ in both hemispheres. Not all results are plotted for each B_0, but are included and discussed where appropriate. In this section, the data set results sample seven different convective velocity flow fields, for a total of 6927 flux tube simulations in all. See Appendix G for a breakdown of the number of flux tube simulations considered for each B_0, Φ pair.

4.2. Latitude of Emergence

The latitude of emergence of a flux tube apex in dependent on the relative magnitude of the buoyancy, drag, and Coriolis forces, and to a small degree the magnetic tension force. The radially directed buoyancy force (directed away from the rotation axis) is proportional to the magnetic field strength of the flux tube. As discussed in Section 3.4, the drag force is inversely proportional to magnetic flux, whereas the Coriolis force is proportional to $\Omega \mathbf{v} \sin\theta$.

An increased drag force with decreasing flux acts to reduce the flux tube motion in all directions, and therefore reduces the Coriolis force acting on the flux tube.

As a result of the conservation of angular momentum, the initial radial motion of the flux tube supplied by the buoyancy force drives a motion of the flux tube plasma in the negative ϕ direction. The component of the Coriolis force due to this motion in the negative ϕ direction is directed inward toward the rotation axis. If the magnetic buoyancy force of the flux tube apex (directed outward from the rotation axis) is significantly greater than the Coriolis force, the flux tube will rise more radially. Therefore, flux tubes of 10^{20} Mx emerge at lower latitudes than do flux tunes of 10^{22} Mx, as has been found in previous thin flux tube calculations in the absence of convection (e.g. Choudhuri and Gilman 1987; D'Silva and Choudhuri 1993; Fan, Fisher, and Deluca 1993). Our simulations without the addition of convective flows verify these findings as shown in Figure 4.1.

Also, as shown here and in previous studies, a low latitude zone void of flux emergence due to poleward deflection is found for magnetic field strengths of $15 - 40$ kG for flux values of $10^{21} - 10^{22}$ Mx. As such, these flux tubes suffer from *poleward slippage* and would not be able to produce active regions near the equator, unlike what is observed on the Sun. This phenomenon occurs because the outward directed buoyancy force is not strong enough to overcome the inward directed Coriolis force component, and the flux tube apex subsequently drifts less radially, more parallel to the rotation axis.

With convection, the previous problem of poleward slippage for flux tubes of weak initial field strength is rectified, as shown in Figure 4.2. In Figure 4.2, a latitudinal deflection of 0° means that the flux tube emerges at the same latitude as where it originated, while a positive (negative) deflection indicates the flux tube emerges farther from (closer to) the

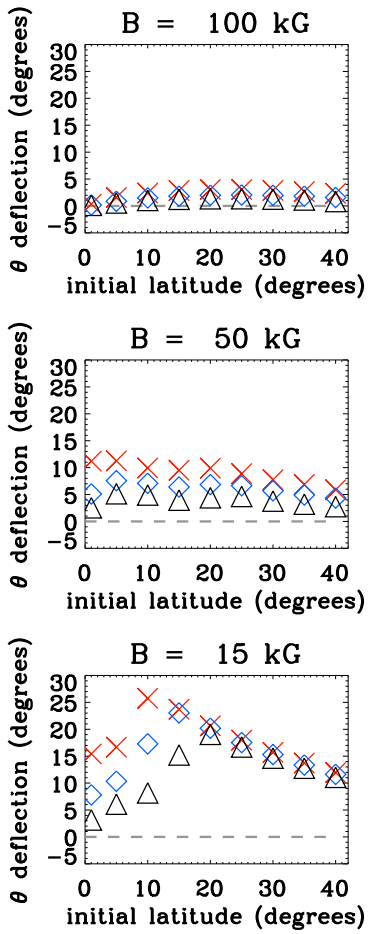

FIGURE 4.1. Latitudinal deflection (emergence latitude minus initial latitude) of the flux tube apex as a function of initial latitude for flux tubes with initial magnetic field strengths of 100, 50, and 15 kG (top to bottom) in the absence of convection. This is shown for tubes with flux values of 10^{20} Mx (black triangles), 10^{21} Mx (blue diamonds), and 10^{22} Mx (red crosses). An increased drag force for tubes with a smaller flux reduces the poleward deflection of the flux tube.

Equator than where it originated. Convection produces a scatter in the emerging latitude compared to the cases without convection, which can be either poleward or equatorward. Especially for flux tubes of low initial field strength, there is a clear trend of reduced poleward deflection of the flux tube apex compared to the case without convection. In some cases, especially for flux tubes originating near the equator, it is even possible for flux tubes to cross into the opposite hemisphere. It is also evident from Fig. 4.2 that there is a greater

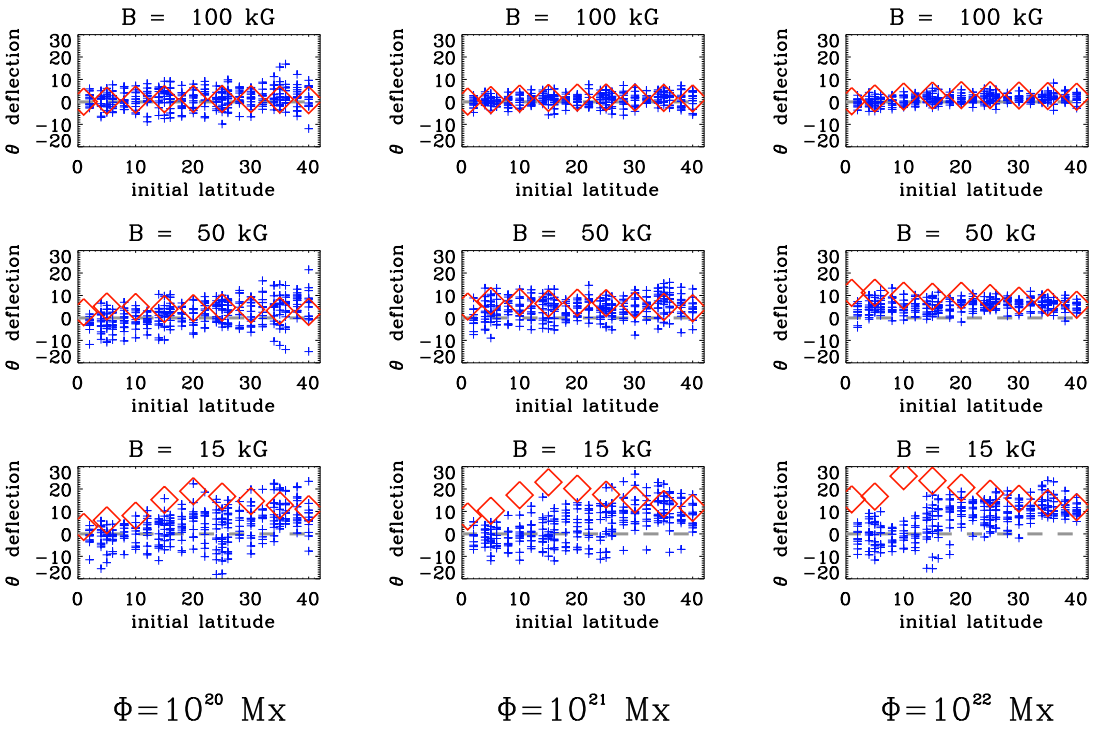

FIGURE 4.2. Latitudinal deflection of the flux tube apex as a function of initial latitude for flux tubes with initial magnetic field strengths of 100, 50, and 15 kG (top to bottom) with magnetic flux of 10^{20} Mx (left column), 10^{21} Mx (center column), and 10^{22} Mx (right column). Red diamonds show the deflection for flux tubes without convection as plotted in Fig. 4.1, and plus signs are for flux tubes with convective effects. Both axes are in units of degrees. Addition of a convective velocity field results in flux tubes that are able to emerge near the Equator even at low magnetic field strengths.

amount of scatter in the latitudinal deflection at lower magnetic flux, which occurs because the tube is advected more by convective flows than at larger magnetic flux. Also, as the magnetic field strength increases for a particular flux, the latitudinal deflection decreases, as is the case for tubes both with and without convection. This is a result of the buoyancy force overpowering the Coriolis force at large magnetic fields, forcing the tube to rise more radially.

4.3. Tilt Angles

Solar active regions tend to emerge with their leading polarity (in the direction of solar rotation) closer to the equator than the following, such that a line drawn between the center of the two bipolar regions will be tilted with respect to the East – West direction (Hale *et al.* 1919). The tilt angle is computed as the angle between the tangent vector at the apex of the emerging loop (once it has reached the top of the simulation domain), and the local East – West direction. We define a positive sign of tilt as a clockwise (counter-clockwise) rotation of the tangent vector away from the East – West direction in the Northern (Southern) hemisphere, consistent with the direction of the observed mean tilt of active regions. If the magnitude of the tilt angle exceeds 90°, then the active region violates Hale's Law (Hale *et al.* 1919), possessing the *wrong* leading polarity in the direction of solar rotation for that particular hemisphere.

To align our statistical results with those obtained from observations, unless otherwise stated, tilt angles that do not fall in the range [-90°, 90°] are shifted to be brought back into this interval, thereby losing information about anti-Hale tilt angles. This approach is usually what is done for tilt angle statistical studies of active regions on the Sun, starting with Hale *et al.* (1919) (e.g. Wang and Sheeley 1989; Fisher, Fan, and Howard 1995; Howard 1996; Dasi-Espuig *et al.* 2010; Stenflo and Kosovichev 2012; Li and Ulrich 2012; McClintock and Norton 2013). If the leading bipolar region in the direction of solar rotation, regardless of polarity, is closer to the equator than the following, it will then be identified as a positive tilt in the range [0°, 90°]. Similarly, if the leading bipolar region is farther from the equator than the following region, the tilt angle will be identified as negative in the range [-90°, 0°]. This approach is different from what was done in Weber, Fan, and Miesch (2011) and Weber, Fan,

and Miesch (2013), where tilt angles where in the range of [-180°, 180°]. In retrospect, we feel that shifting the tilt angles to fall in the [-90°, 90°] range is probably a better diagnostic for comparison with observations.

In this Section, we perform numerous diagnostics on tilt angles of our simulated flux tubes. First, we investigate the Joy's Law trend following three methods employed by various authors (Sections 4.3.1.1-4.3.1.3). Next, we investigate the scatter of the tilt angles about the Joy's Law trend (Section 4.3.2.1) as well as the average tilt angle (Section 4.3.2.2). Finally, we calculate the tilt angle distribution from our simulations in Section 4.3.3.

4.3.1. The Joy's Law Trend. Known as Joy's Law, the average tilting behavior of emerging flux regions tends to increase in magnitude as the latitude of emergence increases (e.g. Hale *et al.* 1919). Many authors have recovered Joy's Law from observations, however there is generally no agreed upon common method to obtain an empirical Joy's Law equation (e.g. Fisher, Fan, and Howard 1995; Dasi-Espuig *et al.* 2010; Stenflo and Kosovichev 2012; Li and Ulrich 2012; McClintock and Norton 2013). Within this section, we will employ three different methods in order to compare our simulation results to those of the Joy's Law trend recovered from observations. Tilt angles calculated from our flux tube simulations are plotted as a function of emergence latitude in Figure 4.3 for tubes of $\Phi = 10^{20}$, 10^{21}, and 10^{22} Mx (left to right) and initial magnetic field strength $B_0 = 100$, 50, and 15 kG (top to bottom), for flux tubes allowed to evolve both with (plus signs) and without convection (diamonds symbols).

4.3.1.1. *The Joy's Law Trend: Method 1.* For our first method of obtaining an empirical equation for the Joy's Law trend from our simulations, we assume that the tilt angle increases monotonically with increasing emergence latitude. We perform a linear least-squares fit of

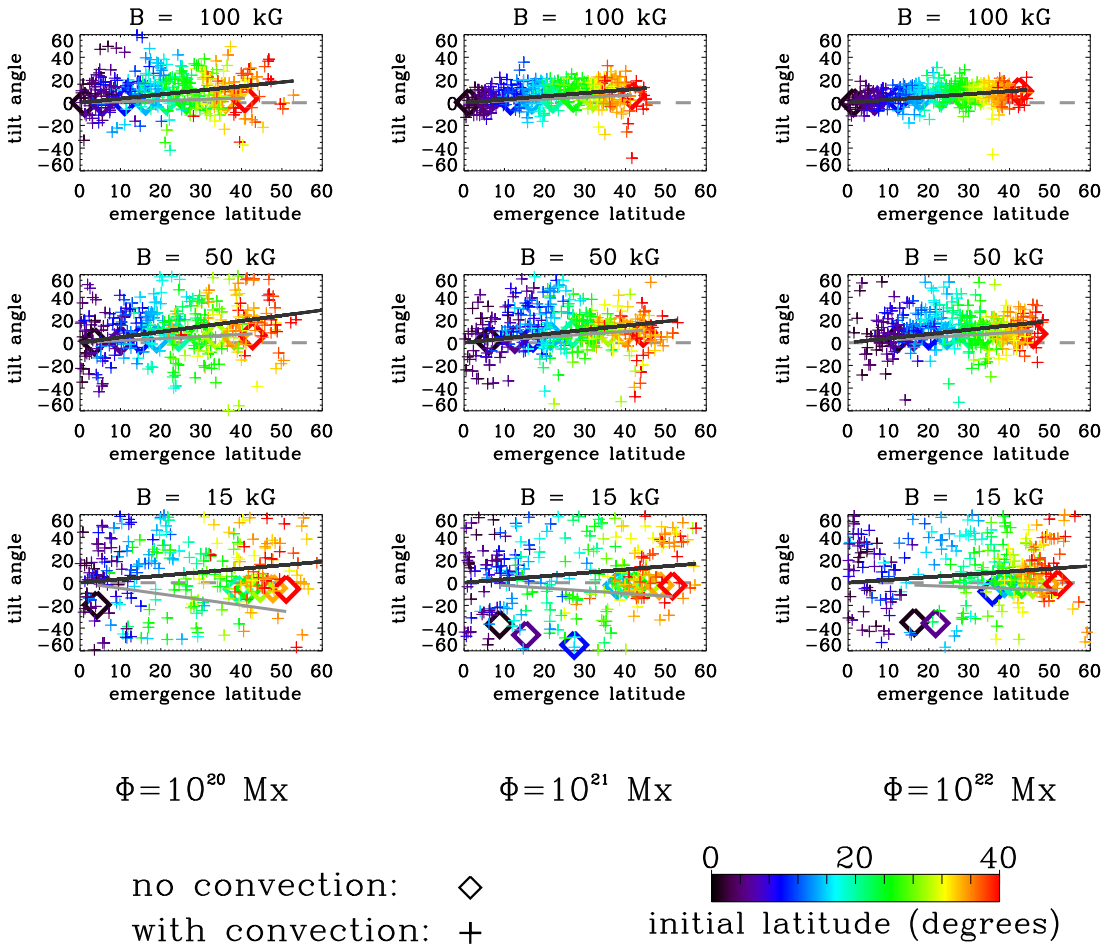

FIGURE 4.3. Tilt angles as a function of emergence latitude for initial magnetic field strengths of 100, 50, and 15 kG (top to bottom) for simulations both with (plus signs) and without (diamond points) the influence of convection. This is done for magnetic flux of 10^{20} Mx in the left column, 10^{21} Mx in the middle column, and 10^{22} Mx in the right column, with data sets sampling seven different convective velocity flow fields. The gray line is the linear best-fit following Method 1 for flux tubes in the absence of convection (slopes reported in Table 4.1), and the black line is the best-fit line for the cases subjected to convective flows (slopes reported in Table 4.2). A color bar indicates the original starting latitude of the flux tube. All axes are in units of degrees. Convection introduces a scatter of the tilt angle about the best-fit line, and also aids in increasing the slope of the best-fit line, especially at lower magnetic field strengths.

the tilt angle as a function of emergence latitude following:

$$\alpha = m_A \theta, \tag{4.1}$$

TABLE 4.1. Slopes m_A of the linear best-fit lines (Method 1) to the tilt angle as a function of emergence latitude for flux tubes without convective effects. Slopes calculated following Method 1 are unitless. See Appendix H for a discussion on the least squares fitting method and the determination of the uncertainties on the fit parameters. At low magnetic field strengths, the slope of the best-fit line is negative, indicating a departure from the Joy's Law trend.

B (kG) without convection	10^{20} Mx	10^{21} Mx	10^{22} Mx
100	0.10 ± 0.01	0.16 ± 0.01	0.25 ± 0.01
80	0.12 ± 0.01	0.20 ± 0.01	0.31 ± 0.01
60	0.18 ± 0.01	0.27 ± 0.01	0.30 ± 0.02
50	0.18 ± 0.01	0.25 ± 0.01	0.22 ± 0.02
40	0.16 ± 0.01	0.16 ± 0.01	0.12 ± 0.01
30	-0.12 ± 0.01	-0.08 ± 0.03	-0.07 ± 0.05
15	-0.50 ± 0.38	-0.24 ± 0.22	-0.13 ± 0.13

where α and θ represent the tilt angle and emergence latitude respectively, both in units of degrees, of our simulated flux tubes once the apex has reached the simulation upper boundary, and m_A is the slope (unitless) of the best-fit line. For this method, the fit is forced to go through zero because it is assumed that no tilt is expected for equatorial sunspot groups. Figure 4.3 shows in gray the best-fit line for the data without convection, and black for the flux tubes with convection. The slopes m_A of these best-fit lines along with their uncertainties are reported in Table 4.1 for flux tubes without convective effects, and Table 4.2 for flux tubes with convective effects. The uncertainties reported in relation to Eq. 4.1 are uncertainties in the determination of the fit parameter m_A, which takes into account both propagation of error and the variance of the data around the best-fit line. See Appendix H, Section 8.1.1 for a discussion on our least-squares fitting method and the calculation of the parameter uncertainties following Method 1. These uncertainties increase with decreasing magnetic field and flux, as the flux tube is more susceptible to deformation by convective flows, and the tilt angles exhibit more of a scatter about the best-fit trend.

TABLE 4.2. Slopes m_A of the linear best-fit lines (Method 1) for flux tubes with convective effects. Convection aids in increasing the slope of the best-fit line, and the slope also peaks at mid-field strengths of 40 kG and 50 kG. In comparison, using white light sunspot group tilt angle data, Dasi-Espuig *et al.* (2010) find $m_A = 0.26 \pm 0.05$ for Mount Wilson data and $m_A = 0.28 \pm 0.06$ for Kodikanal data.

B (kG) with convection	10^{20} Mx	10^{21} Mx	10^{22} Mx
100	0.36 ± 0.04	0.28 ± 0.02	0.25 ± 0.02
80	0.44 ± 0.04	0.29 ± 0.03	0.29 ± 0.02
60	0.41 ± 0.06	0.37 ± 0.04	0.35 ± 0.02
50	0.48 ± 0.06	0.38 ± 0.04	0.38 ± 0.03
40	0.40 ± 0.07	0.38 ± 0.06	0.40 ± 0.04
30	0.43 ± 0.06	0.33 ± 0.07	0.31 ± 0.06
15	0.31 ± 0.08	0.29 ± 0.07	0.25 ± 0.07

Without the influence of convection, untwisted flux tubes (i.e. $\mathbf{B} = \mathrm{B}\mathbf{l}$) tilt in the appropriate direction for their respective hemispheres (i.e. toward the equator) due to the Coriolis force acting on the limbs of the emerging loop (e.g. D'Silva and Choudhuri 1993). However, for weaker initial field strengths of 15 kG and 30 kG, some emerging loops show negative tilt angles, opposite to the sign of the active region mean tilts. This occurs because plasma flow along the flux tube near the apex changes from diverging to converging as it enters the upper convection zone (e.g. Caligari, Moreno-Insertis, and Schüssler 1995; Fan and Fisher 1996). The Coriolis force acting on the converging flow drives a tilt of the wrong sign (i.e. with leading polarity away from the equator). Fan, Fisher, and McClymont (1994) show that for a converging parallel flow to set in, the temperature inside the flux tube has to be sufficiently higher than the external temperature such that $|(\beta/2)\delta T/T_e| > (1/\gamma - 1/2)$, where $\beta = 8\pi p_e/B^2$ and γ is the ratio of specific heats. The quantity $\delta T = T_e - T$ becomes more negative as the flux tube apex rises because the flux tube rises adiabatically, whereas the external temperature gradient is super-adiabatic ($\nabla_e > \nabla_{ad}$). The quantity β is proportional to B^{-2}, where as $\delta T/T_e$ is determined mostly by the external stratification. Therefore, the

converging flow sets in at lower portions of the convection zone for flux tubes of weaker magnetic field strengths.

This tilting effect opposite the Joy's Law trend is especially severe for flux tubes of 15 kG, 10^{20} Mx. The tilt angles of these tubes are so large and of the wrong sign for initial latitudes of 5°, 10°, and 15°, that they do not appear on the tilt angle plot, however have been included in the Joy's Law fit (Fig. 4.3, lower left). Additionally, these tilt angles of the wrong sign result in a negative slope for the best fit line (see Table 4.1). As such, without convection, $15 - 30$ kG flux tubes would not be capable of producing the observed Joy's Law trend. Without convective effects, the tilt angles, and likewise best-fit line slopes, tend to decrease for decreasing magnetic flux. Similar to the discussion on rise times in Chapter 3.4 and latitudinal deflection in Section 4.2, an increased drag force for weaker flux values reduces the motion of the flux tube in all directions, therefore suppressing the Coriolis force acting on the flux tube apex that results in a tilting motion toward the equator.

With convection, flux tubes of all Φ and B_0 exhibit a positive best-fit line slope, agreeing with Joy's Law (see Table 4.2). Additionally, except for the 10^{22} Mx, 80 and 100 kG cases where convection has little effect on the evolution of rising flux tubes, the slope of the best-fit line increases with convection as compared to the case without convection. This happens in part because upflows in the convective velocity field have an associated kinetic helicity that helps to drive the tilt of the flux tube apex in the appropriate Joy's Law direction for its respective hemisphere (i.e. toward the equator). Such a mean kinetic helicity corresponds to a vertical vorticity in upflows that is clockwise in the northern hemisphere, and counter-clockwise in the southern hemisphere.

In comparison to the best-fit slope values reported in Table 4.2, from white light sunspot group data spanning solar cycles 15 – 21, Dasi-Espuig *et al.* (2010) find an empirical Joy's Law equation (following Eq. 4.1) of slope $m_A = 0.26 \pm 0.05$ for Mount Wilson sunspot data, and $m_A = 0.28 \pm 0.06$ for Kodikanal data. The values we report in Table 4.2 agree well with Dasi-Espuig *et al.* (2010) for $10^{21} - 10^{22}$ Mx (on the order of magnetic fiux associated with sunspots), with the exception of $40 - 50$ kG flux tubes which show a slightly larger best-fit slope within the uncertainties.

It is interesting to note that with convection, the mid-field strength flux tubes of $40 - 50$ kG at all flux values have the largest best-fit slopes m_A. This is probably due to the fact that at these mid-field strengths, the joint effects of magnetic buoyancy and the convective flows are such that the tubes have a longer rise time (see Chapter 3.4) compared to the other field strengths. Therefore, the systematic effects from the Coriolis force and kinetic helicity in convective upflows have a longer time to act on the flux tubes, and the flux tube will likely encounter multiple convective cells during its evolution. Since the mean kinetic helicity is obtained by averaging the kinetic helicity of many cells over time, a flux tube which takes a longer time to emerge will be influenced more by the mean kinetic helicity rather than stochastic fluctuations.

According to Fan, Fisher, and McClymont (1994), in the absence of convection, the tilt angle of the flux tube should increase with increasing flux as a result of the Coriolis force acting on the buoyantly rising flux tube. With convection, given the uncertainties that we obtain using Method 1, we do not find a statistically significant dependence of the Joy's Law slope on magnetic flux (see Table 4.2), which agrees with the results of Stenflo and Kosovichev (2012). In this section, we have shown that the addition of convection increases

the empirical Joy's Law equation slope, regardless of the amount of time the flux tube stays in the bulk of the convection zone. This indicates that convective effects can have a significant contribution to the tilt angle of the flux tube throughout its evolution. Therefore, the results of Stenflo and Kosovichev (2012) do not rule out the paradigm that flux tubes obtain at least a portion of their tilt angle during their buoyant rise.

4.3.1.2. *The Joy's Law Trend: Method 2.* A Joy's Law fit can also be performed using the equation:

$$\alpha = m_B sin\theta, \tag{4.2}$$

which is a good choice assuming the origin of the tilt angle is related to the Coriolis force, as this force varies with latitude as $\sin(\theta)$. Here, the tilt angle α is again in units of degrees and m_B also has units of degrees. See Appendix H, Section 8.1.2 for a discussion on the least squares fit and parameter uncertainties for Method 2. Stenflo and Kosovichev (2012) perform such a fit using 15 years of MDI full-disk magnetograms, finding a slope of $m_B = 32.1^\circ \pm 0.7^\circ$. However, using Mount Wilson sunspot group data from 1917-1985, Fisher, Fan, and Howard (1995) find a best-fit equation slope of m_B=15.69° ± 0.66°.

Table 4.3 shows the slope m_B of the best-fit equation (Eq. 4.2) applied to our simulation tilt angles, which exhibit a similar trend to the slopes m_A in Table 4.2. For all flux values, the slopes m_B still peak at magnetic field strengths of 40-50 kG, and the uncertainties on the fit increase with decreasing magnetic field and flux. The values reported in Table 4.3 all fall between $m_B = 15.69^\circ$ as found by Fisher, Fan, and Howard (1995) and $m_B = 32.1^\circ$ as found by Stenflo and Kosovichev (2012). This large difference in m_B obtained from observations might occur because weaker active regions can be identified in magnetograms, which may not

TABLE 4.3. Slopes m_B of the best-fit lines following Method 2 for flux tubes with convective effects. Slopes m_B are in units of degrees. Convection aids in increasing the slope of the best-fit line, and the slope also peaks at mid-field strengths of 40 kG and 50 kG as in Table 4.2. In comparison, Fisher, Fan, and Howard (1995) find $m_B = 15.7° \pm 0.7$ for Mount Wilson sunspot data and Stenflo and Kosovichev (2012) find $m_B = 32.1° \pm 0.7°$ from MDI magnetograms. Reported uncertainties are uncertainties in the determination of the fit parameter m_B, as described in Appendix H, Section 8.1.2.

B (kG) with convection	10^{20} Mx	10^{21} Mx	10^{22} Mx
100	$22.5° \pm 2.3°$	$17.5° \pm 1.4°$	$15.5° \pm 1.1°$
80	$27.6° \pm 3.3°$	$17.9° \pm 1.8°$	$17.7° \pm 1.2°$
60	$25.5° \pm 3.5°$	$22.9° \pm 2.3°$	$21.6° \pm 1.5°$
50	$29.6° \pm 3.8°$	$23.6° \pm 2.7°$	$23.8° \pm 2.1°$
40	$25.2° \pm 4.1°$	$24.0° \pm 3.7°$	$25.2° \pm 2.5°$
30	$27.0° \pm 4.0°$	$20.6° \pm 4.2°$	$19.6° \pm 3.5°$
15	$19.7° \pm 5.0°$	$17.8° \pm 4.7°$	$15.4° \pm 4.2°$

appear in white light sunspot group images. However, it may also be the result of selection effects employed by the authors.

4.3.1.3. *The Joy's Law Trend: Method 3.* It has been suggested by McClintock and Norton (2013) that the best-fit line should not be forced to go through zero such that:

$$\alpha = m_C \theta + \lambda, \tag{4.3}$$

where m_C is the slope of the best-fit line (unitless), and λ is the y-intercept value (i.e. value of tilt angle at $\theta = 0°$). See Appendix H, Section 8.1.3 for a description of the linear least-squares fit following Method 3 and the calculated fit parameter uncertainties. When not forced to go through zero, using Mount Wilson sunspot group tilt angles from 1917-1985, McClintock and Norton (2013) find that the best-fit equation for the tilt angle as a function of emergence latitude is $\alpha = 0.26\theta + 0.58°$ in the Northern hemisphere, and $\alpha = 0.13\theta + 1.38°$ in the Southern hemisphere. Joy's Law trends are usually performed

by including the Northern and Southern hemispheres together, but McClintock and Norton (2013) show that the Joy's Law trend can be substantially different for each hemisphere. Using Mount Wilson and MDI magnetograms spanning years 1974-2012, Li and Ulrich (2012) find a best-fit equation of $\alpha = (0.5 \pm 0.2)\theta - (0.9^\circ \pm 0.3^\circ)$. As is evident by the many different Joy's Law empirical equations discussed in Sections 4.3.1.1-4.3.1.3, obtaining a best-fit equation to the observed Joy's Law trend must be dependent on the choice of data set and the fitting method. However, it is clear that there is a positive slope associated with the Joy's Law best-fit equation such that the tilt angle *does* increase with increasing latitude, whether or not the fit is forced to go through zero.

To obtain an equation for the Joy's Law trend following Eq. 4.3, rather than fitting all of the tilt angles as a function of the emergence latitude as we have done in Sections 4.3.1.1-4.3.1.2, we instead compute the average tilt angle in bins of 2.5° in latitude, then perform a least-squares fit following Eq. 4.3 to the average binned tilt angles. This treatment of the data is more in line with analysis of tilt angles from solar observations (e.g. McClintock and Norton 2013; Li and Ulrich 2012; Stenflo and Kosovichev 2012; Dasi-Espuig *et al.* 2010). Additionally, as the values of the binned average tilt angles observed at high latitudes are not well fit, the Joy's Law trend equation is usually only found for emergence latitudes of $\leq 30^\circ - 40^\circ$. For Method 3, we also restrict our fit to emergence latitudes $\leq 30^\circ$. The results of the linear least-squares fit following Eq. 4.3 to the binned average tilt angles calculated from our flux tube simulations for each Φ and B_0 considered are shown in Table 4.4.

Using Methods 1 and 2 to arrive at an empirical equation for the Joy's Law trend derived from our simulations does not aid in constraining the magnetic field strength at which the solar dynamo might be operating, as the reported values in Tables 4.2-4.3 agree fairly well

with empirical Joy's Law equations obtained from observations. However, using Method 3, it is possible to identify some magnetic field strength regimes where Joy's Law following Eq. 4.3 does not agree closely with those obtained from observations. By analyzing observational data, McClintock and Norton (2013) and Li and Ulrich (2012) find that while the tilt angle at the equator (i.e. y-intercept of Eq. 4.3) is not necessarily zero, it is small and close to zero. For our simulated flux tubes of $10^{21} - 10^{22}$ Mx, on the order of magnitude of sunspots, the tilt angle at the equator begins to deviate substantially from zero as the magnetic field strength of the flux tube decreases. For our flux tubes of 10^{20} Mx, which would result in smaller, ephemeral regions on the solar surface, the best-fit equations exhibition no clear trend in regard to magnetic field strength, and have larger uncertainties on the fit parameters than those for $10^{21} - 10^{22}$ Mx. Such behavior in our simulation is a result of the increasing dominance of convection over magnetic buoyancy on the evolution of the flux tube as the magnetic field strength decreases. For $10^{21} - 10^{22}$ Mx flux tubes, those of $B_0 = 60 - 100$ kG best match the Joy's Law empirical equations of McClintock and Norton (2013) and Li and Ulrich (2012) considering both the tilt angle at the equator and the slope m_C of the best-fit line.

To gain a better idea of how average tilt angles vary with latitude and flux, we find the average, binned tilt angles for all of the flux tubes in the magnetic field strength range of $60 - 100$ kG, and plot them separately in Fig. 4.4 for the three different magnetic flux values of 10^{20}, 10^{21}, and 10^{22} Mx. The Joy's Law equations following Method 3 are also shown in Fig. 4.4 for each plot. Average tilt angles in the 10^{22}, $60 - 100$ kG regime show well the expected linear Joy's Law trend. However, as the magnetic flux decreases, average tilt angles deviate more from the linear trend. Perhaps the most striking feature of Figure 4.4

TABLE 4.4. Slopes m_C (unitless) and the y-intercept (units of degrees) of the Joy's Law best-fit line following Method 3 for flux tubes with convective effects. Flux tubes of $\Phi = 10^{21} - 10^{22}$ Mx and $B_0 = 40 - 100$ kG most closely agree with the Joy's Law empirical equations found by McClintock and Norton (2013) and Li and Ulrich (2012). See Appendix H, Section 8.1.3 for a description of the fitting method and the calculation of the uncertainties on the fit parameters.

B (kG)	10^{20} Mx
100	$(0.25\pm0.16)\theta + (7.7^\circ\pm2.7^\circ)$
80	$(0.60\pm0.21)\theta + (2.3^\circ\pm3.6^\circ)$
60	$(0.11\pm0.30)\theta + (9.5^\circ\pm5.2^\circ)$
50	$(0.45\pm0.20)\theta + (1.9^\circ\pm3.5^\circ)$
40	$(0.03\pm0.25)\theta + (8.7^\circ\pm4.4^\circ)$
30	$(0.29\pm0.26)\theta + (7.2^\circ\pm4.5^\circ)$
15	$(-0.03\pm0.35)\theta + (11.7^\circ\pm6.1^\circ)$
B (kG)	10^{21} Mx
100	$(0.47\pm0.07)\theta - (0.54^\circ\pm1.29^\circ)$
80	$(0.34\pm0.10)\theta + (3.9^\circ\pm1.7^\circ)$
60	$(0.36\pm0.26)\theta + (4.2^\circ\pm4.6^\circ)$
50	$(0.78\pm0.25)\theta - (0.42^\circ\pm4.36^\circ)$
40	$(0.67\pm0.19)\theta - (0.61^\circ\pm3.34^\circ)$
30	$(0.11\pm0.18)\theta + (10.9^\circ\pm3.2^\circ)$
15	$(-0.55\pm0.29)\theta + (8.6^\circ\pm5.0^\circ)$
B (kG)	10^{22} Mx
100	$(0.33\pm0.04)\theta + (0.71^\circ\pm0.75^\circ)$
80	$(0.26\pm0.06)\theta + (1.9^\circ\pm1.1^\circ)$
60	$(0.38\pm0.09)\theta + (3.4^\circ\pm1.6^\circ)$
50	$(0.40\pm0.17)\theta + (6.9^\circ\pm2.9^\circ)$
40	$(0.90\pm0.22)\theta - (5.0^\circ\pm3.8^\circ)$
30	$(0.91\pm0.24)\theta - (8.1^\circ\pm4.2^\circ)$
15	$(-0.27\pm0.53)\theta + (8.5^\circ\pm9.1^\circ)$

is the sharp linear increase in average tilt angles of 10^{20} Mx between latitudes of $0^\circ - 17.5^\circ$. Above 17.5°, the average tilt angles decrease to $\sim12.5^\circ$ where the tilt angle value then remains fairly steady. A similar behavior is present for 10^{21} Mx flux tubes, although not as pronounced. The reason for this behavior may have something to do with the fact that flux tubes originating at latitudes of $\sim15^\circ - 20^\circ$ take the longest time to rise in or simulation. As a result, these flux tubes will spend a larger amount of time in the convective envelope and

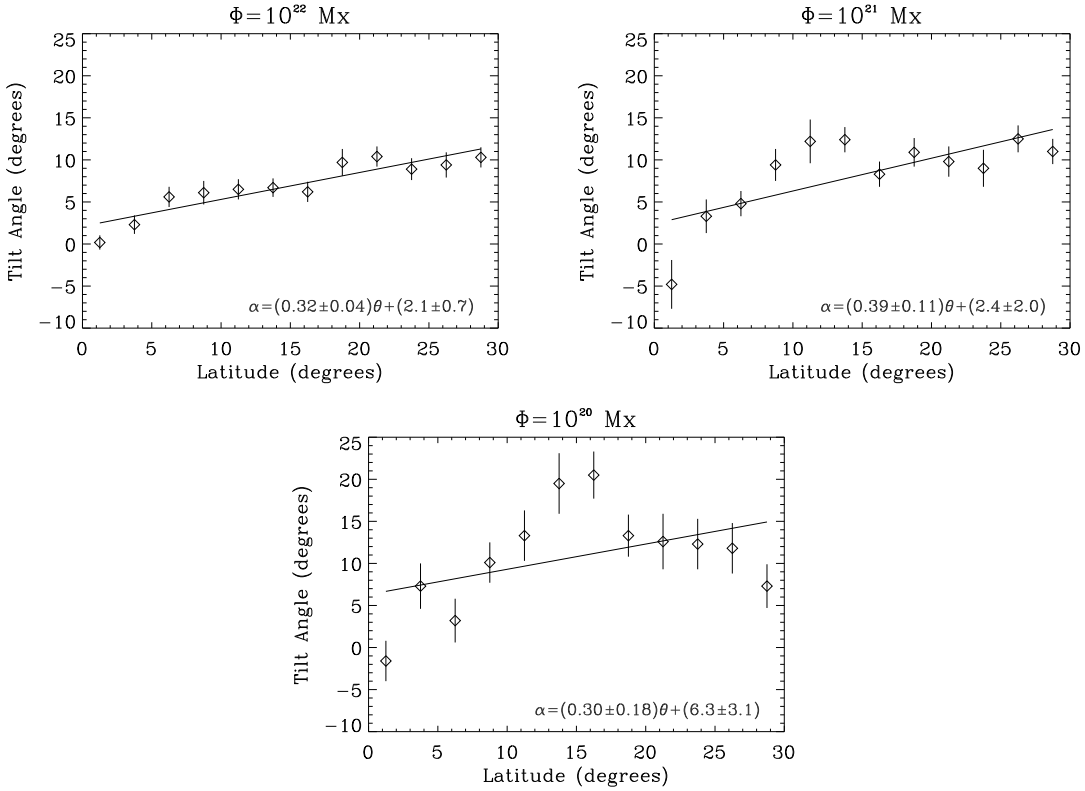

FIGURE 4.4. Average binned tilt angles for 60-100 kG flux tubes considered together. These results are shown for tube with magnetic flux of 10^{22} Mx (top left), 10^{21} Mx (top right), and 10^{20} Mx (bottom center). Results of the linear best-fit following Method 3 are also shown for each plot. Error bars are the standard deviation of the mean for each for each binned average tilt angle (2.5° in latitude). The average tilt angle deviates from the best-fit line as the flux decreases.

will experience the effects of kinetic helicity for a longer amount of time. In all three figures, the y-intercept and slopes of the best-fit line agree well, within the uncertainties, to those those reported in McClintock and Norton (2013) and Li and Ulrich (2012). Additionally, giant cells present in the convection simulation tend to extend to ±15° latitude. This may also contribute to the decline in the average tilt angles at larger emergence latitudes.

McClintock and Norton (2013) do not specifically state a reason why they should expect the tilt angle at the equator to be non-zero, corresponding to a non-zero y-intercept of the best-fit line. If tilting of the flux tube toward the equator is an effect due to the Coriolis

force, then tilt angles should be proportional to $\sin(\theta)$, corresponding to no tilting motion if a flux tube emergence near the equator. One possibility for the small, but non-zero tilt at the equator could be that the flux tube starts with an intrinsic tilt when it is generated by the dynamo mechanism. Within the uncertainties, the y-intercept values found by McClintock and Norton (2013) and Li and Ulrich (2012) do not deviate substantially from zero, nor do our for flux tubes of $10^{21} - 10^{22}$ Mx and magnetic field strengths of $\geq$40 kG. In our simulations, this small deviation from $\lambda = 0^{\circ}$ could be attributed to *noise* introduced by convection to the tilt angle trend.

4.3.2. Tilt Angle Scatter. In Figure 4.3, there is a clear scatter of the tilt angle about the best-fit line (Method 1) for flux tubes subject to convection, which becomes greater at lower magnetic flux. Again, this trend is the result of stronger coupling between the flux tube and convective flows at a reduced magnetic flux. We attempt to further constrain the magnetic field strength at which the solar dynamo might be operating by calculating the scatter of tilt angles our simulated flux tubes produce about the Joy's Law trend best fit equations (Section 4.3.2.1) as well as the mean tilt angle (Section 4.3.2.2).

4.3.2.1. *Scatter about the Joy's Law best-fit equation.* To quantify the scatter of the tilt angles around the best fit line, we calculate the standard deviation of the tilt about its fitted value following:

$$\sigma_{fit} = \sqrt{\frac{\sum_{i=1}^{N}(\alpha_i - \alpha_{fit})^2}{N}}, \tag{4.4}$$

where α_i is the i^{th} tilt angle, α_{fit} is the i^{th} tilt angle as a result of the fit following Method 1 for which the slopes m_A are reported in Table 4.2, N is the number of points considered, and α is in units of degrees. See Appendix G for the number N of flux tube simulations

TABLE 4.5. Standard deviation σ_{fit} (units of degrees) of the tilt angle about the best-fit Joy's Law equation (Method 1), where tilt angles are shifted to fall within the range of [-90°, 90°]. The standard deviation tends to increase with decreasing magnetic field and flux.

	15 kG	30 kG	40 kG	50 kG	60 kG	80 kG	100 kG
10^{20} Mx	42°	34°	34°	30°	28°	20°	18°
10^{21} Mx	40°	35°	31°	23°	19°	14°	11°
10^{22} Mx	39°	33°	22°	18°	13°	9.1°	8.2°

TABLE 4.6. Standard deviation σ_{fit} (units of degrees) of the tilt angle about the best-fit Joy's Law equation (Method 1) where tilt angles fall within the range of [-180°, 180°]. This is different from what is reported in Table 4.5, where the tilt angles are shifted to fall within the range of [-90°, 90°]. In comparing both Tables 4.5 and 4.6, σ_{fit} remains unchanged for $60 - 100$ kG flux tubes for flux values of $10^{21} - 10^{22}$ Mx.

	15 kG	30 kG	40 kG	50 kG	60 kG	80 kG	100 kG
10^{20} Mx	63°	58°	54°	41°	40°	22°	22°
10^{21} Mx	73°	55°	42°	30°	19°	14°	10°
10^{22} Mx	71°	52°	35°	23 °	13°	9.1°	8.2°

used for each B_0, Φ combination. We evaluate σ_{fit} for each field strength and flux value considered in this Chapter, where the results are given in Table 4.5. When calculating σ_{fit} as reported in Table 4.5, we have shifted the tilt angles appropriately such that all tilts angles fall within the range [-90°, 90°], and the reported uncertainties are the standard deviation of the mean. This is unlike what was done in Weber, Fan, and Miesch (2013) where tilt angles were considered to fall within the range of [-180°, 180°], thereby retaining anti-Hale tilt angle information. The value of σ_{fit} assuming tilt angles fall within the [-180°, 180°], range are reported in Table 4.6.

In comparing both Tables 4.5 and 4.6, σ_{fit} remains unchanged for $60 - 100$ kG flux tubes of $10^{21} - 10^{22}$ Mx. By retaining the anti-Hale tilt angle information, the scatter of the tilt angles about the Joy's Law trend are significantly larger for smaller flux values and magnetic field strengths than in the case where we shift the tilt angles to fall within [-90°,

90°]. Flux tubes can obtain anti-Hale polarities in our simulation if they emerge in the opposite hemisphere from which they originated, or as a result of the flux tube becoming so distorted by convection that the legs of the emerging loop can become reversed. Both these situations usually occur for weak magnetic field strength cases, while the majority of anti-Hale flux tubes with moderate magnetic field between $40 - 50$ kG happen as a result of hemisphere crossing due to convective flows. The σ_{fit} values reported in Tables 4.5 and 4.6 vary little when the best-fit equation following Method 2 is used instead.

Using Mount Wilson white light sunspot group data (1917 – 1985), Fisher, Fan, and Howard (1995) find that $\sigma_{fit} \sim 30°$. Fisher, Fan, and Howard (1995) use tilt angles in the range of [-90°, 90°], and assume that the tilt angle trend is dependent on sinθ and the separation of the leading and following polarity spots. A value of $\sigma_{fit} \leq 30°$ following Table 4.5 would definitely exclude $10^{21} - 10^{22}$ Mx flux tubes in the 15 kG range according to our simulation results as the possible progenitors of solar active regions. Active regions of flux values of 10^{20} Mx would appear on magnetograms, but would probably not be associated with white light sunspot groups. Since we have simulations for 10^{20} Mx, we calculate σ_{fit} for these values as well in Tables 4.5 and 4.6. We do note that while the Joy's Law trend is not statistically dependent on flux (see Section 4.3.1), the scatter of the tilt angles about their best-fit line tends to increase with decreasing flux.

4.3.2.2. *Scatter about the mean tilt angle.* Using Mount Wilson Observatory sunspot data, McClintock and Norton (2013) compute the standard deviation of the tilt angle around the mean tilt angle value. We also do the same here for flux tubes emerging between ±30° in latitude with tilt angles shifted to fall in the range of [-90°, 90°], so as to mirror the treatment of the analysis by McClintock and Norton (2013). In this section, the standard

TABLE 4.7. The standard deviation from the mean tilt angle σ_{avg} (units of degrees) for tilt angles in the range of [-90°, 90°] and emergence latitude of ±30°. Similar to σ_{fit}, σ_{avg} tends to increase with decreasing magnetic field.

	15 kG	30 kG	40 kG	50 kG	60 kG	80 kG	100 kG
10^{20} Mx	42°	35°	33°	31°	28°	20°	17°
10^{21} Mx	43°	38°	36°	25°	19°	13°	9°
10^{22} Mx	44°	41°	27°	20°	12°	10°	8°

deviation of the tilt angle is defined as:

$$\sigma_{avg} = \sqrt{\frac{\sum_{i=1}^{N}(\alpha_i - \alpha_{avg})^2}{N}}, \tag{4.5}$$

where α_i is the i^{th} tilt angle, α_{avg} is the mean tilt angle for flux tubes that emerge between ±30° in latitude for each value of B_0 and Φ, N is the number of points considered, and α is in units of degrees. See Appendix G for the number N of flux tube simulations used for each B_0, Φ combination. Table 4.7 shows the standard deviation of the tilt angle σ_{avg} for each Φ and B_0 considered.

McClintock and Norton (2013) find $\sigma_{avg} \sim 30°$ for both the Northern and Southern hemispheres over six solar cycles. Using this criteria, we can exclude flux tubes resulting from our simulations of $10^{21} - 10^{22}$ Mx and magnetic field strength of ≤30 kG as possible candidates for the progenitors of solar active regions due to their large σ_{avg}. We also note that the spread in the distribution of the tilt angles increases as one goes to smaller regions, or smaller magnetic flux, as is found in Wang and Sheeley (1989) and Stenflo and Kosovichev (2012). Especially at moderate to strong magnetic field strengths of ≥50 kG, the values of σ_{avg} are not significantly different from those of σ_{fit} as shown in Table 4.5.

McClintock and Norton (2013) report an average tilt angle of ∼6° or less regardless of hemisphere or solar cycle. These results are similar to those reported in Dasi-Espuig *et al.*

TABLE 4.8. Mean tilt angles (units of degrees) for tilt angles in the range of [-90°, 90°] and emergence latitude of ±30°. Reported uncertainties are the standard deviation of the mean (not σ_{avg} or σ_{fit}). Average tilt angles for flux tubes of $10^{21} - 10^{22}$ Mx and $40 - 60$ kG have a large average tilt compared to the ∼6° and less observed on the Sun.

	15 kG	30 kG	40 kG	50 kG	60 kG	80 kG	100 kG
10^{20} Mx	12° ± 3°	11° ± 2°	9° ± 2°	9° ± 2°	9° ± 2°	11° ± 1°	12° ± 1°
10^{21} Mx	2° ± 3°	11° ± 3°	10° ± 3°	13° ± 2°	11° ± 1°	9° ± 1°	7° ± 1°
10^{22} Mx	3° ± 4°	9° ± 3°	11° ± 2°	14° ± 1°	10° ± 1°	6° ± 1°	6° ± 1°

(2010). The average tilt angle calculated from our flux tube simulations for each B_0 and Φ are reported in Table 4.8. The average tilt angles in our simulation tend to be larger than this value, especially at 10^{20} Mx and moderate magnetic field strengths of $40 - 50$ kG. In our simulations, tilt angles are systematically increased from the value obtained without the influence of convective flows. Most probably the larger-than-observed average tilt angles we report in most cases are due to the fact that the kinetic helicity in upflow regions associated with the convective velocity field may be larger than on the Sun. Taking the average tilt angles of $10^{21} - 10^{22}$ Mx together, flux tubes of $40 - 60$ kG have too large an average tilt angle to be considered as the progenitors of solar active regions.

4.3.3. PREFERRED TILT ANGLES. Howard (1996) investigated the distribution of sunspot group tilt angles from a set of Mount Wilson white light photographs (1917 – 1985) as well as sunspot groups derived from plage in Mount Wilson daily magnetograms (1967 – 1995). They bin the tilt angles in 2.5° increments, and plot the number of occurrances of the tilt angles in these bins. In this way, they find that sunspot groups tend to form most often with tilt angles between 2.5° – 5° for white light data, and between 7.5° – 10° for magnetogram data. The tilt angle distribution that we obtain for flux tubes of all magnetic fields and

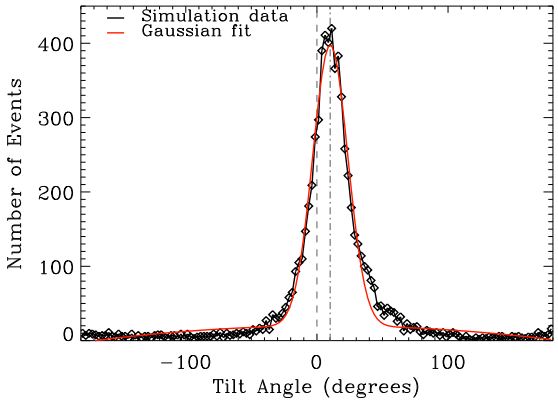

FIGURE 4.5. Distribution of tilt angles in 2.5° bins for all flux tubes considered in this Chapter. The peak of the distribution function is between $10° - 12.5°$ (black line), with a non-linear least-squares Gaussian fit (red line) of center $10.2° \pm 3.6°$, as shown by the gray dash-dotted line.

magnetic flux studied here using tilt angle bins of 2.5° is shown in Figure 4.5. In Figure 4.5, tilt angles in the range of [-180°, 180°] are shown.

We find that for all magnetic flux tubes considered in this Chapter, the tilt angle distribution from our simulation peaks between bins of $10° - 12.5°$ (black line), where a non-linear least-squares Gaussian fit (red line) gives a center, or preferred tilt, of $10.2° \pm 3.6°$. The uncertainty on the preferred tilt angle is the standard deviation of the Gaussian fit. If we shift the tilt angles to a range of [-90°, 90°], the preferred tilt angle only changes by 0.1°. This is in good agreement with the magnetogram data of Howard (1996) and Stenflo and Kosovichev (2012), who find a preferred, or most common, tilt of $\sim 10°$ for all bipolar regions emerging between a $15° - 20°$ latitude range including the largest active regions down to regions of $\sim 10^{20}$ Mx. If we only consider $60 - 100$ kG flux tubes, following results from the previous tilt angle sections, the preferred tilt angle decreases to $9.1° \pm 3.3°$. Whereas, if we only consider $80 - 100$ kG flux tubes, this value then decreases even more to $8.1° \pm 3.2°$. Our preferred tilt angle results are also in very good agreement with the tilting of buoyantly rising

portions of magnetic wreaths resulting from global 3D simulations of convective dynamos (Nelson *et al.* 2013).

Figure 4.5 represents a total of 6927 flux tubes. Of all these flux tubes, only 6.3% emerge with anti-Hale tilt angles (i.e. outside the range of $\pm 90^{\circ}$). The percentage of flux tubes with anti-Hale tilt angles increases with decreasing magnetic flux and magnetic field values. This is slightly larger than the $\sim$4% as found via observations of medium to large-sized active regions (Wang and Sheeley 1989; Stenflo and Kosovichev 2012).

4.4. Bipolar Region Rotations Rates

Observations show that sunspots tend to rotate faster than the solar surface plasma (Howard and Harvey 1970; Golub and Vaiana 1978; Gilman and Howard 1985). In addition, the leading sunspot in a large bipolar region ($\sim 10^{21} - 10^{22}$ Mx) tends to rotate faster than the following spot (Gilman and Howard 1985; van Driel-Gesztelyi and Petrovay 1990). We investigate both of these phenomena in our simulations by first observing the asymmetry of inclination of the flux tube legs in Section 4.4.1, then tracking the rotation rate of the centroid between the leading and following legs of a rising loop in Section 4.4.2.

4.4.1. Asymmetry of Inclination. When looking down on a flux tube from the pole at the end of its rise, as in Figure 3.2, it is apparent that there is an asymmetry in the inclination of the leading and following legs with respect to the vertical direction. The following leg tends to have a steeper slope than the leading leg. This asymmetry is caused by the Coriolis force and the conservation of angular momentum as the tube rises through the convection zone (Moreno-Insertis, Caligari, and Schüssler 1994; Caligari, Moreno-Insertis, and Schüssler 1995; Caligari, Schüssler, and Moreno-Insertis 1998), and provides an explanation for the apparent asymmetric East – West proper motions of the two polarities of an emerging

active region. Generally, the leading polarity region appears to rotate forward faster than the following region. One such explanation of this phenomenon is as follows: as the tube rises above a constant r surface, the inclination of the legs of the loop cause an apparent, more rapid motion of the leading polarity spot (which has a larger angle of inclination) as compared to the motion of the following polarity spot (which has a smaller angle of inclination). As the active region develops, it will appear as though the leading spot is moving away from the following spot, while the active region as a whole rotates forward in longitude.

Here we quantify the steepness of each leg of the emerging loop by calculating what we call the inclination angle. To do this, first we find the portion of the emerging loop which is concave downward. Then we find the best fit line for each leg from the flux tube apex in the concave down portion. The angle between the best fit line for each leg and $-\hat{\mathbf{r}}$ is the inclination angle. The smaller this angle, the steeper the slope of the leg. In Figure 4.6 we have plotted the average difference of the inclination angles (leading leg minus the following leg). Only the average inclination difference for each magnetic field strength is plotted because we find that the inclination difference does not vary systematically with latitude. Positive inclination difference means the following leg is steeper, consistent with previous results (Moreno-Insertis, Caligari, and Schüssler 1994; Caligari, Moreno-Insertis, and Schüssler 1995; Caligari, Schüssler, and Moreno-Insertis 1998). We find that at all field strengths and magnetic flux, the majority of the emerging loops develop a steeper slope for the following leg. The inclination angle differences are overall reduced with the inclusion of convection, and appear to have no clear trend with respect to magnetic field strength or flux when solar-like convective motions are included.

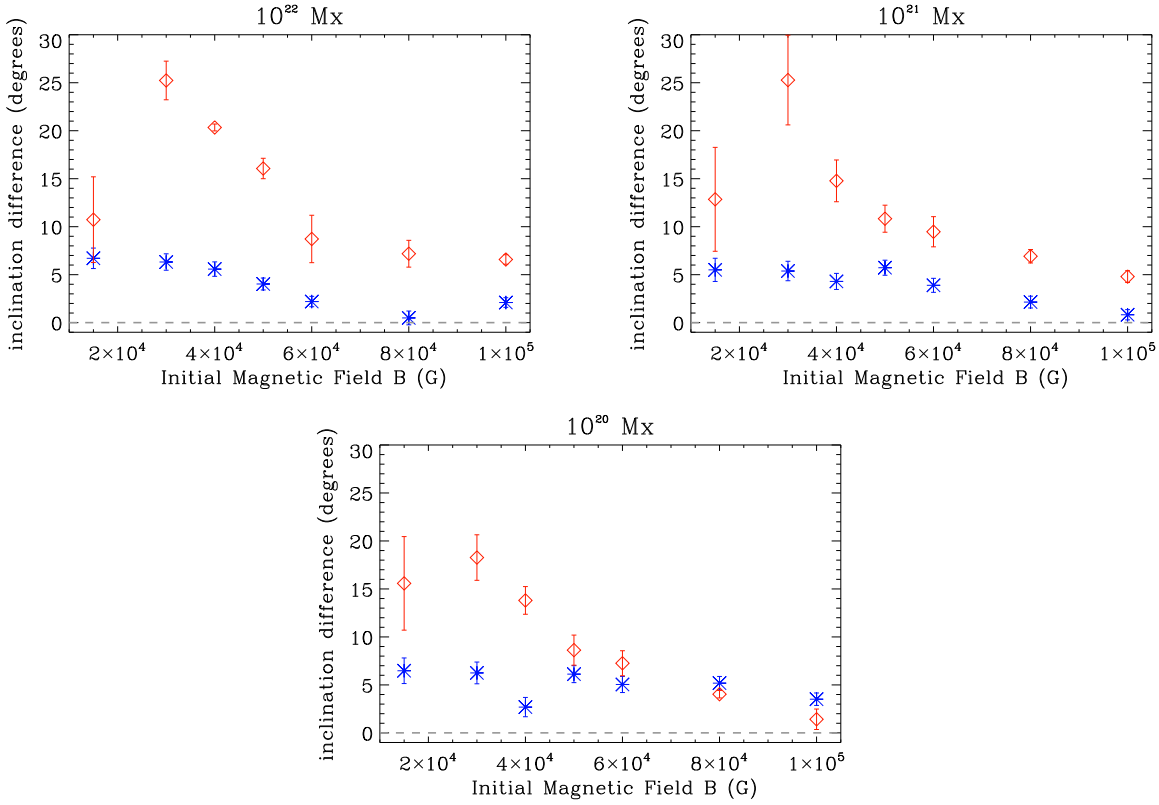

FIGURE 4.6. Average difference of the inclination angles between the leading and following sides of the emerging loop for cases with (blue) and without (red) the influence of convection. Bars represent the standard deviation of the mean. Positive inclination difference means the following leg is steeper. Inclination angle difference are overall reduced with the inclusion of convection.

4.4.2. ROTATION RATE OF THE CENTROID. The azimuthal velocity of leader, follower, and all sunspots (in the reference frame with a solid body rotation rate of $\Omega_0 = 2.7 \times 10^{-6}$ rad s^{-1}) as derived from Gilman and Howard (1985) are plotted in Figure 1.4, as well as the observed azimuthal rotation rate of the solar plasma at the surface (blue line) as determined from surface spectroscopic Doppler-velocity measurements (e.g. Thompson *et al.* 2003) and the rotation rate at $r = 0.95R_\odot$ (red line) as found via inversions of helioseismic observations (Howe *et al.* 2000). This image suggests that sunspots tend to rotate at nearly the same rate as the solar plasma at $0.95R_\odot$, and therefore rotate faster than solar surface plasma.

In order to quantify the rotation rate of emerging loops from our thin flux tube simulation, we calculate the apparent azimuthal speed of the center point between the leading and following intersections of the emerging loop with the constant r surface of $0.95R_{\odot}$ during the last two time steps before the loop apex reaches the top of the simulation domain. This reflects the apparent azimuthal speed of an emerging active region, and it is not the actual azimuthal speed of the flux tube plasma at the tube apex. We do this only for flux tubes of 10^{21} Mx and 10^{22} Mx, assuming tubes of flux order 10^{20} Mx do not produce large sunspots.

Caligari, Moreno-Insertis, and Schüssler (1995) compute the azimuthal phase speed of the summit of an emerging flux loop without convective effects throughout its rise. This phase motion is related to the wave character of the rising flux loop, which is similar in behavior to a transversal wave propagating along a string. They find that the azimuthal phase speed decreases with increasing height of the summit, and that it changes sign at about 50 Mm below the solar surface such that the angular velocity of the summit is smaller than that of the external plasma. They suggest that the resulting active region will still show a higher rotation velocity than the surrounding plasma because of the inclination difference of the leading and following legs with respect to the local vertical, as discussed in Section 4.4.1. However, to make comparisons to actual sunspot rotation rates, we feel that the method presented in this section is a better alternative .

Figure 4.7 *Left* and *Right* show the average of the apparent azimuthal speed in 5° bins, for cases with a magnetic flux of 10^{21} Mx and 10^{22} Mx respectively, where bars on the points are the standard deviation of the mean. For comparison, these plots also show the average azimuthal rotation rate of the ASH simulation at $r = 0.95R_{\odot}$ (red line), and the azimuthal flow speed one would expect at the surface (blue line) assuming the differential rotation in

the top shear layer between the surface and $0.95R_\odot$ decreases by $\sim$10 nHz (what we will subsequently call the *inferred* surface rate) as found by helioseismology (e.g. Thompson *et al.* 2003).

In all cases, flux tubes that emerge at high latitudes above 40° rotate at a rate that is close to, or faster than, the ASH rate at $r = 0.95R_\odot$ and hence faster than the inferred surface rate expected of our simulation. With initial magnetic field strengths of 15 kG and 30 kG, for both magnetic fluxes, the average rotation rates of the majority of flux tubes that emerge at $\leq$35° are less than the inferred surface rate. However, at mid-magnetic-field strengths of 40 kG and 50 kG, the rotation rates of the flux tubes roughly follow the inferred surface rate. Only for initial magnetic field strengths of $\geq$60 kG are the flux tubes capable of rotating at or faster than the inferred surface rate for all emergence latitudes, considering magnetic fluxes of 10^{21} Mx and 10^{22} Mx.

We recognize that this method of quantifying the rotation rate of the emerging flux tubes in our simulation has some limitations. Due to the nature of the ASH convection simulation and the fact that the thin flux tube simulation breaks down in the upper portion of the convection zone, it is not possible to allow the thin flux tube to emerge all the way to the solar surface. Instead, we operate under the assumption that the rotation rate of the emerging loop at a constant r surface of $0.05R_\odot$ below the solar surface is a good representation for how an active region will behave at the solar surface, as is reflected in Figure 1.4 for solar observations. The discrepancy between the observed and simulated rotation rates could in part be attributed to the particular ASH simulation that we use, which does not precisely reproduce the solar Ω-profile. Our simulated flux tubes are effectively anchored at the convection zone base, whereas real flux tubes may decouple from the deep convection zone

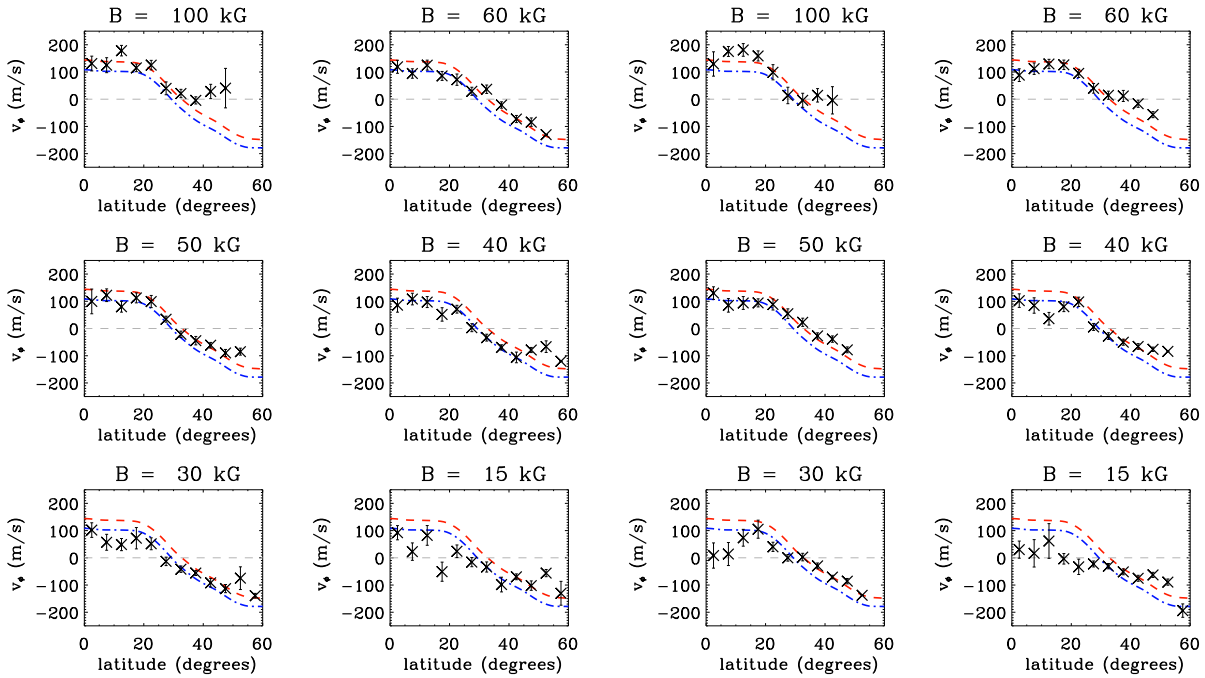

FIGURE 4.7. Average rotation rate of emerging flux loops subjected to the convective flow with magnetic flux of (a) 10^{21} Mx on the left (leftmost six panels) and (b) 10^{22} Mx on the right (rightmost six panels). Averages are taken in 5° bins, with bars representing the standard deviation of the mean. Red and blue lines correspond to the ASH rotation rate at $r = 0.95R_\odot$ and inferred solar surface rotation rate respectively, assuming a difference of 10 nHz between the two. All values are plotted with reference to the solid body rotation rate of $\Omega_0 = 2.7 \times 10^{-6}$ rad s^{-1}, so that the zero line is the solid body rotation of the Sun. Strong flux tubes with initial field strengths of $\geq$50 kG rotate faster than or nearly equal to the inferred surface rate.

at some point during their evolution, and become anchored closer to the surface. This is why we choose to investigate the rotation rate closer to the surface. As our thin flux tube is a one-dimensional string of mass elements, we cannot address the issue that the flux tube could lose its coherency and become fragmented (Longcope, Fisher, and Arendt 1996), which may result in a stronger coupling between the tube and convective fluid motions, and could be a significant contributing factor to the rotation rate of active regions.

In an attempt to gain a stronger coupling between the flux tube and convective fluid motions, we perform some simulations where the drag coefficient C_d in the last term of

Equation 2.1 is increased from unity to the constant values of 1.5 and 2. Also, we perform simulations where we adjust the drag coefficient such that it exponentially varies from 1 at the base of the convection zone to 1.5 or 2 at the top of the simulation domain. These tests were performed for flux tubes with initial field strengths of 40 kG and magnetic flux of 10^{22} Mx. These efforts to alter the drag coefficient to produce stronger coupling to convection did not result in faster rotation rates compared to the surface rate for all latitudes less than 25°. This indicates that 40 kG flux tubes or less will probably not be able to reproduce sunspot rotation rates utilizing the thin flux tube model as it currently stands.

4.5. Magnetic Fields

4.5.1. Magnetic Field Asymmetry. A well-known asymmetry of solar active regions is observed in the morphology of the leading and the following polarities of an active region. The leading polarity flux tends to be concentrated into a well formed sunspot, whereas the following polarity flux tends to appear more fragmented and dispersed (e.g. Bray and Loughhead 1979). The thin flux tube simulations of Fan, Fisher, and Deluca (1993) showed that the preceding leg of an emerging magnetic flux loop has a stronger magnetic field than the following leg as a result of the differential stretching of the rising loop due to the Coriolis force. This gives an explanation for the observed more coherent and less fragmented morphology for the leading polarity flux in an active region. However subsequent simulations (e.g. Caligari, Moreno-Insertis, and Schüssler 1995; Fan and Fisher 1996) using the mechanical equilibrium initial state (which is more physical) as opposed to the temperature equilibrium as used by Fan, Fisher, and Deluca (1993), found that the leading leg of the emerging loop has a stronger magnetic field than the following only for flux tubes with

an initial field strength that is below about 60 kG. For flux tubes with higher initial field strengths, the field strength asymmetry reverses at the top of the loop.

Here we investigate this magnetic field asymmetry by calculating dB/ds, the derivative of the magnetic field in the direction of solar rotation, at the apex of the emerging flux loop as shown in Figure 4.8. If dB/ds is greater (less) than zero, then the leading (following) leg has a stronger magnetic field. As can be seen in Figure 4.8, at 50 kG and below, the majority of the emerging loops show stronger field in the leading leg than the following leg in the presence of convection. However, for flux tubes of 100 kG subject to convection effects, only some of the emerging flux loops at higher latitudes have stronger field in the preceding leg. At 60 kG there are about equal number of positive and negative dB/ds cases. Thus with convection, loops with initial field $\leq$50 kG tend to emerge with the appropriate magnetic field asymmetry (i.e. with a stronger field in the preceding leg and therefore can be expected to result in an emerging active region with a more coherent leading polarity).

Recent three-dimensional radiative MHD simulations of magnetic flux emergence and sunspot formation in the top layer of the convection zone and the photosphere by Rempel (private communication, 2012) have suggested that the morphological asymmetry of sunspots may be caused by a flow of plasma along the emerging tube out of the leading portion of the active region into the following leg, and is less dependent on the asymmetry in field strength of the emerging loop. This flow of plasma is related, in part, to the conservation of angular momentum as the flux tube rises. If this is indeed the case, then we can not rule out flux tubes with stronger initial magnetic field strengths of >50 kG at the base of the solar convection zone as the progenitors of solar active regions simply due to their magnetic field asymmetries.

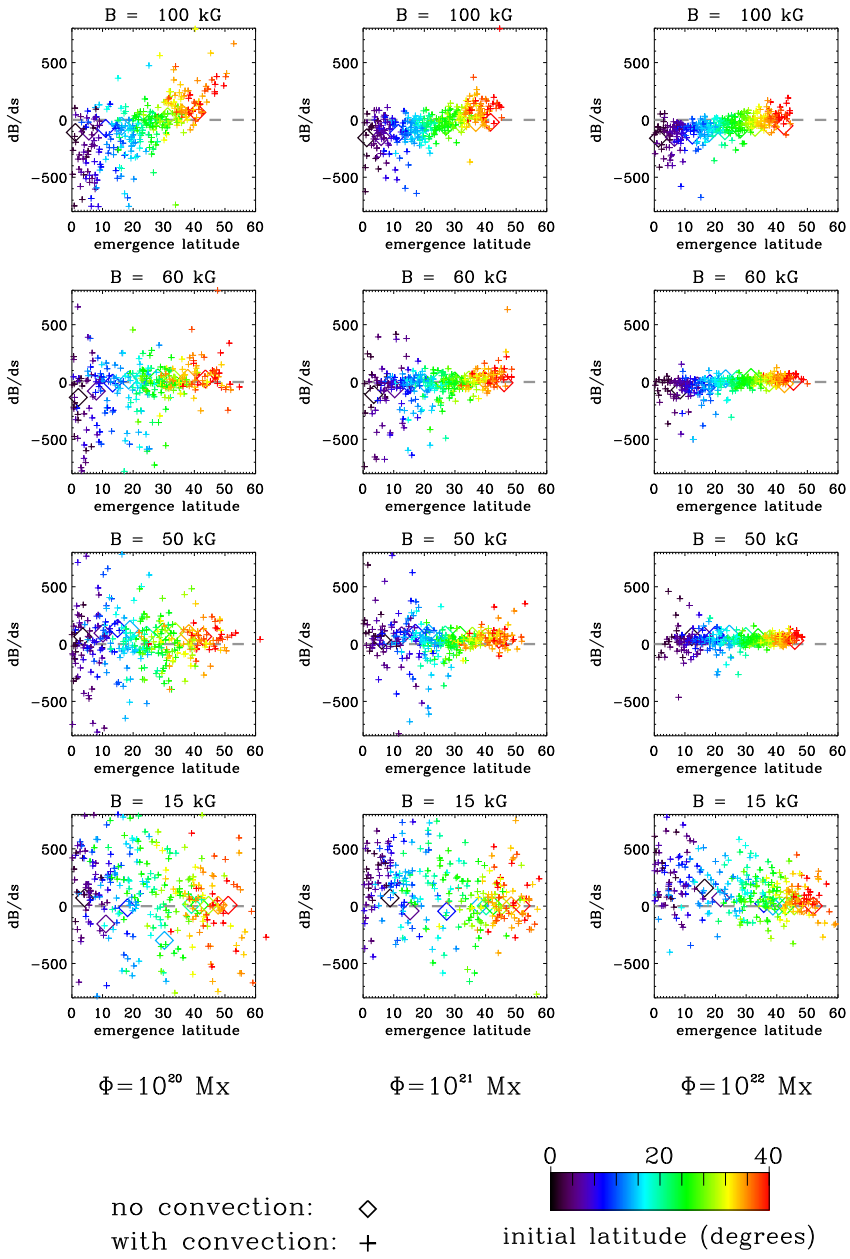

FIGURE 4.8. The quantity dB/ds at the apex of the emerging flux loop as a function of emergence latitude for cases with (plus signs) and without (diamonds) the influence of convection. A color bar indicates the original starting latitude of the flux tube. With Increasing flux, there quantity dB/ds deviates less from the values without the influence of convection. At low latitudes for magnetic field strengths of $\geq$60 kG, dB/ds is negative, indicating the leading leg has a smaller magnetic field than the following, unlike observations might suggest.

4.5.2. Apex Magnetic Field Strength. The nature of the magnetic field below the visible surface of the Sun is not well known. Simulations of flux emergence in the upper layers of the convection zone have been computed in domains that span from the photosphere to depths of 2 Mm to 20 Mm below the surface (e.g. Cheung, Schüssler, and Moreno-Insertis 2007; Rempel, Schüssler, and Knölker 2009; Stein *et al.* 2011). The simulations assume a range of initial magnetic field strengths of the flux tube at the bottom of their simulation domain anywhere from ∼2 kG to ∼30 kG. We report the average magnetic field strength at the apex of our thin flux tube simulations, once the tube has reached the top of the simulation domain at a depth of 21 Mm below the solar surface, for multiple initial magnetic field strengths and flux in Table 4.9. We have averaged these results for each B_0 and Φ because the magnetic field strength at the apex is not dependent on emergence latitude. Our results do support average magnetic field strength values of ∼1 kG to ∼15 kG for flux tubes reaching a height of ∼21 Mm below the solar surface, assuming initial field strengths of 15 kG to 100 kG at the base of the convection zone for magnetic fluxes of $10^{20} - 10^{22}$ Mx. The magnetic field strength of the flux tube at the apex is largest for larger initial fields, and the scatter of the magnetic field at the apex for a particular magnetic field strength tends to increase with decreasing flux. Additionally, for each B_0, the magnetic field strength of the flux tube apex at 21 Mm increases with decreasing flux. The value Φ only effects the thin flux tube equations through the drag force term. As a result, tubes with a weaker flux experience a stronger coupling to convection, and will be buffeted more by convective flows. This increase in the magnetic field strength of the flux tube apex is likely a result of the increased stretching of the flux tube at weaker magnetic flux, especially by convective

TABLE 4.9. Average magnetic field strength of the flux tube apex at 21 Mm below the solar surface (simulation upper boundary). Uncertainties represent the standard deviation of the mean. The magnetic field strength at the flux tube apex increases with decreasing flux, and decreases with decreasing B_0.

B	10^{20} Mx	10^{21} Mx	10^{22} Mx
100 kG	15000 ± 400 G	11800 ± 300 G	9300 ± 200 G
80 kG	13000 ± 600 G	8900 ± 300 G	7500 ± 300 G
60 kG	10000 ± 1000 G	6800 ± 400 G	5000 ± 200 G
50 kG	6400 ± 500 G	4800 ± 300 G	4000 ± 200 G
40 kG	4000 ± 400 G	3500 ± 300 G	2800 ± 200 G
30 kG	3200 ± 300 G	2700 ± 300 G	1700 ± 100 G
15 kG	1800 ± 200 G	1400 ± 200 G	1100 ± 100 G

downflows. Even flux tubes of large magnetic field strength with a weak flux of 10^{20} Mx are significantly deformed by convective influences.

Typical magnetic field strength of sunspots are in the range of ∼1 kG for small spots to ∼4 kG for very large spots. The values we have reported in Table 4.9 at ∼21 Mm below the solar surface fall in this range only for flux tubes of $B_0 \leq 40$ kG. However, this does not exclude larger magnetic field strength flux tubes as the progenitors of solar active regions. We cannot model the last ∼21 Mm of the flux emergence process because the thin flux tube approach no longer holds in this region. Additional processes in the upper convection zone such as fragmentation of the flux tube and convective collapse (strong intensification of magnetic field) likely hold the key to understanding how the magnetic field strength of the flux tube evolves in the last portion of its rise toward the surface.

4.6. DISCUSSION

By embedding the thin flux tube model in a three-dimensional, turbulent, convective velocity field representing the solar convective envelope, we study how convection can influence the local properties of emerging active region flux tubes. In comparing these properties to those obtained from solar active region observations, we attempt to constrain the magnetic

field strengths of dynamo-generated magnetic fields at the base of the solar convection zone. The thin flux tube approximation, although idealized, allows us to investigate active region scale flux tubes at near-equipartition to strongly equipartition magnetic field strengths of $15 - 100$ kG under perfect frozen-in flux conditions. We find that subjecting the thin flux tube to turbulent convective flows does indeed alter flux tube dynamics, and that it can have a significant impact on the properties of the emerging flux loop in comparison to flux tube simulations performed in the absence of a convective velocity field.

Decreasing the magnetic flux of the tube results in an increase of the drag force acting on the rising flux loop, thereby flux tubes of 10^{20} Mx are advected by turbulent convective flows more strongly than 10^{22} Mx flux tubes. For all magnetic flux values that we consider here, flux tubes are able to emerge near the equator with the aid of convective flows, which solves the previous problem of poleward slippage encountered by thin flux tube simulations for flux tubes of low magnetic field strengths without convective effects. With convection, flux tubes are also able to emerge closer to the equator than the latitude where they originated at the bottom of the convection zone. Such behavior provides a possible explanation for active regions near the equator ($\pm 10^{\circ}$) that exhibit anti-Hale polarities.

There is no agreed upon empirical Joy's Law equation, and the results of Joy's Law best-fit equations vary widely, presumably a result of the chose data set and selection methods. However, we attempt to fit the tilt angles from our thin flux tube simulations following three different methods used by a number of authors to facilitate comparison between our results and solar observations. Dasi-Espuig *et al.* (2010) perform a linear best-fit on tilt angles (α) as a function of latitude (θ) following $\alpha = m_A \theta$ (Method 1), and obtain a slope m_A of the best-fit line of $m_A = 0.26 \pm 0.05$ and $m_A = 0.28 \pm 0.06$ for Mount Wilson and Kodikanal

sunspot data, respectively. Following Method 1, the slopes m_A we obtain (Table 4.2) are significantly boosted from the cases without convection (Table 4.1). This occurs because helical convective upflows help to drive the tilt angle of the flux tube in the appropriate Joy's Law direction for both hemispheres (i.e. toward the equator). The values of the slopes m_A agree well with Dasi-Espuig *et al.* (2010) for $10^{21} - 10^{22}$ Mx, with the exception of $40 - 50$ kG flux tubes which show a slightly larger best-fit slope within the uncertainties.

Assuming the origin of the tilt angle is related to the Coriolis force, as this force varies with latitude as $\sin(\theta)$, some authors fit tilt angles as a function of $\sin(\theta)$ following $\alpha = m_B \sin(\theta)$ (Method 2). Using this method, Stenflo and Kosovichev (2012) find $m_B = 32.1^\circ \pm 0.7^\circ$, whereas Fisher, Fan, and Howard (1995) find $m_B = 15.69^\circ \pm 0.66^\circ$. Values of m_B obtained by performing a fit to our simulation tilt angles following Method 2 (see Table 4.3) all fall within this vary wide spread. Finally, following the suggestion by some authors that the Joy's Law empirical equation should not be forced to go through zero, we fit our tilt angles with the equation $\alpha = m_C \theta + \lambda$, where λ is the value of the tilt angle at $\theta = 0^\circ$. Comparing our results (Table 4.4) to those of McClintock and Norton (2013) and Li and Ulrich (2012), we could exclude $10^{21} - 10^{22}$ Mx flux tubes of $15 - 30$ kG as the progenitors of solar active regions because their tilt angles at the equator are too large within the uncertainties. We also note that average tilt angles peak at mid-latitudes of $\sim 15^\circ - 20^\circ$ for flux tubes of 10^{20} Mx. Above 20°, the average tilt angles relax back to $\sim 12.5^\circ$. This deviates from the Joy's Law trend that tilt angles should increase with increasing latitude. We believe this occurs in our simulation due to the nature of the giant cell convection pattern in our simulation.

The scatter of the tilt angles around their linear Joy's Law fit line σ_{fit} is shown to be too large for initial magnetic field strengths of 15 kG with fluxes of 10^{21} Mx and 10^{22} Mx,

as compared to the observed value of $\leq 30^{\circ}$ for white light sunspot group images (Fisher, Fan, and Howard 1995). While the scatter of the tilt angle increases with decreasing flux (Table 4.5), we find no statistically significant dependence of the Joy's Law trend on flux (see Table 4.2), consistent with the results of Stenflo and Kosovichev (2012). According to McClintock and Norton (2013), the scatter of the tilt angle about the mean value σ_{avg} should also be $\sim 30^{\circ}$, and the average tilt angle should be $\leq 6^{\circ}$. From our simulations, flux tubes of $10^{21} - 10^{22}$ Mx and magnetic field strengths of ≤ 30 kG have too large a scatter about the average tilt angle. However, $30 - 60$ kG flux tubes in the range of $10^{21} - 10^{22}$ Mx have a larger average tilt angle than is reported from observations. We also find that the most common tilt angle produced by our study is 10.1° for tubes with a flux of $10^{20} - 10^{22}$ Mx, which agrees well with analysis of solar active region observations performed by Howard (1996) and Stenflo and Kosovichev (2012), and simulation results from Nelson *et al.* (2013).

Observations show that sunspot groups tend to rotate faster than the surrounding solar surface plasma (Howard and Harvey 1970; Golub and Vaiana 1978). We investigate this in two ways, first by examining the asymmetry of inclination of rising flux tubes, and second by calculating the rotation rate of the centroid between both legs of the emerging magnetic flux loop. We find that the asymmetry of inclination does not vary systematically with latitude, nor does it depend on the magnetic field strength for magnetic flux of the tube when subjected to convective flows. On average, the asymmetry of inclination of all our flux tube simulations is such that the leading leg would appear to rotate forward faster than the following leg, mirroring the observed behavior of solar active regions. For tubes with a flux of 10^{21} Mx and 10^{22} Mx, we find that at high emergence latitudes, the average rotation rate of the emerging loops tends to be greater than the inferred surface rotation rate for

all field strengths considered. At lower latitudes, below about 35°, loops with initial field strength $\geq$60 kG tend to rotate faster than the inferred surface rate, consistent with the observed sunspot rotation rate, while loops with initial fields of about $40 - 50$ kG tend to rotate at a similar rate as the surface rate. However, for initial magnetic fields below 40 kG, the rotation rate at low latitudes tends to be slower than the surface rate, contrary to observations. Thus comparison with the observed sunspot rotation rate seem to favor stronger fields as the progenitor of solar active regions.

Similar to previous studies (Caligari, Moreno-Insertis, and Schüssler 1995; Fan and Fisher 1996), we find that for magnetic field strengths $\leq$50 kG, the leading leg of the emerging loop tends to have a larger magnetic field than the following, which may provide an explanation for the observed better cohesion of the leading polarity of an emerging active region as compared to the following polarity. This trend of asymmetry in field strength reverses for tubes with an initial magnetic field of $\geq$60 kG. However, it may be the case that the morphological asymmetry of sunspot regions is less dependent on magnetic field asymmetry, and is rather a result of the retrograde plasma flow inside the flux tube from the leading leg into the following leg, and therefore may not be a good diagnostic for constraining the magnetic field strength at which the solar dynamo may be operating. A study of the magnetic field of the flux tube at the top of the simulation domain suggests typical values of $\sim 1 - 15$ kG for tubes that reach $\sim$21 Mm below the photosphere.

The results in this Chapter suggest that the initial field strength of active region progenitor flux tubes needs to be sufficiently large, probably $\geq$30 kG, in order for them to satisfy the Joy's Law trend for mean tilt angles as well as the observed amount of scatter of the tilt angles about the mean Joy's Law behavior. Weaker magnetic fields tend to produce

too large a scatter to be consistent with the observed results. However, flux tubes of $\geq$80 kG and $10^{21} - 10^{22}$ Mx agree both with the observed Joy's Law trends, observed tilt angle scatter, and average observed tilt angle. Also, only 60 kG or greater magnetic field strength flux tubes can rotate at or faster than the solar surface rate. So, according to our thin flux tube approach, magnetic field values need to be of moderate to large field strengths for tubes with fluxes of 10^{21} Mx and 10^{22} Mx to produce sunspot rotation behavior.

Taking all of the results in this Chapter into consideration, according to the results of our thin flux tube simulations, we can exclude $\leq$15 kG magnetic field strength flux tubes as progenitors of solar active regions. It is likely that in order to achieve the appropriate rotation rate and average tilt angle as observed on the Sun, flux tubes of $\geq$60 kG are required. Additionally, it is clear that convective flows can alter local flux emergence properties, especially at weak to moderate magnetic field strengths, and should be considered as a significant contributing factor in the flux emergence process.

CHAPTER 5

A Theory on the Convective Origins of Active Longitudes on Solar-like Stars

Using a thin flux tube model in a rotating spherical shell of turbulent, solar-like convective flows, we find that the distribution of emerging flux tubes in our simulation is inhomogeneous in longitude, with properties similar to those of active longitudes on the Sun and other solar-like stars. The large-scale pattern of flux emergence our simulations produce exhibits preferred longitudinal modes of low order, drift with respect to a fixed reference system, and alignment across the Equator at low latitudes between $\pm 15°$. We suggest that these active-longitude-like emergence patterns are the result of columnar, rotationally aligned giant cells present in our convection simulation at low latitudes. If giant convecting cells exist in the bulk of the solar convection zone, this phenomenon, along with differential rotation, could in part provide an explanation for the behavior of active longitudes.

5.1. Introduction

For longer than half a century, it has been observed that solar active regions tend to emerge near the location of previous or currently existent magnetic flux (Bumba and Howard 1965; Gaizauskas *et al.* 1983; Castenmiller, Zwaan, and van der Zalm 1986; Brouwer and Zwaan 1990; Harvey and Zwaan 1993). Solar observations also show that the emergence of active features is distributed inhomogeneously in longitude according to sunspot activity, solar flares, and coronal streamers (Jetsu *et al.* 1997; Berdyugina and Usoskin 2003; Zhang, Wang, and Du 2008; Zhang *et al.* 2011; Olemskoy and Kitchatinov 2009; Li 2011). Periodic

signals have been observed in the solar wind and geomagnetic activity, which may also be attributed to an inhomogeneous longitudinal distribution of emerging magnetic flux on the solar surface (Mursula and Zieger 1996; Neugebauer *et al.* 2000; Love, Joshua Rigler, and Gibson 2012). These preferential longitudes of solar activity are commonly referred to as active longitudes, and have been observed on some cool, active stars and young solar analogs (Olah, Hall, and Henry 1991; Järvinen *et al.* 2005; Lanza *et al.* 2009; García-Alvarez *et al.* 2011).

The Sun typically has two active longitudes separated by 180° (Usoskin, Berdyugina, and Poutanen 2005; Zhang *et al.* 2011), although there may be upwards of four or more active longitudes per rotation near solar maximum, and even as few as one or none during solar minimum (de Toma, White, and Harvey 2000). Active longitudes are also fairly long-lived, with lifetimes of up to seven rotations (de Toma, White, and Harvey 2000), while Berdyugina and Usoskin (2003) suggest that active longitudes can persist longer than a century. Owing to the observed North/South asymmetry of solar activity cycles (Verma 1993; Temmer *et al.* 2006), the Northern and Southern hemispheres often exhibit different magnetic behavior, although it is not uncommon for both hemispheres to exhibit the same active longitude (Benevolenskaya *et al.* 1999; de Toma, White, and Harvey 2000). Furthermore, these bands of flux emergence migrate with respect to a rigidly rotating frame (Usoskin *et al.* 2007), and appear to propagate prograde near the Equator at a rate faster than the Carrington sidereal rate (Benevolenskaya *et al.* 1999).

The physical mechanisms which give rise to the active longitude phenomenon still remain relatively unknown, although there exist a few theories. Ruzmaikin (1998) suggests that the localization of a non-axisymmetric mean magnetic field at the base of the convection zone

can result in clustering of active regions at a particular longitude. A fluctuating magnetic field super-imposed on the non-axisymmetric mean field can experience an amplification of its field strength at the longitudinal position of the mean field enhancement. Subsequently, the magnetic flux loop will rise to the surface provided the field strength is large enough for the onset of the magnetic buoyancy instability. Non-axisymmetric toroidal magnetic fields that produce buoyant loops have recently been found in convective dynamo simulations by Nelson *et al.* (2011, 2013). Conversely, Dikpati and Gilman (2005) show that the toroidal mean magnetic field does not have to be enhanced at a particular longitudinal position in order for active regions to appear at preferred longitudes. Using a shallow-water model of the tachocline, they find that magnetohydrodynamic (MHD) instabilities can simultaneously produce tipping instabilities of the toroidal magnetic field bands and variations in the thickness of the tachocline material. A correlation between the tipped toroidal band and a bulge of the tachocline material can force magnetic fields in to the less dense layers of the convection zone, where they will continue to rise because they are more buoyant than the surrounding medium.

Simon and Weiss (1968) allude to the fact that large convecting cells ∼300,000 km in diameter may be responsible for what Bumba and Howard (1965) call *complexes of activity*, which are clusters of active regions compact spatially in latitude and longitude. These *giant cells* were posited by Simon and Weiss (1968) as an efficient mechanism of heat transport over multiple density scale heights. Their observational existence (e.g. Hathaway *et al.* 1996; Beck, Duvall, and Scherrer 1998) is supported by giant convecting cellular structures present in three-dimensional simulations of turbulent stellar convection, which align with the rotation axis at low latitudes, remain coherent for at least a rotation period or longer,

and propagate prograde near the equator (Miesch *et al.* 2008; Bessolaz and Brun 2011). However, many other attempts to detect giant cells on the Sun have failed (e.g. Labonte, Howard, and Gilman 1981; Snodgrass and Howard 1984; Chiang, Petro, and Foukal 1987), as their signature is difficult to extract from those of granulation ($\sim$1,000 km in diameter) and super-granulation ($\sim$30,000 km in diameter), upon which the giant cell signature may be super-imposed.

Using a thin flux tube model in a rotating spherical shell of turbulent, solar-like convective flows as described in Section 5.2, we find evidence which suggests that giant convecting cells (on the order of $\sim 50 - 100$ Mm in diameter) in the bulk of the solar convection zone can organize buoyantly rising flux tubes such that large-scale emergence patterns at or near the solar surface are formed. We describe how we extract large-scale flux emergence patterns from our simulations in Section 5.3, and properties of the resulting flux emergence patterns are presented in Section 5.4. In performing our analysis, we find that the large-scale flux emergence patterns exhibit some similarities to properties of active longitudes on the Sun. While the actual physical mechanism responsible for the active longitude phenomenon on the Sun and other stars is most likely a complex process involving contributions from multiple sources, we discuss in Section 5.5 how convection alone can organize flux emergence in a large-scale way.

5.2. Model Description

It is believed that magnetic flux emergence at the solar surface is the result of buoyantly rising magnetic flux tubes generated by a dynamo mechanism at or near the base of the convection zone (Spiegel and Weiss 1980; Gilman 2000; Charbonneau 2010). The thin flux tube model has been used by a number of authors to model how thin, isolated magnetic flux

tubes traverse the solar convection zone (see Chapter 2.1). As described in Chapter 2, we employ a thin flux tube model subject to a turbulent, time-dependent, solar-like convective velocity field to investigate longitudinal patterns of flux tube emergence. These simulations considered a range of flux tube magnetic field strengths from 15 kG (equipartition) to 100 kG (super-equipartition) (more specifically 15, 30, 40, 50, 60, and 100 kG), at latitudes ranging from 2° to 40° around the equator in both hemispheres, with magnetic flux values of 10^{20} Mx to 10^{22} Mx. This range of magnetic flux is typical of ephemeral regions and pores to the strongest sunspots (Zwaan 1987). We perform ten simulation sets sampling different time ranges of the convective flow field for each initial latitude, field strength, and magnetic flux we consider, for a total of 8640 flux tubes. Each set of flux tubes are released at the base of the convection zone at the same starting time, although do not interact with each other (i.e. are isolated), and are allowed to evolve until some portion of the tube reaches the top of the simulation domain. The flux tube release times for the ten sets are arbitrary, but are at least separated by the convective turnover time scale of the convection simulation, which is ∼30 days. In this way, the flux tubes are able to sample significantly different portions of the convective velocity field.

The thin flux tube model we use and the associated equations which describe the evolution of the flux tube have been described in detail in Chapter 2.1. The three-dimensional global convection simulation in which the flux tube evolves is computed separately from the thin flux tube simulation using the Anelastic Spherical Harmonic (ASH) code, as described by Miesch, Brun, and Toomre (2006). This time-dependent convective velocity field, which is computed relative to the rotating frame of reference with angular velocity $\Omega_0 = 2.7 \times 10^{-6}$ rad s^{-1} , impacts the thin flux tube through its drag force term. In the anelastic approximation,

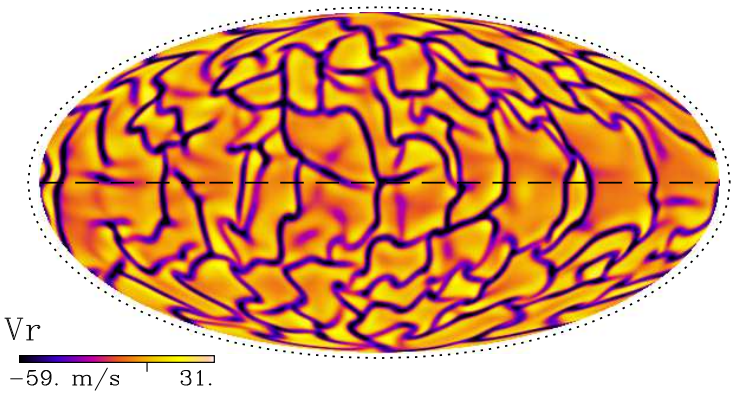

FIGURE 5.1. Snapshot of convective radial velocity at a depth of 23 Mm below the solar surface ($r = 0.97R_\odot$) in a Mollweide projection. This figure shows strong downflow lanes (purple/blue) at the boundary of giant convective cells. Also known as banana cells, the structures at low latitudes are rotationally aligned and propagate prograde. The dotted line is the solar radius $r = R_\odot$. The radial velocity approaches zero at the upper boundary of the simulation, so the velocity amplitudes shown in this figure are lower than in the middle convection zone.

the velocity of convective flows is taken to be much slower than the speed of sound in the fluid, and convective flows and thermal variations are treated as a linear perturbation to a background state taken from a one-dimensional solar structure model. The computed convective velocity field captures giant-cell convection, and associated mean flows such as meridional circulation and differential rotation, in a rotating convective envelope spanning $r = 0.69R_\odot$ to $r = 0.97R_\odot$ (4.8×10^{10} cm to 6.75×10^{10} cm from Sun center). For a more detailed description of this particular convection simulation, see Chapter 2.2.

A typical giant-cell convection pattern at a depth of 25 Mm below the solar surface is shown in Figure 5.1. Broad upflow cells are surrounded by narrow downflow lanes, which can reach maximum downflow speeds of nearly 600 m s^{-1} at a mid-convection zone depth of ~86 Mm below the surface. Columnar, elongated downflow lanes associated with these giant cells align preferentially with the rotation axis at low latitudes, and propagate in a prograde

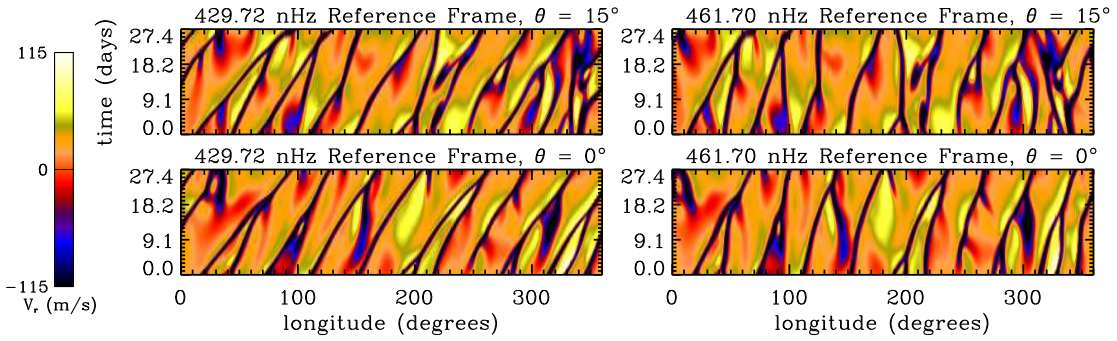

FIGURE 5.2. Radial velocity at the Equator (bottom) and 15° latitude (top) plotted as a function of longitude and time (i.e. (ϕ,t) diagrams), at a depth of $r = 0.95R_\odot$ for a 27.4 day period in the reference frame rotating at angular velocity $\Omega_0/2\pi$ (429.72 nHz, left), and in the faster ASH equivalent Carrington frame $\Omega_{AC}/2\pi$ (461.70 nHz, right). In the $\Omega_0/2\pi$ reference frame, the rightward tilt of the dark blue downflow lanes indicates a prograde propagation of the downflow lanes at low latitudes within ±15° latitude of the Equator, although their rate of prograde propagation decreases as the latitude increases. In the faster rotating reference frame $\Omega_{AC}/2\pi$, downflow lanes still propagate prograde near the Equator, but at a slower relative rate than in the $\Omega_0/2\pi$ reference frame. At higher latitudes in the $\Omega_{AC}/2\pi$ reference frame, some downflow lanes no longer appear to propagate prograde, remaining almost stationary or moving retrograde.

direction relative to the polar regions, due in part to differential rotation and an intrinsic phase drift similar to traveling Rossby waves (Miesch and Toomre 2009). Such structures also can remain coherent for at least a rotation period or longer. The prograde propagation and coherency of the giant-cell-associated downflows is exhibited in the (ϕ,t) diagrams of Figure 5.2. This Figure shows a strip of radial velocity at the Equator (bottom) and 15° (top) for ∼27 consecutive days, or about one rotation period. In Figure 5.2, the (ϕ,t) diagrams are also shown in two different rotating reference systems, with the two panels on the left shown in the reference frame co-rotating with the mean angular velocity $\Omega_0/2\pi = 429.72$ nHz of our simulation, and the two panels on the right in the reference frame rotating at a faster rate of $\Omega_{AC}/2\pi = 461.70$ nHz. These features dominate the convective Reynolds stress, aiding in the maintenance of a strong differential rotation. The total angular velocity $\Omega/2\pi$ (with

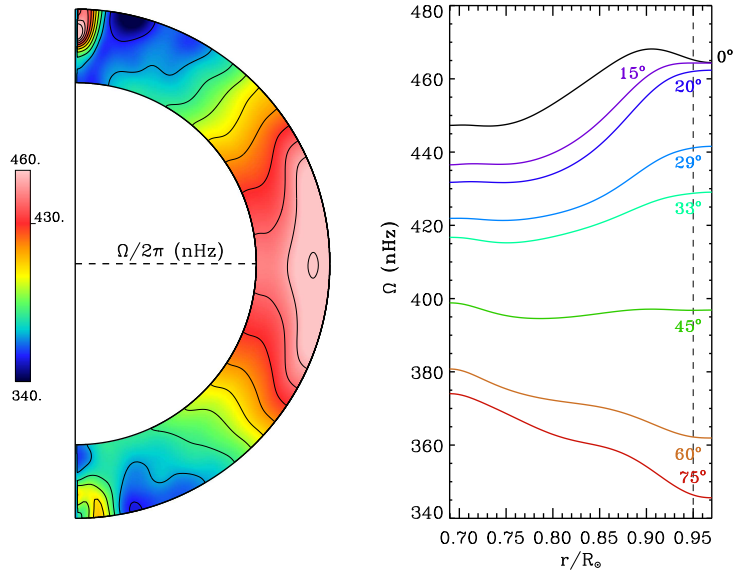

FIGURE 5.3. (Left) Angular velocity in the convection simulation, averaged over longitude and time (time interval of 755 days). Color table saturates at the values indicated, with extrema ranging from $326 - 468$ nHz. (Right) Angular velocity of the convection simulation at specific latitudes as a function of radius. At $0.95R_\odot$, the angular velocity $\Omega/2\pi$ is 461.70 nHz at 20° latitude, 440.64 nHz at 29°, and 429.72 nHz at 33° latitude.

respect to the inertial frame) is solar-like, and decreases monotonically from ∼470 nHz at the equator to ∼330 nHz at the poles, and exhibits nearly conical contours at mid-latitudes (see Figure 5.3), as observed in the solar convection zone via helioseismic inversions (Thompson *et al.* 2003).

A spectral decomposition of the velocity variance in terms of azimuthal (longitudinal) wavenumbers demonstrates the distribution of contributing convective modes in the ASH simulation. This is shown in Figure 5.4 for three radial levels in the convection zone, only at the Equator. Peaks in the spectra at $m = 0$ for the curves in Figure 5.4 are primarily caused by differential rotation, with a small contribution from the meridional circulation. Other prominent peaks in the spectra in the upper convection zone at $r = 0.95R_\odot$ are found at azimuthal wavenumbers of 6, 8 and 9. This reflects the nature of the elongated, periodic,

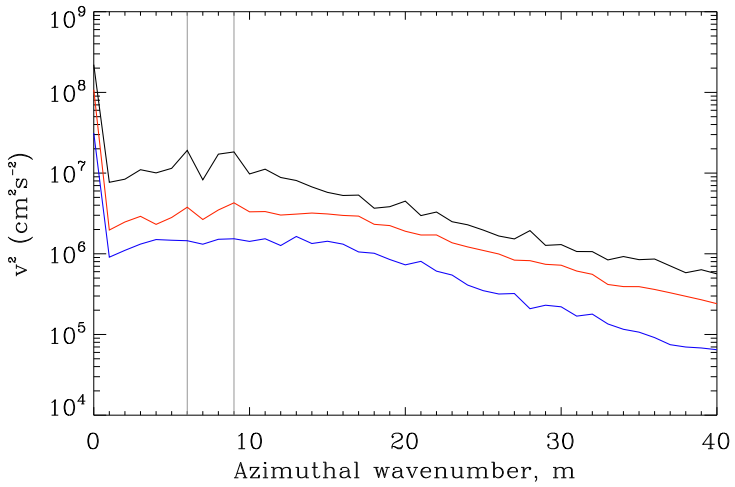

FIGURE 5.4. Spectral decomposition of the velocity variance of the ASH convection simulation in terms of azimuthal (longitudinal) wavenumbers, computed at the Equator for three shells of radii: $0.95R_\odot$ (black), $0.83R_\odot$ (red), and $0.73R_\odot$ (blue). All curves are averaged over the Northern and Southern hemisphere for a time interval of 19 rotation periods (26.93 days each). Prominent peaks in the spectra at wavenumbers of $m = 6$ and $m = 9$, corresponding to the gray vertical lines, are representative of the periodic banana-like convective cells present in the simulation.

banana-like downflow structures obvious in Figure 5.1. Signatures of these banana cells are also evident near the Equator in the mid-convection zone at $r = 0.83R_\odot$.

While this ASH simulation, with a mid-convection zone Raleigh number of 5×10^6 and Reynolds number of $\sim$50, is more laminar than some others (e.g. Miesch *et al.* 2008; Jouve and Brun 2009), it still possesses all of the relevant features necessary to explore the fundamental interactions between thin flux tubes and the mean flows associated with global convection. These features include: asymmetric, rotationally aligned cells at low latitudes (density-stratified banana cells), rapidly-evolving downflows in the upper convection zone at high latitudes dominated by helical plumes, and a strong, solar-like differential rotation. We believe that large-scale, columnar banana cells must persist even in highly turbulent parameter regimes in order to provide the requisite Reynolds stresses to account for the

solar differential rotation. Therefore, we would not expect the essential results to change significantly with more turbulent convection.

The coupling of the thin flux tube model with the ASH convection simulation results in a large-scale longitudinal emergence pattern of the flux tubes at low latitudes, to which we devote the rest of this Chapter.

5.3. Extracting Large-Scale Flux Emergence Patterns from Simulations

Convective downflows and the growth of the magnetic buoyancy instability anchor portions of the flux tube in the overshoot region, allowing buoyant loops to rise through the simulation domain (see Chapter 3). When these simulated flux tubes emerge near the surface, we find that they do not emerge randomly during a rotation period, but rather in distinct longitudinal bands or clusters as depicted in Figure 5.5. For this Chapter, we choose only to investigate flux tube emergence patterns $\pm 15^\circ$ around the equator, so as to focus on the low latitude behavior of these longitudinal bands of flux emergence. In Figure 5.5, we note that there are wide longitudinal regions void of any flux emergence, and particular longitudinal spans where flux emergence prefers to cluster.

To more quantitatively investigate the longitudinal flux emergence distribution pattern our simulation produces, we create *emergence histograms* wherein we count the number of flux tubes that emerge within one of 180 evenly distributed longitudinal bins during a particular rotation period. We only count the first portion of each tube that reaches the simulation upper boundary, therefore we count each flux tube only once. This is done separately for the Northern and Southern hemispheres for each of the 19 consecutive rotation periods considered for this study, only for flux emergence within $\pm 15^\circ$ of the Equator. These histograms are shown in Figure 5.6 for the reference frame rotating at angular velocity $\Omega_0/2\pi$.

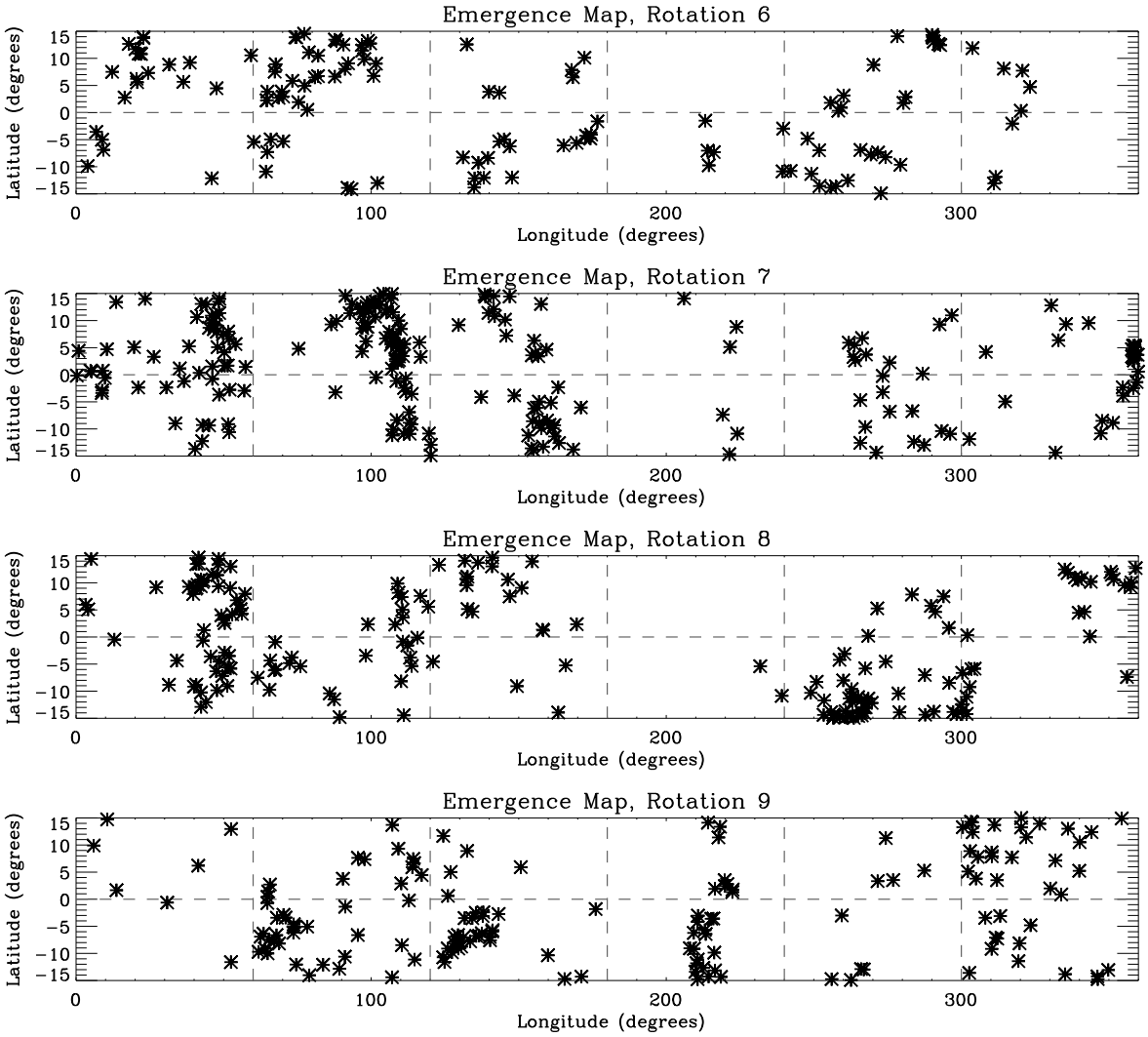

FIGURE 5.5. Emergence maps for 4 consecutive rotation periods in the reference frame rotating at angular velocity $\Omega_0/2\pi$. The latitudinal (θ) and longitudinal (ϕ) position of the flux tube apex is plotted for all flux tubes which reach the top of our simulation domain within one rotation period of each other, $\pm 15^\circ$ from the Equator. This figure indicates that our simulation produces flux tubes which emerge neither randomly nor uniformly.

The choice of 180 bins of each 2° in longitude is a rather arbitrary one. We have chosen to use small longitudinal bins in order to more accurately capture the drift rate of the flux emergence patterns as discussed in Section 5.4.2.

In Figures 5.5 and 5.6, we have used $\Omega_0/2\pi = 429.72$ nHz as the angular velocity of the rotating reference frame, with a rotation period of 26.93 days. This corresponds to

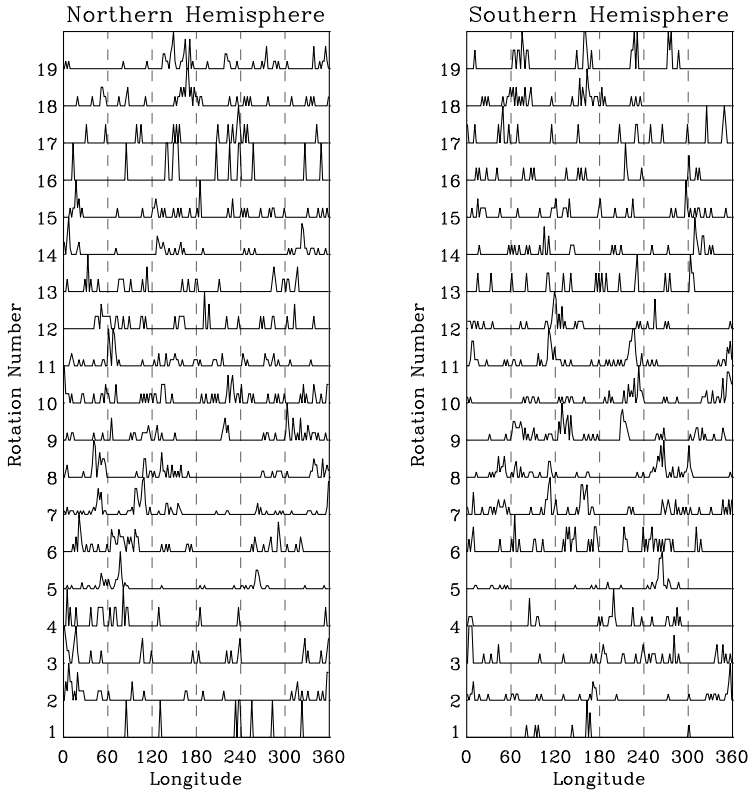

FIGURE 5.6. Normalized histograms of flux tube apex longitudinal position (emergence histograms) once some portion of the flux tube has reach the top of our simulation domain. For one rotation period of our simulation, we count the number of flux tubes which emerge within 1 of 180 evenly distributed bins in longitude. In this Figure, longitudinal coordinates are with respect to a reference frame rotating at the angular velocity $\Omega_0/2\pi$. This is done for the Northern (left) and Southern (right) hemispheres for flux tubes that emerge within $\pm 15^\circ$ of the equator for 19 consecutive rotations.

the angular velocity of fluid flows in the ASH simulation at latitude $\theta = 33^\circ$ and radius $r = 0.95 R_\odot$. However, when investigating active longitude behavior on the Sun, the sidereal Carrington rotation rate of 456.03 nHz (25.38 days) is often used as the rotating frame of reference, because active longitudes drift relative to this reference frame. This rotation rate corresponds to the rotation of sunspots at $\sim 20^\circ$ latitude on the solar surface (Thompson *et al.* 2003). The observed rotation rate of sunspots at all emergence latitudes also closely follows the plasma rotation rate of the Sun at a depth of $r = 0.95 R_\odot$ for the same latitude

(see Fig. 1.4). Therefore, we identify what we call the *ASH equivalent Carrington rate* as the rotation rate of the convection simulation at latitude $\theta = 20^\circ$ and radius $r = 0.95R_\odot$, which is $\Omega_{AC}/2\pi = 461.72$ nHz (25.07 days). We also identify a third reference frame that rotates at the average drift rate of the flux emergence patterns, which we identify and discuss in section 5.4.2. (See the right side of Figure 5.3 for the angular velocity profile of the convection simulation at specified latitudes.) In order to generate emergence histograms in the two reference frames which do not rotate at angular velocity $\Omega_0/2\pi$, we translate the flux emergence longitude coordinates in to the new reference frame, using the new rotation periods to identify 19 consecutive rotations that all start at the same reference time. We utilize these histograms in Section 5.4 to characterize the large-scale pattern of flux emergence generated by our simulations.

Our study is limited to only 19 rotation periods due to the duration of the three-dimensional volume cube data set of our convection simulation, as well as the rise times of our flux tubes. It is important to note that the methods used in the context of this thesis do not produce a solar cycle dynamo simulation. This model allows us to investigate how convection can alter the rise of many magnetic flux tubes with various initial conditions. As such, this simulation will not allow us to investigate changes which occur in flux emergence during the course of a solar cycle. Due to this, our simulation is not capable of producing the solar butterfly diagram, and we will often have more flux tubes which emerge at the top of our simulation domain than may actually emerge on the solar surface during a rotation period.

Throughout the Results section, we adopt a 99.7% confidence level to indicate the significance of our results. When our analysis reveals results above this value, we are 99.7%

confident the results of our simulation are not due to a random (non-uniform) distribution of flux tube emergence. For each rotation period and hemisphere, a certain number of flux tubes N emerge within 15° of the Equator. We then create a corresponding array of N elements, representing flux tubes which have random longitudinal emergence positions from 0° to 360°. These arrays representing random longitudinal flux tube emergence are then subjected to the same treatment throughout the Results section as the longitudinal emergence positions for flux tubes allowed to evolve in convection. Rather than directly plotting the results from the random emergence position arrays, we compute the standard deviation σ of the result as well as the average X, then plot $X + 3\sigma$ as our 99.7% confidence level. See Appendix H for a more detailed discussion on the determination of confidence levels.

5.4. Active-longitude-like Behavior of Flux Emergence Pattern

5.4.1. Longitudinal Inhomogeneity of Emerging Flux Loops.

A distinct longitudinal pattern of magnetic activity is observed on the Sun not only in terms of sunspot activity (de Toma, White, and Harvey 2000; Berdyugina and Usoskin 2003), but also in solar x-ray flares (Zhang *et al.* 2011) and coronal streamers (Li 2011). Interestingly, this phenomena is not unique to the Sun, and has been observed on other young solar analogues such as AB Dor (K0V) (Järvinen *et al.* 2005) and LQ Hydrae (K2V) (Berdyugina, Pelt, and Tuominen 2002). To capture the longitudinal inhomogeneity of flux tube emergence in our simulations, we calculate the variability coefficient V for each rotation period and hemisphere based on Olemskoy and Kitchatinov (2009). We begin by identifying the quantity S_i, which is the longitudinal distribution of relative flux tube emergence over each of nine

evenly spaced bins in longitude per a particular rotation period:

$$S_i = \frac{9n_i}{N}, \tag{5.1}$$

where n_i is the number of events in a certain longitudinal interval, and N is the total number of events. Values of $S_i = 1$ for each of the nine bins per rotation period implies a homogeneous distribution of flux tube emergence. We consider only the longitudinal position of the flux tube apex once it has reached the top of our simulation domain. Next the variability coefficient is computed, which is the sum of absolute deviations of S_i from the average value of unity:

$$V = \sum_{i=1}^{9} |S_i - 1|. \tag{5.2}$$

The calculated variability coefficient ranges from zero to 16, with the minimum value typical of a homogenous distribution of events in the longitudinal intervals, and the maximum value typical of all events falling in one longitudinal interval. The longitudinal variability in the Northern and Southern hemispheres for each of 19 rotation periods in the reference frame which rotates at the angular velocity $\Omega_0/2\pi$ is shown in Figure 5.7. The dotted line represents the 99.7% (3σ) confidence level, above which we are 99.7% positive the variability is not the result of a longitudinally random (non-uniform) distribution of flux tube emergence. All of the variability coefficients lie above this line, with the exception of rotation 6 for the Southern hemisphere. As expected, most rotation periods exhibit a variability coefficient above the 99.7% confidence level regardless of the choice of reference frame. Therefore, we can reasonably say that the distribution of flux tube emergence in our simulation is not uniform or random in longitude for the majority of the rotation periods we consider.

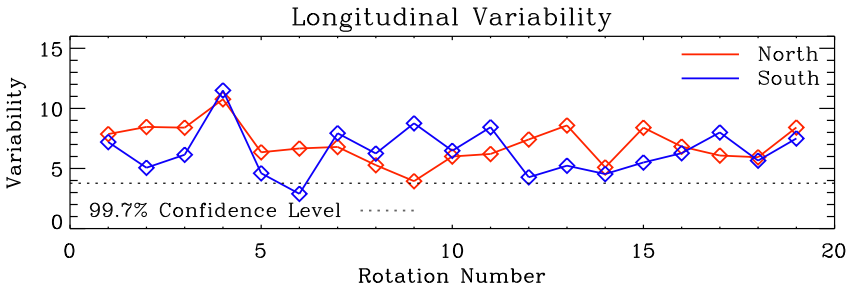

FIGURE 5.7. Longitudinal variability per rotation period for each hemisphere in reference frame rotating at the angular velocity $\Omega_0/2\pi$ of the simulation. The dotted line is the level above which we are 99.7% sure the result is not due to a random longitudinal distribution of flux tube emergence. For the same rotation period, the longitudinal variability can vary significantly for each hemisphere.

The above analysis shows that more flux tubes may emerge per a certain longitudinal span for each hemisphere, i.e. there is a significant non-random clustering of flux tube emergence. On the Sun, there are typically two active longitudes separated by 180° (Usoskin, Berdyugina, and Poutanen 2005; Zhang *et al.* 2011), although this number may increase to as many as four or more near solar maximum (de Toma, White, and Harvey 2000). In order to identify whether or not our simulation produces flux tubes which emerge with a preferred longitudinal mode, we perform a power spectrum analysis for each of the emergence histograms in Figure 5.6. We then take the average of these power spectra for both the Northern and Southern hemispheres separately in order to identify an overall trend for the 19 rotation periods we consider, which is shown in Figure 5.8 in the reference frame rotating at $\Omega_0/2\pi$.

While we identify relative maxima of the power spectra in the $\Omega_0/2\pi$ reference frame at low spatial frequencies, corresponding to a low order number of longitudinal modes, we need to compare these results to a random distribution in longitude of flux tube emergence to assess the significance of these maxima. The dash-dotted line in Figure 5.8 represents the level above which we are 99.7% positive the result of the averaged power spectrum is

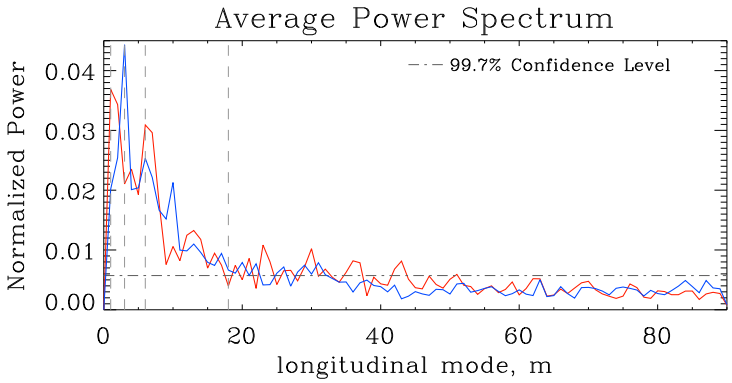

FIGURE 5.8. Average power spectrum for the Northern (red) and Southern (blue) hemispheres for 19 rotation periods in the reference frame rotating at $\Omega_0/2\pi$, considering all magnetic field strengths and magnetic flux. The power spectrum peaks for a longitudinal mode of $m = 1$ in the Northern hemisphere, and $m = 3$ in the Southern hemisphere, shown by dashed lines. In addition, the $m = 6$ and $m = 18$ modes are also shown. The dash-dotted line is the level above which we are 99.7% certain the result is not due to a random distribution of emerging flux tubes in longitude. The nature of our convection simulation results in flux emergence at preferred longitudinal modes.

not due to a longitudinally random distribution of emerging flux tubes. The averaged power spectra for both hemispheres is above the 99.7% confidence level for spatial frequencies of 0.05 deg^{-1} and less. This spatial frequency corresponds to a longitudinal mode of $m = 18$, indicating that lower order modes ($m \leq 18$) are the significant modes present in the flux tube emergence patterns.

Dominant peaks in the averaged power spectra occur at longitudinal modes of $m = 1$ for the Northern hemisphere, and $m = 3$ for the Southern hemisphere. This corresponds to one active longitude in the Northern hemisphere, and three in the Southern hemisphere on average for a particular rotation period. The different dominant modes in the power spectra for both hemispheres reflect the fact that the convection pattern is not perfectly symmetric across the Equator on a short time scale. Additionally, the power spectra of the convection simulation does not show significant power in any mode below $m = 6$ (see Fig. 5.4). It is

likely that there are substantial differences between the Northern and Southern hemisphere convection at these modes. However, both the Northern and Southern hemispheres do have corresponding relative maxima at $m = 6$. This is most likely related to the $m = 6$ peak in the power spectra of the convection simulation shown in Fig. 5.4 at $r = 0.95R_{\odot}$, indicating that in the upper convection zone, on average six strong, periodic downflow lanes exist. Using SOHO MDI data, Norton and Gilman (2005) find that longitudinal modes of $m = 2$ and $m = 6$ are simultaneously present with the $m = 1$ mode in observed toroidal bands of magnetic flux emergence.

Considering the conclusions of Chapter 4, we suggest that the most likely candidate magnetic field strengths for solar dynamo generated flux tubes is on the order of $\geq$40 kG, but most likely not exceeding $\sim$100 kG. With this in mind, if we perform the power spectrum analysis considering only $40 - 100$ kG flux tubes, peaks in the power spectra remain at the same longitudinal mode as the case where we consider all magnetic field strengths together. Maximum peaks in the power spectra also remain the same regardless of the choice of reference frame.

In the absence of convection, flux tubes will emerge randomly distributed in longitude if they are perturbed with random undular motions to initiate a buoyancy instability. Therefore, these flux tubes will not rise to create flux emergence patterns with preferred longitudinal modes. The fact that the flux emergence patterns our simulation produces exhibits low order longitudinal modes suggests that the convective velocity field aides flux tubes in emerging in preferred longitudinal spans, specifically a result of the discrete azimuthal modes of convection, corresponding to strong downflow lanes. Additionally, both hemispheres do not exhibit the same dominant mode in the power spectrum, indicating that the large-scale

nature of the convection simulation is not identical in both hemispheres, nor would we expect it to be on the Sun.

For each rising flux tube, only the longitude of the first rising loop that reaches the simulation upper boundary is included in the analysis. It is perhaps possible that the 180° separation of active longitudes on the Sun is in part a result of a non-axisymmetric $m = 2$ mode which a flux tube of large magnetic field strength ($\sim 60 - 100$ kG) may develop due to the non-linear growth of the magnetic buoyancy instability (see Chapter 3), which we do not investigate here. In any case, our simulation suggests that convective flows have some part to play in the preferred modes of active longitude organization.

5.4.2. Propagation of Flux Emergence Patterns. While the exact rotation velocity of active longitudes on the Sun is still being debated, along with the methods used to determine this value, the general consensus is that active longitudes drift prograde relative to Carrington longitudes (e.g. Benevolenskaya *et al.* 1999; Usoskin *et al.* 2007; Plyusnina 2010). To identify the drift rate of our longitudinal flux emergence patterns, we cross-correlate the emergence histograms of consecutive rotation periods for both the Northern and Southern hemispheres. We average these cross-correlations for each hemisphere separately in order to identify an overall trend, as shown below in equation form for the Northern hemisphere:

$$CC_{Nh} = \frac{1}{18} \sum_{i=1}^{18} (Nh_i \star Nh_{i+1}) \tag{5.3}$$

where the symbol $\star$ represents the cross-correlation, and Nh_i (Sh_i) represents the ith emergence histogram for the Northern (Southern) hemisphere in a particular rotating reference frame. Next we apply a 3-point running average to smooth the curve, then fit the curve with a Gaussian function to identify where a significant lead/lag occurs. Such cross-correlations

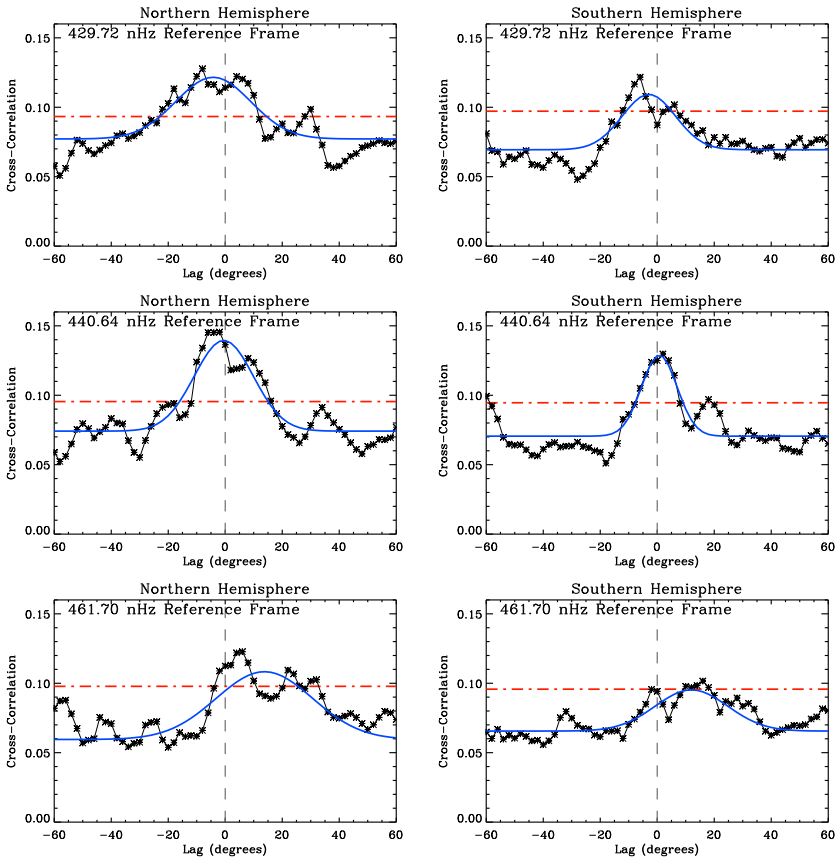

FIGURE 5.9. Average cross-correlations of emergence histograms for the Northern (CC_{Nh}, left column) and Southern (CC_{Sh}, right column) hemispheres between consecutive rotation periods. This has been done for three different rotating reference frames. A Gaussian fit (blue line) to the maximum of the cross-correlation curves peak at or above the 99.7% confidence level (3σ, red dash-dotted line), above which we are 99.7% certain the result is not due to a random distribution of flux tube emergence. These curves indicate that the flux emergence pattern propagates at a steady rate and remains coherent between consecutive rotation periods. Depending on the choice of rotating reference frame, the flux emergence pattern appears to drift prograde (top panels), retrograde (bottom panels), or remain stationary (middle panels). The values of these drift rates are quoted in columns 2 and 3 of Table 5.1.

are shown in Figure 5.9 using three different rotating reference frames. Values for the centers of the Gaussian fits in various reference frames are shown in Table 5.1 for both the Northern and Southern hemispheres in columns 2 and 3, respectively.

In the reference frame rotating with angular velocity $\Omega_0/2\pi$, the Gaussian fit to the cross-correlation curves produce centers at small negative spatial lags. These results indicate that

TABLE 5.1. Centers of the Gaussian fit to the average of the cross-correlations for 19 consecutive rotation periods are shown in columns 2 (CC_{Nh}) and 3 (CC_{Sh}). In columns 4 and 5, the cross-correlations for the Northern and Southern hemispheres are averaged together (CC_{Avg}) for different magnetic field strength regimes. Uncertainties are the standard deviation of the Gaussian function. This is shown for three different reference frames rotating at angular velocities given in column 1. Negative values imply prograde propagation, and positive values imply retrograde propagation.

Angular Velocity $\Omega/2\pi$ (nHz)	North 15 kG - 100 kG	South 15 kG - 100 kG	Avg N/S 15 kG - 100 kG	Avg N/S 40 kG - 100 kG
$\Omega_0/2\pi$, 429.72	$-4.2^\circ \pm 3.6^\circ$	$-2.9^\circ \pm 3.1^\circ$	$-2.9^\circ \pm 3.3^\circ$	$-9.0^\circ \pm 3.2^\circ$
$\Omega_{AL}/2\pi$, 440.64	$-0.5^\circ \pm 3.2^\circ$	$0.7^\circ \pm 2.4^\circ$	$0.6^\circ \pm 3.0^\circ$	$-1.0^\circ \pm 3.1^\circ$
$\Omega_{AC}/2\pi$, 461.70	$13.7^\circ \pm 4.1^\circ$	$12.0^\circ \pm 3.6^\circ$	$13.0^\circ \pm 3.7^\circ$	$10.6^\circ \pm 3.7^\circ$

the longitudinal flux emergence pattern in the $\Omega_0/2\pi$ reference frame propagate prograde at an average rate per rotation period of 4.2° in the Northern hemisphere, and 2.9° in the Southern hemisphere. As this reference frame rotates at $\Omega_0/2\pi$, it is most likely the case that differential rotation present in the convection simulation helps to move the rising flux tube legs slightly prograde. The prograde motion of the individual tubes contributes to a large-scale prograde drift of the flux emergence pattern between consecutive rotation periods. In Chapter 4 we find that with the addition of a time-varying convective velocity field, most flux tubes that emerge within ±15° of the Equator rotate faster than the angular velocity $\Omega_0/2\pi$ of the simulation. Although the large-scale flux emergence pattern in the reference frame rotating at $\Omega_0/2\pi$ does propagate prograde in each hemisphere, the pattern still rotates slower than the differentially rotating fluid in our convection simulation at a radius of $0.97R_\odot$ (simulation upper boundary), between latitudes of ±15°.

Since the propagation rate of flux emergence patterns in the reference frame rotating at $\Omega_0/2\pi$ is only slightly prograde by a few degrees, it stands to reason that this flux emergence pattern will appear to propagate retrograde in a more rapidly rotating reference frame. In the reference frame rotating at the ASH equivalent Carrington rate of $\Omega_{AC}/2\pi = 461.70$ nHz,

we find that the flux emergence pattern drifts retrograde by 13.7° per rotation period in the Northern hemisphere, and 12.0° in the Southern hemisphere between consecutive rotations. Although this rotation is not prograde, as is most often the case for active longitudues on the Sun in the Carrington frame, these results show that the flux emergence patterns our simulation produces remain coherent for at least consecutive rotation periods in all reference frames. Therefore, it is possible to identify a reference frame in which the flux emergence pattern appears to remain stationary. We find the angular velocity of this reference frame to be $\Omega_{AL}/2\pi = 440.64$ nHz, which corresponds to the ASH rotation rate at a depth of $r = 0.95R_{\odot}$ and latitude $\theta = 29°$. In finding this reference frame, we have also pinpointed the average drift rate of our flux emergence pattern. It is important to note that the perceived prograde or retrograde drift rate of the flux emergence pattern depends on the details of the global differential rotation profile and the choice of reference frame, which are somewhat different in this ASH simulation relative to the Sun.

In the above analysis, we have included flux tubes of magnetic field strengths from $15 - 100$ kG. However, taking the results of Chapters 3 and 4 into consideration, we suggest that the solar dynamo generated magnetic field strength is most likely between $40 - 100$ kG. In Figure 5.10, we show the average of all the cross-correlations between consecutive rotation periods in both the Northern and Southern hemispheres together, in three different reference frames for flux tubes of $15 - 100$ kG (left), and $40 - 100$ kG (right). We have averaged the cross-correlations for the Northern and Southern hemispheres together ($CC_{Avg} = (CC_{Nh} + CC_{Sh})/2$) in order to identify whether or not the drift rate of the flux emergence pattern changes for flux tubes of larger magnetic field strengths. Since the difference between the centers of the Gaussian fits for the Northern and Southern hemispheres for

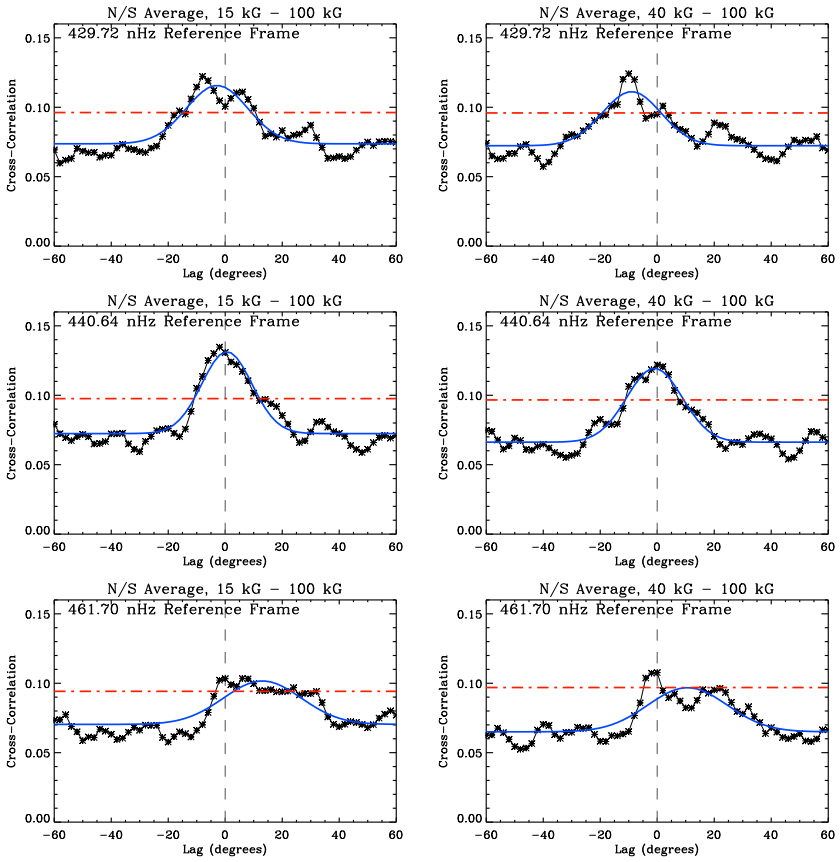

FIGURE 5.10. Similar to Fig. 5.9, but for the Northern and Southern hemispheres averaged together (CC_{Avg}), with the left column representing initial magnetic field strength of $15-100$ kG, and the right column for $40-100$ kG flux tubes. The values of these drift rates are quoted in columns 4 and 5 of Table 5.1. The center of the Gaussian fit is shifted prograde when flux tubes of $40-100$ kG are considered.

each reference frame are not statistically significant, we feel it is valid to average the Northern and Southern hemisphere cross-correlation curves together for comparison between the magnetic field strength regimes.

Values for the centers of the Gaussian fits to the average cross-correlation curves CC_{Avg} are shown in columns 4 and 5 of Table 5.1. In the slowly rotating $\Omega_0/2\pi$ reference frame, the flux emergence pattern for $40-100$ kG flux tubes drifts prograde in longitude an additional 6.1° per rotation period compared to the flux emergence pattern of $15-100$ kG flux tubes. In the much faster ASH equivalent Carrington frame, $\Omega_{AC}/2\pi$, the flux emergence pattern

for $40-100$ kG flux tubes still rotates retrograde, but at a rate of only 10.6° per rotation period compared to the 13.0° for flux tubes of all magnetic field strengths. This indicates that for $40-100$ kG , the flux emergence pattern in the $\Omega_{AC}/2\pi$ frame moves forward in longitude faster than the $15-100$ kG flux tube emergence pattern. In Chapter 4, we find that $\geq$60 kG flux tubes are capable of rotating at, or faster than, the inferred surface rate of our convection simulation at low latitudes of $\pm 15^\circ$. The faster prograde motion of $40-100$ kG individual flux tubes contributed to a flux emergence pattern which rotates prograde in longitude compared to the $15-100$ kG case. In the $\Omega_{AL}/2\pi$ reference frame, the flux emergence pattern still remains relatively stationary for $40-100$ kG flux tubes. However, Gaussian fits to the cross-correlation curves are rather broad, resulting in uncertainties which renders the difference in flux emergence drift rates between $15-100$ kG flux tubes and $40-100$ kG flux tubes statistically insignificant.

Our simulation produces a flux emergence pattern which rotates forward in longitude with respect to the reference frame rotating at $\Omega_0/2\pi = 429.72$ nHz. However, we do acknowledge that this pattern does not move prograde between consecutive rotation periods in the ASH equivalent Carrington frame $\Omega_{AC}/2\pi = 461.72$ nHz, unlike active longitudes do on the Sun relative to the Carrington frame. We attribute this to the fact that while the differential rotation of the convection simulation is very solar-like, it does not reproduce exactly the solar differential rotation profile. Additionally, as found in Chapter 4, simulated flux tubes of $\leq$50 kG are not capable of rotating at, or faster than, the sunspot rotation rate. The thin flux tube approximation breaks down near the top of the convection zone, so we cannot address the fact that the flux tube could lose its coherency and become fragmented in the upper convection zone. It is possible that in these upper layers, the fragmented flux tube

exhibits a stronger coupling to the convective fluid motions than is capable in this model, and could be a significant contributing factor to the rotation rate of flux tubes and their subsequent large-scale flux emergence pattern.

5.4.3. Alignment of Flux Emergence Patterns Across the Equator. Occasionally an active zone is found on the Sun at the same longitude in both hemispheres (Benevolenskaya *et al.* 1999; de Toma, White, and Harvey 2000). A more recent example of this behavior on the Sun is shown in Figure 5.11. Although the longitudes may be the same, the activity level of active longitudes in either hemisphere can vary greatly. To identify the overall alignment trend of flux emergence in our simulation for a rotation period, we cross-correlate the emergence histograms of the Northern and Southern hemispheres for the same rotation period, then compute the average as follows:

$$CC_{NS} = \frac{1}{19}\sum_{i=1}^{19}(Nh_i \star Sh_i) \tag{5.4}$$

In this way, common alignment trends will be amplified, and uncommon trends will be smeared out. A 3-point running average is applied to smooth the cross-correlation result. We then perform a Gaussian fit to the maximum, with the result of the fits for the three different reference frames in the $15 - 100$ kG and $40 - 100$ kG magnetic field strength regimes shown in Table 5.2. In all reference frames, the flux emergence patterns align very well across the Equator, regardless of magnetic field strength or rotation period. These results are significant to the 99.7% confidence level.

All flux tubes in this simulation are perturbed with the exact same undular motions. Although these perturbations are no longer needed because those provided by the convective

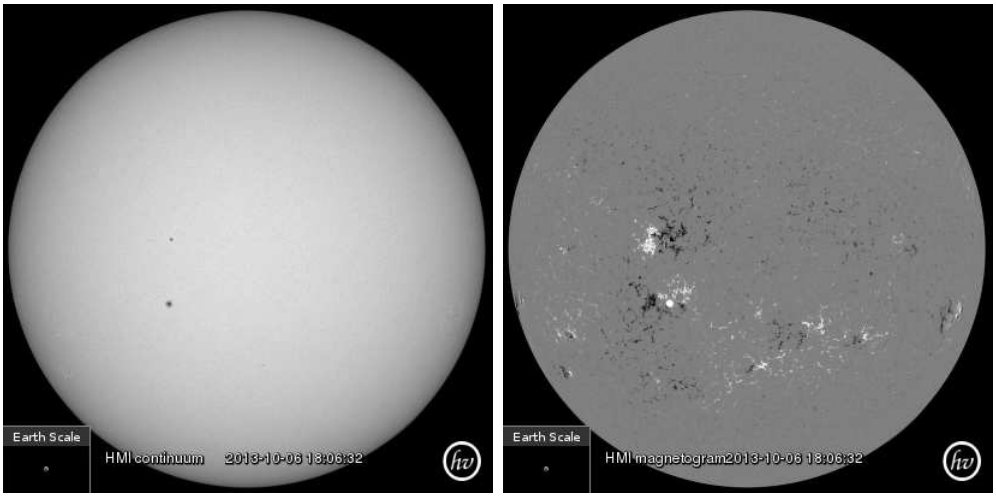

FIGURE 5.11. SDO HMI continuum (left), and SDO HMI magnetogram (right) of the solar disk on October 6, 2013. Two active regions are aligned across the solar equator. Images generated using Helioviewer.org.

TABLE 5.2. Centers of the Gaussian fit for cross-correlations of emergence histograms of the average of the Northern and Southern hemispheres for the same rotation period (CC_{NS}). Uncertainties are the standard deviation of the Gaussian function. These are shown for three different reference frames rotating at angular velocities given in column 1. In all reference frames, the flux emergence patterns align well across the Equator, regardless of magnetic field strength or rotation period. These results are significant to the 99.7% confidence level.

$\Omega/2\pi$ (nHz)	15 kG - 100 kG	40 kG - 100 kG
$\Omega_0/2\pi$, 429.72	$1.1^\circ \pm 2.7^\circ$	$-1.5^\circ \pm 2.1^\circ$
$\Omega_{AL}/2\pi$, 440.64	$1.9^\circ \pm 2.9^\circ$	$-4.1^\circ \pm 2.6^\circ$
$\Omega_{AC}/2\pi$, 461.70	$0.5^\circ \pm 2.3^\circ$	$0.1^\circ \pm 2.0^\circ$

velocity field are much stronger in amplitude, they have been included in order to facilitate comparison between flux tube properties with and without convection as presented in Chapters 3 and 4. Removing the random phase relations from the thin flux tube model embedded in convection has a negligible effect on the dynamics and properties of the flux tube at all magnetic field strengths and magnetic flux. Without convective effects, the flux tubes would emerge randomly distributed in longitude if perturbed initially with random

undular motions. Therefore, we would not expect to find a correlation between the North and South emergence histograms for the same rotation period.

Even though we initiate identical flux tubes in the convection simulation at the same time in either hemisphere, the flux tubes do not evolve identically as each one is subjected to convective flows that are not symmetric across the Equator. The fact that flux emergence patterns in our simulation align across the Equator suggests that the average near-hemispheric alignment trend of the longitudinal flux emergence pattern is convection dependent. The different dominate modes in the power spectra found in Section 5.4.1 for both hemispheres, $m = 1$ in the Northern hemisphere and $m = 3$ in the Southern hemisphere, do not contradict the findings in this Section. On average, as long as the single active longitude in the Northern hemisphere aligns with any of the three in the Southern hemisphere, the correlation between hemispheric flux emergence patterns will be greater than what would be expected from random longitudinal flux tube emergence. This effect is most probably related to the elongated downflow lanes present in our convection simulation, which span across the Equator and are rotationally aligned at low latitudes (see Fig. 5.1).

5.5. Discussion

By coupling a thin flux tube model with a three-dimensional, solar-like, rotating convection simulation, we are able to examine the interaction of turbulent convective flows with buoyantly rising flux tubes. As a result of this interaction, we find that flux tubes emerge at the upper boundary of our simulation domain in a large-scale longitudinal pattern which resembles the behavior of active longitudes on the Sun and other solar-like stars. While the active longitude phenomenon most likely results from a combination of various physical mechanisms, we suggest that convection also has some part to play.

Flux emergence on the Sun and other solar-like stars is often concentrated in distinct bands with low order longitudinal modes. The large-scale organization of convection in our simulation produces a flux emergence pattern that does exhibit low order longitudinal modes present at $m \leq 18$, consistently greater than the 99.7% confidence level, above which we are 99.7% sure the result is not due to a random distribution in longitude of flux tube emergence (Fig. 5.8). In the Northern hemisphere, the peak in the power spectrum occurs for longitudinal mode $m = 1$, and $m = 3$ in the Southern hemisphere. However, the more important result is that both hemispheres exhibit secondary peaks in their power spectra for longitudinal modes of $m = 6$. This corresponds to the dominant longitudinal wavenumber of the convection simulation, which is representative of periodic, giant-cell convection. The maxima in the power spectrum for either hemisphere are independent of reference frame and magnetic field strength. This is also not the result of a non-axisymmetric ($m \neq 0$) mode which a flux tube might develop due to the non-linear growth of the magnetic buoyancy instability, as we are only capable of recording the emergence position of the first apex of any flux tube that reaches the upper boundary of our simulation domain. Rather, these longitudinal modes are imposed by the strong downflows at the boundaries of the giant cells in our convection simulation. Additionally, the extent of the upflows determines the *window* where flux tubes can emerge.

Active longitudes on the Sun are known to drift prograde relative to a fixed reference system. The flux emergence patterns in our simulation propagate prograde relative to the mean angular velocity of our solar-like star, $\Omega_0/2\pi = 429.72$ nHz. Average drift rates are similar for each hemisphere, rotating at $4.2^\circ \pm 3.6^\circ$ prograde in the Northern hemisphere, and $2.9^\circ \pm 3.1^\circ$ in the Southern hemisphere (Fig. 5.9, top) per rotation period. However, in

the more rapidly rotating ASH equivalent Carrington frame with $\Omega_{AC}/2\pi = 461.72$ nHz, the flux emergence pattern propagates retrograde at $13.7^\circ \pm 4.1^\circ$ in the Northern hemisphere, and $12.0^\circ \pm 3.6^\circ$ in the Southern hemisphere (Fig. 5.9, bottom). We also identify a reference frame rotating at the angular velocity $\Omega_{AL}/2\pi = 440.64$ nHz, in which the flux emergence pattern remains stationary, indicating that the flux emergence pattern in our simulation has an average angular velocity of $\sim$441 nHz. This angular velocity corresponds to the rotation rate of the ASH simulation at $r = 0.95R_\odot$ and a latitude of 29°. Although the flux emergence patterns in the $\Omega_{AC}/2\pi$ reference frame do not propagate prograde, they do have an average rotation rate of $\sim$441 nHz, which is faster than the mean angular velocity of the simulation, $\Omega_0/2\pi$. Differential rotation present in the convection simulation helps to usher the flux emergence pattern forward in longitude. The fact that we are capable of calculating cross-correlations that peak at or above the 99.7% confidence level means that the flux emergence pattern persists between at least consecutive rotation periods. We also note that on average, the flux emergence pattern for any particular rotation period tends to align very closely across the Equator. This trend is related to the elongated downflow lanes which span across the Equator in the convection simulation (see Fig. 5.1).

Throughout this Chapter, we highlight the ability of convection to organize flux emergence in a large-scale way. The flux emergence pattern present in our simulations exhibits properties similar to those of active longitudes on the Sun. We attribute the cause of these characteristics in our simulation to differential rotation and the columnar, rotationally aligned giant cells which exist in the equatorial to mid-latitude regions of our ASH convection simulation. Convective downflows which mark the boundary of giant cells are capable of deforming even the strongest flux tubes, forcing them to emerge along the boundaries

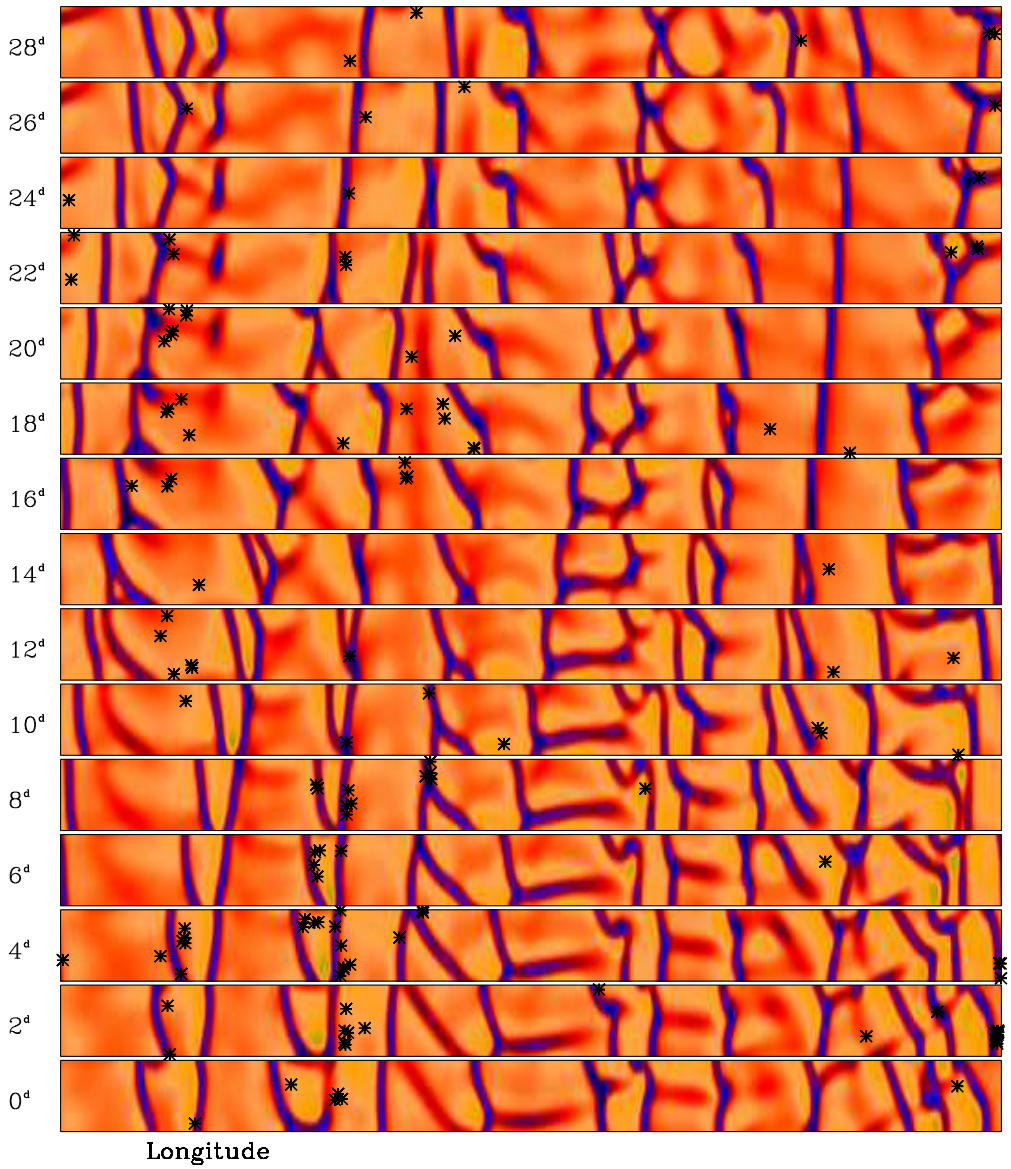

FIGURE 5.12. ASH radial velocity snapshots at a depth of $0.95R_\odot$ in strips of longitude (0° to 360°) and latitude (0° to +15°) for 28 consecutive days, at increments of every 2 days, in the reference frame rotating at the angular velocity $\Omega_0/2\pi$. The initial starting time is arbitrary. Black asterisks mark the apex of all flux tubes which emerge within ±1 day of the ASH snapshot. This figure depicts how the nature of giant cells force flux tubes to emerge along the giant cell boundaries, and occasionally near the center.

of the giant cells, and occasionally near the center as depicted in Figure 5.12. These flux tubes tend to emerge at $r = 0.97R_{\odot}$ near the giant cell boundaries because the strongest upflows occur near the downflow lanes (Miesch *et al.* 2008). Additionally, there is a positive horizontal divergence of the velocity field within the upflow region of the giant cell, which helps expel the rising flux tube toward the cell boundary (Miesch *et al.* 2008).

Rising flux tubes are subject not only to the mean flows of the convection simulation, such as differential rotation, but also to the prograde propagation of the ever changing giant cells near the Equator. Although continually evolving, some of the giant cells are capable of remaining coherent for a rotation period or longer (see Fig. 5.2). The giant cells *corral* flux tubes in a sense, forcing them to emerge within the boundaries of a particular cellular feature. The periodic nature of the giant cells in longitude is most likely the reason why the flux emergence patterns in our simulation exhibit low order longitudinal modes, as the downflow lanes can restrict the rise of flux tubes over certain longitudinal spans. Differential rotation aids these distinct longitudinal bands of flux in rotating prograde in longitude. Downflow lanes of these giant cells extend across the Equator and are rotationally aligned, forcing the alignment of the flux emergence pattern across the Equator, which is depicted well in the flux tube emergence maps for both hemispheres in Figure 5.5. The sum of these results suggest to us that giant cells may play a significant role in the active longitude phenomena on the Sun and other solar-like stars.

CHAPTER 6

Influence of Radiative Diffusion on Rising Magnetic Flux Tubes

We study the combined effects of convection and radiative diffusion on the evolution of thin magnetic flux tubes in the solar interior. Radiative diffusion from the interior to the convection zone is the primary supplier of heat to large scale global convective motions, and results in a heat input per unit volume of magnetic flux tubes that has been ignored by most previous thin flux tube studies. We modify the energy equation of the thin flux tube model to capture the influence of radiative heating on 10^{22} Mx flux tubes. Our simulations show that flux tubes of $\leq$60 kG do not anchor in the overshoot region, but rather drift upward due to the increased buoyancy of the flux tube earlier in its evolution. These flux tubes have rise times of $\leq$0.2 years, and exhibit a positive Joy's Law tilt angle trend, as is observed for solar active regions. Our results suggest that radiative heating is an effective mechanism by which flux tubes can escape from the stably stratified overshoot region, and that flux tubes do not necessarily need to be anchored in the overshoot region to produce emergence properties similar to those of active regions on the Sun.

6.1. Introduction

Many previous thin flux tube studies assume that flux tubes evolve adiabatically throughout the convection zone. This is a valid assumption for the upper $\sim$2/3 of the solar convection zone. However, in the lower $\sim$1/3 of the convection zone, closer to the radiative interior of the Sun, there is a significant non-zero divergence of radiative heat flux due to the deviation

from radiative equilibrium. Radiative diffusion from the interior into the convection zone is the primary supplier of heat to large-scale global convective motions. It also results in a heat input per unit volume Q_v of magnetic flux tubes, which may have a substantial effect on their buoyancy, and hence their dynamic evolution.

Due to radiative heating, Fan and Fisher (1996) find that flux tubes of $10^{21} - 10^{22}$ Mx rise through the convection zone in $\sim 2 - 4$ months, a comparable or shorter timescale compared to flux tubes allowed to evolve adiabatically, which have rise times of $\sim 2 - 10$ months (Fan, Fisher, and Deluca 1993). This large spread in rise times for adiabatically evolving flux tubes is a result of the combined effects of magnetic buoyancy and the drag force at various initial magnetic field strengths and magnetic flux. When heating due to radiative diffusion is considered in flux tube evolution, all flux tubes experience the same uniform heating rate. The effect of radiative diffusion near the base of the convection zone provides additional growth of the flux tube buoyancy $(\rho_e - \rho)g$ earlier in its evolution, thereby forcing the flux tube to begin its rise toward the surface sooner than it would if it were evolving totally adiabatically. These emerging flux loops subject to radiative diffusion also show similar qualitative features to solar active regions such as tilt angles and morphological asymmetries, not significantly different from simulations results where flux tubes evolve adiabatically (e.g. Fan, Fisher, and Deluca 1993; Caligari, Moreno-Insertis, and Schüssler 1995; Caligari, Schüssler, and Moreno-Insertis 1998).

Fan and Fisher (1996) also find that flux tubes subject to radiative diffusion will rise quasi-statically (i.e. all forces closely balance) through the convective overshoot region. The overshoot region is a thin layer in the solar atmosphere between the radiative zone and convection zone with a thickness of $\sim 0.01 - 1$ pressure scale heights H_p, a few percent of

the solar radius (e.g. Miesch 2005). Here, convective motions from the unstably stratified convection zone penetrate into the stably stratified solar interior. It is in this region where it is thought that magnetic fields are stored until they enter the convection zone, eventually emerging at the surface to form sunspots. Subject to heating by radiative diffusion, using typical values for the overshoot region as computed by numerical models, flux tubes take $\sim$1 year or less to emerge from the overshoot region (e.g. Fan and Fisher 1996; Rempel 2003). This short storage time compared to the $\sim$11 year solar cycle may have significant implications for the solar dynamo mechanism.

The purpose of this Chapter is to study the combined effects of turbulent solar-like convection and heating due to radiative diffusion on the evolution of active-region-scale magnetic flux tubes. We begin in Section 6.2 with a discussion of temperature gradients and methods of energy transport for various regions within the Sun, pertinent to our topic of radiative diffusion in the convection zone and overshoot region. In Section 6.3, we develop a formulation for the rate of heat input per unit volume (dQ_v/dt) of the flux tube plasma, which modifies the thin flux tube energy equation. In Section 6.4, we address how the addition of radiative diffusion to the energy equation alters the dynamic evolution of flux tubes subject to solar-like convective flows. Emergence properties of these flux tubes, specifically latitude of emergence and tilt angle properties, will be compared in Sections 6.5.1 and 6.5.2 respectively, to those of flux tubes that evolve adiabatically, as reported in Chapter 4. We will briefly mention the problem of flux storage in Section 6.6, and end with a summary in Section 6.7.

6.2. A Note on Energy Transport and Temperature Gradients ∇

As noted in Chapter 1.3, the method of energy transport for various regions within a star is dictated by its local temperature gradient dT/dr. Often, we refer to an alternative

definition for the temperature gradient represented by the symbol ∇, which is defined as a double-logarithmic derivative of temperature with respect to pressure (see Eq. 1.4), which varies radially. We will denote ∇_e as the local temperature gradient of the plasma environment, ∇_{ad} as the temperature gradient required for a parcel of gas to evolve adiabatically (see Appendix section 1.3.4), and ∇_{rad} as the temperature gradient required for energy to be transported only by radiation, given by (e.g. Hansen and Kawaler 1994):

$$\nabla_{rad} \equiv \left(\frac{d\ln T}{d\ln P}\right)_{rad} = \frac{3}{16\pi acG}\frac{\tilde{\kappa}P}{T^4}\frac{L}{M}, \tag{6.1}$$

where c is the speed of light, G is the gravitational constant, and a is the radiation density constant. (The energy density of radiation is given by aT^4, where T is temperature and $a = 7.566\times10^{-15}$ erg cm^{-3} K^{-4} (e.g. Prialnik 2000).) Additionally, P is pressure, T is temperature, $\tilde{\kappa}$ is the Rosseland mean absorption coefficient (opacity), L is the luminosity of the star, and M is the mass of the star, all of which are a function of radius.

A region inside a star is said to be in radiative equilibrium when ∇_e at that depth is equal to ∇_{rad}. It is also the value of ∇ required to transport all of the energy generated by the star out by radiative transport. The magnitude of ∇_{rad} is determined mainly by $\tilde{\kappa}$ and L/M. The opacity $\tilde{\kappa}$ generally increases away from the center of the star, and L/M decreases very slowly with increasing r in a star such as the Sun. Unlike ∇_{rad}, which increases substantially in steepness in the outer $\sim$1/3 of the solar radius, $\nabla_{ad} \sim 0.4$ throughout most of the solar interior and convection zone (see Appendix C, Section 1.3.4). However, this value changes significantly near the solar surface, as the hydrogen and helium that make up the plasma become partially ionized. The radiative and adiabatic temperature gradients in the solar interior for our computational domain are shown in Figure. 6.1.

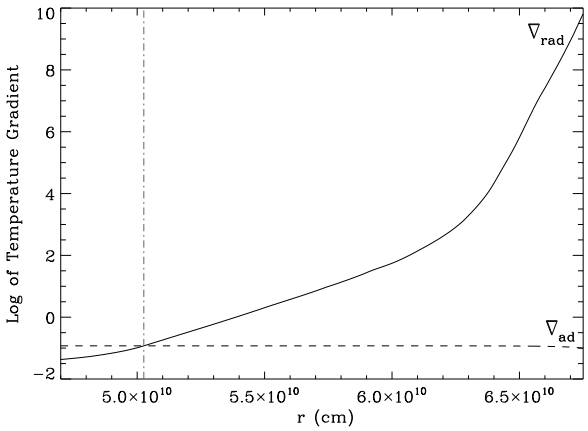

FIGURE 6.1. Radiative temperature gradient ∇_{rad} and adiabatic temperature gradient ∇_{ad} as a function of radius for the computational domain of our simulations. These gradients are taken from the 1D solar structure model of Christensen-Dalsgaard *et al.* (1996). To the right of the vertical dash-dotted line, $\nabla_{rad} > \nabla_{ad}$, therefore the solar plasma becomes convectively unstable.

In order for a stratified plasma to remain stable, the local temperature gradient ∇_e must be less than the local adiabatic temperature gradient ∇_{ad} (see Appendix D). In the deep interior of a star such as the Sun, $\nabla_e = \nabla_{rad}$. However, in the overshoot region where turbulent motions from the convection zone penetrate into the stable stratification of the interior, convective mixing in this layer brings the local temperature gradient away from ∇_{rad} and closer to ∇_{ad} such that:

$$\nabla_{rad} < \nabla_e < \nabla_{ad}. \tag{6.2}$$

An instability in the plasma sets in when ∇_{rad} becomes greater than ∇_{ad}. At this point, energy transport by radiation alone demands a temperature gradient that is unstable for the plasma, so convection sets in to take over some of the energy transport load. Therefore,

convection occurs when the following condition arises (see also Appendix D):

$$\nabla_{rad} > \nabla_e > \nabla_{ad}. \tag{6.3}$$

The bottom of the convection zone is here defined as the region where $\nabla_{rad} = \nabla_{ad}$, which occurs at $r = 5.026{\times}10^{10}$ cm as obtained from the reference solar structure model by Christensen-Dalsgaard *et al.* (1996) (see Fig. 6.1). The local temperature gradient of the plasma ∇_e remains very close to ∇_{ad} throughout the convection zone domain we consider for our simulations, such that the quantity $\delta = \nabla_e - \nabla_{ad}$ is positive but never greater than $\sim 10^{-5}$ in this region. In our model, we incorporate a thin convective overshoot region, just below the base of the convection zone, where flows from the convection zone proper overshoot into a stably stratified atmosphere. Such behavior brings the temperature gradient of the plasma in the overshoot region away from radiative equilibrium, closer to the adiabatic value, although it still maintains a small sub-adiabaticity such that δ is negative, therefore the overshoot region still remains stably stratified (see Fig. 2.1 for a graph of δ as a function of radius in our simulation). Only when reaching the boundary between the overshoot region and the radiative interior does ∇_e jump sharply to the radiative equilibrium value.

In the interior of the Sun, where the plasma is in radiative equilibrium, the divergence of radiative heat flux is necessarily zero. However, as a result of this abrupt deviation from radiative equilibrium in the overshoot region and base of the convection zone due to the local temperature gradient, there is a non-zero divergence of radiative heat flux, which results in plasma heating by radiative diffusion. Near the photosphere in the upper portion of the convection zone (above our computational model domain), the divergence of radiative heat flux acts to cool the plasma.

6.3. Energy Equation with Radiative Heating

In this Chapter, we perform numerical simulations of flux tubes evolving in an external convective velocity field as described in Chapter 2. However, we modify the energy equation such that the flux tube is no longer assumed to evolve adiabtically as in Chapters 3-5. The modification of the energy equation, and its subsequent effect on the equation $d\Delta\rho/dt$, the evolution of the density deficit $\Delta\rho = \rho_e - \rho$ of the flux tube solved in the numerical model, are the only changes made to the simulations discussed in Chapters 3-5.

Starting from the thin flux tube energy equation (Eq. 2.3), the rate of heat input per unit volume ($\mathrm{d}Q_v/\mathrm{dt}$) of the flux tube plasma is given by:

$$\rho T \frac{dS}{dt} = \frac{dQ_v}{dt} = \nabla \cdot (\kappa \nabla T), \tag{6.4}$$

where S is the entropy per unit mass, the right-most expression is a divergence of a radiative flux $\kappa\nabla T$, and κ is the coefficient of radiative conductivity. (Note that in the adiabatic regime, $dS/dt = 0$.) Letting $\delta T = T - T_e$ and $\delta\kappa = \kappa - \kappa_e$ represent small difference between the external quantities and internal quantities introduced due to the presence of a magnetic field in the flux tube, this expression can be rewritten as the following, where we drop second order terms of $\delta\kappa\delta T$:

$$\frac{dQ}{dt} = \nabla \cdot (\kappa_e \nabla T_e) + \nabla \cdot (\delta\kappa \nabla T_e) + \nabla \cdot (\kappa \nabla \delta T). \tag{6.5}$$

The first term in Equation 6.5 represents radiative heating of the flux tube caused by the divergence of radiative flux in the external plasma, and can be calculated directly from a

reference solar model. The second and third terms represent perturbations to the radiative heat flux due to the presence of the magnetic field inside the flux tube.

To evaluate the terms on the RHS of Equation 6.5, we introduce a cylindrical polar coordinate system (ϖ, ϕ, s) where s is along the flux tube axis, ϖ is the horizontal radius of the flux tube cross-section, and ϕ is the azimuthal angle of the tube cross-section. In this coordinate system, the gradient vector is written as:

$$\nabla = \left(\frac{\partial}{\partial\varpi}, \frac{1}{\varpi}\frac{\partial}{\partial\phi}, \frac{\partial}{\partial s}\right) = \nabla_\perp + \nabla_{||}, \tag{6.6}$$

$$\nabla_\perp = \left(\frac{\partial}{\partial\varpi}, \frac{1}{\varpi}\frac{\partial}{\partial\phi}, 0\right), \tag{6.7}$$

$$\nabla_{||} = \left(0, 0, \frac{\partial}{\partial s}\right). \tag{6.8}$$

Applying Equations 6.7-6.8 to the last two terms in Equation 6.5:

$$\nabla\cdot(\delta\kappa\nabla T_e) = \frac{\partial}{\partial s}\left(\delta\kappa\frac{\partial T_e}{\partial s}\right) + \delta\kappa\nabla_\perp^2 T_e + \nabla_\perp\delta\kappa\cdot\nabla_\perp T_e, \tag{6.9}$$

$$\nabla\cdot(\kappa\nabla\delta T) = \frac{\partial}{\partial s}\left(\kappa\frac{\partial\delta T}{\partial s}\right) + \kappa\nabla_\perp^2\delta T + \nabla_\perp(\kappa_e+\delta\kappa)\cdot\nabla_\perp\delta T. \tag{6.10}$$

In the thin flux tube approximation, it is assumed that length scale variations along the flux tube axis are on the order of the local pressure scale height H_p, which is greater than the cross-sectional radius a of the flux tube. We also note that for the flux tubes we consider here, $\delta\kappa/\kappa \sim \delta T/T \ll 1$. For the background plasma, the magnitudes of the derivatives of the external quantities $\partial A_e/\partial s$ and $\nabla_\perp A_e$, where A_e is any thermodynamic quantity of the external plasma, are expected to be at most $\sim A_e/H_p$. Derivatives of the perturbation quantities along the flux tube axis $\partial\delta A/\partial s$, where A is a thermodynamic quantity of the flux tube, are also at most $\sim\delta A/H_p$. However, derivatives of the perturbation quantities in

the plane perpendicular to the flux tube axis (in the plane of the flux tube cross-section) are of magnitude $\nabla_\perp \delta A \sim \delta A/a$, such that length scale variations perpendicular to the flux tube axis are on the order of the cross-sectional radius of the flux tube a. Applying these estimates for the magnitude of the derivatives in Equations 6.9-6.10:

$$\nabla \cdot (\delta\kappa \nabla T_e) \sim \frac{\delta\kappa T_e}{H_p^2} + \frac{\delta\kappa T_e}{H_p^2} + \frac{\delta\kappa T_e}{a H_p}, \tag{6.11}$$

$$\nabla \cdot (\kappa \nabla \delta T) \sim \frac{\kappa \delta T}{H_p^2} + \frac{\kappa \delta T}{a^2} + \left(\frac{\kappa_e}{H_p} + \frac{\delta\kappa}{a}\right)\frac{\delta T}{a}. \tag{6.12}$$

Comparing the magnitudes of the above terms in Equations 6.11-6.12, recalling that the pressure scale height is much greater than the cross-sectional radius of the flux tube $H_p \gg a$, the dominant contribution comes from the second term in Eq. 6.12, $\kappa \nabla_\perp^2 \delta T \sim \kappa \delta T/a^2$. Therefore, the equation for the rate of heat input per unit volume can be reduced to:

$$\frac{dQ_v}{dt} \approx \nabla \cdot (\kappa_e \nabla T_e) + \kappa \nabla_\perp^2 \delta T. \tag{6.13}$$

The first term in Eq. 6.13, which we will subsequently refer to as $(dQ/dt)_1$, is dependent only on the external plasma thermodynamic quantities κ_e and T_e, which vary only as a function of radial distance from Sun center. The second term, subsequently referred to as $(dQ/dt)_2$, represents a radiative diffusion across the flux tube due to the temperature difference between the flux tube and the external plasma.

For $(dQ/dt)_1$, the term $\kappa_e \nabla T_e$ is simply the radiative energy flux F_{rad} of the background plasma environment, where F_{rad} can be written in terms of the total energy flux F_{tot} of the

Sun (e.g. Spruit 1974):

$$F_{rad} = \frac{\nabla_e}{\nabla_{rad}} F_{tot}. \tag{6.14}$$

Replacing F_{rad} with Eq. 6.14, the term $(dQ/dt)_1$ becomes:

$$\left(\frac{dQ}{dt}\right)_1 = \nabla \cdot (\kappa_e \nabla T_e) = -\nabla \cdot (F_{rad}) = -F_{tot} \frac{d}{dr}\left(\frac{\nabla_e}{\nabla_{rad}}\right), \tag{6.15}$$

where ∇_e and ∇_{rad} are radial functions only. In Equation 6.15, we have also used the fact that $\nabla \cdot F_{tot} = 0$. The magnitude of the total energy flux is $F_{tot} = L/(4\pi r^2)$, where L is the total luminosity of the Sun. The last expression in Eq. 6.15 is what is evaluated in the thin flux tube code for $(dQ/dt)_1$, with all relevant quantities provided by the solar structure model of Christensen-Dalsgaard *et al.* (1996).

For an order of magnitude estimate of $(dQ/dt)_1$, $F_{tot} = \kappa_e T_e \nabla_{rad}/H_p$ (e.g. Spruit 1974). We also assume that length scale variations in the quantities ∇_e and ∇_{rad} are on the order of the local pressure scale height H_p. The magnitude of $(dQ/dt)_1$ is then:

$$\left|-F_{tot} \frac{d}{dr}\left(\frac{\nabla_e}{\nabla_{rad}}\right)\right| \sim \left(\kappa_e \frac{T_e}{H_p} \nabla_{rad}\right)\left(\frac{\nabla_e}{\nabla_{rad}} \frac{1}{H_p}\right) \sim \kappa_e \nabla_e \frac{T_e}{H_p^2}. \tag{6.16}$$

To compute the second component of the heating rate $(dQ/dt)_2 = \kappa \nabla_\perp^2 \delta T$, which represents radiative diffusion across the flux tube due to the temperature difference between the flux tube and the external plasma, we should express it in terms of the mean temperature difference $\delta\bar{T} = \bar{T} - \bar{T}_e$. This is in line with the thin flux tube approximation, which assumes that all relevant quantities are averages over the flux tube cross-section. Following Fan and Fisher (1996), we assume that the profile of δT over the flux tube cross section follows the

shape of the Bessel function $AJ_0(k_1\varpi)$, where A is a constant, $\alpha_1 = k_1 a$ is the first zero of Bessel function $J_0(x)$, and a is the flux tube radius. This corresponds to the slowest decaying mode of the solution to the thermal diffusion equation (Eq. 6.17) across a cylinder surrounded by a fixed temperature environment:

$$\frac{\partial \delta T}{\partial t} + \kappa \nabla_\perp^2 \delta T = 0. \tag{6.17}$$

Taking the average of $\kappa \nabla_\perp^2 \delta T$ over the flux tube cross section, and approximating the radiative conductivity of the flux tube to be equal to that of the external plasma, we arrive at an expression for $(dQ/dt)_2$:

$$\left(\frac{dQ}{dt}\right)_2 \simeq -\kappa_e \frac{\alpha_1^2}{a^2}(\bar{T} - \bar{T_e}), \tag{6.18}$$

where $\alpha_1 \simeq 2.4048$ is the first zero of Bessel function $J_0(x)$. The quantity $(dQ/dt)_2$ then has a magnitude of $\sim \kappa_e \alpha_1^2 \delta T / a^2$.

Next, we will compare the magnitudes of $(dQ/dt)_1$ and $(dQ/dt)_2$ to determine their relative contribution to the energy equation:

$$\frac{\left|\left(\frac{dQ}{dt}\right)_1\right|}{\left|\left(\frac{dQ}{dt}\right)_2\right|} \sim \frac{a^2}{H_p^2} \frac{\nabla_e}{\alpha_1^2} \frac{T_e}{\delta T}. \tag{6.19}$$

For a neutrally buoyant flux tube at the base of the convection zone, $\rho = \rho_e$. Such that the conditions of pressure balance (Eq. 2.5) are satisfied, the internal temperature of the flux tube is less than the surrounding environment. This temperature deficit $(\delta T / T_e) \sim 1/\beta = 8\pi p_e / B^2$. The quantity β, a ratio of the plasma pressure to the magnetic pressure, is $>>1$ in the solar interior, meaning that the environment is plasma dominated and the plasma

TABLE 6.1. Ratio of $|(dQ/dt)_1|$ to $|(dQ/dt)_2|$ following Eq. 6.20. The term $|(dQ/dt)_1|$ is much larger than $|(dQ/dt)_2|$ for tubes of 10^{22} Mx. As the width of the flux tube decreases, $|(dQ/dt)_2|$ increases and becomes comparable to $|(dQ/dt)_1|$, and even larger than $|(dQ/dt)_1|$ in some cases.

B	10^{20} Mx	10^{21} Mx	10^{22} Mx
100 kG	0.083	0.83	8.6
80 kG	0.17	1.7	17
60 kG	0.39	4.0	40
50 kG	0.68	6.9	67
40 kG	1.3	14	130
30 kG	3.4	31	340
15 kG	25	270	2500

influences the magnetic field structure. Additionally, $\nabla_e \simeq 0.4$ throughout the convection zone, so $\nabla_e/\alpha_1^2 \sim 7{\times}10^{-2}$. Therefore:

$$\frac{\left|\left(\frac{dQ}{dt}\right)_1\right|}{\left|\left(\frac{dQ}{dt}\right)_2\right|} \sim 7 \times 10^{-2}\beta\frac{a^2}{H_p^2}. \tag{6.20}$$

For typical values at the base of the convection zone, the pressure scale height $H_p \sim 5.6{\times}10^9$ cm, and β ranges from $1.2{\times}10^5$ for 100 kG magnetic fields to $5.4{\times}10^6$ for 15 kG magnetic fields. The cross-sectional radius of the flux tube $a = (\Phi/B\pi)^{1/2}$ decreases with decreasing flux, but increases with decreasing magnetic field. As a result, a will be largest for $B_0 = 15$ kG, $\Phi = 10^{22}$ Mx, but smallest for flux tubes of $B_0 = 100$ kG, $\Phi = 10^{20}$ Mx. The ratios of $|(dQ/dt)_1|$ to $|(dQ/dt)_2|$ following Eq. 6.20 are given in Table 6.1.

The second heating term $(dQ/dt)_2$ acts to reduce the temperature difference between the flux tube and the external plasma environment, bringing it closer to a state of thermal equilibrium, enhancing the density deficit of the flux tube in the process. As this term is inversely proportional to the flux tube cross-section, it will increase in magnitude as the cross-sectional radius of the flux tube decreases. However, the first heating term $(dQ/dt)_1$ is

dependent only on properties of the background plasma as a function of distance r from Sun center. Therefore each flux tube will experience the same heating from $(dQ/dt)_1$ at the same distance r. Following the results in Table 6.1, it is a valid assumption to neglect $(dQ/dt)_2$ for flux tubes of 10^{22} Mx in the $15-100$ kG range. However, for weaker flux and stronger magnetic field, $(dQ/dt)_2$ becomes comparable to and even larger than the radiative heating term supplied by $(dQ/dt)_1$. A larger $(dQ/dt)_2$ term will drive the temperature difference δT between the flux tube and the external plasma to zero, adding to the buoyancy $(\rho_e - \rho)g$ of the flux tube, thereby allowing it to become buoyant earlier in its evolution process. We have chosen in this Chapter to neglect the term $(dQ/dt)_2$ in the thin flux tube energy equation so as to focus on how radiative heating supplied by $(dQ/dt)_1$ in conjunction with convection influences the dynamic evolution and emergence properties of 10^{22} Mx flux tubes. We will also investigate the rise times of $10^{20}-10^{22}$ Mx flux tubes, using the rise times of $10^{20}-10^{21}$ Mx flux tubes as an upper limit in the strong magnetic field strength regime.

Combining the thin flux tube energy equation (Eq. 2.3) with equation 6.15, the energy equation for the thin flux tube model becomes:

$$\frac{1}{\rho}\frac{d\rho}{dt} = \frac{1}{\gamma P}\frac{dP}{dt} - \frac{\nabla_{ad}}{P}\left(\frac{dQ}{dt}\right)_1, \tag{6.21}$$

$$\frac{1}{\rho}\frac{d\rho}{dt} = \frac{1}{\gamma P}\frac{dP}{dt} + \nabla_{ad}\frac{F_{tot}}{P}\frac{d}{dr}\left(\frac{\nabla_e}{\nabla_{rad}}\right). \tag{6.22}$$

Incorporating this new energy equation to the thin flux tube model only affects the equation for the density deficit $d\Delta\rho/dt$ solved in the thin flux tube code (see Appendix E, Section

5.2), which is now given by:

$$\begin{aligned}\frac{d\Delta\rho}{dt} &= \left[v_r\rho_e g\left[\alpha - \frac{B^2}{4\pi\rho}\left(\frac{d\rho_e}{dP_e}+\alpha\right)\frac{d\rho_e}{dP_e}\right] + \frac{B^2}{4\pi}\left(\frac{\partial v_l}{\partial s} - \mathbf{v}\cdot\mathbf{k}\right)\left(\frac{d\rho_e}{dP_e}+\alpha\right)\right] \\ &\times\left[1+\frac{B^2}{4\pi}\left(\frac{d\rho_e}{dP_e}+\alpha\right)\right]^{-1} - \frac{\rho_e}{P_e}\nabla_{ad}F_{tot}\frac{d}{dr}\left(\frac{\nabla_e}{\nabla_{rad}}\right). \qquad (6.23)\end{aligned}$$

6.4. Flux Tube Dynamics: Addition of Heating Due to Radiative Diffusion

To study the role of radiative heating in the flux emergence process, we have performed ∼7000 flux tube simulations (see Appendix G for a more detailed description) in the same way as was done for Chapters 3-5, except the energy equation has been modified following the discussion in Section 6.3. As mentioned previously, we will only investigate the dynamic properties of 10^{22} Mx flux tubes, where it is a valid assumption to neglect the term $(dQ/dt)_2$ in the energy equation. We will only calculate the average rise times of $10^{20} - 10^{21}$ Mx flux tubes, where $(dQ/dt)_2$ is not always smaller than $(dQ/dt)_1$, for comparison with flux tubes of 10^{22} Mx, treating these rise time values as upper limits.

6.4.1. Flux Tube Morphology. When flux tubes from our simulations evolve adiabatically in the absence of convection, rising buoyant loops develop solely as a result of the non-linear growth of the magnetic buoyancy instability, as discussed in Chapter 3.2. The troughs of these rising loops penetrate into the overshoot region where they remain anchored for the duration of the flux emergence process. However, when heating due to radiative diffusion is considered, flux tubes of ≤60 kG no longer anchor in the overshoot region (see Fig. 6.2).

The term $(dQ/dt)_1$ acts to heat the flux tube uniformly (i.e. uniformly for flux tube portions at the same distance r), especially near the base of the convection zone where the

divergence of radiative heat flux from the external plasma environment is the greatest. This uniform heating increases the flux tube's density deficit early in its rise, thereby increasing the buoyancy of the flux tube in the lower convection zone. Flux tubes of $\geq$80 kG, while still subject to the same uniform heating, develop undular magnetic buoyancy instabilities that grow fast enough to allow the troughs of their rising loops to penetrate into the overshoot region before their density deficit becomes substantially large. Magnetic buoyancy instabilities develop more slowly in weak magnetic field strength flux tubes. Therefore, such flux tubes develop a density deficit (i.e. larger buoyancy) faster than magnetic buoyancy instabilities can anchor the flux tube in the overshoot region, and consequently the flux tube drifts away from the lower convection zone. Even though flux tubes of $\geq$80 kG do anchor in our simulations, their footpoints continue to drift slowly out of the overshoot region as the flux tube developes due to the uniform heating supplied by $(dQ/dt)_1$.

Flux tubes that evolve non-adiabatically without convective effects also suffer from poleward slippage of the flux tube as a whole, which is most severe for flux tubes of $\leq$60 kG, as they do not anchor (see Fig. 6.2). When the $m = 0$ unstable magnetic buoyancy mode grows faster than the higher order modes, the tube slips upward as a whole, a phenomenon driven by the tension in the magnetic field lines (e.g. Spruit and van Ballegooijen 1982b). The addition of solar-like convective flows to the thin flux tube model keeps flux tubes originating at low initial latitudes θ_0 from suffering such severe poleward slippage (see Fig. 6.3). Also as shown in Figure 6.3, with convection and radiative heating considered, 15 kG flux tubes are affected most strongly by convection, whereas 100 kG flux tubes only have minimal deformations resulting from the strongest convective downdrafts. This trend is the

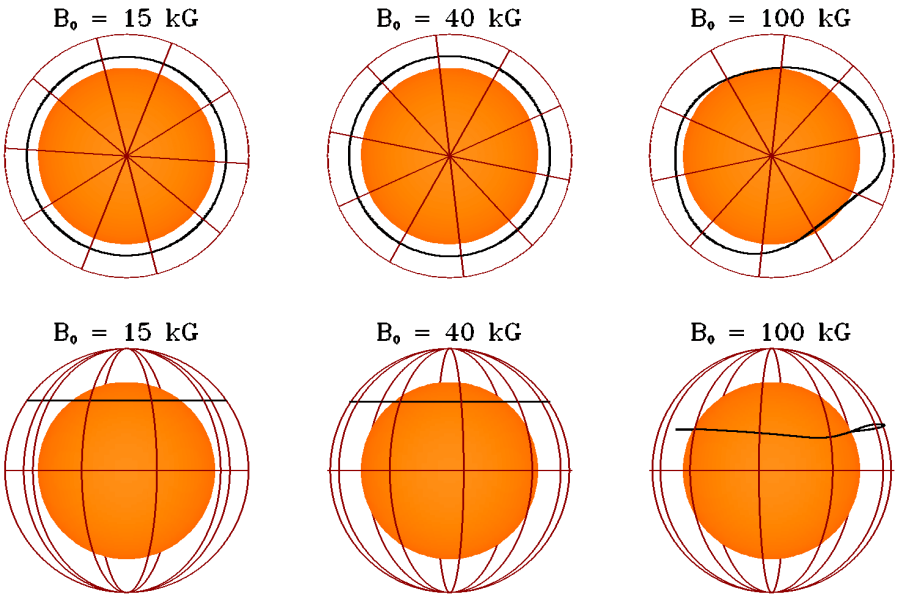

FIGURE 6.2. Polar (top) and equatorial (bottom) view of flux tubes once the apex has reached the simulation upper boundary. Flux tubes are allowed to evolve in the absence of convection, but with the addition of heating due to radiative diffusion. Each tube has a magnetic flux of 10^{22} Mx and an initial latitude of $\theta_0 = 8°$. (Figure specifics are the same as in Fig. 3.1.) The addition of radiative heating forces flux tubes of $\leq$60 kG to drift upward as a whole and away from the overshoot region.

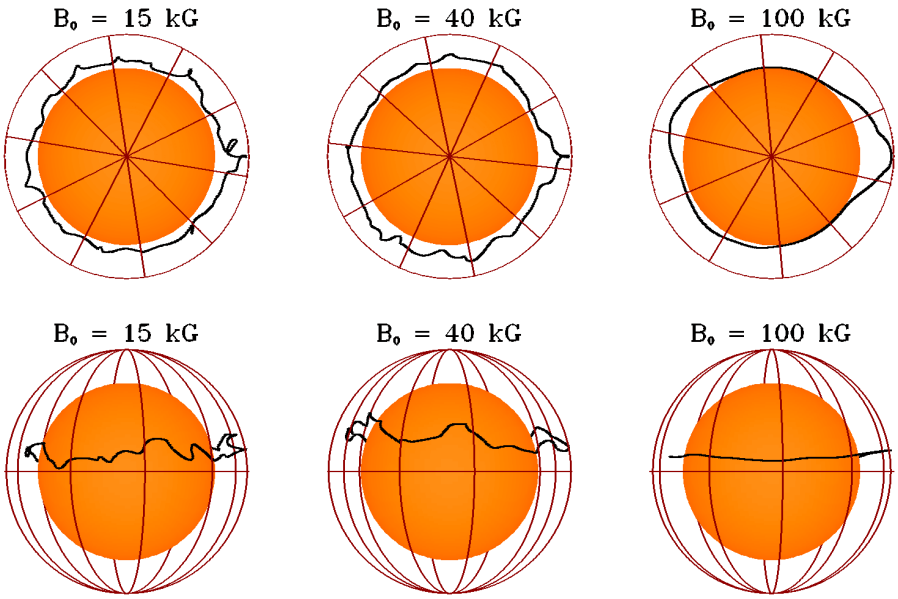

FIGURE 6.3. Same as Figure 6.2, except the flux tube is subjected to the external convective flow. Convection prevents severe poleward slippage of the flux tube as depicted in Fig. 6.2.

same as observed for adiabatically evolving flux tubes in a convective flow field as discussed in Chapter 3.2.

6.4.2. Convection vs. Magnetic Buoyancy. As in Section 3.3, we compare the magnitude of the drag force to the magnetic buoyancy force acting on the flux tube to understand their relative importance on flux tube evolution in the non-adiabatic regime. Following Equation 3.4, the drag force dominates the magnetic buoyancy of the flux tube when $v_{cr} > v_a(a/H_p)^{1/2}$, where v_{cr} is a representative convective radial velocity, v_a is the Alfvén speed, a is the cross-sectional radius of the flux tube, and H_p is the pressure scale height. In Figure 6.4, we have plotted the right hand side (RHS) of Eq. 3.4 for flux tubes of $\Phi = 10^{22}$ Mx and $\theta_0 = 15^\circ$ for four different initial magnetic field strengths. For comparison, the left panel shows the RHS of Eq. 3.4 for adiabatically evolving flux tubes, and the right panel shows flux tubes subject to radiative heating. Each flux tube is subjected to the same flow field, and representative radial convective flow speeds are also plotted. Flux tubes of $B_0 = 100$ kG in both the left and right panels of Fig. 6.4 are only affected by the strongest downflows, and the plots of $v_a(a/H_p)^{1/2}$ at the apex of the loop are very similar. However, at weaker initial magnetic field strengths, the quantity $v_a(a/H_p)^{1/2}$ is decreased in the upper convection zone for flux tubes subject to radiative heating as compared to flux tubes that evolve adiabatically. Figure 6.4 shows that flux tubes of $\leq$60 kG subject to the effects of radiative heating are affected more strongly by convection than adiabatically evolving flux tubes of the same initial magnetic field strength. This occurs because the field strength of the flux tube becomes weaker for the case with radiative heating.

Due to radiative diffusion in the lower convection zone, flux tubes experience an increase in their internal temperature. The quantity $\Delta T = T_e - T_i$ at the apex of a flux tube

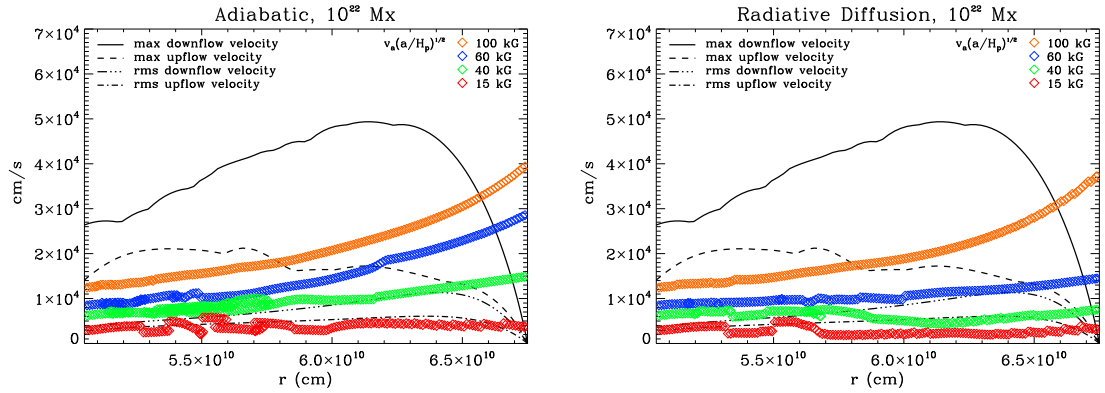

FIGURE 6.4. The RHS of Eq. 3.4 plotted for flux tubes evolving in a convective velocity field assuming adiabatic evolution (left), and with the addition of radiative heating (right). Also plotted are representative convective velocity field radial speeds. Flux tubes of $\leq$60 kG are more susceptible to convective influences when heating due to radiative diffusion is included.

evolving adiabatically and non-adiabatically, both subject to the same convective flows, is shown in Figure 6.5. In the lower portion of the convection zone, heating due to radiative diffusion brings the temperature inside the flux tube closer to that of the external plasma environment. This will increase the internal pressure of the flux tube earlier in its rise, forcing the magnetic field strength of the flux tube to decrease so that the conditions of pressure balance are fulfilled (Eq. 2.5). The magnetic pressure at the apex of two flux tubes, one allowed to evolve adiabatically and one subject to radiative diffusion, is also shown in Fig. 6.5. Indeed, the magnetic pressure, and therefore the magnetic field at the apex of the flux tube subject to radiative heating are less than the adiabatically evolving flux tube throughout the bulk of the convection zone. This reduced magnetic field at the flux tube apex implies that the flux tube will be advected more strongly by convection.

Figure 6.6 shows snapshots of the radial distance r from Sun center of $\Phi = 10^{22}$ Mx, $\theta_0 = 15°$ flux tubes subject to radiative diffusion as a function of the azimuthal angle ϕ (black lines), as well as the external radial velocity experienced by the tube at the height

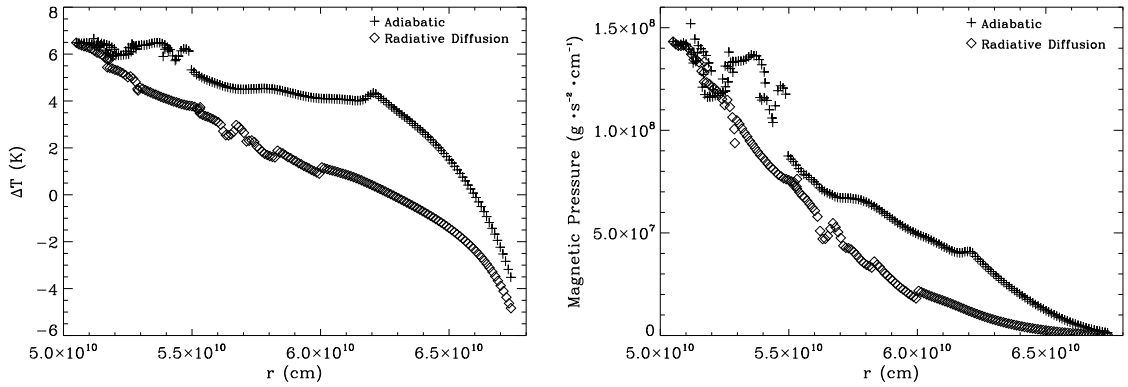

FIGURE 6.5. (Top left) $\Delta T = T_e - T$ and (Top right) magnetic pressure at the apex of a flux tube as a function of height, where $\Phi = 10^{22}$ Mx, $B_0 = 60$ kG, and $\theta_0 = 15°$. These quantities are shown for an adiabatically evolving flux tube (plus symbols), and one subject to heating by radiative diffusion (diamond symbols), both rising through a turbulent solar-like convection zone. Heating supplied by radiative diffusion brings the temperature of the flux tube closer to that of the surrounding environment, increasing its internal gas pressure, resulting in a decrease of magnetic pressure.

r of each tube segment (red lines), similar to Figure 3.4 in Chapter 3.3. These snapshots show clearly that flux tubes of $\leq$60 kG do not anchor in the overshoot region. Rather, these flux tubes, due to heating from radiative diffusion, develop a density deficit very early in their evolution and begin to float away from the overshoot region. They reach the middle of the convection zone, where they are continually buffeted by convection until a buoyant loop reaches the simulation upper boundary.

6.4.3. RADIAL ACCELERATION AND RISE TIMES. Adiabatically evolving flux tubes spend the majority of their rise times at the base of the convection zone waiting for the magnetic buoyancy instability to grow. In our simulations, when convection is present, convective flows provide perturbations to the flux tube that initiate the growth of these instabilities. However, when radiative heating is included, the flux tube gets a *kickstart* in its rise toward the surface, as the flux tube is heated uniformly by the non-zero divergence

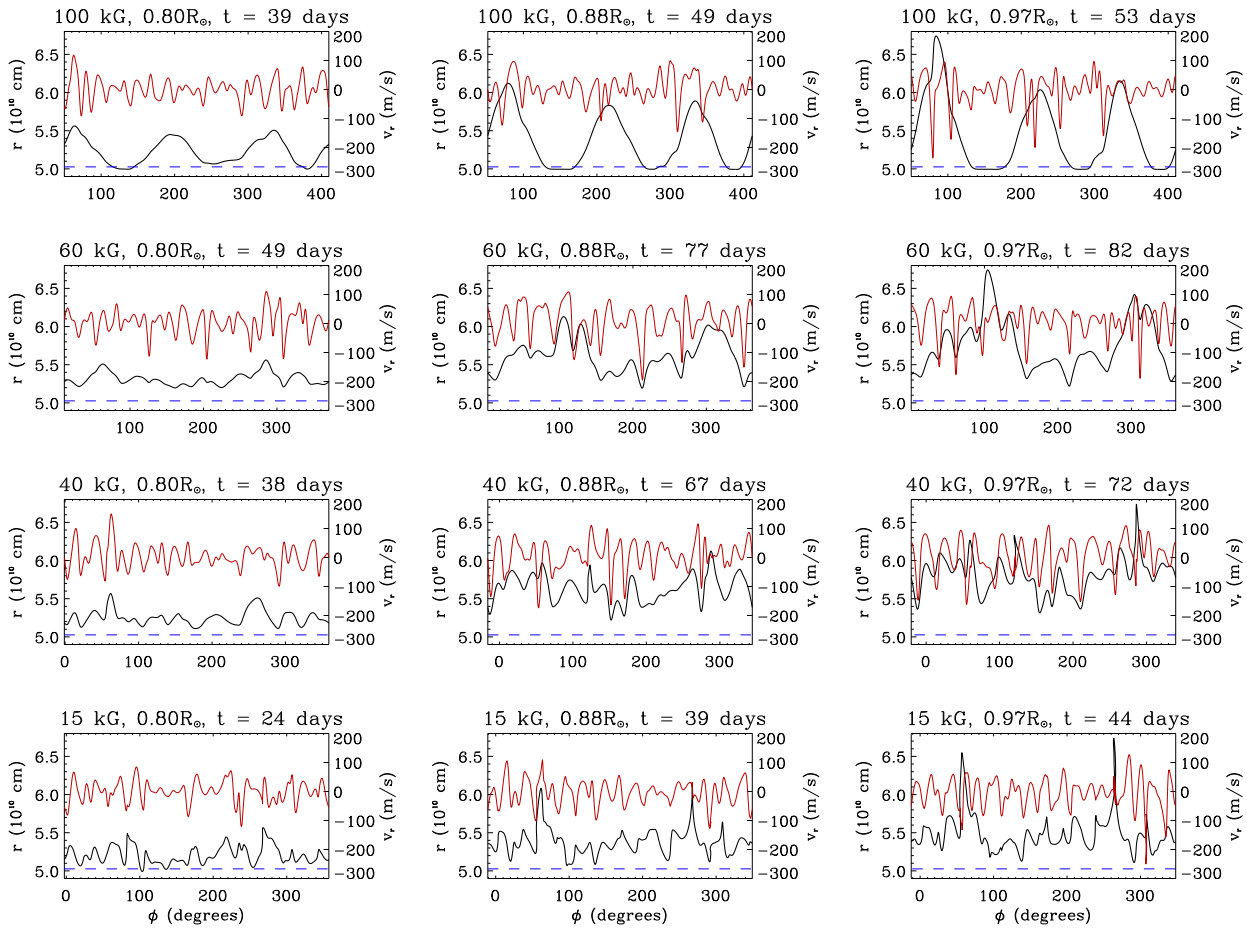

FIGURE 6.6. Flux tube radial distance from Sun center r (black line), plotted with the external radial velocity experienced by the flux tube at the height r of the flux tube segment (red line), both as functions of the azimuthal angle ϕ. These snapshots are for flux tubes with $\Phi = 10^{22}$ Mx, $\theta_0 = 15^\circ$ subject to radiative heating. The dashed line represents the base of the convection zone, below which is the stably stratified overshoot region. These plots show the evolution of the flux tubes in time for various initial magnetic field strengths, indicating that $\leq$60 kG flux tubes subject to radiative heating do not anchor in the overshoot region.

of radiative heat flux in the lower convection zone, thereby increasing its density deficit $\Delta\rho = \rho_e - \rho$ earlier on, helping it to rise in the solar convection zone. The growth of $\Delta\rho$ due to radiative heating is given from Eq. 6.23 by:

$$\left(\frac{d\Delta\rho}{dt}\right)_{rad} = \frac{\rho_e}{P_e}\nabla_{ad}\left(\frac{dQ}{dt}\right)_1, \tag{6.24}$$

and an order of magnitude estimate of the growth due to adiabatic expansion of the flux tube is given by (see Fan and Fisher (1996)):

$$\left(\frac{d\Delta\rho}{dt}\right)_{ad} = \rho_e\frac{v_r}{H_p}\delta, \tag{6.25}$$

where $\delta = \nabla_e - \nabla_{ad}$ and v_r is the radial velocity of the flux tube apex.

Figure 6.7 shows the contribution of radiative heating and adiabatic expansion to the buoyancy evolution of the flux tube. It is clear that in the lower $\sim$1/3 of the convection zone, $d\Delta\rho/dt$ is dominated by contributions from radiative heating. In the remaining $\sim$2/3 of the convection zone above $\sim 0.80 R_\odot$, the evolution of the flux tube can be described as essentially adiabatic, as the heating rate $(dQ/dt)_1$ decreases with height and δ and v_r increase with height.

Components of the radial acceleration at the apex of the flux tube as a function of height following Eq. 3.5 in Section 3.5 are shown in Figure 6.8 for flux tube subject to radiative heating, both with and without convection. In comparing these plots to Fig. 3.6 for flux tubes evolving adiabatically, the total radial acceleration of the flux tubes very near the simulation upper boundary are not substantially different. However, for flux tube evolution when heating due to radiative diffusion is considered, the contribution to the acceleration from buoyancy is larger in the lower $\sim$1/3 of the convection zone than for adiabatically

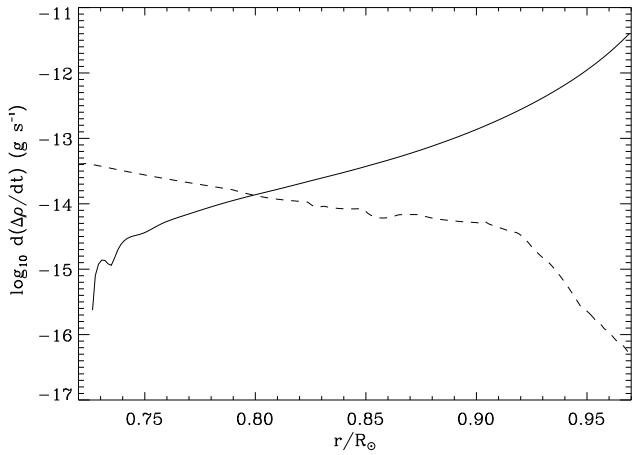

FIGURE 6.7. Adiabatic (solid line) and radiative heating (dashed line) components of $d\Delta\rho/dt$ as computed by Eqs. 6.25 and 6.24 respectively, for a flux tube evolving without convective effects where $B_0 = 60$ kG, $\theta_0 = 15°$, and $\Phi = 10^{22}$ Mx.

evolving flux tubes. This effect is shown best when comparing the left panels of Figure 6.8 to Figure 3.6. When radiative heating is considered, the contribution to radial acceleration from buoyancy increases steadily with height until reaching the upper $\sim$1/3 of the convection zone. Once in the upper convection zone, the evolution of the flux tube becomes essentially adiabatic, similar to the flux tubes discussed in Chapter 3.

The inclusion of radiative diffusion reduces the flux tube rise time to $\leq$0.2 years in all cases, as compared to $\leq$0.7 years for flux tubes evolving adiabatically (see Fig. 6.9). The reduction is minimal for 80 and 100 kG flux tubes of all flux values, and for flux tubes of 10^{20} Mx for all initial magnetic field strengths. In the large magnetic field strength regime $\geq$80 kG, the average rise times are nearly the same for flux tubes both with and without radiative diffusion because of their strong magnetic buoyancy and tension, and because their undular magnetic buoyancy instabilities of order $m = 1$ to $m = 3$ grow quickly, facilitating anchoring in the overshoot region. For flux tubes of $\Phi = 10^{20}$ Mx, adiabatically evolving flux tubes do have a slightly larger rise time than flux tubes subject to radiative diffusion,

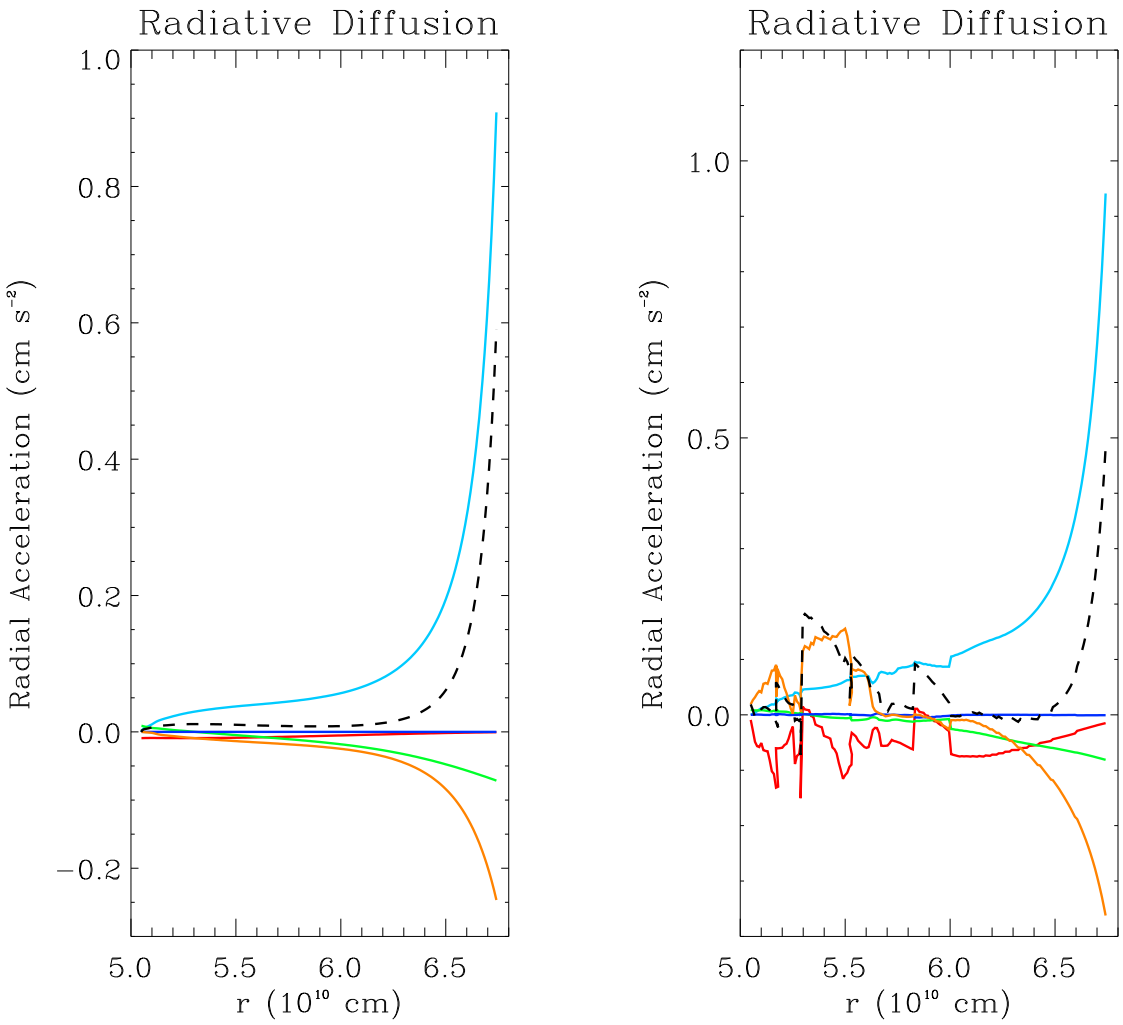

FIGURE 6.8. Radial acceleration of the flux tube apex for a flux tube of $\Phi = 10^{22}$ Mx, $B_0 = 60$ kG, $\theta_0 = 15°$, without (left) and with (right) convective effects, but both subject to radiative heating. Components contributing to the radial acceleration following Eq. 3.5 are plotted as a function of r: (light blue) buoyancy, (red) tension, (green) Coriolis force, (orange) drag force, (dark blue) additional terms, (dotted line) total acceleration.

but only by a few days on average. At small magnetic flux, tubes are coupled more strongly to convection, so their very similar average rise times in this regime are due to convection rather than the difference in buoyancy considerations.

There is a large reduction of rise times for flux tubes subject to radiative heating in the $10^{21} - 10^{22}$ Mx, $B_0 = 15 - 60$ kG regime as compared to flux tubes that evolve adiabatically:

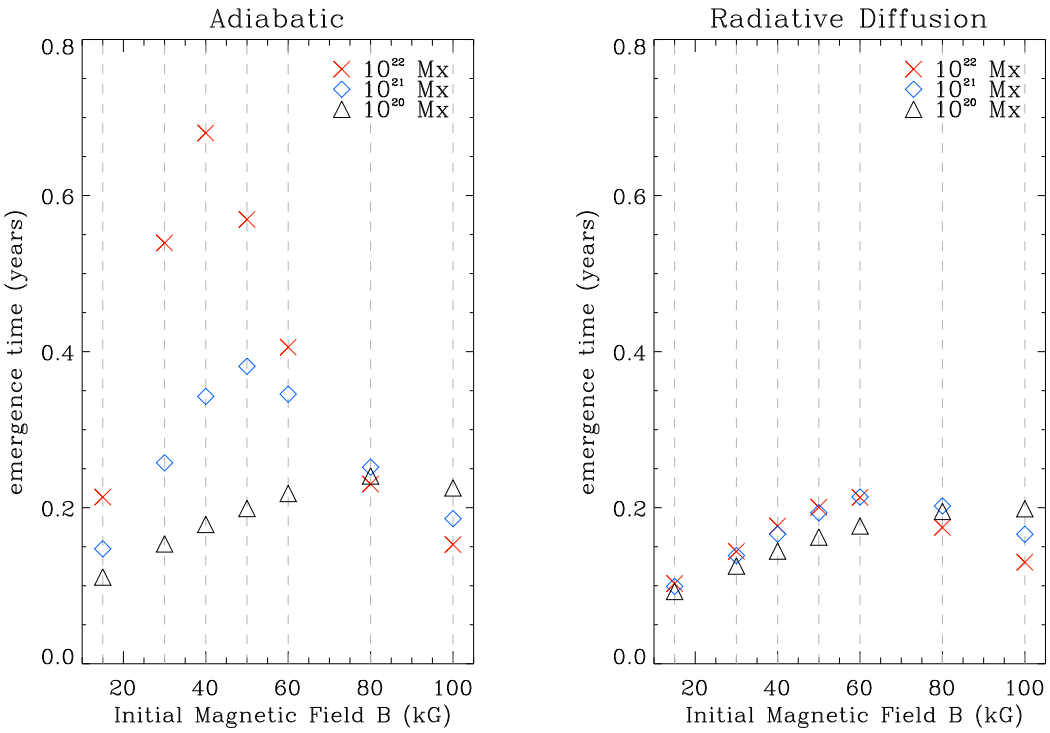

FIGURE 6.9. (Left) Average rise times for adiabatically evolving flux tubes subject to convection. (Right) average rise times for flux tubes evolving with the influence of heating due to radiative diffusion, also subject to convection. Radiative heating reduces the average rise time of the flux tube in most cases.

a difference of $\sim 0.05 - 0.5$ years. This reduction is a result of radiative heating contributing a significant increase to the buoyancy of the flux tube early in its rise, allowing the tubes to begin their buoyant rise toward the surface earlier than flux tubes with only adiabatic effects. Radiative diffusion also increases the internal pressure of the tube early on, forcing a reduction in its magnetic field strength, therefore it is more susceptible to convection.

It should be noted that $(dQ/dt)_1$ is significantly greater than $(dQ/dt)_2$ for all flux tubes of $B_0 = 15 - 100$ kG and flux of 10^{22} Mx. As the cross-section of the flux tube decreases, $(dQ/dt)_1$ is no longer significantly dominant at magnetic flux values of 10^{21} Mx for tubes of $B_0 \geq 80$ kG, and flux values of 10^{20} Mx for tubes of $B_0 \geq 40$ kG. Since we have chosen to neglect $(dQ/dt)_2$ in our treatment of the thin flux tube energy equation, the average rise

times for flux tubes where $(dQ/dt)_1$ is not significantly dominant should be treated as upper limits. The addition of $(dQ/dt)_2$ would bring the internal temperature of the flux tube closer to temperature equilibrium with the outside plasma, thereby increasing the flux tube density deficit even more, resulting in an even shorter rise time.

6.5. Emergence Properties

In this section, we investigate the latitude of emergence and tilt angle trends of 10^{22} Mx flux tubes subject to both convection and heating due to radiative diffusion. As discussed in Appendix G, the results in this section are drawn from a total of 2293 flux tube simulations. We will compare these results to those of Chapter 4 for flux tubes that evolve adiabatically.

6.5.1. Latitude of Emergence.

In Figure 6.10, we have plotted the emergence latitude (θ_{em}) of the flux tube apex as a function of the flux tube's initial latitude (θ_0) at the base of the convection zone. For comparison, this was done for flux tubes that evolve adiabatically (left panel), and for flux tubes subject radiative heating (right panel). A gray dashed line indicates where the emergence latitude equals the initial latitude. If convective effects are ignored, a flux tube would emerge with $\theta_{em} \approx \theta_0$ if its dynamic evolution is dominated significantly by the buoyancy force. When flux tubes evolve adiabatically, the values of their emergence latitudes are primarily the result of a combination of the effects of buoyancy, the Coriolis force, and convection. Convection introduces a scatter in the emergence latitude values, which increases as the magnetic field strength of the flux tube decreases, and flux tubes become more susceptible to deformation by convective flows.

Adiabatically evolving flux tubes of $\geq$80 kG rise mostly radially as the buoyancy force acting on the flux tube overpowers the Coriolis force (see Chapter 4.2 for more details). However, especially at weak magnetic field strengths of $\leq$30 kG, the buoyancy force is reduced

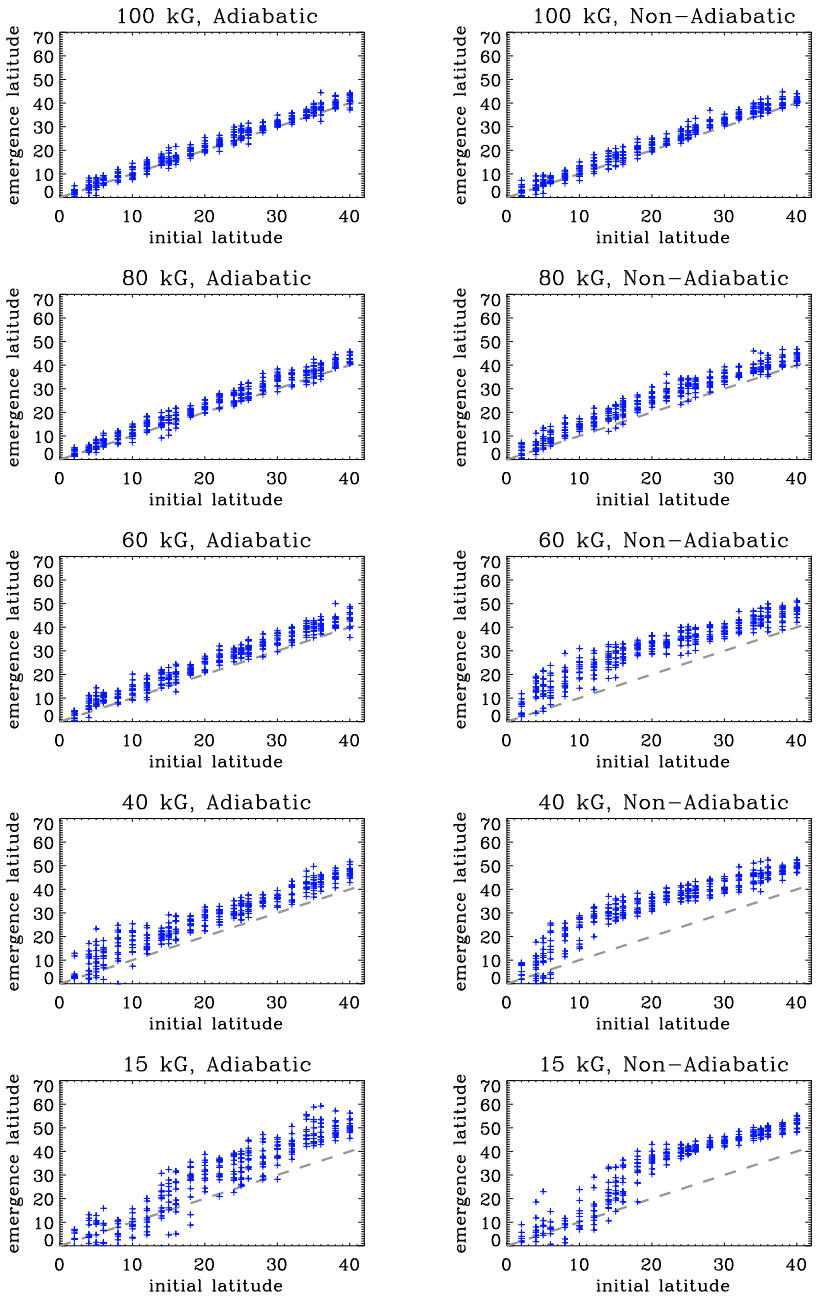

FIGURE 6.10. Initial latitude versus emergence latitude of the flux tube apex for tubes with initial magnetic field strengths of 100, 80, 60, 40, and 15 kG (top to bottom) with magnetic flux of 10^{22} Mx. The left column shows the latitudinal deflection for flux tubes that evolve adiabatically, and the right column for flux tubes that evolve with the influence of radiative heating. Both axes are in units of degrees. With the addition of radiative heating, middle-to-high latitude flux tube of moderate to weak magnetic field strength deflect poleward.

compared to the Coriolis force acting on the flux tube, forcing the apex of the flux tube to deflect poleward. This effect is responsible for the moderate latitudinal deflection of 15 kG flux tubes, especially at high latitudes (see Fig. 6.10, lower left panel).

When the effects of radiative heating are included in the flux tube energy equation (right panel of Fig. 6.10), flux tubes of $80 - 100$ kG emerge with latitudes similar to flux tubes that evolve adiabatically. This is not surprising, as flux tubes in this magnetic field strength regime do anchor in the overshoot region. However, as the magnetic field strength of these flux tubes decrease, we begin to notice that flux tubes subject to radiative heating tend to emerge at latitudes larger than adiabatically evolving flux tubes, especially in mid-latitudes. As discussed previously, this occurs because the heat input to the flux tube supplied by radiative diffusion in the lower convection zone increases the buoyancy of the flux tube early in its evolution, forcing it to float away from the convection zone base before undular magnetic buoyancy instabilities set in to help anchor the flux tube in the overshoot region. At low latitudes for flux tubes of $\leq$60 kG, convective flows are able to keep the flux tube from slipping poleward, and there are no latitudinal zones void of flux emergence, a problem encountered by previous thin flux tube simulations where $B_0 \leq$30 kG, and flux tubes evolve adiabatically without convection (e.g. D'Silva and Choudhuri 1993; Caligari, Moreno-Insertis, and Schüssler 1995).

6.5.2. Tilt Angles. In this section, we present tilt angle trends for 10^{22} Mx flux tubes allowed to evolve with the influence of radiative heating and solar-like convection. Except for our discussion on the preferred tilt angle, all tilt angles have been shifted to fall within the range of [-90°, 90°], as per the discussion in Chapter 4.3. Figure 6.11 shows the tilt angle as a function of emergence latitude for flux tubes of 10^{22} Mx that evolve adiabatically (left

TABLE 6.2. (Column 2) Slopes m_A (unitless) of the best-fit line following Method 1 for flux tubes of 10^{22} Mx, and (Column 3) slopes m_B (units of degrees) of the best-fit line following Method 2 for flux tubes of 10^{22} Mx. Slopes of the best fit lines following Methods 1 and 2 show a similar trend, reaching a maximum at 60 kG. (Column 4) Standard deviation σ_{fit} (units of degrees) of the tilt angle about the best-fit Joy's Law equation (Method 1), where tilt angles are shifted to fall within the range of [-90°, 90°]. For magnetic field strengths of $40 - 60$ kG, the values of σ_{fit} are substantially larger than for 10^{22} Mx flux tubes that evolve adiabatically, as given in Table 4.5.

B	m_A	m_B	σ_{fit}
100 kG	0.32 ± 0.02	19.8° ± 1.0°	7.6°
80 kG	0.40 ± 0.02	25.7° ± 1.2°	10.4°
60 kG	0.44 ± 0.04	27.1° ± 2.4°	23.6°
50 kG	0.42 ± 0.04	26.2° ± 2.6°	26.2°
40 kG	0.27 ± 0.05	16.7° ± 3.4°	34.8°
30 kG	0.32 ± 0.05	20.0° ± 3.3°	33.7°
15 kG	0.31 ± 0.07	19.1° ± 4.3°	42.5°

panel), and those that evolve with the influence of radiative heating included (right panel). For magnetic field strengths of 100 kG, the tilt angle plots are very similar. However, for magnetic field strengths of 15 and 50 kG, the tilt angle distribution for flux tubes subject to radiative heating is spread out more at low latitudes than for flux tubes that evolve adiabatically. The best-fit lines shown in Figure 6.11 are calculated following Method 1 as discussed in Chapter 4.3.1.1, and are given in the second column of Table 6.2 for flux tubes of 10^{22} Mx subject to radiative heating. Table 6.2 also reports the tilt angle trend following Method 2 discussed in Chapter 4.3.1.2 (column 3), and the scatter of the tilt angle around the best-fit line, σ_{fit}, following the discussion in Chapter 4.3.2.1 for tilt angles that fall in the range [-90°, 90°] (column 4).

In comparison to the slopes m_A and m_B for adiabatically evolving flux tubes of 10^{22} Mx (see Tables 4.2 and 4.3 in Chapter 4, Section 4.3), the slopes of the best-fit lines we obtain for flux tubes subject to radiative heating are larger within the reported uncertainties for flux tubes of $60 - 100$ kG, and smaller for flux tubes of 40 kG. We expected that the overall

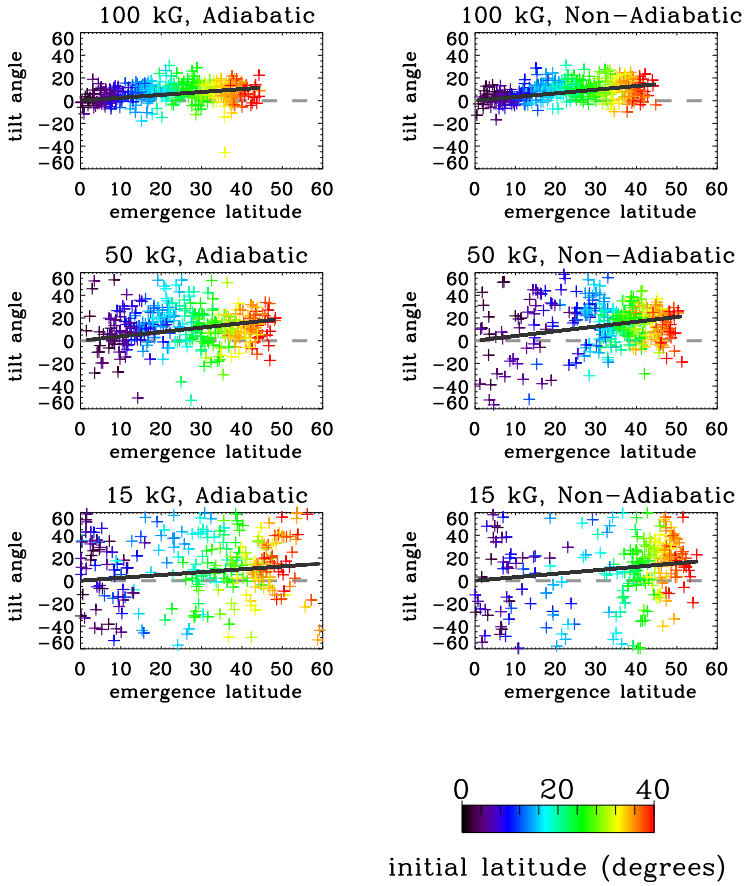

FIGURE 6.11. Tilt angles as a function of emergence latitude for initial magnetic field strengths of 100, 50, and 15 kG (top to bottom) for simulations with the influence of convection. This is done for magnetic flux of 10^{22} Mx for flux tubes that evolve adiabatically (left column), and those subject to the influence of radiative heating (right column). The black line is the linear best-fit following Method 1. A color bar indicates the original starting latitude of the flux tube. All axes are in units of degrees.

tilt angle best-fit slope would be reduced for flux tubes subject to radiative heating because the value of $\delta T = T_e - T$ is decreased, initiating a converging parallel flow of mass elements at the flux tube apex at greater depths (e.g. Fan, Fisher, and McClymont 1994). Due to this converging flow, the Coriolis force acts to tilt the flux tube apex away from the equator in either hemisphere (opposite the Joy's Law trend), thereby reducing the tilt angle (also see Chapter 4.3.1.1).

We suggest that the increased tilt angle trend of $60 - 100$ kG flux tubes subject to radiative heating, as compared to adiabatically evolving flux tubes, is related to a decrease in magnetic field strength, and thus a stronger coupling to helical convective upflows. This effect is capable of overcoming the Coriolis force induced tilt of the wrong sense (i.e. away from the equator) due to a converging parallel flow at the flux tube apex. However, this does not explain why 40 kG flux tubes subject to radiative diffusion show a reduced tilt angle trend compared to adiabatically evolving flux tubes. While flux tubes of $\leq$60 kG do not anchor, one or both of the footpoints of the buoyantly rising loops are usually located within the lower $\sim$1/3 of the convection zone (see Fig. 6.6). However, for non-adiabatically evolving flux tubes of 40 kG, the flux tube as a whole resides in the middle of the convection zone throughout much of its evolution, where it is continually pummeled by convective upflows and downflows. Buoyant loops of these flux tubes that reach the simulation upper boundary tend to have their footpoints located in the middle of the convection zone (see again Fig. 6.6). Perhaps the fact that in this regime, the flux tube footpoints are higher in the convection zone also contributes to the reduced tilt angle trend. If stretching of the flux tube loop contributes to the tilting motion supplied by the Coriolis force (e.g. D'Silva and Choudhuri 1993), then loops with troughs that do not extend to the base of the convection zone will experience a reduced tilt angle trend. The combined effects of the reduced stretching of the loop and the increased converging parallel flow at the flux tube apex due to a reduction in δT may be strong enough at 40 kG magnetic field strengths to overcome the increased coupling to convective helical upflows in the non-adiabatic regime.

The tilt angle slopes for flux tubes subject to radiative heating peak at 60 kG, whereas they peak at 40 kG for adiabatically evolving flux tubes of 10^{22} Mx. In both cases, this peak

corresponds with the magnetic field strength where the flux tubes take the longest time to emerge. Owing to the large spread in empirical Joy's Law equations as discussed in Chapter 4, all of the slopes m_A and m_B for our Joy's Law best-fit equations to the simulation data still fall within those derived from observations (e.g. Dasi-Espuig *et al.* 2010; Fisher, Fan, and Howard 1995; Stenflo and Kosovichev 2012).

Figure 6.12 shows the average binned tilt angles for $80 - 100$ kG flux tubes of 10^{22} Mx that evolve with the influence of radiative heating (i.e. the flux tubes that anchor). The average tilt angles have been fit following Method 3 in Chapter 4.3.1.3, which assumes that the fit has not been forced to go through the origin. The best-fit equation obtained is $\alpha = (0.39 \pm 0.07)\theta + (1.1^\circ \pm 1.3^\circ)$. When 60 kG flux tubes are included, the slope of the best-fit line increases as do the uncertainties on the fit parameters, but the y-intercept remains unchanged, with $\alpha = (0.47 \pm 0.11)\theta + (1.1^\circ \pm 1.9^\circ)$. For flux tubes of 10^{22} Mx and magnetic field strengths of $60 - 100$ kG that evolve adiabatically, the best-fit line as found in Chapter 4.3.1.3 is $\alpha = (0.32 \pm 0.04)\theta + (2.1^\circ \pm 0.7^\circ)$. While the two best-fit equations derived following Method 3 for flux tubes subject to radiative heating agree with the equation obtained by Li and Ulrich (2012), they still show a larger slope than the equation derived from our adiabatically evolving flux tube simulations. The best-fit line found following Method 3 for the adiabatically evolving flux tubes in Chapter 4 agrees more closely with McClintock and Norton (2013), who use Mount Wilson sunspot group tilt angles. However, the best-fit line for the flux tubes subject to radiative heating agrees more closely with Li and Ulrich (2012), who use magnetograms to derive active region tilt angles.

The scatter of the tilt angles about the Joy's Law best-fit equation found using Method 1, denoted as σ_{fit} following Eq. 4.4, are shown in the fourth column of Table 6.2 for 10^{22}

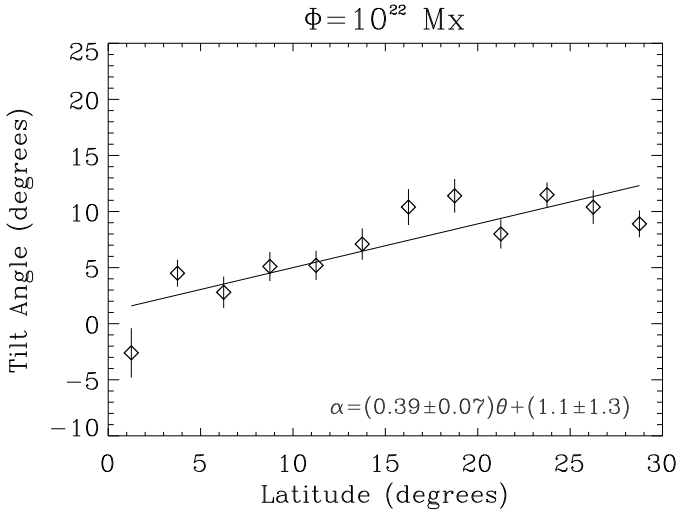

FIGURE 6.12. Average binned tilt angles for 10^{22} Mx, $80-100$ kG flux tubes subject to radiative heating. The result of the linear best-fit following Method 3 is also shown. Error bars are the standard deviation of the mean for each binned average tilt angle (2.5° in latitude).

Mx flux tubes evolving with the addition of radiative heating. Due to the tilt angle scatter introduced by convection, σ_{fit} of the $40-60$ kG flux tubes are larger than in the adiabatic regime, as reported in Table 4.5 in Chapter 4. Using Mount Wilson white light sunspot group data, Fisher, Fan, and Howard (1995) found that $\sigma_{fit} \sim 30°$. A value of $\sigma_{fit} \leq 30°$ is found for flux tubes of $\geq$50 kG from our simulations when heating due to radiative diffusion is considered.

Additionally, the most preferred tilt angle for 10^{22} Mx flux tubes subject to radiative heating is $12.7° \pm 3.6°$, as compared to $9.13° \pm 3.2°$ for 10^{22} Mx flux tubes that evolve adiabatically. These values were found by performing a Gaussian fit to a histogram of the distribution of tilt angles in the range of [-180°, 180°], as was done in Chapter 4, Section 4.3.3 for adiabatically evolving flux tubes. The uncertainty on the preferred tilt angle is the standard deviation of the Gaussian fit. Again, we note an increase in tilt angle for flux tubes with the inclusion of radiative heating, and also a wider distribution around the mean. When

heating due to radiative diffusion is included, 9.9% of flux tubes emerge with anti-Hale tilt angles (i.e. $\geq |90°|$) as compared to 5.0% for 10^{22} Mx flux tubes that evolve adiabatically, and ∼4% as found via observations of medium to large-sized active regions (Wang and Zirin 1989; Stenflo and Kosovichev 2012). Such that our simulations of 10^{22} Mx flux tubes subject to radiative heating exhibit only ∼4% anti-Hale tilt angles, we would have to exclude flux tubes with magnetic field strengths of ≤40 kG.

6.6. A Note on Flux Tube Storage in the Overshoot Region

In one solar dynamo paradigm, it is suggested that the dynamo generated magnetic field is *stored* in the overshoot region until it becomes buoyant enough to rise toward the surface (e.g. Spiegel and Weiss 1980; Galloway and Weiss 1981; Miesch 2005). It has been recognized that while the stable stratification of the overshoot region stabilizes magnetic flux tubes against buoyancy instabilities, the inflow of heat to the flux tube due to radiative diffusion forces the flux tube to rise quasi-statically (i.e. all forces closely balance) out of the overshoot region in ∼1 year or less, short compared to the ∼11 year solar cycle period (e.g. van Ballegooijen 1982; Rempel 2003; Fan and Fisher 1996).

From the equation for $d\Delta\rho/dt$ (Eq. 6.23), it is possible to derive an expression for the radial velocity (rise speed) of the flux tube in the overshoot region, and subsequently a characteristic rise time for an upward drift of the flux tube out of the overshoot region when radiative diffusion is considered. For simplicity, we consider a uniform horizontal flux tube that remains nearly neutrally buoyant (i.e. in quasi-equilibrium) in the overshoot region such that $\partial v_l/\partial s$, $\mathbf{v}\cdot\mathbf{k}$, $d\Delta\rho/dt$, and $\Delta\rho$ are equal to zero. Using these assumptions, and

only retaining terms to first order in $1/\beta = B^2/8\pi p_e$, Equation 6.23 becomes:

$$0 = \rho_e \frac{v_r}{H_p}\left[\delta + \left(\frac{1}{\gamma} - \frac{2}{\gamma^2}\right)\frac{1}{\beta}\right] + \frac{\rho_e}{P_e}\nabla_{ad}\left(\frac{dQ}{dt}\right)_1. \tag{6.26}$$

Solving Equation 6.26 for v_r:

$$v_r = \frac{H_p}{P_e}\nabla_{ad}\left(\frac{dQ}{dt}\right)_1\left[-\delta + \frac{1}{\beta}\left(\frac{2}{\gamma^2} - \frac{1}{\gamma}\right)\right]^{-1}, \tag{6.27}$$

where $\delta = \nabla_e - \nabla_{ad}$, and is referred to as the superadiabaticity in a stably stratified region where δ takes on a negative value. For typical values in the overshoot region, $H_p \sim 6{\times}10^9$ cm, $P_e \sim 6{\times}10^{13}$ g cm^{-1} s^{-2}, $(dQ/dt)_1 \sim 30$ erg cm^{-3} s^{-1}, $\nabla_{ad} \sim 0.4$, and $\gamma \sim 5/3$. Then an estimate for the rise speed (cm s^{-1}) of the flux tube in the overshoot region becomes:

$$v_r \sim 1.2 \times 10^{-3}\left[-\delta + \frac{0.12}{\beta}\right]^{-1}. \tag{6.28}$$

In the overshoot region, β ranges from $1.5{\times}10^5$ for 100 kG magnetic fields to $6.7{\times}10^6$ for 15 kG magnetic fields. The rise speed of the flux tube is highly dependent on the suparadiabaticity δ of the overshoot region, which has yet to be pinned down, but is most likely in the range of -10^{-3} to -10^{-6} (e.g. Rempel 2003, 2004). As δ gets closer to zero, the term $0.12/\beta$ becomes increasingly important. The quantity $0.12/\beta$ is largest for larger magnetic field strengths. A large magnetic field therefore has a slower upward drift of the flux tube out of the overshoot region. Using $B_0 = 100$ kG, and for different estimates of the value δ, the rise speed v_r and time τ for a flux tube to escape from the overshoot region are shown in Table 6.3, assuming the depth of the overshoot region is $\sim 10^9$ cm. Thus for flux tubes to remain stored in the overshoot region for the length of the solar cycle, δ needs to be

TABLE 6.3. The rise speed v_r (Column 2) and rise time τ (Column 3) for a flux tube to escape from the overshoot region for varying estimates of the superadiabaticity δ (Column 1). In comparison, the length of the solar cycle is only $\sim$11 years.

δ	v_r (cm s^{-1})	τ
-10^{-3}	1.2	26 years
-10^{-4}	12	2.6 years
-10^{-5}	110	98 days
-10^{-6}	670	17 days

somewhere between -10^{-4} and -10^{-3}. The value of δ may also change with height in the overshoot region, so the formation level of the flux tubes is also an important consideration.

It is likely that a strong magnetic field in the overshoot region can suppress the overshooting motions into the stably stratified region below the convection zone such that ∇_e deviates more substantially from ∇_{ad}, coming closer to ∇_{rad} (e.g. Fan and Fisher 1996; Rempel 2003). This would result in a larger value for $|\delta|$, and a longer storage time in the overshoot region. It has been suggested by van Ballegooijen (1982) that instead, an equatorward meridional flow present in the overshoot region may be sufficient to keep flux tubes stable in the overshoot region for a solar cycle.

It is as of yet not clear whether magnetic flux tubes are generated at a tachocline interface in the overshoot region of the Sun, however, this is the paradigm we adopt for this study. If indeed flux tubes are stored in the overshoot region, the superadiabaticity δ in the region where they are stored is not well known. For the thin flux tube simulations used in this work, it is assumed that the flux tube has already risen out of the overshoot region. Flux tubes with footpoints that do anchor in the overshoot region do so because convective motions initiate buoyancy instabilities and amplify undulations, which cause the flux tube troughs to penetrate into the stably stratified plasma. In Chapters 3 and 4 where radiative diffusion is not considered, all flux tubes that evolve with convection have footpoints that penetrate

into the overshoot region. However, when radiative heating is considered, flux tubes of $\leq$60 kG do not anchor because their magnetic buoyancy instabilities do not grow fast enough, and subsequently the flux tube floats away from the base of the convection zone because of its enhanced buoyancy. When radiative diffusion is considered, flux tubes of $\geq$80 kG have anchored footpoints that continue to drift out of the overshoot region.

We have performed some simulations where the flux tube is initiated in the overshoot region and allowed to evolve with overshooting convective flows and the influence of radiative diffusion. Regardless of magnetic field strength, magnetic flux, or the superadiabaticity of the overshoot region, all flux tubes rise quasi-statically through the overshoot region, with all portion of the toroidal flux tube emerging from the overshoot region at roughly the same time. Once the toroidal flux tube has emerged as a whole from the overshoot region, the evolution of the flux tube proceeds in the same way as when we initiate the flux tube at only 2.4 Mm above the base of the convection zone, as is the procedure following the discussion in Chapter 2. In order to initiate the flux tube in the overshoot region such that the flux tube always remains anchored except for buoyantly rising loops, we would have to artificially introduce an entropy perturbation to the flux tube of large amplitude, as was done in Fan and Fisher (1996), rather than allowing convective flows to provide the perturbations self-consistently.

6.7. Summary

In this Chapter, we modify the energy equation of our thin flux tube model to include the effect of flux tube heating due to radiative diffusion. This allows us to study the influence of radiative diffusion, in conjunction with solar-like convective flows, on the dynamic evolution of active-region-scale magnetic flux tubes. In our treatment of the heat input per unit volume

of the flux tube dQ_v/dt, we only include $(dQ/dt)_1$, the contribution from the deviation of the mean temperature gradient in the external plasma environment from that of radiative equilibrium. We have here neglected $(dQ/dt)_2$, the contribution from radiative diffusion across the flux tube due to the temperature difference between the flux tube and the external plasma environment. This is only a valid approach for flux tubes in the range of $15 - 100$ kG for magnetic flux values of 10^{22} Mx. In a future study, we will incorporate $(dQ/dt)_2$ to the energy equation to more accurately capture dQ_v/dt for all active-region-scale flux tubes.

As a result of the inclusion of radiative diffusion to the thin flux tube energy equation, we find that flux tubes of $\leq$60 kG subject to convective flows are no longer able to anchor in the overshoot region, unlike the flux tubes discussed in Chapters 3, 4, and 5. Heating of the flux tubes supplied by radiative diffusion brings the internal temperature of the flux tube closer to that of the external plasma, increasing its density deficit (i.e. buoyancy) in the process. The flux tube is now more buoyant earlier in its rise, and floats away from the base of the convection zone before magnetic buoyancy instabilities can set in to anchor the troughs of the flux tube in the overshoot region. This uniformly increased buoyancy of the flux tube early in its evolution results in a rise time of $\leq$0.2 years for all flux tubes, which is significantly less than the maximum rise times of adiabatically evolving flux tubes by $\sim$0.5 years. This increased buoyancy does not translate to a faster acceleration of the flux tube apex, but rather jumpstarts the flux tube's rise toward the surface. In comparison, a large portion of the flux tube's rise time in the adiabatic regime is spent waiting for a magnetic buoyancy instability to develop such that it can rise toward the surface.

Unlike adiabatically evolving flux tubes of 10^{22} Mx, flux tubes of $\leq$60 kG that evolve with the addition of radiative heating exhibit a larger poleward deflection, especially at mid

to high latitudes. The drift of $\leq$60 kG flux tubes from the base of the convection zone and subsequent lack of anchoring facilitates a poleward slippage, which is especially severe when convective flows are not included. As flux tubes rise buoyantly due to the uniform heating supplied by radiative diffusion, conservation of angular momentum drives a retrograde flow of plasma inside the flux tube. which enhances the Coriolis force acting on the flux tube in comparison to the buoyancy force. When convective motions are included, the flux tube is prevented by convective motions from emerging significantly poleward.

Compared to flux tubes that evolve adiabatically, we note that tilt angles of the flux tubes studied in the Chapter show an increased Joy's Law best-fit line slope for $60 - 100$ kG magnetic field strengths, but a decreased slope for 40 kG flux tubes. We attribute the increase in tilt angles of the $60-100$ kG flux tubes to a stronger coupling to helical convective upflows than adiabatically evolving flux tubes possess for the same magnetic field strength. At these magnetic field strengths, this effect is able to overcome the tilting action of the wrong sense induced by the converging parallel flow of plasma at the flux tube apex, which sets in at lower depths for flux tubes subject to radiative heating. However, the reduced tilt angles for 40 kG flux tubes studied in this Chapter as compared to the adiabatically evolving flux tubes in Chapter 4 is likely due to both the converging parallel flow at the flux tube apex at lower depths as well as the fact that these flux tubes have their buoyant loop footpoints in the middle of the convection zone rather than near the base of the convection zone. As such, a rising loop will not be stretched as much, exacerbating the convergence rather than divergence of the plasma elements at the flux tube apex, resulting in a tendency of the Coriolis force to induce a tilting of the flux tube away from, rather than toward, the equator. Even with radiative heating considered, 10^{22} Mx flux tubes of all magnetic field

strengths considered exhibit a Joy's Law equation in agreement with observations. However, magnetic field strengths of $\leq$40 kG exhibit too large a tilt angle scatter as compared to solar observations and also have too large a percentage of anti-Hale tilt angles, pointing toward larger magnetic field strengths as the progenitors of solar active regions as reported in Chapter 4.

We also discuss the problem of flux storage in the overshoot region, suggesting that the time for flux tubes to escape from the overshoot region is highly sensitive to the value of the superadiabaticity δ. When we allow flux tubes to originate in the overshoot region, all magnetic field strength flux tubes rise quasi-statically through the overshoot region. Once they drift out of the overshoot region, the evolution of the flux tube proceeds in the same way as when we initiate the flux tube 2.4 Mm above the base of the convection zone.

The simulations performed in the Chapter lead us to a better and more comprehensive understanding of the processes involved in flux emergence on the Sun and solar-like stars. It is likely that if flux tubes are generated in the overshoot region by the dynamo process, that they drift upward out of the overshoot region due to heating of the tube plasma as a result of the deviation of the temperature gradient from that of radiative equilibrium. Once out of the overshoot region, flux tubes have a density deficit which allows them to drift upward without initially requiring a magnetic buoyancy instability. Only when reaching the middle to upper convection zone does the dynamic evolution of the flux tube apex proceed adiabatically. Our simulations show that flux tubes do not necessarily need to anchor in the overshoot region to produce emergence properties similar to those of active regions on the Sun.

CHAPTER 7

Future Directions for the TFT+ASH Model

By coupling the thin flux tube (TFT) model to a solar-like convective flow field computed through the Anelastic Spherical Harmonic (ASH) code, we are able to investigate both the local and global dynamics evolution properties of active-region-scale flux tubes. This approach is advantageous, as it incorporates a well-tested stellar convection model with the computationally inexpensive TFT approximation model. The TFT+ASH approach also effectively preserves the ideal flux frozen-in condition, unlike three-dimensional simulations which suffer from artificial diffusion. We foresee some interesting and fruitful future projects for the TFT+ASH model, a few of which are discussed here.

7.1. The Magnetic Field Twist in Rising Flux Tubes

From photospheric vector magnetograms, it is clear that there is an intrinsic twist associated with the magnetic field lines of emerging active region flux tubes (e.g. Pevtsov, Canfield, and Metcalf 1995; Pevtsov, Canfield, and Latushko 2001; Pevtsov, Maleev, and Longcope 2003). This means that magnetic field lines twist about the flux tube axis rather than being parallel to the axis of the tube, as is the assumption made in the thin flux tube model discussed in Chapter 2. The magnetic field twist associated with solar active regions shows a small, but statistically significant preference of a left-handed twist in the Northern hemisphere, and a right-handed twist in the Southern hemisphere, which is independent of the solar cycle. In fact, it is likely that flux tubes require some twist to remain coherent as

they traverse the convection zone (e.g. Longcope, Fisher, and Arendt 1996; Moreno-Insertis and Emonet 1996; Fan, Abbett, and Fisher 2003).

To interpret such observations, Longcope and Klapper (1997) and Fan and Gong (2000) have explicitly included a weak twist in a thin flux tube model. Magnetic helicity is defined as $H = \int \mathbf{A} \cdot \mathbf{B}\ dV$, where $\mathbf{A}$ is the vector potential of the magnetic field $\mathbf{B}$. For a closed flux tube, the magnetic helicity of the tube can be divided into two components: writhe (W) and twist (T) (e.g. Berger and Field). The twist represents the twisting of the field lines about the flux tube axis, and writhe is a measure of the *helicalness* of the flux tube axis. Because of the conservation of helicity $H = T + W$, a reduction in twist will increase the writhe, and vice versa. As a result, the change in writhe will have the opposite sign as the change in twist.

A tilting motion of the flux tube apex imparted by the Coriolis force causes a writhing of the flux tube toward the equator, a motion resulting in a right-handed (left-handed) helix in the Northern (Southern) hemisphere. Due to the conservation of helicity this motion induces a local magnetic field twist at the flux tube apex of opposite sense. It has been posited that tilting of the flux tube provided by the Coriolis force as well as the helical turbulent flows in the solar convection zone may be sufficient enough to produce the magnetic field twist associated with solar active regions (e.g. Longcope, Fisher, and Pevtsov 1998; Fan and Gong 2000). Both of these effects are hemispheric dependent, rather than solar cycle dependent.

With our thin flux tube model, it is possible to explore the twist of the magnetic field lines associated with the writhing of magnetic flux tubes. Similar to Longcope and Klapper (1997) and Fan and Gong (2000), we can derive an equation that describes the evolution of the twist rate of the flux tube in response to the helical motion of the flux tube. Incorporating

this into our currently existing flux tube model, we will be able to shed light on the possible generation of magnetic field twist imparted by solar-like convective motions. It is not known whether the solar dynamo mechanism generates flux tubes with an intrinsic twist, or no twist at all. In particular, we can investigate whether or not untwisted flux tubes originating at the base of the convection zone are capable of emerging with twist similar to solar active regions, or if an intrinsic twist of some amplitude is required. This is a promising application of the thin flux tube model, of importance to our understanding of the operation of the solar dynamo and the manifestation of active region emergence properties.

7.2. Magnetic Flux Emergence on a Young Sun

Our Sun rotated much more rapidly when it was younger, as is suggested by observations of rapidly rotating solar-like stars (e.g. Strassmeier 2009) and the influence of the solar wind, which removes angular momentum from the Sun over time in a process known as magnetic braking (e.g. Weber and Davis 1967). By studying how flux emergence may have occurred on the young, rapidly rotating Sun, we are likely to learn more about the nature of the solar dynamo early in the Sun's history. This section describes results from some preliminary simulations of a thin flux tube model as described in Chapter 2 embedded in an Anelastic Spherical Harmonic (ASH) simulation for a star with the same structure and radius of the Sun, except the star is rotating at 5 times the current solar rate, with an angular speed of $\Omega = 1.3\times10^{-5}$ s^{-1}. These preliminary simulations assume that the flux tube evolves adiabatically, however, inclusion of the effect of radiative diffusion on flux tube evolution is an important component that should be included. In the future, we hope to perform flux emergence simulations utilizing an ASH convective velocity field for solar-like stars rotating

at 0.8, 3, 5, and 10 times the current solar rotation rate to obtain a picture of how flux emergence changes as a function of rotation rate in a star such as the Sun.

7.2.1. Preliminary Simulations. Similar to our simulations discussed in Chapters 3-6, the time dependent ASH velocity field impacts flux tube evolution through the drag force the flux tube experiences as it traverses through the turbulent, stratified medium of the convection zone. Figure 7.1 shows a snapshot of the ASH radial velocity of a solar-like star rotating at 5 times the current solar rate. This simulation extends from $0.71R_\odot$ to $0.97R_\odot$, is resolved by a grid of 145 points in r, 256 points in θ, and 512 points in ϕ, and exhibits north-south rotationally aligned giant cells, with networks of strong downflow lanes surrounded by weaker upflows. The number of radial grid points is increased by 16 compared to the ASH simulation used in previous Chapters. The mid-convection zone Reynolds number $R_e = v_{rms}d/\nu$ is of order 200, larger than the $R_e \sim 50$ of the ASH simulation rotating at the current solar rate as described in Chapter 2. We assume the same solar structure model as computed by Christensen-Dalsgaard *et al.* (1996).

Giant cell convection establishes a solar-like differential rotation with a fast prograde equator and slow retrograde poles, and a kinetic helicity pattern typical for rotating compressible convection, as described in Chapter 2 for an ASH simulation rotating at the current solar rate. The angular velocity profile also decreases monotonically from the equator to the pole, and exhibits a differential profile which is more cylindrical, less conical than on the Sun and in the ASH simulation we discuss in Chapter 2. Giant cells become increasingly rotationally aligned as the rotation rate of the star increases, and the number of such structures tends to increase. This behavior is evident when we compare Figure 7.1 for the rapidly rotating Sun with Figure 2.2 for our ASH simulation rotating at the current solar rate.

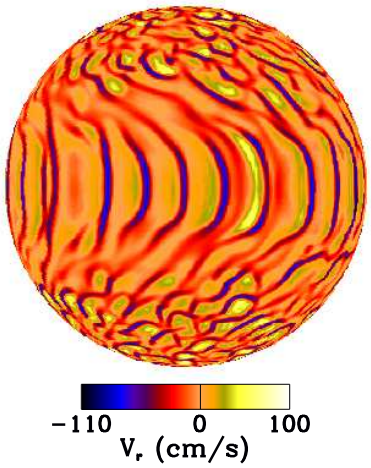

FIGURE 7.1. Snapshot of ASH convective radial velocities at a depth of about 26 Mm below the surface for a solar-like star rotating at 5 times the current solar rate. With more rapid rotation, giant cells become increasingly aligned with the rotational axis, and increase in number.

It is likely that the rapidly rotating young Sun had a much higher level of magnetic activity (e.g. Güdel 2007). This trend is seen in other low mass (F through M-type) dwarfs, as activity levels increase with more rapid rotation until reaching a saturation point (e.g. Pizzolato *et al.* 2003; Reiners 2012). As the magnetic field strength at which the solar dynamo currently operates is not well known, neither is the magnetic field strength of the Sun's early dynamo. However, it is likely that a more rapid rotation rate would contribute to an increase in the dynamo magnetic field strength. It is also known that rapid rotation can stabilize the flux tube against magnetic buoyancy instabilities (e.g. Gilman 1970; Schüssler *et al.* 1996). For a solar-like star rotating at $10\Omega_\odot$, Schüssler *et al.* (1996) suggests that in order to develop a magnetic buoyancy instability in less than 300 days at low latitudes $\leq 40°$, the magnetic field strength of the flux tube needs to be between $200 - 400$ kG. For the $5\Omega_\odot$ ASH simulation used here, the equipartition magnetic field strength at the base of the convection zone is comparable to the equipartition field strength of the ASH simulation

rotating at $\Omega_\odot$. In Chapter 3.1, we found that 10^{22} Mx flux tubes must have field strengths of $15 - 30$ kG in order for the flux tube to rise without being significantly pummeled and perhaps shredded by convection. Such that flux tubes evolving in the $5\Omega_\odot$ ASH simulation emerge in a reasonable time frame (i.e. $\sim$ one year), we have here chosen to investigate 10^{22} Mx magnetic flux tubes of >100 kG.

Following our discussion in Chapter 3.3, we compare the magnitude of the drag force to the magnetic buoyancy force acting on flux tubes of various initial magnetic field strengths to understand their relative importance on flux tube evolution. In order for convection to dominate flux tube evolution as compared to the buoyancy force, $v_{cr} > v_a(a/H_p)^{1/2}$ (Eq. 3.4), where v_{cr} is a representative convective radial velocity, v_a is the Alfvén speed, a is the cross-sectional radius of the flux tube, and H_p is the pressure scale height. In Figure 7.2, we have plotted the right hand side (RHS) of Eq. 3.4 for flux tubes of $\Phi = 10^{22}$ Mx and $\theta_0 = 15^\circ$ for three different initial magnetic field strengths of 130, 200, and 300 kG. Representative convective radial velocities are also plotted. Only the strongest downflows are capable of impacting the evolution of $\geq$200 kG flux tubes throughout the bulk of the convection zone, while strong upflows and downflows can alter the evolution of $\leq$130 kG flux tubes. Both ASH simulations rotating at $\Omega_\odot$ and $5\Omega_\odot$ have comparable rms upflow and downflow velocity profiles as a function of radius. However, the maximum upflow velocities for the $5\Omega_\odot$ ASH simulation are larger in the upper convection zone, while the maximum downflow velocities are slightly less in the upper convection zone compared to the $\Omega_\odot$ case.

Figure 7.3 shows both the polar and equatorial view of a 130 kG flux tube once some portion has reached the simulation upper boundary. This flux tube originates at 10° latitude

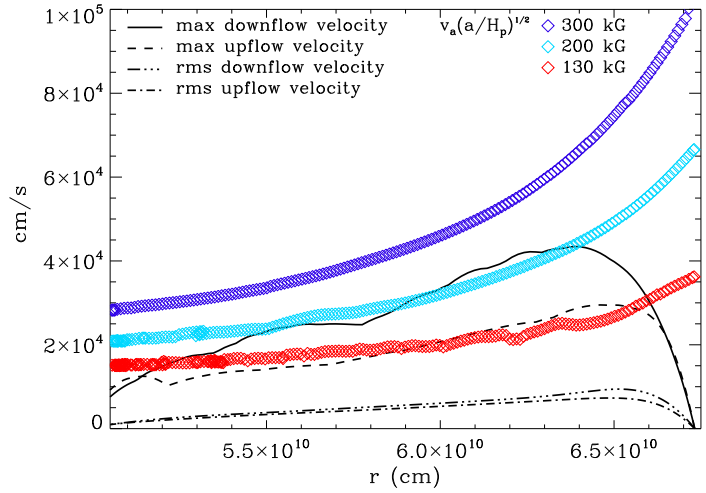

FIGURE 7.2. Peak downflows and upflows, and the root mean square of the downflows and upflows of the convective velocity field (5Ω Sun) at each constant r surface as a function of r. Also plotted is the right-hand side of Eq. 3.4 at the apex of a 10^{22} Mx, $\theta_0 = 15°$ flux tube with various initial magnetic field strengths.

and emerges at 24.7° with a positive tilt angle of 30°. For flux tubes originating in the Northern hemisphere, we expect that the flux tube would emerge with a negative tilt (i.e. towards the equator), as is the trend for active regions that emerge in the Northern hemisphere on the Sun. Generally flux tubes of 130 kG that evolve in this convective velocity field emerge with negative tilt angles in the Northern hemisphere. This flux tube simulation was chosen to illustrate that flux tubes of this magnetic field strength can emerge with tilt angles of the wrong sign due to interaction with convective flows.

A variety of observational tools and diagnostic techniques are currently employed for studying starspots and mapping stellar surfaces (see e.g. Berdyugina 2005). One method of starspot detection utilizes high-precision photometry provided by the CoRoT and Kepler missions. Deviations in stellar light curves during planetary transits can be identified as signatures of starspots through light curve modeling efforts. Recovered starspot latitudes

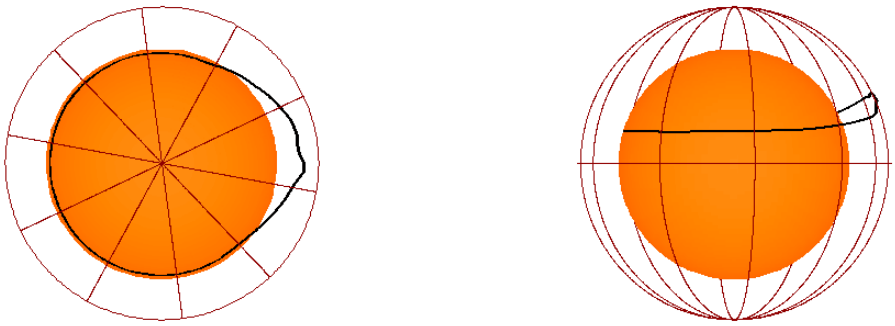

FIGURE 7.3. Snapshots of a 10^{22} Mx, $B_0 = 130$ kG, $\theta_0 = 10^\circ$ flux tube from a TFT+ASH simulation rotating at 5 times the current solar rate. The left image shows a polar view, whereas the right image shows an equatorial view. The image has ben rotated such that the flux tube apex in on the right, and at the 3 o'clock position is looking down from the north stellar pole. The orange sphere has a radius of 4.9×10^{10} cm. This flux tube suffers from deformation by convective flows, emerging with a tilt angle of the wrong sign for the Northern hemisphere.

suggest that some rapidly rotating stars may have concentrations of magnetic flux emergence at or near the poles. One possible explanation of such behavior is due to the dominance of the Coriolis force over the magnetic buoyancy force at the flux tube apex for such rapid rotations (e.g. Schüssler and Solanki 1992; Schüssler *et al.* 1996).

In Figure 7.4, we have plotted the latitudinal deflection (emergence latitude minus initial latitude) of the flux tube apex as a function of initial latitude for five different initial magnetic field strengths. Each symbol on the graph represents one flux tube, with some symbols for the same magnetic field strength lying directly on top of each other at low latitudes. Flux tubes of $400 - 500$ kG exhibit nearly radial emergence, as their magnetic buoyancy is very strong compared to the Coriolis force acting on the flux tube apex. However, between magnetic field strengths of 200 to 300 kG, there is a departure from the trend of low latitude emergence. For magnetic field strengths of $\leq$200 kG in this rapid rotator, most flux tubes are deflected by at least 5° or more. Therefore, we find that there is a region void of equatorial sunspots

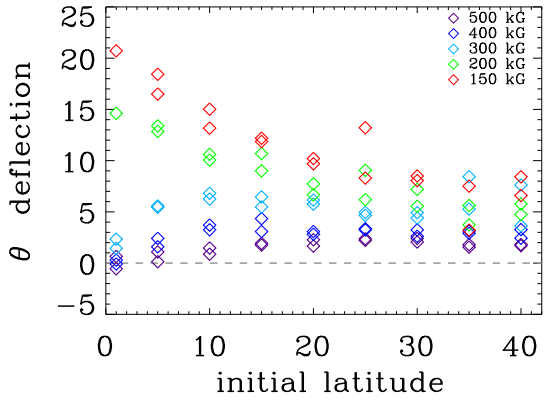

FIGURE 7.4. Latitudinal deflection (emergence latitude minus initial latitude) of the flux tube apex as a function of initial latitude for five different initial magnetic field strengths. Each symbol represents one flux tube simulation, and some symbols overlap each other at low latitudes. Between 200 and 300 kG, there is a departure from the trend of low latitude emergence.

for magnetic field strengths of $\leq$200 kG. The largest latitude at which we initiate a flux tube in these simulations is 40°. When $\theta_0 = 40°$, we do not find any flux tubes that emerge at latitudes of greater than $\sim$50°.

For the magnetic field strengths we have consider here, no flux tubes would exhibit polar starspots. Perhaps an even weaker magnetic field strength flux tube of $<$150 kG is required to exhibit polar emergence on a rapid rotator, or the dynamo mechanism operates in a different way than the picture we have for the current Sun. However, including heating due to radiative diffusion in this model may facilitate polar flux emergence. As we have shown in Chapter 6, flux tubes of weak magnetic field strength do not anchor due to the uniform heating of the flux tube in the lower convection zone. If flux tubes in these rapid rotators do not anchor, they may be deflected significantly poleward due to the conservation of angular momentum and the subsequent increase in the Coriolis force acting on the rising flux tube.

We have no evidence to confirm that the Joy's Law trend existed on the early Sun, nor do we have enough observational evidence to confirm that such a trend exists on other solar-like stars. However, assuming the tilting action of an active region toward the equator is a result of the Coriolis force acting on the plasma elements of the rising flux tube, we fit the tilt angles from our simulations according to the equation $\alpha = m \sin(\theta)$, following Method 2 in Chapter 4.3.1.2. Figure 7.5 shows a graph of the tilt angle as a function of emergence latitude for five different initial magnetic field strengths, with the best-fit curve plotted as well. Table 7.1 shows the slope m_B of the best-fit lines for each magnetic field strength. The tilt angle trend increases significantly as the magnetic field strength of the flux tube decreases. Presumably, following our discussion in Chapters 4 and 6, this is a result of weaker magnetic field strength flux tubes essentially becoming more coupled to convection, and therefore experience more strongly the helical upflows present in the giant cell convection. This increase in tilt angle is also related to the fact that weaker magnetic field strength flux tubes are deflected significantly poleward by convection, and the Coriolis force is proportional to the sine of latitude. However, it may also be related to the fact that 150 kG flux tubes have an average rise time of $\sim$200 days as compared to the average rise time of $\sim$50 days and less for $300 - 500$ kG flux tubes. As such, the Coriolis force will have a longer time to act on the rising loops of weaker magnetic field strength flux tubes. In addition, convection introduces a scatter of the tilt angles around the best-fit line, which increases as the magnetic field strength decreases.

In this Section, we have demonstrated that it is possible to perform flux emergence simulations utilizing the TFT+ASH model as outlined in Chapter 2 for a solar-like star with a rotation rate faster than the current Sun. Due to the way we have designed the

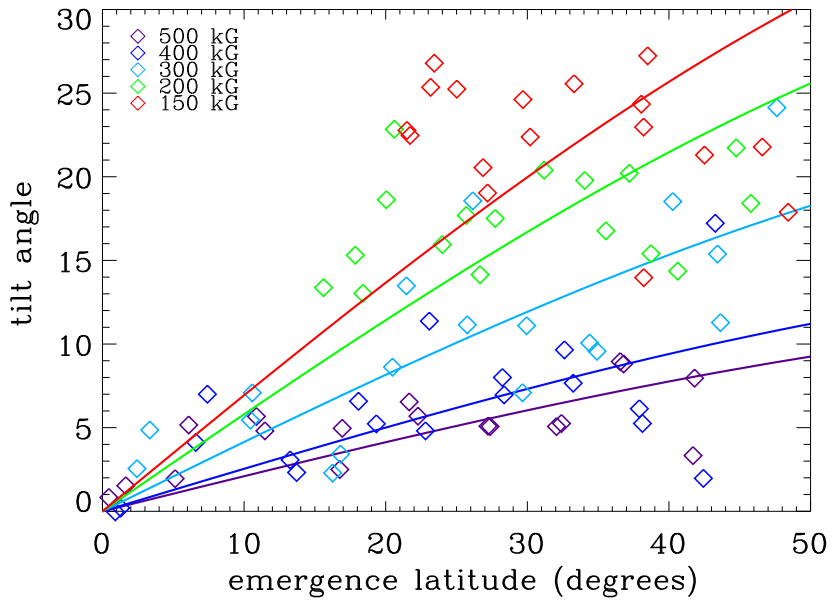

FIGURE 7.5. Tilt angles plotted as a function of emergence latitude for flux tube simulations of five different initial magnetic field strengths in a star rotating at five times the current solar rate. The best-fit line to the tilt angles is also plotted, with the slopes of these best-fit lines shown in Table 7.1. Tilt angles increase significantly as magnetic field strength decreases.

TABLE 7.1. Slopes m_B of the best-fit line following Method 2 for flux tubes of 10^{22} Mx that evolve in a star rotating at five times the current solar rate. The slope increases as the magnetic field strength decreases, a result of the poleward deflection of flux tubes at lower magnetic field strengths.

B	m_B
500 kG	$12.1^\circ \pm 1.1^\circ$
400 kG	$14.7^\circ \pm 1.8^\circ$
300 kG	$23.9^\circ \pm 1.9^\circ$
200 kG	$33.4^\circ \pm 2.2^\circ$
150 kG	$39.9^\circ \pm 3.0^\circ$

TFT+ASH model, the ASH convection simulation as well as the solar structure model can be easily swapped out and replaced. The simulation results presented in this Section actually raise more questions than answers about the nature of flux emergence in the young Sun and other solar-like rapid rotators. We hope to expand on the preliminary study in this Section

by performing a comparative study of flux emergence properties as a function of rotation rate in a star similar to the Sun. As the rotation rate of the star increases, the convective flow properties also change, which adds an extra component to the flux emergence study. Particularly, as convection becomes increasingly modulated at higher rotation rates, some ASH simulations exhibit localized patterns of convection, or *nests* (e.g. Brown *et al.* 2008) that may contribute to the active longitude phenomenon observed on young, low mass dwarfs such as AB Doradus and Kepler-17 (e.g. Järvinen *et al.* 2005; Bonomo and Lanza 2012).

7.3. Magnetic Flux Emergence Across the Hertzsprung-Russel Diagram

The simulations discussed in Chapters 2-6 and mentioned above in Section 7.2 only investigate flux emergence for the parameter space of solar-like, G2V stars. However, most main sequence stars of spectral type F-M exhibit magnetic fields, with $\sim$10% of A type stars exhibiting observable magnetic fields as well (e.g. Moss 2001). There is thus a broad parameter space over which flux emergence simulations can be performed. Additionally, much work has been documented on the nature of convection in ASH simulations for F, G, and K dwarfs (e.g. Miesch *et al.* 2008; Brown *et al.* 2008, 2010; Matt *et al.* 2011; Augustson *et al.* 2012), as well as low mass M-type stars (e.g. Browning 2008) and high mass A-type stars (e.g. Featherstone *et al.* 2009). Coupling such ASH simulations to the thin flux tube model and a representative stellar structure model appropriate for the star should be a straight-forward task, and opens up the possibility for the investigation of flux emergence as a function of rotation rate and spectral type.

Along the main sequence, stellar luminosity increases with increasing mass, while the radial fraction of the outer convective envelope decreases such that $0.5 - 1.3 M_{\odot}$ stars (K-F type) have convection zone depths of $\sim 44\% - 14\%$, respectively, of their total radius.

Therefore, convection becomes more vigorous with increasing stellar mass, as the amount of required energy flux transport increases and the convection zone becomes shallower in radius. Similar to the picture we have for the solar dynamo paradigm, it is thought that rotation, global-scale plasma motions, and shearing at the convection zone-radiative zone interface all contribute to the generation of magnetic fields in stars with outer convection zones. Since convection becomes less vigorous with decreasing stellar mass, flux tubes subjected to turbulent fluid motions in stars of $0.5-0.9\mathrm{M}_{\odot}$ may be less affected by convective downflows. However, a deeper convection zone and more rapid rotation may favor the emergence of polar starspots. Conversely, convection becomes more vigorous with increasing stellar mass for stars in the range of $1.1-1.3\mathrm{M}_{\odot}$, and may have profound impacts on the dynamic evolution of magnetic flux tubes as they are pummeled by convective flows. An exploration of magnetic flux emergence in stars with outer convection zones utilizing the TFT+ASH approach may help shed light on the nature of the Sun's flux emergence properties in comparison to other F-K type dwarf stars.

Main sequence stars of mass $\geq 1.6\mathrm{M}_{\odot}$ do not possess convective outer shells, but rather are comprised of a convective core and a convectively stable radiative outer envelope. The question as to whether or not their magnetism is a result of a fossil field of primordial origin, dynamo action in the convective core, or the interaction of the core dynamo with a fossil field is still not resolved (see Featherstone *et al.* 2009). If magnetic flux tube structures are produced by dynamo action in the convective core, then a mechanism for transport of the field from the convective interior through the outer radiation zone can be studied utilizing an ASH simulation of an A-type star in concert with a thin flux tube model. Flux emergence

simulations using a thin flux tube model for an early-type A star have been conducted by MacGregor and Cassinelli (2003).

Main sequence M-type stars are the most populous dwarf stars in the solar neighborhood. Such stars with masses $\leq 0.35 M_{\odot}$ are fully convective and magnetically active despite lacking a tachocline. As a result, it is unclear whether magnetic fields built in these stars are fundamentally different from those in stars with tachoclines (i.e. those with a convection zone-radiative zone interface). Browning (2008) shows that cyclic dynamos with equipartition magnetic field strengths can be generated and sustained in fully convective stars. However, when the magnetic field reaches sufficiently large values, the differential rotation of the star is strongly suppressed. It may be interesting to use the TFT+ASH model in fully convective stars to observe how magnetic flux tubes may be influences by representative cases of convection in such stars.

The expansive *project* laid out in this section for the TFT+ASH model will take many years to conclude and will encounter modifications as computing power increases and more is learned about the nature of stellar dynamos. However, it is an interesting and worthwhile endeavor that will shed light on stellar dynamo mechanisms, and will provide information on the magnetically-driven space weather conditions in the vicinity of exoplanets in the habitable zone. The recent detection of Kepler-186f, a 1.11 Earth radius planet in the habitable zone of a $0.47 R_{\odot}$ M-type main sequence star (Quintana *et al.* 2014), suggests that comparative heliophysics will likely be a blossoming branch of astrophysics in the near future.

CHAPTER 8

Conclusions

Our Sun is a magnetic star, exhibiting a ∼11 year cycle of magnetic activity. The manner by which dynamo-generated magnetic fields, the progenitors of solar active regions, traverse the convection zone to eventual emergence at the solar surface still remains unclear. Here we have proposed a method to provide a connection between the deep-seated solar dynamo and sunspots by performing simulations of magnetic flux emergence through the bulk of a turbulent, solar-like convective envelope. To capture the global effects of convection on rising magnetic flux tubes while circumventing the problem of artificial diffusion encountered by fully three-dimensional models, we have performed the first large statistical study of active-region-scale magnetic flux tube simulations in a three-dimensional, rotating spherical shell of turbulent, solar-like convection by employing a thin flux tube (TFT) model subject to interaction with flows taken from a hydrodynamic Anelastic Spherical Harmonic (ASH) simulation (see Chapter 2). The ASH velocity field interacts with the flux tube through the drag force it experiences as it traverses through the turbulent convective medium.

In the Introduction (Chapter 1), we identified four main topics which we proposed for the TFT+ASH model to address:

- Identify the magnetic-buoyancy-dominated and convection-dominated regimes for active-region-scale flux tubes of equipartition to super-equipartition magnetic field strengths

- Characterize the influence of large-scale, global convection on flux tube properties at the simulation upper boundary - a proxy for active regions observed on the solar surface
- Better constrain the dynamo generated magnetic field strength by comparing simulation results to those of active region observations
- Address the influence of radiative diffusion through the base of the convection zone on the dynamic evolution of magnetic flux tubes

We will summarize our findings in response to each of these topics in turn.

Many previous thin flux tube models neglect the effects of turbulent, solar-like convection on buoyantly rising flux tubes (e.g. Spruit 1981a,b; Moreno-Insertis 1986; Ferriz-Mas and Schüssler 1993; Longcope and Klapper 1997; Caligari, Moreno-Insertis, and Schüssler 1995; Caligari, Schüssler, and Moreno-Insertis 1998; Fan, Fisher, and Deluca 1993). Within the range of $15 - 100$ kG (equipartition to super-equipartition) for the possible value B_0 at which the solar dynamo may be operating (e.g. Caligari, Moreno-Insertis, and Schüssler 1995; Rempel 2006b,a), there are different convection-dominated and magnetic-buoyancy-dominated regimes for the dynamic evolution of active-region-scale flux tubes depending on their magnetic field strengths. In the absence of convection, rising buoyant loops develop solely as the result of the non-linear growth of the magnetic buoyancy instability of the initial toroidal flux tube. However, when we include the effect of solar-like convective flows on flux tube evolution, we find in Chapter 3 that convective influences are a significant contributing factor, and should not be neglected except perhaps in the case of $\geq$80 kG flux tubes of 10^{21} and 10^{22} Mx flux.

Convection also decreases the time it takes for flux tubes to travel the depth of the convection zone, reducing the time from at most $\sim$4.5 years in the case without convection to $\sim$8 months with convection. For magnetic flux values of $10^{21} - 10^{22}$ Mx, tubes of $30 - 60$ kG have the longest average rise times, as the average convective downflows and magnetic buoyancy force acting on the flux tube apex are of similar magnitudes. While the buoyancy force is the largest contributing factor to the radial acceleration of the flux tube apex, in the presence of convection, contributions to the flux tube evolution from convective upflows can act to boost the flux tube apex toward the surface faster than it could in the absence of convection.

Rotation and the Coriolis force acting on a rising flux loop are responsible for a number of flux emergence properties such as: emergence latitudes, tilt angle trends, average rotation rates, and magnetic field asymmetries. We have investigated the effect convection has on such flux emergence properties in Chapter 4. Thin flux tube simulations of weak magnetic field strength tend to deflect significantly poleward in the absence of convection, as the radially directed magnetic buoyancy force acting on the flux tube is reduced compared to the component of the Coriolis force directed inward toward the rotation axis (e.g. Choudhuri and Gilman 1987). At weak magnetic field strengths, convective flow fields are able to keep the flux tube from deflecting poleward. Convection can also force flux tubes to emerge closer to the equator that the latitude where they initiated at the base of the convection zone, and can even force them to emerge in the opposite hemisphere from which they originated. Such behavior provides a possible explanation for active regions near the equator ($\pm 10^{\circ}$) that exhibit anti-Hale polarities.

It is generally assumed that the Joy's Law tilt angle trend of solar active regions arises due to a tilting motion of the flux tube imparted by the Coriolis force (e.g. D'Silva and Choudhuri 1993). We find that the slope of the best-fit line applied to the tilt angles as a function of emergence latitude or $\sin(\theta)$ increases when convection is added in our simulation. This happens in part because upflows in the convective velocity field have an associated kinetic helicity that helps to drive the tilt of the flux tube apex in the appropriate Joy's Law direction (i.e. toward the equator). Convection also introduces a spread of the tilt angle about the Joy's Law trend, which increases with decreasing flux and magnetic field.

To provide an explanation for the apparent asymmetric East – West proper motion of the two polarities of an emerging region, it is posited that there is an asymmetry in the inclination of the leading and following legs of a rising flux loop with respect to the vertical direction (e.g. Moreno-Insertis, Caligari, and Schüssler 1994; Caligari, Moreno-Insertis, and Schüssler 1995). We find that convection acts to reduce this inclination. The rotation rate of a rising flux loop, corresponding to the rotation rate of an individual active region, is dependent on the magnetic field strength of the flux tube, the rotation rate of the system, and the differential rotation present in the convection simulation. We also find that the asymmetry of the magnetic field at the flux tube apex does not change significantly with the addition of convection, although convection does introduce a scatter about the mean trend.

Our simulations exhibit a large-scale pattern of flux emergence at low latitudes of $\pm 15^{\circ}$, which may be associated with the observed phenomena called *active longitudes* (Chapter 5). This large-scale pattern of flux emergence is inhomogenous in longitude and exhibits low order longitudinal modes. Furthermore, the pattern shows a strong North-South alignment and drifts (either prograde or retrograde) with respect to the chosen rotating reference

frame. We attribute this behavior in our simulation to differential rotation and the columnar, rotationally aligned giant cells which exist in the equatorial to mid-latitude regions of our convection simulation. These giant cells *corral* flux tubes in a sense, forcing them to emerge within boundaries of a particular cellular feature. These results suggest that giant cells may play a significant role in the observed active longitude phenomenon on the Sun and other solar-like stars.

The magnetic field strength at which the solar dynamo operates is not well known, nor is it directly accessible via observations. Previous thin flux tube simulations ignoring the effects of convection have found that the toroidal magnetic field at the base of the convection zone needs to be in the range of $\sim$30 kG to $\sim$100 kG such that the simulated flux tubes exhibit tilt angles and latitudes of emergence that agrees well with solar active regions (Choudhuri and Gilman 1987; Schüssler *et al.* 1994; D'Silva and Choudhuri 1993; Caligari, Moreno-Insertis, and Schüssler 1995). However, solar cycle mean field dynamo models that incorporate the Lorentz force from large scale mean fields indicate that the magnetic field strength generated and amplified at the base of the convection zone is $\sim$15 kG, and most likely cannot exceed 30 kG (Rempel 2006b,a). In Chapter 4, we attempt to constrain the magnetic field strength at which the solar dynamo may be operating by comparing the results of our simulations to those of solar observations.

The comparisons made between our simulation results and solar observations suggests that the initial field strength of active region progenitor flux tubes needs to be sufficiently large, probably $\geq$30 kG, in order for them to satisfy Joy's Law for active region mean tilt angles as well as the observed amount of scatter of the tilt angles about the mean Joy's Law. Weaker magnetic fields tend to produce too large a scatter to be consistent with the observed

results. Flux tubes of $\geq$80 kG and $10^{21} - 10^{22}$ Mx agree both with the observed Joy's Law trends for the mean tilt, and the observed tilt angle scatter. However, only 60 kG or greater magnetic field strength flux tubes can have an apparent rotation rate at or faster than the solar surface rate. So, according to our thin flux tube approach, magnetic field values need to be of moderate to large field strengths for tubes with fluxes of 10^{21} Mx and 10^{22} Mx to produce sunspot rotation behavior. Taking all of our results into consideration, we can exclude $\leq$15 kG magnetic field strength flux tubes as progenitors of solar active regions, and suggest that flux tubes of $\geq$60 kG are most likely required.

With the exception of Fan and Fisher (1996), all previous thin flux tube studies assume that the flux tube evolves adiabatically throughout the convection zone. This is a valid assumption for the upper $\sim$2/3 of the solar convection zone. However, in the lower $\sim$1/3 of the convection zone, radiative diffusion from the interior into the convection zone results in a heat input per unit volume Q_v of magnetic flux tubes, which has a substantial effect on their buoyancy and dynamic evolution. We modify the thin flux tube energy equation to include a heating term supplied by the deviation of the background plasma environment from that of radiative equilibrium. As a result, we find that flux tubes of 10^{22} Mx with magnetic field strengths of $\leq$60 kG no longer anchor at the base of the convection zone, unlike the case where flux tubes evolve entirely adiabatically. Rather, heating due to radiative diffusion increases the buoyancy of the flux tube earlier in its evolution, allowing the whole flux tube to drift upward, away from the overshoot region faster than magnetic buoyancy instabilities can set in to anchor the flux tube.

Although flux tubes of $\leq$60 kG do not anchor, they do still exhibit a Joy's Law tilt angle trend that falls within the range suggested by statistical analysis of solar active region

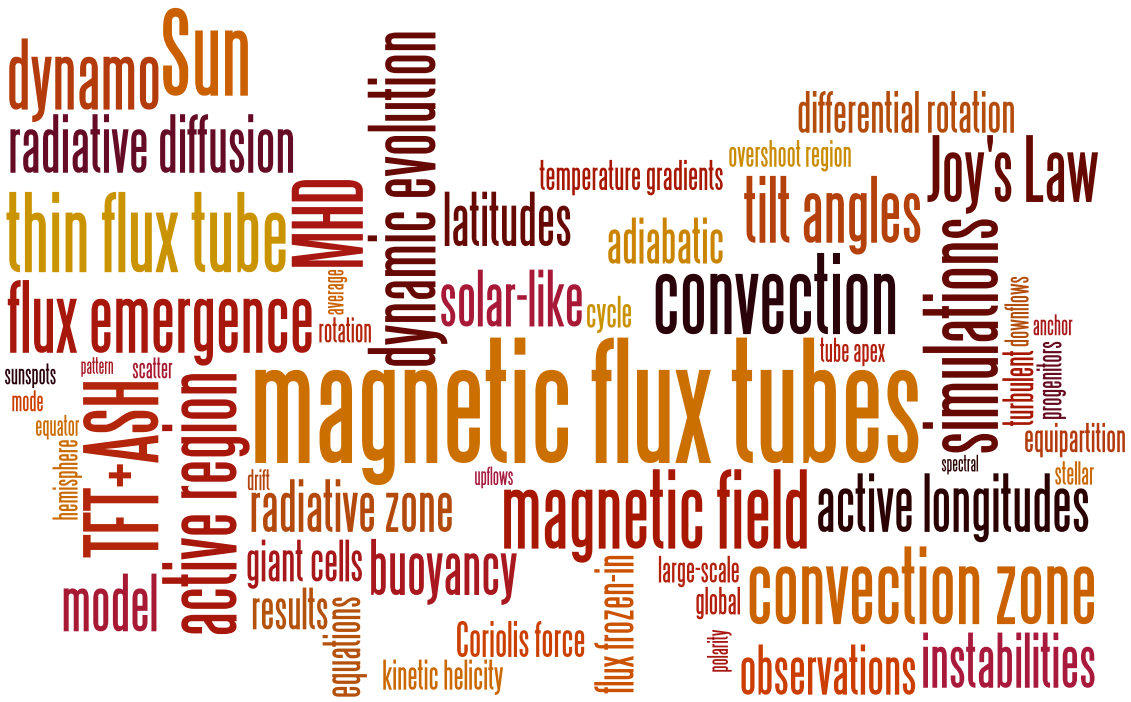

FIGURE 8.1. Word cloud created from the text of this dissertation. Word clouds are visual representations of text data, useful for perceiving the most prominent words used in the text. This word cloud was generated using www.wordle.net.

observations (e.g. Dasi-Espuig *et al.* 2010; Stenflo and Kosovichev 2012; Fisher, Fan, and Howard 1995). However, the scatter of the tilt angles around the Joy's Law trend is too large for magnetic field strengths of $\leq$40 kG, still pointing toward larger magnetic field strengths as the progenitors of solar active regions. Including the effects of radiative diffusion also reduces the flux tube rise times to less than 0.2 years, $\sim$0.5 years less than the average maximum rise time for completely adiabatically evolving flux tubes. We also find that flux tubes will drift quasi-statically as a whole out of the overshoot region, and only show anchoring of emerging flux loop troughs for magnetic field strengths of $\geq$80 kG because of their fast growing undular magnetic buoyancy instabilities.

There are many more investigations into the nature of solar and stellar magnetic fields for which we feel the TFT+ASH model is suitable. As outlined in Chapter 7, this model will hopefully help to shed some light on the nature of the generation of magnetic field twist in active region flux tubes. Also as demonstrated in Chapter 7, this model can be applied to stars other than the Sun, most notably rapid rotators and F-K type stars with convective outer shells. Performing such simulations will bring us to a more comprehensive understanding of the nature of flux emergence as a function of rotation rate and spectral type for main-sequence stars, and will help us to paint a picture of the Sun's unique position within this parameter space.

Our understanding of stellar magnetism is historically driven by what we have learned about the Sun, which represents only a small portion of the varieties of stellar behavior. It is of great importance to observe magnetism in solar-like stars so as to better understand the intricacies of the stellar dynamo mechanism, thereby deciphering the magnetic mysteries of our own star in the process. Observations from ESA's CoRoT and NASA's Kepler missions have identified thousands of candidate planets orbiting stars of all spectral types, including those that are very similar to the Sun. The new Daniel K. Inouye Solar Telescope (DKIST, formerly the Advanced Technology Solar Telescope), expected to be completed in 2019, will undoubtedly shed much light on the nature of solar magnetism utilizing its 4 m mirror to achieve a resolution of $\sim$0.1 arcsec (70 km) in the photosphere. It is now timely to perform numerical simulations of magnetic flux emergence on the Sun and similar stars in order to interpret observations of stellar magnetic activity and prepare for the high resolution observations of the Sun to come.

BIBLIOGRAPHY

Abbett, W.P., Fisher, G.H., Fan, Y.: 2000, The Three-dimensional Evolution of Rising, Twisted Magnetic Flux Tubes in a Gravitationally Stratified Model Convection Zone. *ApJ* **540**, 548 – 562. doi:10.1086/309316.

Abbett, W.P., Fisher, G.H., Fan, Y.: 2001, The Effects of Rotation on the Evolution of Rising Omega Loops in a Stratified Model Convection Zone. *ApJ* **546**, 1194 – 1203. doi:10.1086/318320.

Acheson, D.J.: 1979, Instability by magnetic buoyancy. *Sol. Phys.* **62**, 23 – 50. doi:10.1007/BF00150129.

Alissandrakis, C.E., Dialetis, D., Tsiropoula, G.: 1987, Determination of the mean lifetime of solar features from photographic observations. *A&A* **174**, 275 – 280.

Augustson, K.C., Brown, B.P., Brun, A.S., Miesch, M.S., Toomre, J.: 2012, Convection and Differential Rotation in F-type Stars. *ApJ* **756**, 169. doi:10.1088/0004-637X/756/2/169.

Babcock, H.W.: 1961, The Topology of the Sun's Magnetic Field and the 22-YEAR Cycle. *ApJ* **133**, 572. doi:10.1086/147060.

Baliunas, S.L., Donahue, R.A., Soon, W.H., Horne, J.H., Frazer, J., Woodard-Eklund, L., Bradford, M., Rao, L.M., Wilson, O.C., Zhang, Q., Bennett, W., Briggs, J., Carroll, S.M., Duncan, D.K., Figueroa, D., Lanning, H.H., Misch, T., Mueller, J., Noyes, R.W., Poppe, D., Porter, A.C., Robinson, C.R., Russell, J., Shelton, J.C., Soyumer, T., Vaughan, A.H., Whitney, J.H.: 1995, Chromospheric variations in main-sequence stars. *ApJ* **438**, 269 – 287. doi:10.1086/175072.

Barnes, J.R., Collier Cameron, A., Unruh, Y.C., Donati, J.F., Hussain, G.A.J.: 1998, Latitude distributions and lifetimes of star-spots on G dwarfs in the alpha Persei cluster. *MNRAS* **299**, 904 – 920. doi:10.1046/j.1365-8711.1998.01805.x.

Barnes, J.R., Collier Cameron, A., Donati, J.-F., James, D.J., Marsden, S.C., Petit, P.: 2005, The dependence of differential rotation on temperature and rotation. *MNRAS* **357**, L1 – L5. doi:10.1111/j.1745-3933.2005.08587.x.

Basri, G., Walkowicz, L.M., Batalha, N., Gilliland, R.L., Jenkins, J., Borucki, W.J., Koch, D., Caldwell, D., Dupree, A.K., Latham, D.W., Marcy, G.W., Meibom, S., Brown, T.: 2011, Photometric Variability in Kepler Target Stars. II. An Overview of Amplitude, Periodicity, and Rotation in First Quarter Data. *AJ* **141**, 20. doi:10.1088/0004-6256/141/1/20.

Batchelor, G.K.: 1967, *Fluid Dynamics*.

Beck, J.G., Duvall, T.L., Scherrer, P.H.: 1998, Long-lived giant cells detected at the surface of the Sun. *Nature* **394**, 653 – 655. doi:10.1038/29245.

Beer, J., Blinov, A., Bonani, G., Hofmann, H.J., Finkel, R.C.: 1990, Use of Be-10 in polar ice to trace the 11-year cycle of solar activity. *Nature* **347**, 164 – 166. doi:10.1038/347164a0.

Benevolenskaya, E.E., Hoeksema, J.T., Kosovichev, A.G., Scherrer, P.H.: 1999, The Interaction of New and Old Magnetic Fluxes at the Beginning of Solar Cycle 23. *ApJL* **517**, L163 – L166. doi:10.1086/312046.

Benz, A.O.: 2008, Flare Observations. *Living Reviews in Solar Physics* **5**, 1. doi:10.12942/lrsp-2008-1.

Berdyugina, S.V.: 2005, Starspots: A Key to the Stellar Dynamo. *Living Reviews in Solar Physics* **2**, 8. doi:10.12942/lrsp-2005-8.

Berdyugina, S.V., Usoskin, I.G.: 2003, Active longitudes in sunspot activity: Century scale persistence. *A&A* **405**, 1121 – 1128. doi:10.1051/0004-6361:20030748.

Berdyugina, S.V., Pelt, J., Tuominen, I.: 2002, Magnetic activity in the young solar analog LQ Hydrae. I. Active longitudes and cycles. *A&A* **394**, 505 – 515. doi:10.1051/0004-6361:20021179.

Berger, M.A., Field, G.B.: The topological properties of magnetic helicity. *J. Fluid Mech.* **147**, 133 – 148.

Bessolaz, N., Brun, A.S.: 2011, Hunting for Giant Cells in Deep Stellar Convective Zones Using Wavelet Analysis. *ApJ* **728**, 115. doi:10.1088/0004-637X/728/2/115.

Bethea, R.M., Duran, B.S., Boullion, T.L.: 1985, *Statistical Methods for Engineers and Scientists*.

Bhardwaj, A., Michael, M.: 2002, Io-Jupiter system: a unique case of moon-planet interaction. In: Foing, B.H., Battrick, B. (eds.) *Earth-like Planets and Moons*, *ESA Special Publication* **514**, 115 – 121.

Birch, A.C., Braun, D.C., Leka, K.D., Barnes, G., Javornik, B.: 2013, Helioseismology of Pre-emerging Active Regions. II. Average Emergence Properties. *ApJ* **762**, 131. doi:10.1088/0004-637X/762/2/131.

Böhm-Vitense, E.: 2007, Chromospheric Activity in G and K Main-Sequence Stars, and What It Tells Us about Stellar Dynamos. *ApJ* **657**, 486 – 493. doi:10.1086/510482.

Bonomo, A.S., Lanza, A.F.: 2012, Starspot activity and rotation of the planet-hosting star Kepler-17. *A&A* **547**, A37. doi:10.1051/0004-6361/201219999.

Braun, D.C., Lindsey, C.: 2001, Seismic Imaging of the Far Hemisphere of the Sun. *ApJL* **560**, L189 – L192. doi:10.1086/324323.

Bray, R.J., Loughhead, R.E.: 1979, *Sunspots.*.

Brouwer, M.P., Zwaan, C.: 1990, Sunspot nests as traced by a cluster analysis. *Sol. Phys.* **129**, 221 – 246. doi:10.1007/BF00159038.

Brown, B.P., Browning, M.K., Brun, A.S., Miesch, M.S., Toomre, J.: 2008, Rapidly Rotating Suns and Active Nests of Convection. *ApJ* **689**, 1354 – 1372. doi:10.1086/592397.

Brown, B.P., Browning, M.K., Brun, A.S., Miesch, M.S., Toomre, J.: 2010, Persistent Magnetic Wreaths in a Rapidly Rotating Sun. *ApJ* **711**, 424 – 438. doi:10.1088/0004-637X/711/1/424.

Brown, B.P., Miesch, M.S., Browning, M.K., Brun, A.S., Toomre, J.: 2011, Magnetic Cycles in a Convective Dynamo Simulation of a Young Solar-type Star. *ApJ* **731**, 69. doi:10.1088/0004-637X/731/1/69.

Browning, M.K.: 2008, Simulations of Dynamo Action in Fully Convective Stars. *ApJ* **676**, 1262 – 1280. doi:10.1086/527432.

Browning, M.K., Miesch, M.S., Brun, A.S., Toomre, J.: 2006, Dynamo Action in the Solar Convection Zone and Tachocline: Pumping and Organization of Toroidal Fields. *ApJL* **648**, L157 – L160. doi:10.1086/507869.

Brun, A.S., Toomre, J.: 2002, Turbulent Convection under the Influence of Rotation: Sustaining a Strong Differential Rotation. *ApJ* **570**, 865 – 885. doi:10.1086/339228.

Brun, A.S., Browning, M.K., Toomre, J.: 2005, Simulations of Core Convection in Rotating A-Type Stars: Magnetic Dynamo Action. *ApJ* **629**, 461 – 481. doi:10.1086/430430.

Brun, A.S., Miesch, M.S., Toomre, J.: 2004, Global-Scale Turbulent Convection and Magnetic Dynamo Action in the Solar Envelope. *ApJ* **614**, 1073 – 1098. doi:10.1086/423835.

Bumba, V., Howard, R.: 1965, Large-Scale Distribution of Solar Magnetic Fields. *ApJ* **141**,

1502. doi:10.1086/148238.

Busse, F.H.: 1970, Thermal instabilities in rapidly rotating systems. *Journal of Fluid Mechanics* **44**, 441 – 460. doi:10.1017/S0022112070001921.

Caligari, P., Moreno-Insertis, F., Schüssler, M.: 1995, Emerging flux tubes in the solar convection zone. 1: Asymmetry, tilt, and emergence latitude. *ApJ* **441**, 886 – 902. doi:10.1086/175410.

Caligari, P., Schüssler, M., Moreno-Insertis, F.: 1998, Emerging Flux Tubes in the Solar Convection Zone. II. The Influence of Initial Conditions. *ApJ* **502**, 481. doi:10.1086/305875.

Castenmiller, M.J.M., Zwaan, C., van der Zalm, E.B.J.: 1986, Sunspot nests - Manifestations of sequences in magnetic activity. *Sol. Phys.* **105**, 237 – 255. doi:10.1007/BF00172045.

Charbonneau, P.: 2010, Dynamo Models of the Solar Cycle. *Living Reviews in Solar Physics* **7**, 3. doi:10.12942/lrsp-2010-3.

Cheung, M.C.M., Schüssler, M., Moreno-Insertis, F.: 2007, Magnetic flux emergence in granular convection: radiative MHD simulations and observational signatures. *A&A* **467**, 703 – 719. doi:10.1051/0004-6361:20077048.

Chiang, W.-H., Petro, L.D., Foukal, P.V.: 1987, A photometric search for solar giant convection cells. *Sol. Phys.* **110**, 129 – 138. doi:10.1007/BF00148208.

Choudhuri, A.R., Gilman, P.A.: 1987, The influence of the Coriolis force on flux tubes rising through the solar convection zone. *ApJ* **316**, 788 – 800. doi:10.1086/165243.

Christensen-Dalsgaard, J., Dappen, W., Ajukov, S.V., Anderson, E.R., Antia, H.M., Basu, S., Baturin, V.A., Berthomieu, G., Chaboyer, B., Chitre, S.M., Cox, A.N., Demarque, P., Donatowicz, J., Dziembowski, W.A., Gabriel, M., Gough, D.O., Guenther, D.B., Guzik, J.A., Harvey, J.W., Hill, F., Houdek, G., Iglesias, C.A., Kosovichev, A.G., Leibacher, J.W.,

Morel, P., Proffitt, C.R., Provost, J., Reiter, J., Rhodes, E.J. Jr., Rogers, F.J., Roxburgh, I.W., Thompson, M.J., Ulrich, R.K.: 1996, The Current State of Solar Modeling. *Science* **272**, 1286 – 1292. doi:10.1126/science.272.5266.1286.

Collier Cameron, A., Donati, J.-F., Semel, M.: 2002, Stellar differential rotation from direct star-spot tracking. *MNRAS* **330**, 699 – 706. doi:10.1046/j.1365-8711.2002.05120.x.

Connerney, J.E.P., Acuña, M.H., Ness, N.F., Satoh, T.: 1998, New models of Jupiter's magnetic field constrained by the Io flux tube footprint. *JGR* **103**, 11929 – 11940. doi:10.1029/97JA03726.

Dasi-Espuig, M., Solanki, S.K., Krivova, N.A., Cameron, R., Peñuela, T.: 2010, Sunspot group tilt angles and the strength of the solar cycle. *A&A* **518**, A7. doi:10.1051/0004-6361/201014301.

De Rosa, M.L., Gilman, P.A., Toomre, J.: 2002, Solar Multiscale Convection and Rotation Gradients Studied in Shallow Spherical Shells. *ApJ* **581**, 1356 – 1374. doi:10.1086/344295.

de Toma, G., White, O.R., Harvey, K.L.: 2000, A Picture of Solar Minimum and the Onset of Solar Cycle 23. I. Global Magnetic Field Evolution. *ApJ* **529**, 1101 – 1114. doi:10.1086/308299.

Dikpati, M., Gilman, P.A.: 2005, A Shallow-Water Theory for the Sun's Active Longitudes. *ApJL* **635**, L193 – L196. doi:10.1086/499626.

Dikpati, M., Gilman, P.A.: 2007, Global solar dynamo models: simulations and predictions of cyclic photospheric fields and long-term non-reversing interior fields. *New Journal of Physics* **9**, 297. doi:10.1088/1367-2630/9/8/297.

Dikpati, M., Gilman, P.A.: 2009, Flux-Transport Solar Dynamos. *Space Sci. Rev.* **144**, 67 – 75. doi:10.1007/s11214-008-9484-3.

Drake, S.: 1957, *Discoveries and Opinions of Galileo.*

D'Silva, S., Choudhuri, A.R.: 1993, A theoretical model for tilts of bipolar magnetic regions. *A&A* **272**, 621.

Emonet, T., Moreno-Insertis, F.: 1998, The Physics of Twisted Magnetic Tubes Rising in a Stratified Medium: Two-dimensional Results. *ApJ* **492**, 804. doi:10.1086/305074.

Fan, Y.: 2001, Nonlinear Growth of the Three-dimensional Undular Instability of a Horizontal Magnetic Layer and the Formation of Arching Flux Tubes. *ApJ* **546**, 509 – 527. doi:10.1086/318222.

Fan, Y.: 2008, The Three-dimensional Evolution of Buoyant Magnetic Flux Tubes in a Model Solar Convective Envelope. *ApJ* **676**, 680 – 697. doi:10.1086/527317.

Fan, Y.: 2009a, Magnetic Fields in the Solar Convection Zone. *Living Reviews in Solar Physics* **6**, 4. doi:10.12942/lrsp-2009-4.

Fan, Y.: 2009b, The Emergence of a Twisted Flux Tube into the Solar Atmosphere: Sunspot Rotations and the Formation of a Coronal Flux Rope. *ApJ* **697**, 1529 – 1542. doi:10.1088/0004-637X/697/2/1529.

Fan, Y., Fisher, G.H.: 1996, Radiative Heating and the Buoyant Rise of Magnetic Flux Tubes in the Solar interior. *Sol. Phys.* **166**, 17 – 41. doi:10.1007/BF00179354.

Fan, Y., Gong, D.: 2000, On the twist of emerging flux loops in the solar convection zone. *Sol. Phys.* **192**, 141 – 157. doi:10.1023/A:1005260207672.

Fan, Y., Abbett, W.P., Fisher, G.H.: 2003, The Dynamic Evolution of Twisted Magnetic Flux Tubes in a Three-dimensional Convecting Flow. I. Uniformly Buoyant Horizontal Tubes. *ApJ* **582**, 1206 – 1219. doi:10.1086/344798.

Fan, Y., Featherstone, N., Fang, F.: 2013, Three-Dimensional MHD Simulations of Emerging

Active Region Flux in a Turbulent Rotating Solar Convective Envelope: the Numerical Model and Initial Results. *ArXiv e-prints*.

Fan, Y., Fisher, G.H., Deluca, E.E.: 1993, The origin of morphological asymmetries in bipolar active regions. *ApJ* **405**, 390 – 401. doi:10.1086/172370.

Fan, Y., Fisher, G.H., McClymont, A.N.: 1994, Dynamics of emerging active region flux loops. *ApJ* **436**, 907 – 928. doi:10.1086/174967.

Fan, Y., Zweibel, E.G., Lantz, S.R.: 1998, Two-dimensional Simulations of Buoyantly Rising, Interacting Magnetic Flux Tubes. *ApJ* **493**, 480. doi:10.1086/305122.

Fang, F., Manchester, W. IV, Abbett, W.P., van der Holst, B.: 2012, Dynamic Coupling of Convective Flows and Magnetic Field during Flux Emergence. *ApJ* **745**, 37. doi:10.1088/0004-637X/745/1/37.

Featherstone, N.A., Browning, M.K., Brun, A.S., Toomre, J.: 2009, Effects of Fossil Magnetic Fields on Convective Core Dynamos in A-type Stars. *ApJ* **705**, 1000 – 1018. doi:10.1088/0004-637X/705/1/1000.

Ferriz-Mas, A., Schüssler, M.: 1993, Instabilities of magnetic flux tubes in a stellar convection zone I. Equatorial flux rings in differentially rotating stars. *Geophysical and Astrophysical Fluid Dynamics* **72**, 209 – 247. doi:10.1080/03091929308203613.

Ferriz-Mas, A., Schüssler, M.: 1995, Instabilities of magnetic flux tubes in a stellar convection zone II. Flux rings outside the equatorial plane. *Geophysical and Astrophysical Fluid Dynamics* **81**, 233 – 265. doi:10.1080/03091929508229066.

Fisher, G.H., Fan, Y., Howard, R.F.: 1995, Comparisons between theory and observation of active region tilts. *ApJ* **438**, 463 – 471. doi:10.1086/175090.

Florinski, V., Pogorelov, N.V., Zank, G.P., Wood, B.E., Cox, D.P.: 2004, On the Possibility of a Strong Magnetic Field in the Local Interstellar Medium. *ApJ* **604**, 700 – 706. doi:10.1086/382017.

Frasca, A., Fröhlich, H.-E., Bonanno, A., Catanzaro, G., Biazzo, K., Molenda-Żakowicz, J.: 2011, Magnetic activity and differential rotation in the very young star KIC 8429280. *A&A* **532**, A81. doi:10.1051/0004-6361/201116980.

Gaizauskas, V., Harvey, K.L., Harvey, J.W., Zwaan, C.: 1983, Large-scale patterns formed by solar active regions during the ascending phase of cycle 21. *ApJ* **265**, 1056 – 1065. doi:10.1086/160747.

Galloway, D.J., Weiss, N.O.: 1981, Convection and magnetic fields in stars. *ApJ* **243**, 945 – 953. doi:10.1086/158659.

García-Alvarez, D., Lanza, A.F., Messina, S., Drake, J.J., van Wyk, F., Shobbrook, R.R., Butler, C.J., Kilkenny, D., Doyle, J.G., Kashyap, V.L.: 2011, Starspots on the fastest rotators in the β Pictoris moving group. *A&A* **533**, A30. doi:10.1051/0004-6361/201116646.

Gilman, P.A.: 1970, Instability of Magnetohydrostatic Stellar Interiors from Magnetic Buoyancy. I. *ApJ* **162**, 1019. doi:10.1086/150733.

Gilman, P.A.: 1977, Nonlinear Dynamics of Boussinesq Convection in a Deep Rotating Spherical Shell. I. *Geophysical and Astrophysical Fluid Dynamics* **8**, 93 – 135. doi:10.1080/03091927708240373.

Gilman, P.A.: 1978, Nonlinear Dynamics of Boussinesq Convection in a Deep Rotating Spherical Shell. II. Effects of Temperature Boundary Conditions. *Geophysical and Astrophysical Fluid Dynamics* **11**, 157 – 179. doi:10.1080/03091927808242661.

Gilman, P.A.: 1979, Model calculations concerning rotation at high solar latitudes and the

depth of the solar convection zone. *ApJ* **231**, 284 – 292. doi:10.1086/157191.

Gilman, P.A.: 2000, Fluid Dynamics and MHD of the Solar Convection Zone and Tachocline: Current Understanding and Unsolved Problems - (Invited Review). *Sol. Phys.* **192**, 27 – 48.

Gilman, P.A., Howard, R.: 1985, Rotation rates of leader and follower sunspots. *ApJ* **295**, 233 – 240. doi:10.1086/163368.

Gilman, P.A., Miller, J.: 1981, Dynamically consistent nonlinear dynamos driven by convection in a rotating spherical shell. *ApJS* **46**, 211 – 238. doi:10.1086/190743.

Gilman, P.A., Miller, J.: 1986, Nonlinear convection of a compressible fluid in a rotating spherical shell. *ApJS* **61**, 585 – 608. doi:10.1086/191125.

Gizon, L., Birch, A.C.: 2005, Local Helioseismology. *Living Reviews in Solar Physics* **2**, 6. doi:10.12942/lrsp-2005-6.

Gizon, L., Solanki, S.K.: 2004, Measuring Stellar Differential rotation with asteroseismology. *Sol. Phys.* **220**, 169 – 184. doi:10.1023/B:SOLA.0000031378.29215.0c.

Glatzmaier, G.A.: 1984, Numerical simulations of stellar convective dynamos. I - The model and method. *Journal of Computational Physics* **55**, 461 – 484. doi:10.1016/0021-9991(84)90033-0.

Golub, L., Vaiana, G.S.: 1978, Differential rotation rates for short-lived regions of emerging magnetic flux. *ApJL* **219**, L55 – L57. doi:10.1086/182605.

Güdel, M.: 2007, The Sun in Time: Activity and Environment. *Living Reviews in Solar Physics* **4**, 3. doi:10.12942/lrsp-2007-3.

Hagenaar, H.J., Schrijver, C.J., Title, A.M.: 2003, The Properties of Small Magnetic Regions on the Solar Surface and the Implications for the Solar Dynamo(s). *ApJ* **584**, 1107 – 1119.

doi:10.1086/345792.

Hale, G.E.: 1908, On the Probable Existence of a Magnetic Field in Sun-Spots. *ApJ* **28**, 315. doi:10.1086/141602.

Hale, G.E., Ellerman, F., Nicholson, S.B., Joy, A.H.: 1919, The Magnetic Polarity of Sun-Spots. *ApJ* **49**, 153. doi:10.1086/142452.

Hall, J.C.: 2008, Stellar Chromospheric Activity. *Living Reviews in Solar Physics* **5**, 2. doi:10.12942/lrsp-2008-2.

Hansen, C.J., Kawaler, S.D.: 1994, *Stellar Interiors. Physical Principles, Structure, and Evolution.*.

Harvey, K.L., Zwaan, C.: 1993, Properties and emergence of bipolar active regions. *Sol. Phys.* **148**, 85 – 118. doi:10.1007/BF00675537.

Hathaway, D.H.: 2010, The Solar Cycle. *Living Reviews in Solar Physics* **7**, 1. doi:10.12942/lrsp-2010-1.

Hathaway, D.H., Upton, L., Colegrove, O.: 2013, Giant Convection Cells Found on the Sun. *Science* **342**, 1217 – 1219. doi:10.1126/science.1244682.

Hathaway, D.H., Gilman, P.A., Harvey, J.W., Hill, F., Howard, R.F., Jones, H.P., Kasher, J.C., Leibacher, J.W., Pintar, J.A., Simon, G.W.: 1996, GONG Observations of Solar Surface Flows. *Science* **272**, 1306 – 1309. doi:10.1126/science.272.5266.1306.

Hiremath, K.M., Lovely, M.R.: 2007, Magnetic Flux in the Solar Convective Envelope Inferred from Initial Observations of Sunspots. *ApJ* **667**, 585 – 590. doi:10.1086/520842.

Hirzberger, J., Bonet, J.A., Vázquez, M., Hanslmeier, A.: 1999, Time Series of Solar Granulation Images. II. Evolution of Individual Granules. *ApJ* **515**, 441 – 454. doi:10.1086/307018.

Hirzberger, J., Gizon, L., Solanki, S.K., Duvall, T.L.: 2008, Structure and Evolution of Supergranulation from Local Helioseismology. *Sol. Phys.* **251**, 417 – 437. doi:10.1007/s11207-008-9206-8.

Howard, R., Harvey, J.: 1970, Spectroscopic Determinations of Solar Rotation. *Sol. Phys.* **12**, 23 – 51. doi:10.1007/BF02276562.

Howard, R.F.: 1996, Axial Tilt Angles of Active Regions. *Sol. Phys.* **169**, 293 – 301. doi:10.1007/BF00190606.

Howe, R.: 2009, Solar Interior Rotation and its Variation. *Living Reviews in Solar Physics* **6**, 1. doi:10.12942/lrsp-2009-1.

Howe, R., Christensen-Dalsgaard, J., Hill, F., Komm, R.W., Larsen, R.M., Schou, J., Thompson, M.J., Toomre, J.: 2000, Dynamic Variations at the Base of the Solar Convection Zone. *Science* **287**, 2456 – 2460. doi:10.1126/science.287.5462.2456.

Ilonidis, S., Zhao, J., Kosovichev, A.: 2011, Detection of Emerging Sunspot Regions in the Solar Interior. *Science* **333**, –. doi:10.1126/science.1206253.

Järvinen, S.P., Berdyugina, S.V., Tuominen, I., Cutispoto, G., Bos, M.: 2005, Magnetic activity in the young solar analog AB Dor. Active longitudes and cycles from long-term photometry. *A&A* **432**, 657 – 664. doi:10.1051/0004-6361:20041998.

Jetsu, L., Pohjolainen, S., Pelt, J., Tuominen, I.: 1997, Is the longitudinal distribution of solar flares nonuniform? *A&A* **318**, 293 – 307.

Jouve, L., Brun, A.S.: 2007, 3-D non-linear evolution of a magnetic flux tube in a spherical shell: The isentropic case. *Astronomische Nachrichten* **328**, 1104. doi:10.1002/asna.200710887.

Jouve, L., Brun, A.S.: 2009, Three-Dimensional Nonlinear Evolution of a Magnetic Flux

Tube in a Spherical Shell: Influence of Turbulent Convection and Associated Mean Flows. *ApJ* **701**, 1300 – 1322. doi:10.1088/0004-637X/701/2/1300.

Jouve, L., Brun, A.S., Aulanier, G.: 2013, Global dynamics of subsurface solar active regions. *ApJ* **762**, 4. doi:10.1088/0004-637X/762/1/4.

Koutchmy, S., Livshits, M.: 1992, Coronal Streamers. *Space Sci. Rev.* **61**, 393 – 417. doi:10.1007/BF00222313.

Krause, F., Raedler, K.-H.: 1980, *Mean-field magnetohydrodynamics and dynamo theory.*

Labonte, B.J., Howard, R., Gilman, P.A.: 1981, An improved search for large-scale convection cells in the solar atmosphere. *ApJ* **250**, 796 – 798. doi:10.1086/159430.

Lamb, F.K., Aly, J.-J., Cook, M.C., Lamb, D.Q.: 1983, Synchronization of magnetic stars in binary systems. *ApJL* **274**, L71 – L75. doi:10.1086/184153.

Lanza, A.F., Pagano, I., Leto, G., Messina, S., Aigrain, S., Alonso, R., Auvergne, M., Baglin, A., Barge, P., Bonomo, A.S., Boumier, P., Collier Cameron, A., Comparato, M., Cutispoto, G., de Medeiros, J.R., Foing, B., Kaiser, A., Moutou, C., Parihar, P.S., Silva-Valio, A., Weiss, W.W.: 2009, Magnetic activity in the photosphere of CoRoT-Exo-2a. Active longitudes and short-term spot cycle in a young Sun-like star. *A&A* **493**, 193 – 200. doi:10.1051/0004-6361:200810591.

Leighton, R.B.: 1964, Transport of Magnetic Fields on the Sun. *ApJ* **140**, 1547. doi:10.1086/148058.

Leighton, R.B.: 1969, A Magneto-Kinematic Model of the Solar Cycle. *ApJ* **156**, 1. doi:10.1086/149943.

Li, J.: 2011, Active Longitudes Revealed by Large-scale and Long-lived Coronal Streamers. *ApJ* **735**, 130. doi:10.1088/0004-637X/735/2/130.

Li, J., Ulrich, R.K.: 2012, Long-term Measurements of Sunspot Magnetic Tilt Angles. *ApJ* **758**, 115. doi:10.1088/0004-637X/758/2/115.

Lindsey, C., Braun, D.C.: 2000, Seismic Images of the Far Side of the Sun. *Science* **287**, 1799 – 1801. doi:10.1126/science.287.5459.1799.

Longcope, D.W., Klapper, I.: 1997, Dynamics of a Thin Twisted Flux Tube. *ApJ* **488**, 443. doi:10.1086/304680.

Longcope, D.W., Fisher, G.H., Arendt, S.: 1996, The Evolution and Fragmentation of Rising Magnetic Flux Tubes. *ApJ* **464**, 999. doi:10.1086/177387.

Longcope, D.W., Fisher, G.H., Pevtsov, A.A.: 1998, Flux-Tube Twist Resulting from Helical Turbulence: The Sigma-Effect. *ApJ* **507**, 417 – 432. doi:10.1086/306312.

Love, J.J., Joshua Rigler, E., Gibson, S.E.: 2012, Geomagnetic detection of the sectorial solar magnetic field and the historical peculiarity of minimum 23-24. *GeoRL* **39**, 4102. doi:10.1029/2011GL050702.

Low, B.C.: 1996, Solar Activity and the Corona. *Sol. Phys.* **167**, 217 – 265. doi:10.1007/BF00146338.

Lund, M.N., Miesch, M.S., Christensen-Dalsgaard, J.: 2014, Differential Rotation in Main-Sequence Solar-like Stars - Qualitative Inference from Astroseismic Data. *ApJ*.

MacGregor, K.B., Cassinelli, J.P.: 2003, Magnetic Fields in Massive Stars. II. The Buoyant Rise of Magnetic Flux Tubes through the Radiative Interior. *ApJ* **586**, 480 – 494. doi:10.1086/346257.

MacGregor, K.B., Charbonneau, P.: 1997, Solar Interface Dynamos. I. Linear, Kinematic Models in Cartesian Geometry. *ApJ* **486**, 484. doi:10.1086/304484.

Maehara, H., Shibayama, T., Notsu, S., Notsu, Y., Nagao, T., Kusaba, S., Honda, S.,

Nogami, D., Shibata, K.: 2012, Superflares on solar-type stars. *Nature* **485**, 478 – 481. doi:10.1038/nature11063.

Mann, M., Beer, J., Steinhilber, F., Christl, M.: 2012, ^{10}Be in lacustrine sediments-A record of solar activity? *Journal of Atmospheric and Solar-Terrestrial Physics* **80**, 92 – 99. doi:10.1016/j.jastp.2012.03.011.

Martínez-Sykora, J., Hansteen, V., Carlsson, M.: 2008, Twisted Flux Tube Emergence From the Convection Zone to the Corona. *ApJ* **679**, 871 – 888. doi:10.1086/587028.

Matt, S.P., Do Cao, O., Brown, B.P., Brun, A.S.: 2011, Convection and differential rotation properties of G and K stars computed with the ASH code. *Astronomische Nachrichten* **332**, 897. doi:10.1002/asna.201111624.

McClintock, B.H., Norton, A.A.: 2013, Recovering Joy's Law as a Function of Solar Cycle, Hemisphere, and Longitude. *Sol. Phys.* **287**, 215 – 227. doi:10.1007/s11207-013-0338-0.

Miesch, M.S.: 2005, Large-Scale Dynamics of the Convection Zone and Tachocline. *Living Reviews in Solar Physics* **2**, 1. doi:10.12942/lrsp-2005-1.

Miesch, M.S.: 2012, The solar dynamo. *Royal Society of London Philosophical Transactions Series A* **370**, 3049 – 3069. doi:10.1098/rsta.2011.0507.

Miesch, M.S., Toomre, J.: 2009, Turbulence, Magnetism, and Shear in Stellar Interiors. *Annual Review of Fluid Mechanics* **41**, 317 – 345. doi:10.1146/annurev.fluid.010908.165215.

Miesch, M.S., Brun, A.S., Toomre, J.: 2006, Solar Differential Rotation Influenced by Latitudinal Entropy Variations in the Tachocline. *ApJ* **641**, 618 – 625. doi:10.1086/499621.

Miesch, M.S., Elliott, J.R., Toomre, J., Clune, T.L., Glatzmaier, G.A., Gilman, P.A.: 2000, Three-dimensional Spherical Simulations of Solar Convection. I. Differential Rotation and Pattern Evolution Achieved with Laminar and Turbulent States. *ApJ* **532**, 593 – 615.

doi:10.1086/308555.

Miesch, M.S., Brun, A.S., De Rosa, M.L., Toomre, J.: 2008, Structure and Evolution of Giant Cells in Global Models of Solar Convection. *ApJ* **673**, 557 – 575. doi:10.1086/523838.

Moreno-Insertis, F.: 1983, Rise times of horizontal magnetic flux tubes in the convection zone of the sun. *A&A* **122**, 241 – 250.

Moreno-Insertis, F.: 1986, Nonlinear time-evolution of kink-unstable magnetic flux tubes in the convective zone of the sun. *A&A* **166**, 291 – 305.

Moreno-Insertis, F.: 1992, The motion of magnetic flux tubes in the convection zone and the subsurface origin of active regions. In: Thomas, J.H., Weiss, N.O. (eds.) *NATO ASIC Proc. 375: Sunspots. Theory and Observations*, 385 – 410.

Moreno-Insertis, F., Emonet, T.: 1996, The Rise of Twisted Magnetic Tubes in a Stratified Medium. *ApJL* **472**, L53. doi:10.1086/310360.

Moreno-Insertis, F., Caligari, P., Schüssler, M.: 1994, Active region asymmetry as a result of the rise of magnetic flux tubes. *Sol. Phys.* **153**, 449 – 452. doi:10.1007/BF00712518.

Moss, D.: 2001, Magnetic Fields in the Ap and Bp Stars: a Theoretical Overview. In: Mathys, G., Solanki, S.K., Wickramasinghe, D.T. (eds.) *Magnetic Fields Across the Hertzsprung-Russell Diagram*, *Astronomical Society of the Pacific Conference Series* **248**, 305.

Mursula, K., Zieger, B.: 1996, The 13.5-day periodicity in the Sun, solar wind, and geomagnetic activity: The last three solar cycles. *JGR* **101**, 27077 – 27090. doi:10.1029/96JA02470.

Nelson, N.J., Brown, B.P., Brun, A.S., Miesch, M.S., Toomre, J.: 2011, Buoyant Magnetic

Loops in a Global Dynamo Simulation of a Young Sun. *ApJL* **739**, L38. doi:10.1088/2041-8205/739/2/L38.

Nelson, N.J., Brown, B.P., Sacha Brun, A., Miesch, M.S., Toomre, J.: 2013, Buoyant Magnetic Loops Generated by Global Convective Dynamo Action. *Sol. Phys.*. doi:10.1007/s11207-012-0221-4.

Neugebauer, M., Smith, E.J., Ruzmaikin, A., Feynman, J., Vaughan, A.H.: 2000, The solar magnetic field and the solar wind: Existence of preferred longitudes. *JGR* **105**, 2315 – 2324. doi:10.1029/1999JA000298.

Nielsen, M.B., Gizon, L., Schunker, H., Karoff, C.: 2013, Rotation periods of 12 000 main-sequence Kepler stars: Dependence on stellar spectral type and comparison with v sin i observations. *ArXiv e-prints*.

Nordlund, Å., Stein, R.F., Asplund, M.: 2009, Solar Surface Convection. *Living Reviews in Solar Physics* **6**, 2. doi:10.12942/lrsp-2009-2.

Norton, A.A., Gilman, P.A.: 2005, Recovering Solar Toroidal Field Dynamics from Sunspot Location Patterns. *ApJ* **630**, 1194 – 1205. doi:10.1086/431961.

Olah, K., Hall, D.S., Henry, G.W.: 1991, Long-term behaviour of starspots. III - Active longitudes on the long-period RS CVn star HK Lacertae. *A&A* **251**, 531 – 535.

Oláh, K., Jurcsik, J., Strassmeier, K.G.: 2003, Differential rotation on UZ Librae. *A&A* **410**, 685 – 689. doi:10.1051/0004-6361:20031352.

Olemskoy, S.V., Kitchatinov, L.L.: 2009, Active longitudes of sunspots. *Geomagnetism and Aeronomy* **49**, 866 – 870. doi:10.1134/S001679320907007X.

Parker, E.N.: 1955, Hydromagnetic Dynamo Models. *ApJ* **122**, 293. doi:10.1086/146087.

Parker, E.N.: 1979, *Cosmical magnetic fields: Their origin and their activity*.

Parker, E.N.: 1993, A solar dynamo surface wave at the interface between convection and nonuniform rotation. *ApJ* **408**, 707 – 719. doi:10.1086/172631.

Pettersen, B.R.: 1989, A review of stellar flares and their characteristics. *Sol. Phys.* **121**, 299 – 312. doi:10.1007/BF00161702.

Pevtsov, A.A., Canfield, R.C., Latushko, S.M.: 2001, Hemispheric Helicity Trend for Solar Cycle 23. *ApJL* **549**, L261 – L263. doi:10.1086/319179.

Pevtsov, A.A., Canfield, R.C., Metcalf, T.R.: 1995, Latitudinal variation of helicity of photospheric magnetic fields. *ApJL* **440**, L109 – L112. doi:10.1086/187773.

Pevtsov, A.A., Maleev, V.M., Longcope, D.W.: 2003, Helicity Evolution in Emerging Active Regions. *ApJ* **593**, 1217 – 1225. doi:10.1086/376733.

Pinto, R.F., Brun, A.S.: 2013, Flux Emergence in a Magnetized Convection Zone. *ApJ* **772**, 55. doi:10.1088/0004-637X/772/1/55.

Pizzolato, N., Maggio, A., Micela, G., Sciortino, S., Ventura, P.: 2003, The stellar activity-rotation relationship revisited: Dependence of saturated and non-saturated X-ray emission regimes on stellar mass for late-type dwarfs. *A&A* **397**, 147 – 157. doi:10.1051/0004-6361:20021560.

Plyusnina, L.A.: 2010, Determination of the Rotation Periods of Solar Active Longitudes. *Sol. Phys.* **261**, 223 – 232. doi:10.1007/s11207-009-9501-z.

Pontius, D.H. Jr., Wolf, R.A.: 1990, Transient flux tubes in the terrestrial magnetosphere. *GeoRL* **17**, 49 – 52. doi:10.1029/GL017i001p00049.

Press, W.H., Teukolsky, S.A., Vetterling, W.T., Flannery, B.P.: 1992, *Numerical recipes in FORTRAN. The art of scientific computing.*

Prialnik, D.: 2000, *An Introduction to the Theory of Stellar Structure and Evolution.*

Priest, E.R.: 1982, *Solar magneto-hydrodynamics*, 74P.

Quintana, E.V., Barclay, T., Raymond, S.N., Rowe, J.F., Bolmont, E., Caldwell, D.A., Howell, S.B., Kane, S.R., Huber, D., Crepp, J.R., Lissauer, J.J., Ciardi, D.R., Coughlin, J.L., Everett, M.E., Henze, C.E., Horch, E., Isaacson, H., Ford, E.B., Adams, F.C., Still, M., Hunter, R.C., Quarles, B., Selsis, F.: 2014, An Earth-sized Planet in the Habitable Zone of a Cool Star. *ArXiv e-prints*.

Reiners, A.: 2012, Observations of Cool-Star Magnetic Fields. *Living Reviews in Solar Physics* **9**, 1. doi:10.12942/lrsp-2012-1.

Rempel, M.: 2003, Thermal properties of magnetic flux tubes. II. Storage of flux in the solar overshoot region. *A&A* **397**, 1097 – 1107. doi:10.1051/0004-6361:20021594.

Rempel, M.: 2004, Overshoot at the Base of the Solar Convection Zone: A Semianalytical Approach. *ApJ* **607**, 1046 – 1064. doi:10.1086/383605.

Rempel, M.: 2006a, Flux-Transport Dynamos with Lorentz Force Feedback on Differential Rotation and Meridional Flow: Saturation Mechanism and Torsional Oscillations. *ApJ* **647**, 662 – 675. doi:10.1086/505170.

Rempel, M.: 2006b, Transport of Toroidal Magnetic Field by the Meridional Flow at the Base of the Solar Convection Zone. *ApJ* **637**, 1135 – 1142. doi:10.1086/498440.

Rempel, M., Schüssler, M., Knölker, M.: 2009, Radiative Magnetohydrodynamic Simulation of Sunspot Structure. *ApJ* **691**, 640 – 649. doi:10.1088/0004-637X/691/1/640.

Roberts, B., Webb, A.R.: 1978, Vertical motions in an intense magnetic flux tube. *Sol. Phys.* **56**, 5 – 35. doi:10.1007/BF00152630.

Ruzmaikin, A.: 1998, Clustering of Emerging Magnetic Flux. *Sol. Phys.* **181**, 1 – 12.

Saar, S.H.: 1990, Magnetic Fields on Solar-like Stars: The First Decade. In: Stenflo, J.O.

(ed.) *Solar Photosphere: Structure, Convection, and Magnetic Fields*, *IAU Symposium* **138**, 427 – 441.

Schüssler, M., Solanki, S.K.: 1992, Why rapid rotators have polar spots. *A&A* **264**, L13 – L16.

Schüssler, M., Caligari, P., Ferriz-Mas, A., Moreno-Insertis, F.: 1994, Instability and eruption of magnetic flux tubes in the solar convection zone. *A&A* **281**, L69 – L72.

Schüssler, M., Caligari, P., Ferriz-Mas, A., Solanki, S.K., Stix, M.: 1996, Distribution of starspots on cool stars. I. Young and main sequence stars of $1M_{sun}$. *A&A* **314**, 503 – 512.

Silva-Valio, A., Lanza, A.F.: 2011, Time evolution and rotation of starspots on CoRoT-2 from the modelling of transit photometry. *A&A* **529**, A36. doi:10.1051/0004-6361/201015382.

Simon, G.W., Weiss, N.O.: 1968, Supergranules and the Hydrogen Convection Zone. *ZA* **69**, 435.

Snodgrass, H.B., Howard, R.: 1984, Limits on photospheric Doppler signatures for solar giant cells. *ApJ* **284**, 848 – 855. doi:10.1086/162468.

Solanki, S.K.: 2003, Sunspots: An overview. *A&AR* **11**, 153 – 286. doi:10.1007/s00159-003-0018-4.

Spiegel, E.A., Weiss, N.O.: 1980, Magnetic activity and variations in solar luminosity. *Nature* **287**, 616. doi:10.1038/287616a0.

Spitzer, L.: 1962, *Physics of Fully Ionized Gases*.

Spörer, F.W.G.: 1890, Prof. Spörer's researches on Sun-spots. *MNRAS* **50**, 251.

Spruit, H.C.: 1974, A model of the solar convection zone. *Sol. Phys.* **34**, 277 – 290. doi:10.1007/BF00153665.

Spruit, H.C.: 1981a, Equations for thin flux tubes in ideal MHD. *A&A* **102**, 129 – 133.

Spruit, H.C.: 1981b, Motion of magnetic flux tubes in the solar convection zone and chromosphere. *A&A* **98**, 155 – 160.

Spruit, H.C., Roberts, B.: 1983, Magnetic flux tubes on the sun. *Nature* **304**, 401 – 406. doi:10.1038/304401a0.

Spruit, H.C., van Ballegooijen, A.A.: 1982a, Erratum - Stability of Toroidal Flux Tubes in Stars. *A&A* **113**, 350.

Spruit, H.C., van Ballegooijen, A.A.: 1982b, Stability of toroidal flux tubes in stars. *A&A* **106**, 58 – 66.

Spruit, H.C., Zweibel, E.G.: 1979, Convective instability of thin flux tubes. *Sol. Phys.* **62**, 15 – 22. doi:10.1007/BF00150128.

Stein, R.F., Lagerfjärd, A., Nordlund, Å., Georgobiani, D.: 2011, Solar Flux Emergence Simulations. *Sol. Phys.* **268**, 271 – 282. doi:10.1007/s11207-010-9510-y.

Steinhilber, F., Abreu, J.A., Beer, J., Brunner, I., Christl, M., Fischer, H., Heikkila, U., Kubik, P.W., Mann, M., McCracken, K.G., Miller, H., Miyahara, H., Oerter, H., Wilhelms, F.: 2012, 9,400 years of cosmic radiation and solar activity from ice cores and tree rings. *Proceedings of the National Academy of Science* **109**, 5967 – 5971. doi:10.1073/pnas.1118965109.

Stenflo, J.O.: 1989, Small-scale magnetic structures on the sun. *A&AR* **1**, 3 – 48. doi:10.1007/BF00872483.

Stenflo, J.O., Kosovichev, A.G.: 2012, Bipolar Magnetic Regions on the Sun: Global Analysis of the SOHO/MDI Data Set. *ApJ* **745**, 129. doi:10.1088/0004-637X/745/2/129.

Stix, M.: 2002, *The sun: an introduction.*

Strassmeier, K.G.: 2009, Starspots. *A&AR* **17**, 251 – 308. doi:10.1007/s00159-009-0020-6.

Strassmeier, K.G., Bartus, J.: 2000, Doppler imaging of stellar surface structure. XII. Rapid spot changes on the RS CVn binary V711 Tauri = HR 1099. *A&A* **354**, 537 – 550.

Temmer, M., Rybák, J., Bendík, P., Veronig, A., Vogler, F., Otruba, W., Pötzi, W., Hanslmeier, A.: 2006, Hemispheric sunspot numbers $\{R_n\}$ and $\{R_s\}$ from 1945-2004: catalogue and N-S asymmetry analysis for solar cycles 18-23. *A&A* **447**, 735 – 743. doi:10.1051/0004-6361:20054060.

Thompson, M.J., Christensen-Dalsgaard, J., Miesch, M.S., Toomre, J.: 2003, The Internal Rotation of the Sun. *ARA&A* **41**, 599 – 643. doi:10.1146/annurev.astro.41.011802.094848.

Title, A.M., Tarbell, T.D., Topka, K.P., Ferguson, S.H., Shine, R.A., SOUP Team: 1989, Statistical properties of solar granulation derived from the SOUP instrument on Spacelab 2. *ApJ* **336**, 475 – 494. doi:10.1086/167026.

Usoskin, I.G.: 2013, A History of Solar Activity over Millennia. *Living Reviews in Solar Physics* **10**, 1. doi:10.12942/lrsp-2013-1.

Usoskin, I.G., Berdyugina, S.V., Poutanen, J.: 2005, Preferred sunspot longitudes: non-axisymmetry and differential rotation. *A&A* **441**, 347 – 352. doi:10.1051/0004-6361:20053201.

Usoskin, I.G., Berdyugina, S.V., Moss, D., Sokoloff, D.D.: 2007, Long-term persistence of solar active longitudes and its implications for the solar dynamo theory. *Advances in Space Research* **40**, 951 – 958. doi:10.1016/j.asr.2006.12.050.

van Ballegooijen, A.A.: 1982, The overshoot layer at the base of the solar convective zone and the problem of magnetic flux storage. *A&A* **113**, 99 – 112.

van Driel-Gesztelyi, L., Petrovay, K.: 1990, Asymmetric flux loops in active regions. *Sol.*

Phys. **126**, 285 – 298. doi:10.1007/BF00153051.

Verma, V.K.: 1993, On the north-south asymmetry of solar activity cycles. *ApJ* **403**, 797 – 800. doi:10.1086/172250.

Vogt, S.S., Hatzes, A.P., Misch, A.A., Kürster, M.: 1999, Doppler Imagery of the Spotted RS Canum Venaticorum Star HR 1099 (V711 Tauri) from 1981 to 1992. *ApJS* **121**, 547 – 589. doi:10.1086/313195.

Wang, H., Zirin, H.: 1989, Study of supergranules. *Sol. Phys.* **120**, 1 – 17. doi:10.1007/BF00148532.

Wang, Y.-M., Sheeley, N.R. Jr.: 1989, Average properties of bipolar magnetic regions during sunspot cycle 21. *Sol. Phys.* **124**, 81 – 100. doi:10.1007/BF00146521.

Wang, Y.-M., Sheeley, N.R. Jr., Rich, N.B.: 2007, Coronal Pseudostreamers. *ApJ* **658**, 1340 – 1348. doi:10.1086/511416.

Weber, E.J., Davis, L. Jr.: 1967, The Angular Momentum of the Solar Wind. *ApJ* **148**, 217 – 227. doi:10.1086/149138.

Weber, M.A., Fan, Y., Miesch, M.S.: 2011, The Rise of Active Region Flux Tubes in the Turbulent Solar Convective Envelope. *ApJ* **741**, 11. doi:10.1088/0004-637X/741/1/11.

Weber, M.A., Fan, Y., Miesch, M.S.: 2013, Comparing Simulations of Rising Flux Tubes Through the Solar Convection Zone with Observations of Solar Active Regions: Constraining the Dynamo Field Strength. *Sol. Phys.* **287**, 239 – 263. doi:10.1007/s11207-012-0093-7.

Wood, B.E.: 2004, Astrospheres and Solar-like Stellar Winds. *Living Reviews in Solar Physics* **1**, 2. doi:10.12942/lrsp-2004-2.

Zhang, K., Liao, X., Schubert, G.: 2004, A Sandwich Interface Dynamo: Linear Dynamo Waves in the Sun. *ApJ* **602**, 468 – 480. doi:10.1086/380834.

Zhang, L.Y., Wang, H.N., Du, Z.L.: 2008, Prediction of solar active longitudes. *A&A* **484**, 523 – 527. doi:10.1051/0004-6361:200809464.

Zhang, L., Mursula, K., Usoskin, I., Wang, H.: 2011, Global analysis of active longitudes of sunspots. *A&A* **529**, A23. doi:10.1051/0004-6361/201015255.

Zhao, J., Kosovichev, A.G., Duvall, T.L. Jr.: 2004, On the Relationship between the Rotational Velocity and the Field Strength of Solar Magnetic Elements. *ApJL* **607**, L135 – L138. doi:10.1086/421974.

Zwaan, C.: 1987, Elements and patterns in the solar magnetic field. *ARA&A* **25**, 83 – 111. doi:10.1146/annurev.aa.25.090187.000503.

APPENDIX A

The Fundamental Magnetohydrodynamic Equations

Astrophysical plasmas and magnetic fields are ubiquitous in the Universe. Magnetohydrodynamics (MHD) is the study of the dynamics of electrically conducting fluids, such as plasmas in the realm of astrophysics. This Appendix discusses the assumptions made under MHD and presents the full set of MHD equations on which the model used in this thesis research is based.

1.1. Maxwell's Equations under MHD

First, let us begin with the microscopic version of Maxwell's Equations in Gaussian units:

$$\nabla \times \mathbf{B} = \frac{4\pi}{c}\mathbf{J} + \frac{1}{c}\frac{\partial \mathbf{E}}{\partial t} \tag{A.1}$$

$$\nabla \cdot \mathbf{B} = 0 \tag{A.2}$$

$$\nabla \times \mathbf{E} = -\frac{1}{c}\frac{\partial \mathbf{B}}{\partial t} \tag{A.3}$$

$$\nabla \cdot \mathbf{E} = 4\pi\rho, \tag{A.4}$$

where ρ is the charge density and c is the speed of light. The first equation, Eq. A.1, shows that either currents or a time-varying electric field can produce magnetic fields. The second equation, Eq. A.2, states that there are no magnetic monopoles. Equations A.3 and A.4 imply that either time-varying magnetic fields or electric charges may produce electric fields.

A fundamental assumption of MHD is that variations of the electromagnetic field are quasi-steady, or non-relativistic, such that $v_0^2/c^2 \ll 1$, where $v_0 = \ell_0/t_0$ is a characteristic

plasma flow speed, and ℓ_0 and t_0 are typical length and time scales, respectively. As a consequence of these assumptions, the displacement current $\frac{\partial \mathbf{E}}{\partial t}$ can be neglected for MHD treatments, as it can be shown that $\nabla \times \mathbf{B} \gg \frac{1}{c}\frac{\partial \mathbf{E}}{\partial t}$ in Eq. A.1. In order to arrive at an order of magnitude estimate for $\mathbf{E}$, we look to Eq. A.3:

$$\frac{E_0}{\ell_0} \sim \frac{1}{c}\frac{B_0}{t_0} \rightarrow E_0 \sim \frac{B_0}{c}\frac{\ell_0}{t_0}. \tag{A.5}$$

Applying this relation to the second term on the right hand side of Eq. A.1:

$$\left|\frac{1}{c}\frac{\partial \mathbf{E}}{\partial t}\right| \sim \frac{v_0^2}{c^2}\frac{B_0}{\ell_0}, \tag{A.6}$$

whereas,

$$\left|\nabla \times \mathbf{B}\right| \sim \frac{B_0}{\ell_0}. \tag{A.7}$$

Since $v_0^2/c^2 \ll 1$ in MHD, the displacement current term is much smaller than $\nabla \times \mathbf{B}$, therefore the displacement current can be neglected. Thus, under MHD, Eq. A.1 becomes:

$$\nabla \times \mathbf{B} = \frac{4\pi}{c}\mathbf{J} \tag{A.8}$$

In MHD, the magnetic field is regarded as a primary quantity, whereas the electric current and electric field are secondary. The current density $\mathbf{J}$ can be obtained explicitly from Eq. A.8. The electric field is given by Ohm's Law:

$$\mathbf{J} = \sigma \mathbf{E}' = \sigma(\mathbf{E} + \frac{\mathbf{v}}{c} \times \mathbf{B}), \tag{A.9}$$

where $\mathbf{E}'$ is the electric field in the frame of reference stationary to the plasma. Equation A.4 is generally not used in MHD to obtain $\mathbf{E}$ because its magnitude is of order $\sim(\frac{v_0}{c}\frac{B_0}{\ell_0})$, not quite of order $\sim(\frac{v_0^2}{c^2}\frac{B_0}{\ell_0})$, which can be neglected in MHD. However, once $\mathbf{E}$ is obtained from Eq. A.9, Eq. A.4 can be used to obtain the charge density in the desired frame as long as relativistic effects are considered.

1.2. The Magnetic Induction Equation

Combining Ohm's Law (Eq. A.9) and Equations A.8 and A.3, one obtains what is known as the Magnetic Induction equation, which describes how the magnetic field of a conducting plasma changes in time. Starting with Eq. A.3, $\mathbf{E}$ and $\mathbf{J}$ are replaced using Eq. A.9 and Eq. A.8, respectively, such that:

$$\frac{\partial \mathbf{B}}{\partial t} = \nabla \times (\mathbf{v} \times \mathbf{B}) - \nabla \times (\eta \nabla \times \mathbf{B}) \tag{A.10}$$

where $\eta = c^2/4\pi\sigma$ is the magnetic diffusivity. If η is uniform, using $\nabla \cdot \mathbf{B} = 0$ and the following vector identity:

$$\nabla \times (\nabla \times \mathbf{B}) = \nabla(\nabla \cdot \mathbf{B}) - (\nabla \cdot \nabla)\mathbf{B} = -\nabla^2 \mathbf{B}, \tag{A.11}$$

the Induction Equation becomes:

$$\frac{\partial \mathbf{B}}{\partial t} = \nabla \times (\mathbf{v} \times \mathbf{B}) + \eta \nabla^2 \mathbf{B}. \tag{A.12}$$

The first term on the right-hand side of the equation describes how the magnetic field is advected by the fluid, while the second term represents diffusion of the magnetic field. A dimensionless parameter known as the magnetic Reynolds number R_m measures the ratio of

the advection term to the diffusion term:

$$R_m = \frac{\ell_0 v_0}{\eta}, \tag{A.13}$$

where v_0 is a typical plasma speed, and ℓ_0 is a typical length scale. If $R_m \ll 1$, then the magnetic diffusion dominates. However, in the solar interior $R_m \gg 1$, therefore the second term is negligible compared to the first. In this limit, magnetic field lines behave as if they move with the plasma. This property is known as Alfvén's flux frozen-in theorem, and will be discussed in Appendix B.

It is important to point out that the magnetic Reynolds number R_m is large in the solar interior because of the large length scale ℓ_0. Following Spitzer (1962) and Priest (1982), the magnetic diffusivity η is given by:

$$\eta = 5.2 \times 10^{11} \frac{\ln \Lambda}{T^{3/2}} \frac{cm^2}{s}, \tag{A.14}$$

where $\ln \Lambda$ is called the Coulomb logarithm, and T is the temperature of the plasma. The value Λ is weakly dependent on the electron density and temperature. For the solar interior, $\ln \Lambda$ is $\sim$5, and the temperature in the middle of the convection zone is $\sim 10^6$ K. This results in a value for η of $\sim 10^3$ cm^2 s^{-1} and σ of $\sim 10^{16}$ s^{-1} in the bulk of the solar convection zone. Considering that the depth of the convection zone is $\sim 2 \times 10^{10}$ cm, which will serve as ℓ_0 for the bulk of the convection zone, and a typical plasma speed due to convection is $v_0 \sim 10^4$ cm s^{-1} in the middle of the convection zone, an order of magnitude estimate for the magnetic Reynolds number in the solar interior is $\sim 10^{10}$. This value is very large indeed, due more to the relatively large length scales in the solar interior considered rather than the large electrical conductivity (and therefore small magnetic diffusivity).

1.3. Plasma Equations

The behavior of the magnetic field described by the magnetic induction equation, Eq. A.12, is coupled to the motion of the plasma through the advection term (first term on the right hand side). The behavior of the plasma is described by the equations of mass continuity, motion, equation of state, and a final equation which describes the various processes affecting the heating/cooling of the plasma.

1.3.1. Equation of Mass Continuity. The first fluid equation is a result of mass conservation:

$$\frac{d\rho}{dt} + \rho(\nabla \cdot \mathbf{v}) = 0, \tag{A.15}$$

where $d\rho/dt$ is the material (Lagrangian) derivative, ρ is the density of the plasma, and $\mathbf{v}$ is the velocity of the fluid motions. Using the definition of the material derivative (Eq. E.16) and some vector identities, the continuity equation can also be written as:

$$\frac{\partial \rho}{\partial t} + \nabla \cdot (\rho \mathbf{v}) = 0. \tag{A.16}$$

Following this equation, the local density of the fluid increases ($\frac{\partial \rho}{\partial t} > 0$) if there is a convergence of mass flux such that $\nabla \cdot (\rho \mathbf{v}) < 0$. Conversely, the density of the fluid decreases if there is a divergence of mass flux such that $\nabla \cdot (\rho \mathbf{v}) > 0$.

1.3.2. Equation of Motion. The equation of motion of an electrically neutral plasma is given by:

$$\rho \frac{d\mathbf{v}}{dt} = -\nabla P + \rho \mathbf{g} + \frac{\mathbf{J}}{c} \times \mathbf{B} + \mathbf{F}, \tag{A.17}$$

where P is the plasma pressure and $\mathbf{g}$ is the gravitational acceleration. The first and second terms in Eq. A.17 are respectively the pressure gradient and gravitational force, while the fourth term $\mathbf{F}$ represents all other forces acting on an unionized fluid (i.e. Coriolis force in a rotating system, drag force). The third term, called the Lorentz Force, is a force exerted on a conducting fluid due to the presence of a magnetic field. The Lorentz Force can be decomposed into a magnetic tension force and a magnetic pressure force as mentioned in Chapter 3.2, which act to shorten the magnetic field lines and compress the plasma, respectively.

1.3.3. Equation of State. Plasma in the interior of a star is comprised of a mixture of ions, electrons, and photons (radiation). Equations of state must relate the pressure $P(\rho, T, ...)$ exerted by a system to the so-called state variables such as density ρ and temperature T. In stellar interiors, the total pressure is a sum of the associated ion pressure P_I, electron pressure P_e, and radiation pressure P_{rad} due to momentum transfer from photons to gas particles caused by absorption or scattering.

In a star such as the Sun, ions and electrons can be treated as though they are a single fluid satisfying ideal gas conditions, and quantum effects can be neglected such that:

$$P_{I+e} = \frac{\rho R T}{\mu}, \tag{A.18}$$

where $P = P_{I+e}$ is the gas pressure, R is the ideal gas constant, T is temperature, and μ is the mean molecular weight of the plasma. In very dense stars with low enough temperatures, electrons can become degenerate, or partially degenerate, thus requiring an adjustment to

the electron pressure equation. Radiation pressure is given by:

$$P_{rad} = \frac{aT^4}{3}, \tag{A.19}$$

where $a = 7.566\times10^{-15}$ erg cm^{-3} K^{-4} is the radiation constant. Except for stars with high temperatures and low density, the radiation pressure is negligible. Through the solar convection zone, the gas pressure and temperature decreases from $P \sim 10^{13}$ g s^{-2} cm^{-1} and $T \sim 10^6$ K at the base of the convection zone to $P \sim 10^4$ g s^{-2} cm^{-1} and $T \sim 10^3$ K at the solar surface, corresponding to P_{rad} of $\sim 10^9$ to 10^{-3}, respectively. Therefore, it is reasonable to neglect the radiation pressure in the solar case, and the equation of state for the solar interior is given by the ideal gas law in Eq. A.18.

1.3.4. Energy Equation. The energy equation can be derived by considering the First Law of Thermodynamics:

$$\frac{de}{dt} = \frac{dQ}{dt} - P\frac{d}{dt}\left(\frac{1}{\rho}\right), \tag{A.20}$$

where e is the internal energy per unit mass, Q is the heat per unit mass, and volume has been replaced with $1/\rho$.

For an ideal gas, the internal energy per unit mass is defined as $e = c_v T$, where c_v is the specific heat at constant volume. Specific heat is the amount of heat per unit mass of an ideal gas needed to raise its temperature, per degree temperature increase. The specific heat at constant pressure c_p is given by $c_p = c_v + k_B/m$, where m is the mean particle mass and k_B is Boltzmann's constant. We also define γ as the ratio of specific heats $\gamma = c_p/c_v$. Using these definitions, the internal energy per unit mass e can be written in terms of γ, ρ, and P

as:

$$e = \frac{P}{(\gamma - 1)\rho}. \tag{A.21}$$

Substituting Eq. A.21 for e in Eq. A.20, we arrive at a general form of the plasma energy equation:

$$\frac{1}{\rho}\frac{d\rho}{dt} = \frac{1}{\gamma P}\frac{dP}{dt} - \frac{\rho}{P}\left(\frac{\gamma - 1}{\gamma}\right)\frac{dQ}{dt}. \tag{A.22}$$

The quantity $dQ/dt = T\ dS/dt$, where S is the entropy per unit mass and dQ/dt is the rate of heat loss/gain of the system per unit mass, which may include multiple terms related to thermal conduction, radiation, viscous heating, wave heating, and nuclear energy generation depending on the conditions of the plasma. If processes are adiabatic, $dS/dt = 0$. Further discussion on defining an expression for dQ/dt can be found in Chapter 6.

Often the quantity $(\gamma - 1)/\gamma$ in Equation A.22 is written as ∇_{ad}, which is the double logarithmic derivative of T with respect to P required for adiabatic evolution of a fluid parcel. In the following portion of this section, will show that $(\gamma - 1)/\gamma = (d \ln T)/(d \ln P)|_{ad} \equiv \nabla_{ad}$. If an ideal gas evolves adiabatically, $P\rho^{-\gamma} = C$, where C is a constant and γ is the ratio of specific heats. For adiabatic processes then:

$$\gamma\frac{d\rho}{\rho} = \frac{dP}{P}. \tag{A.23}$$

Using the ideal gas law to replace density with pressure and temperature, and applying the logarithmic derivative, Equation A.23 can be rewritten as:

$$\gamma(d\ln P - d\ln T) = d\ln P, \tag{A.24}$$

$$\frac{\gamma - 1}{\gamma} = \frac{d\ln T}{d\ln P} \equiv \nabla_{ad}, \tag{A.25}$$

where $\gamma = 5/3$ and $\nabla_{ad} = 0.4$ throughout the majority of the solar convection zone. Thus, the energy equation can also be written as:

$$\frac{1}{\rho}\frac{d\rho}{dt} = \frac{1}{\gamma P}\frac{dP}{dt} - \nabla_{ad}\frac{\rho T}{P}\frac{dS}{dt}. \tag{A.26}$$

1.4. Summary of MHD Equations

The set of MHD Equations, from which the thin flux tube equations are derived, are as follows:

$$\frac{\partial \mathbf{B}}{\partial t} = \nabla \times (\mathbf{v} \times \mathbf{B}) + \eta \nabla^2 \mathbf{B} \tag{A.27}$$

$$\frac{d\rho}{dt} + \rho(\nabla \cdot \mathbf{v}) = 0 \tag{A.28}$$

$$\rho \frac{d\mathbf{v}}{dt} = -\nabla P + \rho \mathbf{g} + \frac{\mathbf{J}}{c} \times \mathbf{B} + \mathbf{F} \tag{A.29}$$

$$P = \frac{\rho R T}{\mu} \tag{A.30}$$

$$\frac{1}{\rho}\frac{d\rho}{dt} = \frac{1}{\gamma P}\frac{dP}{dt} - \nabla_{ad}\frac{\rho T}{P}\frac{dS}{dt} \tag{A.31}$$

Note:

$$\frac{d}{dt} = \frac{\partial}{\partial t} + \mathbf{v} \cdot \nabla \tag{A.32}$$

APPENDIX B

The Flux Frozen-In Theorem

In a perfectly conducting fluid, magnetic field lines move with the fluid such that they are effectively frozen into the plasma. In this regime $R_m \gg 1$, therefore the second term on the right hand side of the Induction Equation A.12 vanishes, with advection, stretching, shearing, and expansion of magnetic flux tubes all contributing to the time evolution of the magnetic field. In 1943, Hannes Alfvén proved that the magnetic flux through any closed loop moving with the fluid is constant in time, thereafter known as Alfvén's Flux Frozen-In Theorem. A detailed layout of the proof will be considered here.

The end goal is to prove that the total magnetic flux, enclosed by a curve P (arbitrary) bounding a surface F moving with the plasma, is conserved such that $d\Phi/dt = 0$. Consider Figure B.1. Let F be a surface bounded by a closed loop P at time t, and F' be a surface bounded by a closed loop P' in its new position at time $t + dt$. The area F enclosed by P

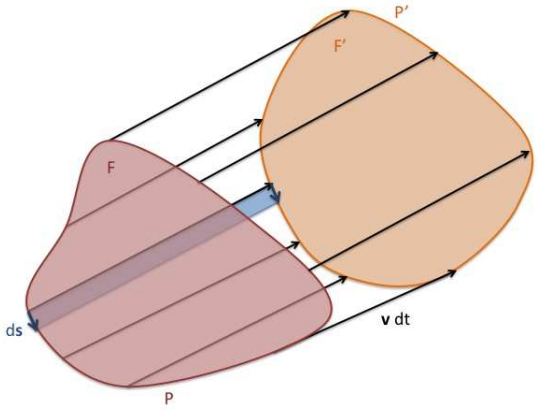

FIGURE B.1. The volume a surface F bounded by loop P sweeps out in time $t + dt$.

is comprised of the same mass elements as those in F' enclosed by P', although the shape of F' and P' may be different from F and P due to stretching or deformation as a result of the various paths followed by the mass elements. We want to investigate whether or not the flux through surface F at time t, represented by $\Phi(t)$, is different from the flux through surface F' at some time $t + dt$, represented by $\Phi(t + dt)$, by calculating the following:

$$d\Phi = \Phi(t + dt) - \Phi(t), \tag{B.1}$$

with magnetic flux given by:

$$\Phi = \int_F \mathbf{B}(t) \cdot d\mathbf{a}, \tag{B.2}$$

where F is a surface bounded by a closed loop P. Therefore, Equation B.1 can be rewritten as:

$$d\Phi = \int_{F'} \mathbf{B}(t + dt) \cdot d\mathbf{a} - \int_F \mathbf{B}(t) \cdot d\mathbf{a}. \tag{B.3}$$

Now, by Gauss' Divergence Theorem and Eq. A.2:

$$\int_V (\nabla \cdot \mathbf{B}(t)) dV = \int_S \mathbf{B}(t) \cdot d\mathbf{a} = 0, \tag{B.4}$$

where V is a volume and S is the surface enclosing volume V. At time t, the surface enclosing the volume is only given by the surface F. However, at time $t+dt$, the total surface enclosing the volume swept out by the loop P and surface F in time $t + dt$ is given by the surfaces F, F', and the *Ribbon* surface that joins F and F'. Applying Gauss' Divergence Theorem at

time $t + dt$:

$$0 = \int_V (\nabla \cdot \mathbf{B}(t+dt))dV = \int_S \mathbf{B}(t+dt) \cdot d\mathbf{a}, \tag{B.5}$$

$$= \int_{Left} \mathbf{B}(t+dt) \cdot d\mathbf{a} + \int_{Right} \mathbf{B}(t+dt) \cdot d\mathbf{a} + \int_{Ribbon} \mathbf{B}(t+dt) \cdot d\mathbf{a}, \tag{B.6}$$

$$= \int_F \mathbf{B}(t+dt) \cdot d\mathbf{a} - \int_{F'} \mathbf{B}(t+dt) \cdot d\mathbf{a} + \int_{Ribbon} \mathbf{B}(t+dt) \cdot d\mathbf{a}, \tag{B.7}$$

where $Left$ and $Right$ indicate integrals for the flux through surfaces F and F', respectively. The subscript *Ribbon* on the third term in Eqs. B.6 and B.7 indicates the flux through the surface joining the perimeters of F and F'. The vector $d\mathbf{a} = \hat{n}\, da$, where da is an infinitesimal area element, and $\hat{n}$ is the outward directed vector normal to the closed surface comprised of F, F', and the *Ribbon*. The negative sign on the second term in Eq. B.7 come from switching the outward $d\mathbf{a}$ to inward $d\mathbf{a}$ such that the integration path along the closed loops P and P' are in the same direction. Solving Eq. B.7 for $\int_{F'} \mathbf{B}(t+dt) \cdot d\mathbf{a}$ and substituting it into Eq. B.3 yields:

$$d\Phi = \int_F \mathbf{B}(t+dt) \cdot d\mathbf{a} + \int_{Ribbon} \mathbf{B}(t+dt) \cdot d\mathbf{a} - \int_F \mathbf{B}(t) \cdot d\mathbf{a}, \tag{B.8}$$

$$= dt \int_F \frac{\partial \mathbf{B}}{\partial t} \cdot d\mathbf{a} + \int_{Ribbon} \mathbf{B}(t+dt) \cdot d\mathbf{a}, \tag{B.9}$$

where for infinitesimal dt, $\mathbf{B}(t+dt) - \mathbf{B}(t) = \frac{\partial \mathbf{B}}{\partial t} dt$. The area element for the *Ribbon* is $d\mathbf{a} = (\mathbf{v} \times d\mathbf{s})dt$ (directed outward), which is the area an element $d\mathbf{s}$ of the closed loop P sweeps out during a time dt. To first order in dt, and using the vector identity $\mathbf{B} \cdot (\mathbf{v} \times d\mathbf{s}) = -(\mathbf{v} \times \mathbf{B}) \cdot d\mathbf{s}$, Eq. B.9 becomes:

$$d\Phi = dt \int_F \frac{\partial \mathbf{B}}{\partial t} \cdot d\mathbf{a} - dt \int_P (\mathbf{v} \times \mathbf{B}) \cdot d\mathbf{s}, \tag{B.10}$$

where P is the closed loop around surface F. Now, by Stokes Theorem:

$$\int_P \mathbf{A} \cdot d\mathbf{s} = \int_F (\nabla \times \mathbf{A}) \cdot d\mathbf{a}, \tag{B.11}$$

where F is a surface bounded by loop P. Therefore, Equation B.10 becomes:

$$\frac{d\Phi}{dt} = \int_F \frac{\partial \mathbf{B}}{\partial t} \cdot d\mathbf{a} - \int_F \nabla \times (\mathbf{v} \times \mathbf{B}) \cdot d\mathbf{a}. \tag{B.12}$$

Substituting in the Induction Equation for the infinite conductivity limit (or $R_m \gg 1$), this equation becomes:

$$\frac{d\Phi}{dt} = \int_F \nabla \times (\mathbf{v} \times \mathbf{B}) \cdot d\mathbf{a} - \int_F \nabla \times (\mathbf{v} \times \mathbf{B}) \cdot d\mathbf{a} = 0, \tag{B.13}$$

thereby proving that the magnetic flux through any closed loop (or surface bounded by this closed loop) moving with the fluid remains constant, as if the magnetic field lines are frozen into the fluid. Therefore, the concept of a magnetic flux tube is often invoked in MHD to refer locally to both the bundle of concentrated magnetic flux and the plasma it contains. The flux tube concept is useful because of (1) the solenoidal nature of magnetic fields, and (2) the frozen-in condition of the magnetic field in a plasma of high electrical conductivity.

APPENDIX C

Derivation of the Thin Flux Tube Equations

In this Appendix chapter, I will derive the thin flux tube equations as they appear in Chapter 2 using Gaussian units. Particularly, I will focus on the equation of motion, energy, and the equation describing the rate of change of the magnetic field with respect to the density of the flux tube, sometimes referred to as the Walén Equation.

3.1. Equation of State and Instantaneous Pressure Balance

The equation of state, relating the flux tube pressure to density and temperature, is given by the ideal gas equation as discussed in Appendix section 1.3.3. The time required for lateral pressure balance between the flux tube and its surrounding environment is given by (e.g. Spruit 1981a):

$$t \sim \frac{d}{\sqrt{v_A^2 + c_s^2}}, \tag{C.1}$$

where d is the flux tube diameter, $v_A = B/(4\pi\rho)^{1/2}$ and $c_s = (\gamma P/\rho)^{1/2}$ are respectively the Alfvén and sound speeds in the external plasma environment, and $\gamma = 5/3$ is the adiabatic constant. At the base of the convection zone, a typical sound speed is c_s $\sim$2.2$\times$10^7 cm s^{-1}. Assuming a flux tube of $B_0 = 100$ kG, the Alfvén speed is $v_A \sim 6.8\times10^4$ cm s^{-1} and the diameter of such a flux tube with $\Phi = 10^{22}$ Mx is $d \sim 3.6\times10^8$ cm. This results in a time of $t \sim 20$ seconds in order for conditions of lateral pressure balance to be achieved. Throughout most of the convection zone, this time is small compared to other relevant time scales associated with the flux tube (e.g. rise time through the convection zone, $\sim$ months)

and convective environment (e.g. convective turnover time scale, $\sim$ one month). As a result, in the thin flux tube approximation, an instantaneous lateral pressure balance between the tube and the external plasma environment is assumed:

$$P_e = P + \frac{B^2}{8\pi}, \tag{C.2}$$

where P_e is the pressure of the external plasma environment, P is the flux tube internal gas pressure, and the term $B^2/8\pi$ is the *magnetic pressure*, or magnetic energy density associated with the magnetic field inside the flux tube.

3.2. Equation of Motion

We begin with the MHD equation of motion (force per unit volume) for an electrically neutral, non-rotating plasma:

$$\rho\frac{d\mathbf{v}}{dt} = -\nabla P + \rho\mathbf{g} + \frac{\mathbf{J}}{c} \times \mathbf{B}, \tag{C.3}$$

where ρ is the plasma density, $\mathbf{v}$ is the velocity vector, P is the plasma pressure assumed to be scalar, $\mathbf{g}$ is the gravitational acceleration, $\mathbf{J}$ is the current density, and $\mathbf{B}$ is the magnetic field of a Lagrangian flux tube element, each of which are a function of arc length s along the flux tube and time t. The terms on the right hand side of the equation are respectively: the plasma pressure gradient, gravitational force, and Lorentz force.

We eliminate the current density $\mathbf{J}$ from the Lorentz force by replacing it with Eq. A.8 such that:

$$\frac{\mathbf{J}}{c} \times \mathbf{B} = \frac{1}{4\pi}(\nabla \times \mathbf{B}) \times \mathbf{B} = -\frac{1}{4\pi}(\mathbf{B} \times (\nabla \times \mathbf{B})). \tag{C.4}$$

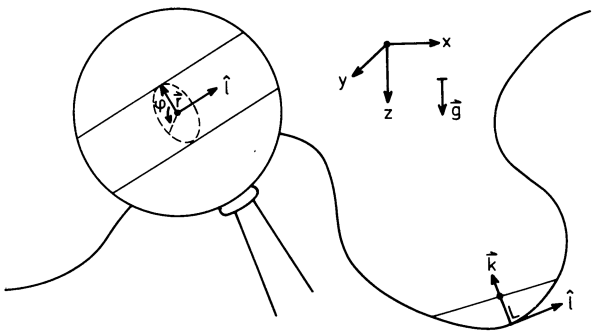

FIGURE C.1. Flux tube coordinate system, showing the unit vector **l** tangent to the flux tube, and the curvature vector **k**. Figure taken from Spruit (1981b).

Using the vector identity $\frac{1}{2}\nabla(\mathbf{A}\cdot\mathbf{A}) = \mathbf{A}\times(\nabla\times\mathbf{A}) + (\mathbf{A}\cdot\nabla)\mathbf{A}$, the Lorentz force equation becomes:

$$\frac{\mathbf{J}}{c}\times\mathbf{B} = -\frac{1}{4\pi}\left(\frac{1}{2}\nabla(\mathbf{B}\cdot\mathbf{B}) - (\mathbf{B}\cdot\nabla)\mathbf{B}\right), \tag{C.5}$$

$$= -\frac{1}{8\pi}\nabla B^2 + \frac{1}{4\pi}(\mathbf{B}\cdot\nabla)\mathbf{B}. \tag{C.6}$$

The first term on the right side of Eq. C.6 represents the effect of a magnetic pressure, acting to compress the plasma. The second term represents the effect of a tension of magnitude $B^2/4\pi$ directed parallel to **B**. Substituting the Lorentz force as derived in Equation C.6 into Equation C.3:

$$\rho\frac{d\mathbf{v}}{dt} = -\nabla\left(P + \frac{B^2}{8\pi}\right) + \frac{1}{4\pi}(\mathbf{B}\cdot\nabla)\mathbf{B} + \rho\mathbf{g}. \tag{C.7}$$

We introduce a local cylindrical coordinate system (r,ϕ,**l**) oriented along the flux tube as shown in Figure C.1, with the position vector **r** of each flux tube element a function of arc length s and time t only. The magnetic field of the flux tube is untwisted such that $B_\phi = 0$, and B_r is negligible because the flux tube is so thin, therefore the local magnetic field is

$\mathbf{B} = B\mathbf{l}$, where $\mathbf{l}$ is the unit vector tangential to the flux tube. Vectors $\mathbf{l}$ and the tube's curvature vector $\mathbf{k}$ are given by:

$$\mathbf{l} = \frac{\partial \mathbf{r}}{\partial s}, \tag{C.8}$$

$$\mathbf{k} = \frac{\partial^2 \mathbf{r}}{\partial s^2} = \frac{\partial \mathbf{l}}{\partial s}. \tag{C.9}$$

Using these relations, next we can rewrite the second term in Eq. C.7 using $\mathbf{l}$ and $\mathbf{k}$ such that:

$$(\mathbf{B}\cdot\nabla)\mathbf{B} = (B\mathbf{l}\cdot\nabla)B\mathbf{l} = B\frac{\partial(B\mathbf{l})}{\partial s}, \tag{C.10}$$

$$= B^2\frac{\partial \mathbf{l}}{\partial s} + B\mathbf{l}\frac{\partial B}{\partial s}, \tag{C.11}$$

where in this coordinate system using Lagrangian elements whose properties are a function of arc length and time only, $\mathbf{l}\cdot\nabla = \frac{\partial}{\partial s}$. The second term in Equation C.11 can also be written as $B\frac{\partial B}{\partial s} = \frac{1}{2}\frac{\partial B^2}{\partial s}$, and $\mathbf{k} = \frac{\partial \mathbf{l}}{\partial s}$, therefore:

$$(\mathbf{B}\cdot\nabla)\mathbf{B} = B^2\mathbf{k} + \frac{1}{2}\frac{\partial B^2}{\partial s}\mathbf{l}, \tag{C.12}$$

and Equation C.7 becomes:

$$\rho\frac{d\mathbf{v}}{dt} = -\nabla\left(P + \frac{B^2}{8\pi}\right) + \frac{B^2}{4\pi}\mathbf{k} + \frac{\partial}{\partial s}\left(\frac{B^2}{8\pi}\right)\mathbf{l} + \rho\mathbf{g}. \tag{C.13}$$

The first term in Equation C.13 can be replaced with P_e according to the condition of instantaneous pressure balance as given in Equation C.2. Assuming the external plasma environment is in hydrostatic pressure balance, as is the case in stellar interiors, then $\nabla P_e =$

$\rho_e \mathbf{g}$. As such, Equation C.13 then becomes:

$$\rho \frac{d\mathbf{v}}{dt} = -(\rho_e - \rho)\mathbf{g} + \frac{B^2}{4\pi}\mathbf{k} + \frac{\partial}{\partial s}\left(\frac{B^2}{8\pi}\right)\mathbf{l}, \tag{C.14}$$

where the first term on the right hand side now represents the net force per unit volume the flux tube experiences due to buoyancy. This is the equation of motion of a flux tube in a non-rotating system without the inclusion of a drag force term.

Mass elements moving in a rotating system will be subject to the Coriolis force, represented here as $-2\rho(\mathbf{\Omega} \times \mathbf{v})$, where $\mathbf{\Omega}$ is the angular velocity of the rotating body (i.e. the Sun). Additionally, there is an outward directed centrifugal force produced by the rotating body that counteracts the gravitational force due to the rotating body's mass. This centrifugal acceleration results in a correction to the acceleration due to gravity $\mathbf{g}$ such that $\mathbf{g} \rightarrow \mathbf{g} - \mathbf{\Omega} \times (\mathbf{\Omega} \times \mathbf{r})$. This term is often referred to as the *effective gravity*. Accounting for a rotating reference system, the equation of motion of the flux tube is now written as:

$$\rho \frac{d\mathbf{v}}{dt} = -2\rho(\mathbf{\Omega_0} \times \mathbf{v}) - (\rho_e - \rho)[\mathbf{g} - \mathbf{\Omega_0} \times (\mathbf{\Omega_0} \times \mathbf{r})] + \frac{\partial}{\partial s}\left(\frac{B^2}{8\pi}\right)\mathbf{l} + \frac{B^2}{4\pi}\mathbf{k}. \tag{C.15}$$

The final term that needs to be accounted for is the drag force per unit volume that the flux tube experiences as it travels through the turbulent convective envelope. Following Batchelor (1967), the drag force experience by a non-streamlined object (i.e. bluff body) moving through a fluid with a large Reynolds number $R_e > 100$, where the Reynolds number $R_e = \ell_0 v_0/\nu$ gives the ratio of inertial effects to viscous effects and ν is the fluid viscosity, is given by:

$$F_D = \frac{1}{2} C_D \rho_e v_\perp^2 d, \tag{C.16}$$

where d is the diameter of the flux tube, $v_\perp$ is the perpendicular component of velocity of the flux tube with respect to the surrounding plasma, and C_D is the drag coefficient which is $\sim$1 for large Reynolds numbers. Assuming that the magnetic flux Φ of the tube remains constant such that $\Phi = BA$, where $A = \pi r^2$ is the cross-sectional area of the flux tube and r is the flux tube radius, the drag force per unit volume on the flux tube becomes:

$$f_D = \frac{C_D \rho_e |(\mathbf{v} - \mathbf{v}_e)|_\perp (\mathbf{v} - \mathbf{v}_e)_\perp}{(\pi\Phi/B)^{1/2}}. \tag{C.17}$$

In a rotating reference system, for a flux tube evolving in a turbulent convecting plasma, the equation of the motion of the flux tube under the thin flux tube approximation becomes:

$$\begin{aligned} \rho \frac{d\mathbf{v}}{dt} &= -2\rho(\mathbf{\Omega_0} \times \mathbf{v}) - (\rho_e - \rho)[\mathbf{g} - \mathbf{\Omega_0} \times (\mathbf{\Omega_0} \times \mathbf{r})] + \frac{\partial}{\partial s}\left(\frac{B^2}{8\pi}\right)\mathbf{l} + \frac{B^2}{4\pi}\mathbf{k} \\ &\quad - \frac{C_D \rho_e |(\mathbf{v} - \mathbf{v}_e)|_\perp (\mathbf{v} - \mathbf{v}_e)_\perp}{(\pi\Phi/B)^{1/2}}. \end{aligned} \tag{C.18}$$

3.3. Walén Equation

The Walén Equation combines the continuity equation and Induction equation in the limit of infinite conductivity to describe the rate of change of the magnetic field with respect to the density, with the equations in their Lagrangian derivative form given respectively as:

$$\frac{d\rho}{dt} = -\rho(\nabla \cdot \mathbf{v}), \tag{C.19}$$

$$\frac{d\mathbf{B}}{dt} = \nabla \times (\mathbf{v} \times \mathbf{B}) + (\mathbf{v} \cdot \nabla)\mathbf{B}. \tag{C.20}$$

Specifically, we want to calculate $\frac{d\mathbf{B}}{dt}$:

$$\frac{d}{dt}\left(\frac{\mathbf{B}}{\rho}\right) = \frac{1}{\rho}\frac{d\mathbf{B}}{dt} - \frac{\mathbf{B}}{\rho^2}\frac{d\rho}{dt}, \tag{C.21}$$

$$= \frac{1}{\rho}\Big[\nabla \times (\nabla \times \mathbf{B}) + (\mathbf{v}\cdot\nabla)\mathbf{B}\Big] + \frac{\mathbf{B}}{\rho}(\nabla\cdot\mathbf{v}), \tag{C.22}$$

where Equations C.19 and C.20 have been substituted in Equation C.22. Using the vector identity $\nabla\times(\mathbf{v}\times\mathbf{B}) = (\mathbf{B}\cdot\nabla)\mathbf{v} - (\mathbf{v}\cdot\nabla)\mathbf{B} + \mathbf{v}(\nabla\cdot\mathbf{B}) - \mathbf{B}(\nabla\cdot\mathbf{v})$ in Equation C.22 and the fact that $\nabla\cdot\mathbf{B} = 0$, the equation becomes:

$$\frac{d}{dt}\left(\frac{\mathbf{B}}{\rho}\right) = \left(\frac{\mathbf{B}}{\rho}\cdot\nabla\right)\mathbf{v}, \tag{C.23}$$

which is often referred to as the Walén Equation. In the thin flux tube formulation, $\mathbf{B} = B\mathbf{l}$ such that:

$$\frac{d}{dt}\left(\frac{B\mathbf{l}}{\rho}\right) = \left(\frac{B\mathbf{l}}{\rho}\cdot\nabla\right)\mathbf{v}, \tag{C.24}$$

$$\frac{B}{\rho}\frac{d}{dt}(\mathbf{l}) + \mathbf{l}\frac{d}{dt}\left(\frac{B}{\rho}\right) = \frac{B}{\rho}(\mathbf{l}\cdot\nabla)\mathbf{v}. \tag{C.25}$$

To remove the unit vector $\mathbf{l}$ from the Lagrangian derivative of B/ρ, we can take the dot product of both sides with $\mathbf{l}$. As $\mathbf{l}\cdot\mathbf{l} = 1$, and $\mathbf{l}\cdot\frac{d(\mathbf{l})}{dt} = 0$ because the rate of change of a unit vector is always perpendicular to itself, the equation becomes:

$$\frac{d}{dt}\left(\frac{B}{\rho}\right) = \frac{B}{\rho}\mathbf{l}\cdot(\mathbf{l}\cdot\nabla)\mathbf{v}, \tag{C.26}$$

$$= \frac{B}{\rho}\mathbf{l}\cdot\frac{\partial\mathbf{v}}{\partial s}, \tag{C.27}$$

where $\mathbf{l} \cdot \nabla = \frac{\partial}{\partial s}$. The right hand side of the equation can also be rewritten in the following way:

$$\frac{\partial}{\partial s}(\mathbf{v} \cdot \mathbf{l}) = \mathbf{v} \cdot \frac{\partial \mathbf{l}}{\partial s} + \mathbf{l} \cdot \frac{\partial \mathbf{v}}{\partial s}, \tag{C.28}$$

$$\mathbf{l} \cdot \frac{\partial \mathbf{v}}{\partial s} = \frac{\partial}{\partial s}(\mathbf{v} \cdot \mathbf{l}) - \mathbf{v} \cdot \frac{\partial \mathbf{l}}{\partial s}, \tag{C.29}$$

$$= \frac{\partial}{\partial s}(\mathbf{v} \cdot \mathbf{l}) - \mathbf{v} \cdot \mathbf{k}, \tag{C.30}$$

where $\frac{\partial \mathbf{l}}{\partial s} = \mathbf{k}$. Finally, the thin flux tube equation describing the Lagrangian derivative of B/ρ can be written as:

$$\frac{d}{dt}\left(\frac{B}{\rho}\right) = \frac{B}{\rho}\left[\frac{\partial(\mathbf{v} \cdot \mathbf{l})}{\partial s} - \mathbf{v} \cdot \mathbf{k}\right]. \tag{C.31}$$

3.4. Energy Equation

A general form of the energy equation for MHD is given as:

$$\frac{1}{\rho}\frac{d\rho}{dt} = \frac{1}{\gamma P}\frac{dP}{dt} - \nabla_{ad}\frac{\rho T}{P}\frac{dS}{dt}. \tag{C.32}$$

If the flux tube does not evolve adiabatically, dS/dt is non-zero. As discussed in more detail in Chapter 6, radiative diffusion is a significant component of flux tube heating in approximately the lower third of the convection zone. The heating rate due to radiative diffusion is given by:

$$\rho T \frac{dS}{dt} = \frac{dQ}{dt} \simeq -F_{tot}\frac{d}{dr}\left(\frac{\nabla_e}{\nabla_{rad}}\right), \tag{C.33}$$

where the total energy flux $F_{tot} = L/(4\pi r^2)$, with L being the total solar luminosity, the radiative equilibrium temperature gradient is ∇_{rad}, and the temperature gradient of the background plasma is ∇_e.

In the case where the flux tube evolves adiabatically, as in Chapters 3, 4, and 5, $dS/dt = 0$. Under adiabatic assumptions, there is no heat transfer between the flux tube and its surrounding environment, and P/ρ^γ remains a constant, where γ is the ratio of specific heats. In this case, the energy equation is simply:

$$\frac{1}{\rho}\frac{d\rho}{dt} = \frac{1}{\gamma P}\frac{dP}{dt}. \tag{C.34}$$

$$\rho\frac{d\mathbf{v}}{dt} = -2\rho(\mathbf{\Omega_0}\times\mathbf{v}) - (\rho_e-\rho)[\mathbf{g}-\mathbf{\Omega_0}\times(\mathbf{\Omega_0}\times\mathbf{r})] + \frac{\partial}{\partial s}\left(\frac{B^2}{8\pi}\right)\mathbf{l} + \frac{B^2}{4\pi}\mathbf{k}$$

$$-C_d\frac{\rho_e|(\mathbf{v}-\mathbf{v}_e)_\perp|(\mathbf{v}-\mathbf{v}_e)_\perp}{(\pi\Phi/B)^{1/2}}, \tag{C.35}$$

$$\frac{d}{dt}\left(\frac{B}{\rho}\right) = \frac{B}{\rho}\left[\frac{\partial(\mathbf{v}\cdot\mathbf{l})}{\partial s} - \mathbf{v}\cdot\mathbf{k}\right], \tag{C.36}$$

$$\frac{1}{\rho}\frac{d\rho}{dt} = \frac{1}{\gamma P}\frac{dP}{dt} - \nabla_{ad}\frac{\rho}{P}T\frac{dS}{dt}, \tag{C.37}$$

$$P = \frac{\rho RT}{\mu}, \tag{C.38}$$

$$P + \frac{B^2}{8\pi} = P_e, \tag{C.39}$$

APPENDIX D

The Schwarzschild Criterion for Convective Stability/Instability and the Brunt-Väisälä Frequency

There exists a limit to the temperature gradient ∇_e inside a star if stability of the plasma environment is to be maintained, referred to as the Schwarzschild criterion, which we will derive here. Consider a plasma parcel in a vertically stratified ideal gas environment that initially has the same density ρ_1, temperature T_1, and pressure P_1 of its surroundings such that it is in neutral buoyancy. The parcel is then displaced in the radial direction a distance r upward. We assume that the plasma parcel's motion is sufficiently fast such that it evolves adiabatically, but still sufficiently slow such that its pressure adjusts to that of the external plasma environment ($P' = P$). At the displacement distance r, the external plasma environment has density ρ_2, pressure P_2, and temperature T_2. The plasma parcel now has density of ρ_2', pressure P_2, and temperature T_2'. The net buoyancy force F_B on the parcel per unit volume is then (assuming the acceleration due to gravity g acts downward):

$$F_B = -g(\rho_2' - \rho_2), \tag{D.1}$$

At the location of the vertical displacement r, the density of the external plasma environment is given by:

$$\rho_2 = \rho_1 + \frac{d\rho_e}{dr} r, \tag{D.2}$$

where the subscript e denotes the gradient is of the external plasma environment. The density of the plasma parcel after a displacement r is given by:

$$\rho_2' = \rho_1 + \frac{d\rho_i}{dr} r, \tag{D.3}$$

where the subscript i denotes the gradient is of the plasma parcel's density. Since the plasma parcel evolves adiabatically, we take the derivative of $P_1 \rho_1^{-\gamma} = C$ with respect to r, where C is a constant and γ is the ratio of specific heats, to obtain an expression for $d\rho_i/dr$:

$$\frac{d\rho_i}{dr} = \frac{1}{\gamma} \frac{\rho_1}{P_1} \frac{dP_e}{dr}, \tag{D.4}$$

which is written in terms of the external pressure gradient, as we assume the plasma parcel evolves such that it remains in pressure equilibrium. Combing Equations D.1-D.4 the buoyant force of the parcel can now be written as:

$$F_B = -g\rho_e \left(\frac{1}{\gamma} \frac{1}{P_e} \frac{dP_e}{dr} - \frac{1}{\rho_e} \frac{d\rho_e}{dr} \right) r, \tag{D.5}$$

where the subscript 1 has been replaced with e to put the equation in terms of the thermodynamic quantities of the external plasma environment.

The solutions to the equation:

$$F_B = \rho_e \frac{d^2 r}{dt^2} = -\rho_e N^2 r, \tag{D.6}$$

where N is referred to as the Brunt-Väisälä frequency:

$$N^2 = g \left(\frac{1}{\gamma} \frac{1}{P_e} \frac{dP_e}{dr} - \frac{1}{\rho_e} \frac{d\rho_e}{dr} \right), \tag{D.7}$$

admit both oscillatory (stable) and unstable solutions to r depending on the sign of N^2. If $N^2 > 0$, then the solutions to Equation D.6 are of form $\sin(Nt)$ or $\cos(Nt)$, representing oscillatory motion such that displacements of r are stable. However, if $N^2 < 0$, solutions are of the form $e^{\pm\sqrt{|N^2|}t}$, which represent *run-away* or unstable motion, resulting in convective instabilities.

For convective stability such that $N^2 > 0$:

$$0 < \left(\frac{1}{\gamma}\frac{\rho}{P}\frac{dP}{dr} - \frac{d\rho}{dr}\right), \tag{D.8}$$

where the subscript e has been dropped. For an ideal gas $P \propto \rho T$, therefore:

$$\frac{d\rho}{dr} = \frac{\rho}{P}\frac{dP}{dr} - \frac{\rho}{T}\frac{dT}{dr}. \tag{D.9}$$

After combining Equations D.8 and D.9, and performing some algebra, the criterion for convective instability becomes:

$$\frac{dT}{dr} > \left(\frac{\gamma - 1}{\gamma}\right)\frac{T}{P}\frac{dP}{dr}. \tag{D.10}$$

Both sides of Equation D.10 are negative, as temperature and pressure decrease with increasing radius in a star. Applying absolute values to both sides of the equation, the conditions necessary for convective stability are:

$$\left|\frac{dT}{dr}\right| < \left(\frac{\gamma - 1}{\gamma}\right)\frac{T}{P}\left|\frac{dP}{dr}\right|, \tag{D.11}$$

$$\nabla_e < \nabla_{ad}, \tag{D.12}$$

where $\nabla_e = d\ln T/d\ln P$ is the actual temperature gradient of the plasma environment and $\nabla_{ad} = (\gamma - 1)/(\gamma)$ is the adiabatic temperature gradient as derived in Equation A.25. A similar derivation can be used to show that convective instability ensues when $\nabla_e > \nabla_{ad}$.

APPENDIX E

Numerical Scheme and Explicit Formulae for the Thin Flux Tube Numerical Model

The thin flux tube code solves explicitly for eight dependent variables $\mathbf{r}(u,t)$, $\mathbf{v}(u,t)$, $B(u,t)$, and $\Delta\rho(u,t)$, each of which is discretized in terms of the fractional arc length of the flux tube u, where $\mathbf{r}$ is a position vector and $\mathbf{v}$ is a velocity each with x, y, and z components. The set of thin flux tube equations listed in C.35-C.39 are used to derive explicit formulae to determine the time evolution of variables $\mathbf{r}$, $\mathbf{v}$, $\Delta\rho$, and B, which are each a function of time and arc length along the flux tube. However, the equations as they stand in C.35-C.39 are not the explicit equations used for the thin flux tube numerical model. This Appendix chapter describes the explicit equations solved in the thin flux tube model code.

5.1. Explicit Equation for the Thin Flux Tube Magnetic Field

To solve for the magnetic field B and density of the flux tube ρ, Equation C.36 must be rearranged such that each quantity is computed in its own equation. To arrive at an equation for dB/dt, first we start by considering Equation C.36, noting that:

$$\frac{\rho}{B}\frac{d}{dt}\left(\frac{B}{\rho}\right) = \frac{d\ln B}{dt} - \frac{d\ln\rho}{dt}, \tag{E.1}$$

such that:

$$\frac{d\ln B}{dt} - \frac{d\ln\rho}{dt} = \left[\frac{\partial(\mathbf{v}\cdot\mathbf{l})}{\partial s} - \mathbf{v}\cdot\mathbf{k}\right]. \tag{E.2}$$

The derivative $d\ln\rho/dt$ can also be written as:

$$\frac{d\ln\rho}{dt} = \frac{1}{\rho}\frac{d\rho}{dP}\frac{dP}{dt} \tag{E.3}$$

$$= \frac{1}{\rho}\frac{d\rho}{dP}\left(\frac{dP_e}{dt} - \frac{2B}{8\pi}\frac{dB}{dt}\right) = \frac{1}{\rho}\frac{d\rho}{dP}\left(\frac{dP_e}{dt} - \frac{2B^2}{8\pi}\frac{d\ln B}{dt}\right), \tag{E.4}$$

and dP/dt has been replaced by the term in the parenthesis, which is a result of taking the time derivative of Equation C.39.

The external pressure P_e comes from a solar model, and is only a function of radius r. Additionally, in a state of hydrostatic equilibrium, $dP_e/dr = -\rho_e g$. As a result, the derivative dP_e/dt is also:

$$\frac{dP_e}{dt} = \frac{dP_e}{dr}\frac{dr}{dt} = -v_r\rho_e g. \tag{E.5}$$

Substituting Eq. E.5 into Eq. E.4, and then Eq. E.4 into Eq. E.2, the equation describing the time evolution of the magnetic field can be written as:

$$\frac{dB}{dt} = B\left[-v_r g\frac{\rho_e}{\rho}\left(\frac{d\rho_e}{dP_e} + \alpha\right) + \left(\frac{\partial v_l}{\partial s} - \mathbf{v}\cdot\mathbf{k}\right)\right]\left[1 + \frac{B^2}{4\pi\rho}\left(\frac{d\rho_e}{dP_e} + \alpha\right)\right]^{-1}, \tag{E.6}$$

where

$$\alpha \equiv \frac{d\rho}{dP} - \frac{d\rho_e}{dP_e}. \tag{E.7}$$

It is numerically advantageous to calculate α as it tracks the difference in $d\rho/dP$ and $d\rho_e/dP_e$, which are both very close to each other in magnitude. The term α can be rewritten in a form which takes advantage of the external quantities from a solar structure model, $\Delta\rho$ calculated

through Eq. E.14, and P which is easily obtained from the condition of instantaneous pressure balance:

$$\alpha = \frac{d\rho}{dP} - \frac{d\rho_e}{dP_e} = \frac{1}{\gamma}\frac{\rho}{P} - \frac{d\rho_e}{dP_e} = -\frac{N^2}{g^2} + \frac{1}{\gamma}\left(\frac{B^2}{8\pi P_e} - \frac{\Delta\rho}{\rho_e}\right)\frac{\rho_e}{P}, \tag{E.8}$$

where,

$$\frac{d\rho_e}{dP_e} = \frac{1}{\gamma}\frac{\rho_e}{P_e} + \frac{N^2}{g^2}, \tag{E.9}$$

$$N^2 = g\left(\frac{1}{\gamma}\frac{d\ln P_e}{dr} - \frac{d\ln\rho_e}{dr}\right). \tag{E.10}$$

The quantity N is referred to as the Brunt-Väisälä frequency (see Appendix D), which is the frequency at which a displaced plasma parcel in a gravitationally stratified atmosphere will oscillate. Also known as the Schwarzschild criterion for convective stability, if $N^2 > 0$, the parcel will execute simple harmonic motion with frequency N. However, if $N^2 < 0$, convective instability ensues, which is the case for stellar convection zones.

5.2. Equation for the Flux Tube Density Deficit $\Delta\rho$

For flux tubes in the solar convection zone, values of the flux tube density ρ and the external density ρ_e are very close to each other. To avoid subtracting two very small density values when computing the buoyancy force $(\rho_e - \rho)/g$, the quantity $\Delta\rho = \rho_e - \rho$ is computed instead to maintain numerical accuracy. (In the convection zone, $\Delta\rho \ll \rho_e$ and $B^2/8\pi \ll P_e$.) Obtaining the value for ρ is easily done if $\Delta\rho$ is known from calculations, and ρ_e comes from

the 1D solar structure model. To arrive at an equation for $d\Delta\rho/dt$, we start with:

$$\frac{d\Delta\rho}{dt} = \frac{d\rho_e}{dt} - \frac{d\rho}{dt}, \tag{E.11}$$

$$= \frac{d\rho_e}{dP_e}\frac{dP_e}{dt} - \frac{d\rho}{dP}\frac{dP}{dt}, \tag{E.12}$$

$$= \rho_e g v_r \left(\frac{d\rho}{dP} - \frac{d\rho_e}{dP_e}\right) + \frac{2B^2}{8\pi}\frac{d\rho}{dP}\left[\frac{-\rho_e g v_r}{\rho}\frac{d\rho}{dP} + \left(\frac{\partial v_l}{\partial t} - \mathbf{v}\cdot\mathbf{k}\right)\right] \times\left[1 + \frac{1}{\rho}\frac{2B^2}{8\pi}\frac{d\rho}{dP}\right]^{-1}, \tag{E.13}$$

where between Equations E.12 and E.13, the relation E.5, the time derivative of Eq. C.39, and Eq. E.6 were used.

After performing some algebra and applying relation E.7, Eq. E.13 becomes the Lagrangian time derivative of $\Delta\rho$ we use in the thin flux tube code:

$$\frac{d\Delta\rho}{dt} = \left[v_r\rho_e g\left[\alpha - \frac{B^2}{4\pi\rho}\left(\frac{d\rho_e}{dP_e} + \alpha\right)\frac{d\rho_e}{dP_e}\right] + \frac{B^2}{4\pi}\left(\frac{\partial v_l}{\partial s} - \mathbf{v}\cdot\mathbf{k}\right)\left(\frac{d\rho_e}{dP_e} + \alpha\right)\right]\left[1 + \frac{B^2}{4\pi}\left(\frac{d\rho_e}{dP_e} + \alpha\right)\right]^{-1}. \tag{E.14}$$

5.3. Applying the Lagrangian Time Derivative

The derivatives on the left hand side of Equations C.35-C.39 are actually the Lagrangian time derivative of the flux tube physical quantities, also referred to as the material or convective derivative, which follow the evolution of a mass element's properties in time as it moves along a trajectory in a velocity field. As time goes on, motion of the mass elements along the flux tube will change their distribution, leaving some portions of the flux tube under-resolved spatially. Therefore in the TFT numerical calculations, we follow the time evolution of physical quantities at mesh points that are always maintained at a uniform spacing in arc length along the tube, even as the tube shape is changing. To this end, we

evaluate the time derivatives following the uniformly spaced mesh points $(\partial A/\partial t)_u$, where u denotes the position of each mesh point along the tube in terms of the fractional arc length such that $u \equiv s/L$, where L is the total length of the tube. Let $A(u,t)$ denote any one of the dependent variables, then the Lagrangian derivative is given by:

$$\frac{dA}{dt} = \left.\frac{\partial A}{\partial t}\right|_u + \mathbf{v}\cdot\nabla A, \tag{E.15}$$

$$= \left.\frac{\partial A}{\partial t}\right|_u + \left.\frac{\partial A}{\partial u}\right|_t \frac{du}{dt}, \tag{E.16}$$

where the symbol $\mathbf{v}$ is the rate of change of position of the Lagrangian element, represented here as du/dt.

The first term on the right hand side of Eq. E.16 is the time derivative we seek to solve numerically. The derivative $(\partial A/\partial u)_t$ denotes the variation of $A(u,t)$ along the tube, and is given by a second order finite difference approximation as discussed in Section 5.4. The time derivatives dA/dt for each physical quantity can be obtained from the thin flux tube equations as given specifically by Eq. C.35 for $\mathbf{v}$, Eq. E.6 for B, Eq E.14 for $\Delta\rho$, and the following for $\mathbf{r}$:

$$\frac{d\mathbf{r}}{dt} = \mathbf{v}. \tag{E.17}$$

The derivative du/dt describes the change of position of each mass element in terms of the fractional arc length along the flux tube, which can be derived by considering Equation

C.36 and the fact that:

$$\frac{du}{dt} = \frac{d}{dt}\left(\frac{s}{L}\right), \tag{E.18}$$

$$= \frac{1}{L}\frac{ds}{dt} - \frac{u}{L}\frac{dL}{dt}. \tag{E.19}$$

Turning our attention to Eq. C.36, where δm is the mass and δs is the length of a single mass element, the quantity $B/\rho = (\Phi\ \delta s)/(\pi\ \delta m)$. Considering that $d\Phi/dt = 0$ and $d\delta m/dt = 0$, the derivative of B/ρ of a Lagrangian element can be written as:

$$\frac{d}{dt}\left(\frac{B}{\rho}\right) = \frac{d}{dt}\left(\frac{\Phi\delta s}{\pi\delta m}\right) = \frac{\Phi}{\pi\delta m}\frac{d\delta s}{dt}, \tag{E.20}$$

and Eq. C.36 can then be rewritten as:

$$\frac{d\delta s}{dt} = \left(\frac{\partial v_l}{\partial s} - \mathbf{v}\cdot\mathbf{k}\right)\delta s. \tag{E.21}$$

The derivatives ds/dt and dL/dt can then be computed as follows, where $\delta u = \delta s/L$, $v_l(u)$ is the parallel velocity of the mass element at fractional arc length u along the tube, and $v_l(0)$ and $v_l(1)$ are the parallel velocities of the mass elements at the beginning of the tube where $u = 0$ and the end of the tube where $u = 1$:

$$\frac{ds}{dt} = \int_0^s \frac{d\delta s}{dt} = v_l(u) - v_l(0) - L\int_0^u \mathbf{v}\cdot\mathbf{k}\delta u, \tag{E.22}$$

$$\frac{dL}{dt} = \int_0^L \frac{d\delta s}{dt} = v_l(1) - v_l(0) - L\int_0^L \mathbf{v}\cdot\mathbf{k}\delta u. \tag{E.23}$$

Substituting Equations E.22 and E.23 into Equation E.19, and noting that due to the periodic boundary conditions of the flux tube $v_l(0) = v_l(1)$, the equation for du/dt used in the thin

flux tube numerical code is:

$$\frac{du}{dt} = \frac{1}{L}[v_l(u) - v_l(0)] - \int_0^u \mathbf{v}\cdot\mathbf{k}\delta u + u\int_0^L \mathbf{v}\cdot\mathbf{k}\delta u. \tag{E.24}$$

The integrals in the above equation are calculated using the Trapezoid Rule, which will be discussed in Section 5.4.

To summarize, the system of equations we solve numerically, following $(\partial A/\partial t)_u$ the time evolution of the desired physical quantities at the uniformly spaced mesh points along the flux tube, is given by:

$$\left.\frac{\partial \mathbf{r}}{\partial t}\right|_u = \mathbf{v} - \left.\frac{\partial \mathbf{r}}{\partial u}\right|_t \frac{du}{dt} \tag{E.25}$$

$$\begin{aligned}\left.\frac{\partial \mathbf{v}}{\partial t}\right|_u = {} & -2(\mathbf{\Omega_0}\times\mathbf{v}) - \frac{(\rho_e-\rho)}{\rho}[\mathbf{g} - \mathbf{\Omega_0}\times(\mathbf{\Omega_0}\times\mathbf{r})] + \frac{1}{\rho}\frac{\partial}{\partial s}\left(\frac{B^2}{8\pi}\right)\mathbf{l} + \frac{B^2}{4\pi\rho}\mathbf{k} \\ & -C_d\frac{\rho_e|(\mathbf{v}-\mathbf{v}_e)_\perp|(\mathbf{v}-\mathbf{v}_e)_\perp}{\rho(\pi\Phi/B)^{1/2}} - \left.\frac{\partial \mathbf{v}}{\partial u}\right|_t \frac{du}{dt},\end{aligned} \tag{E.26}$$

$$\begin{aligned}\left.\frac{\partial \Delta\rho}{\partial t}\right|_u = {} & \left[v_r\rho_e g\left[\alpha - \frac{B^2}{4\pi\rho}\left(\frac{d\rho_e}{dP_e}+\alpha\right)\frac{d\rho_e}{dP_e}\right] + \frac{B^2}{4\pi}\left(\frac{\partial v_l}{\partial s} - \mathbf{v}\cdot\mathbf{k}\right)\left(\frac{d\rho_e}{dP_e}+\alpha\right)\right] \\ & \times\left[1 + \frac{B^2}{4\pi}\left(\frac{d\rho_e}{dP_e}+\alpha\right)\right]^{-1} - \left.\frac{\partial \Delta\rho}{\partial u}\right|_t \frac{du}{dt}\end{aligned} \tag{E.27}$$

$$\begin{aligned}\left.\frac{\partial B}{\partial t}\right|_u = {} & B\left[-v_r g\frac{\rho_e}{\rho}\left(\frac{d\rho_e}{dP_e}+\alpha\right) + \left(\frac{\partial v_l}{\partial s} - \mathbf{v}\cdot\mathbf{k}\right)\right] \\ & \times\left[1 + \frac{B^2}{4\pi\rho}\left(\frac{d\rho_e}{dP_e}+\alpha\right)\right]^{-1} - \left.\frac{\partial B}{\partial u}\right|_t \frac{du}{dt}.\end{aligned} \tag{E.28}$$

5.4. Numerical Algorithms

As the ASH simulation is computed separately from the thin flux tube simulation, the velocity information needs to be extracted from ASH at each TFT time step. In order to provide the most accurate convective velocities $\mathbf{v}_e$ in Eq. E.26 at the spatial position of each

flux tube element for each time step, the convective flows from ASH (computed at 12 hour intervals) in the x, y, and z directions are interpolated in four dimensions: three spatial and one time dimension. The result of the interpolation routine is subsequently the value $\mathbf{v}_e$ used for the external flow in Eq. E.26.

The partial differential equations given in E.25 - E.28 are discretized in u by assuming that each dependent variable $A_k(u,t)$ - ($\mathbf{r}(u,t)$, $\mathbf{v}(u,t)$, $B(u,t)$, $\Delta\rho(u,t)$) is defined on a uniform mesh of N points in u such that $A_{k,j}(u,t) = A_k(u_j,t)$, where $u_j = (j-1)/(N-1)$ for $j = 1...N$.

The spatial derivative $(\partial A/\partial u)_t$ is calculated using a second-order, centered finite difference formula:

$$\left.\frac{\partial A_{k,j}}{\partial u}\right|_t = \frac{A_{k,j+1}(t) - A_{k,j-1}(t)}{2\Delta u}, \tag{E.29}$$

where $\Delta u = 1/(N-1)$.

The integrals in Eq. E.24, where $f_k(u_j,t) = \mathbf{v}\cdot\mathbf{k}$, are calculated using the Trapezoid Rule for numerical integration:

$$\int_a^b f_{k,j}du = \frac{b-a}{N-1}\sum_{j=2}^{N}\left[\frac{1}{2}f_{k,j-1}(t) + \frac{1}{2}f_{k,j}(t)\right], \tag{E.30}$$

recalling that the flux tube boundary conditions are periodic.

The solutions (dependent variables) to the set of differential equations given by Equations E.25-E.28 are advanced in time using the fourth-order Runge-Kutta method as presented by Press *et al.* (1992). The time step Δt is given by a modified Courant-Friedrichs-Lewy (CFL)

condition:

$$\Delta t = 0.1 \text{ MIN} \left(\frac{\Delta s}{\max(|v_a|, |v_l|)}, \frac{\Delta u}{\max(|du/dt|)} \right), \tag{E.31}$$

where Δs is the grid point spacing in arc-length, $\Delta u = \Delta s / L$, and MIN(A,B) is the minimum value of the two arguments A or B. In the above relation, v_a is the Alfvén speed, v_l is the velocity of the flux tube mass elements in the direction parallel to the tube, and du/dt is the change in position of each mass element in terms of the fractional arc length along the flux tube. The CFL condition is required such that the time step interval is smaller than the time it takes information to travel with a characteristic speed given by the denominator of A or B to adjacent grid points in a spatial grid. If the time step is greater than the time it takes information to travel to adjacent points in a spatial grid, the information that left from the previous time step will not have made it to its spatial destination before the next time step is computed, and so divergence, rather than convergence, of the solution will occur.

APPENDIX F

Model Parameters

Table F.1. Parameters used in the TFT+ASH model (Column 1), name of each parameter (Column 2), what each parameter is a function of (Column 3), and the method of calculation for each parameter (Column 4). For a comprehensive description of the parameters, see Chapter 2. The ASH simulation for a solar-like star rotating at the current solar rate was performed by Dr. Mark Miesch of High Altitude Observatory. The $5\Omega_\odot$ ASH simulation was performed by Dr. Benjamin Brown of (at the time of computation) the University of Wisconsin - Madison. KEY: TFT - Calculated by the Thin Flux Tube code. ASH - Calculated by the Anelastic Spherical Harmonic code. SSM - Calculated by a 1D solar structure model (Christensen-Dalsgaard *et al.* 1996). Prescribed - These values are explicitly input into the code.

Parameter	Name	Function of:	Method of Calculation:
$\mathbf{r}$	position vector	(s,t)	TFT
$\mathbf{v}$	velocity vector	(s,t)	TFT
B	magnetic field	(s,t)	TFT
$\Delta\rho$	density $(\rho_e - \rho)$	(s,t)	TFT
ρ	density	(s,t)	TFT
P	pressure	(s,t)	TFT
T	temperature	(s,t)	TFT
$\mathbf{l}$	tangential unit vector	(s,t)	TFT
$\mathbf{k}$	curvature vector	(s,t)	TFT
$\mathbf{v}_e$	external velocity field	(r,θ,ϕ,t)	ASH
ρ_e	external density	(r)	SSM
P_e	external pressure	(r)	SSM
T_e	external temperature	(r)	SSM
μ	mean molecular weight	(r)	SSM
δ	adiabaticity $(\nabla_e - \nabla_{ad})$	(r)	SSM
∇_{ad}	adiabatic temperature gradient	(r)	SSM
S	entropy per unit mass	(r)	SSM
Φ	magnetic flux	constant	Prescribed
B_0	initial magnetic field	constant	Prescribed
θ_0	initial latitude	constant	Prescribed
Ω_0	rotation rate	constant	Prescribed
C_d	drag coefficient	constant	Prescribed
γ	ratio of specific heats	constant	Prescribed

APPENDIX G

Flux Tube Ensembles For Chapters 3, 4, and 6

The thin flux tube model as outlined in Chapter 2, and Appendices C and E describes how one isolated, thin flux tube evolves subject to the influences of solar-like convective flows. For each simulation, we are able to prescribe the initial magnetic field strength B_0, magnetic flux Φ, and initial latitude θ_0. We have chosen to use seven magnetic field strength values B_0 of 15, 30, 40, 50, 60, 80, and 100 kG. For each magnetic field strength B_0, we also perform simulations where the magnetic flux Φ is 10^{20}, 10^{21}, and 10^{22} Mx. Additionally, for each B_0, Φ combination, we perform simulations where we vary the initial latitude of the flux tube θ_0 from 1° to 40°, in 2° and 5° increments for both the Northern and Southern hemispheres of our simulation. This equates to 24 flux tube simulations in each hemisphere per B_0, Φ combination. In order to sample the entire timespan of our ASH convection simulation, which has a duration of ∼3 years, we perform multiple simulation *groups*. The flux tubes comprising one *group* are released at the base of the convection zone at the same starting time, although they do not interact with each other (i.e. are isolated) and are allowed to evolve until some portion of the flux tube reaches the simulation upper boundary. The flux tube release times are arbitrary, but are at least separated by the convective turnover timescale of the ASH convection simulation, which is ∼30 days.

Table G.1 shows the total number of flux tube simulations used for the statistics generated in Chapters 3 and 4, where the flux tube is allowed to evolve adiabatically. For these chapters, we have performed seven simulation groups per B_0 and Φ, for a total of 336 flux tube simulations per B_0, Φ combination. However, not every flux tube simulation results

in a flux tube that reaches the simulation upper boundary. Especially at weaker magnetic field strengths, it is the case that the magnetic field along some portion of the flux tube may reach zero, and the flux tube's rise toward the surface is terminated. This occurs when the internal pressure of the flux tube becomes equal to the pressure of the background fluid. By the conditions of instantaneous pressure balance (Eq. 2.5), the magnetic field of the flux tube must then necessarily become zero. In Table G.1 and the statistics generated in Chapters 3 and 4, we only use simulation information from flux tubes that do reach the simulation upper boundary.

Table G.2 shows the total number of flux tubes simulations used for the statistics generated in Chapter 6, where the flux tube is allowed to evolve with the influence of radiative heating. Similar to Chapters 3 and 4, we have performed seven simulation groups per B_0, Φ combination, only using information from flux tubes that reach the simulation upper boundary without the magnetic field at some point dropping to zero. The seven simulation groups correspond to the same starting time as those used in Chapters 3 and 4.

TABLE G.1. Number of flux tubes simulations used in Chapters 3 and 4, where the flux tube evolves adiabatically. The total number of flux tube simulations considered for adiabatically evolving flux tubes is 6927.

B_0 (kG)	10^{20} Mx	10^{21} Mx	10^{22} Mx
100	336	336	336
80	336	334	334
60	334	336	336
50	332	336	335
40	331	332	335
30	331	333	327
15	312	297	308
total	2312	2304	2311

TABLE G.2. Number of flux tubes simulations used in Chapter 6, where the flux tube evolves with the influence of radiative heating. The total number of flux tube simulations considered for flux tubes evolving with the influence of radiative heating is 6879.

B_0 (kG)	10^{20} Mx	10^{21} Mx	10^{22} Mx
100	334	335	336
80	336	334	334
60	334	335	334
50	334	334	334
40	334	329	327
30	331	327	322
15	296	293	306
total	2299	2287	2293

APPENDIX H

A Note on Fitting Parameter Uncertainties and Confidence Levels

8.1. Uncertainties on Fitting Parameters

We perform a least-squares fitting method to obtain the slope and y-intercept parameters of a function fit to our emergence latitude / tilt angle data pairs (see e.g. Bethea, Duran, and Boullion 1985; Press *et al.* 1992). To obtain the uncertainties on the fit parameters, we will consider the propagation of errors. This Section describes the specifics of the fitting parameters following Methods 1, 2, and 3 in Section 4.3.1.1-4.3.1.3 of the dissertation. We have assumed that our emergence latitude / tilt angle data pairs are already a good fit to our choice of fitting functions.

8.1.1. Joy's Law Fit: Method 1. In Section 4.3.1.1, we wish to fit the tilt angle α as a function of latitude θ following the equation: $\alpha = m\theta$ ($y = mx$), where m is the slope of the best fit line. To obtain a value for the parameter m, we start by minimizing the following function with respect to m:

$$\chi^2 = \sum_{i=1}^{N} (y_i - mx_i)^2, \tag{H.1}$$

where N is the number of data point pairs. Taking the derivative of this function with respect to m, and then solving for m, we obtain the explicit equation used to calculate the

parameter m:

$$\frac{\partial \chi^2}{\partial m} = 0 = -2\sum_{i=1}^{N} x_i(y_i - mx_i), \tag{H.2}$$

$$0 = -2\sum_{i=1}^{N} x_i y_i + 2m\sum_{i=1}^{N} x_i^2, \tag{H.3}$$

(H.4)

therefore,

$$m = \frac{\sum_{i=1}^{N} x_i y_i}{\sum_{i=1}^{N} x_i^2}. \tag{H.5}$$

For the fit following Method 1, we have used units of degrees for both α and θ.

To obtain the variance of any function f, σ_f^2, we consider the propagation of errors, where:

$$\sigma_f^2 = \sigma^2 \sum_{i=1}^{N} \left(\frac{\partial f}{\partial y_i}\right)^2. \tag{H.6}$$

For our purposes, σ^2 is the variance of y_i about the new best fit equation $y(x_i)$ using the value of m calculated above:

$$\sigma^2 = \frac{1}{N}\sum_{i=1}^{N}[y_i - y(x_i)]^2. \tag{H.7}$$

Using the value of m calculated above in Eq. H.5, the derivative of m with respect to y_i is:

$$\frac{\partial m}{\partial y_i} = \frac{x_i}{\sum_{i=1}^{N} x_i^2}. \tag{H.8}$$

Therefore the variance of m is given by:

$$\sigma_m^2 = \sigma^2 \sum_{i=1}^{N} \left(\frac{x_i}{\sum_{i=1}^{N} x_i^2} \right)^2. \tag{H.9}$$

The uncertainty on m in Section 4.3.1.1 is therefore $m \pm \sigma_m$. This uncertainty σ_m takes into account the standard deviation of the data around the best fit line, as well as the uncertainty of the fit parameter. We have assumed that the equation $\alpha = m\theta$ is already a good fit to the data points.

8.1.2. Joy's Law Fit: Method 2. To perform the fit of $\alpha = m\sin(\theta)$ ($y = m\sin(x)$), we have minimized the following function with respect to m:

$$\chi^2 = \sum_{i=1}^{N} [y_i - m \sin(x_i)]^2, \tag{H.10}$$

resulting in the following expressions for the parameter m and σ_m^2, proceeding in the same way as in the above Appendix section 8.1.1:

$$m = \frac{\sum_{i=1}^{N} y_i \sin(x_i)}{\sum_{i=1}^{N} \sin^2(x_i)}, \tag{H.11}$$

$$\sigma_m^2 = \sigma^2 \sum_{i=1}^{N} \left(\frac{\sin(x_i)}{\sum_{i=1}^{N} \sin^2(x_i)} \right)^2. \tag{H.12}$$

For Method 2, we have used units of degrees for α and units of radians for θ. Assuming $\theta \sim \sin(\theta)$, a simple comparison can be made between the slopes m_A following Method 1 and slopes m_B following Method 2 by multiplying m_B by $\pi/180°$. The resulting slope approximation is generally less than the calculated value of m_A by at most 0.04. This

TABLE H.1. (Column 1) angle θ in units of degrees, (Column 2) angle θ in units of radian, (Column 3) $\sin(\theta)$, and (Column 4) percent difference between Columns 2 and 3. The approximation that $\theta \sim \sin(\theta)$ is only valid for small angles.

θ degrees	θ radians	$\sin(\theta)$	% Difference
0	0	0	0
10	0.175	0.174	∼0.5 %
20	0.349	0.342	∼2 %
30	0.524	0.500	∼5 %
40	0.698	0.643	∼8 %
50	0.873	0.766	∼13 %
60	1.047	0.866	∼19 %

difference occurs because the approximation $\theta \sim \sin(\theta)$ only holds for small values of θ. Table H.1 illustrates how θ and $\sin(\theta)$ vary as θ increases.

8.1.3. JOY'S LAW FIT: METHOD 3. In Section 4.3.1.3, we fit the tilt angle as a function of emergence latitude, however we no longer force the best fit equation to pass through the origin such that: $\alpha = m\theta + \lambda$ ($y = mx + b$), where m is the slope and λ (b) is the y-intercept. To perform this fit, we must minimize the following equation with respect to both m and λ:

$$\chi^2 = \sum_{i=1}^{N} (y_i - mx_i - \lambda)^2. \tag{H.13}$$

Performing the minimization:

$$\frac{\partial \chi^2}{\partial m} = 0 \quad = \quad -2 \sum_{i=1}^{N} x_i (y_i - mx_i - \lambda), \tag{H.14}$$

$$\frac{\partial \chi^2}{\partial \lambda} = 0 \quad = \quad -2 \sum_{i=1}^{N} (y_i - mx_i - \lambda). \tag{H.15}$$

Solving the above system of equations, we arrive at the explicit equations for the parameters of the best-fit line:

$$m = \frac{N\sum_{i=1}^{N} x_i y_i - (\sum_{i=1}^{N} x_i)(\sum_{i=1}^{N} y_i)}{N\sum_{i=1}^{N} x_i^2 - (\sum_{i=1}^{N} x_i)^2}, \tag{H.16}$$

$$\lambda = \frac{(\sum_{i=1}^{N} x_i^2)(\sum_{i=1}^{N} y_i) - (\sum_{i=1}^{N} x_i y_i)(\sum_{i=1}^{N} x_i)}{N\sum_{i=1}^{N} x_i^2 - (\sum_{i=1}^{N} x_i)^2}. \tag{H.17}$$

To obtain the variance of σ_m^2 and σ_λ^2, we again consider the propagation of errors following Equation H.6. The derivatives of m and λ with respect to y_i are:

$$\frac{\partial m}{\partial y_i} = \frac{N x_i - \sum_{i=1}^{N} x_i}{N\sum_{i=1}^{N} x_i^2 - (\sum_{i=1}^{N} x_i)^2}, \tag{H.18}$$

$$\frac{\partial \lambda}{\partial y_i} = \frac{\sum_{i=1}^{N} x_i^2 - x_i \sum_{i=1}^{N} x_i}{N\sum_{i=1}^{N} x_i^2 - (\sum_{i=1}^{N} x_i)^2}. \tag{H.19}$$

8.2. Confidence Levels

In Chapter 5, we a 99.7% confidence level (3σ) to indicate the significance of our results. The 3σ confidence level indicates that above this value, we are 99.7% confident the results of our simulations are not due to a random, non-uniform distribution of flux tube emergence. This section describes more in detail how we calculate the confidence levels for longitudinal variability, the average power spectrum, and the average cross-correlations. We have broken this process into three steps.

(1) For each rotation period and hemisphere, a number of flux tubes N emerge within $\pm 15^\circ$ of the equator. A few of these emergence maps are shown in Figure 5.5. We then create a corresponding array of N elements for each rotation period and hemisphere of our simulations with random longitudinal emergence positions from 0° to 360°. We will call these

TABLE H.2. (Column 1) rotation period with duration of 26.93 days ($\Omega_0/2\pi$ = 429.72 nHz), (Column 2) number of emergence events in the Northern Hemisphere, (Column 3) number of emergence events in the Southern Hemisphere. Note that there is generally an asymmetry in the number of events in both hemispheres for the same rotation period.

Rotation Number	North Hemisphere	South Hemisphere
1	8	10
2	44	45
3	35	49
4	20	28
5	89	60
6	74	53
7	135	83
8	83	96
9	61	97
10	71	79
11	69	97
12	38	46
13	31	22
14	58	34
15	44	41
16	15	20
17	17	22
18	50	45
19	62	29

random-longitude emergence arrays. We are only concerned here with the flux emergence pattern in longitude, we so do not need to create a random-latitude emergence array. Table H.2 shows the values of N for each rotation period and hemisphere in the reference frame rotating at $\Omega_0/2\pi$ = 429.72 nHz (26.93 days).

(2) Using the random-longitude emergence arrays, we then perform the variability, power spectrum, and cross-correlation calculations. In the case of the variability calculations, we average the resulting variabilities over all 19 rotation periods, calling this value x_v. For the power spectrum calculations, we average the results separately for the Northern and Southern hemispheres over all 19 rotation periods. As these average power spectrums are distributions over longitudinal mode m, we then average the resulting power spectrums over

TABLE H.3. Confidence level calculations in the reference frame with angular speed $\Omega_0/2\pi = 429.72$ nHz (26.93 days). (Row 1) variability confidence levels, (Row 2) average power spectrum confidence levels for the Northern hemisphere, which is the same for the Southern hemisphere when the values are rounded to the first significant digit, and (Row 3) average cross-correlation confidence levels for the Northern hemisphere following Eq. 5.3. Cross-correlation confidence levels vary between $\sim 0.09 - 0.10$ depending on the hemisphere and choice of reference frame.

Calculation	$\bar{x}$	σ	$\bar{x} + 3\sigma$
Variability	3.17	0.19	3.74
Power Spectrum	0.003	0.001	0.006
Cross-Correlation	0.06	0.01	0.09

m to obtain a singular value, which we will refer to as x_p. The average power spectrum of the random-longitude emergence arrays are flat distributions in m (i.e. with no prominent peaks for any certain longitudinal mode), so averaging the power spectrum over m is reasonable so that we can obtain a baseline value for the normalized power above which our results are significant. We do a similar treatment for the cross-correlation calculations, averaging the cross-correlation calculations from the random-longitude emergence arrays over 19 rotation periods and lag, calling this value x_c. The average cross-correlation is a spatial distribution, however the distribution is also flat when random-longitude emergence arrays are used.

(3) We perform Steps 1 and 2 a total of 1,000 times, averaging over the 1,000 values of x_v, x_p, and x_c to obtain $\bar{x}_v$, $\bar{x}_p$, and $\bar{x}_c$. We then calculate the variance σ^2 for each quantity:

$$\sigma^2 = \frac{1}{N}\sum_{i=1}^{N}[x_i - \bar{x}]^2, \tag{H.20}$$

where $N = 1,000$. We have assumed that the values x are normally distributed around their corresponding values $\bar{x}$. We then arrive at the 3σ confidence level, which takes on a value of $\bar{x} + 3\sigma$ for each quantity $\bar{x}_v$, $\bar{x}_p$, and $\bar{x}_c$. Using the random-longitude emergence arrays, representative values of $\bar{x} + 3\sigma$ are shown in Table H.3.